**Title**

Low-Valent, High-Spin Iron Chemistry and Late Transition Metal Complexes of Benzannulated Boron Heterocycles

**Author**

Essex, Laura Ann

**Publication Date**

2020

UNIVERSITY OF CALIFORNIA
RIVERSIDE

# Low-Valent, High-Spin Iron Chemistry and Late Transition Metal Complexes of Benzannulated Boron Heterocycles

A Dissertation submitted in partial satisfaction
of the requirements for the degree of

Doctor of Philosophy

in

Chemistry

by

Laura Essex

September 2020

Dissertation Committee:
  Dr. W. Hill Harman, Chairperson
  Dr. Vincent Lavallo
  Dr. Matthew Conley

The Dissertation of Laura Essex is approved:

Committee Chairperson

University of California, Riverside

# *Acknowledgements*

There's a number of people I would like to thank, without which this work would not be possible. First, I would like to thank Hill Harman for his patient mentorship (and liberal XRD submission policy) throughout my graduate career. However reclusive, his well-meaning attempts to mimic human behavior were received far better than he believes. I cherished the rare opportunities that he shared his opinions and sincerely wish I had more time to extract them. Hilldawg's a national treasure. The largesse of this work would not have existed without the seminal work done by Alex McSkimming, of which this dissertation merely elaborates on. Alex is an exceptional synthetic chemist and unapologetic Australian whose customs took time to acclimate to. His mark on Hill's lab indeed recapitulates on his endearing title of "Swag Lord." I send my warmest regards to his independent research career. My first three years were entirely fruitless endeavors of which I wouldn't have continued were it not for Jordan Taylor, my lab mate, and now fiancé, whom offered endless encouragement which I could not have survived without. Without exaggeration, Jordan is flawless. I often find it difficult to believe that he can encompass both talent and compassion to such extremes. There's only one Jordan and I can't believe he's with me.

Fook Tham's endless knowledge of crystallography made it possible to solve many of the structures herein. I thank him for his patience in lab and on the dance floor. His tango prowess is legendary. Crystallographer Charlene Tsay was also instrumental in my final year at UCR. Her expertise as both crystallographer and inorganic chemist combined with her great attention to detail was immeasurate. Spectroscopist and tie-dye-wearing Dead-

Head, Dan Borchardt, how you suffered at the expense of our aging NMR instruments until their ultimate replacement in 2019. You deserve a medal for keeping literally every instrument (Raman, UV, etc) on campus functioning after an ceaseless onslaught of first year students “winging-it,” myself included. No amount of Macallan scotch can rectify that, but I’m sure it helped. Under such circumstances your protégé, Lingchao Zhu, has performed admirably. I extend my thanks for him setting up the $^{195}$Pt experiments and being steadfast in the perpetual maintenance of these instruments without which our research could not contiune.

During my undergraduate years, I was fortunate to be placed in Nathaniel Szymczak’s lab, who was instrumental in my formative years as a chemist. Under his tutelage, I was given more free reign in a glovebox than I should’ve been granted. A young chemist is both literally and figuratively a firestarter, and I’m grateful for his guidance. However, if it weren’t for Bing Ye, I would’ve never attempted to become a scientist in the first place. To this day, I still use the careful pipetting technique he taught me, and I do my best to apply the elegant experimental logic of molecular biology (i.e. knock-outs, knock-ins, and over-expression) to solve chemical problems. I must also thank Roy Wentz, artisan glassblower, for the impeccable glassware he created for my research in addition to his spiritual guidance. Hopefully it wasn’t all lost on me.

Finally, I must express my gratitude to my family, old and new. My parents were less than thrilled with my early pursuits in chemistry, however now they can’t stop asking about my ligands or if I have a new crystal. I’m blessed to have been born into a family of both loving and curious people. My mother’s tenacity and my father’s undeterrable attitude created the ideal environment for my brother and I to become tinkerers of our own kind. I have to thank my brother and his wife for always being a shoulder to lean on. I'm grateful that he met his wife Jacqui, who's not only able to understand the wierdness of the Essex family, but able to embrace it. I must also extend my thanks to Tariq Bhatti, who's part of our adopted family with whom delivered advice and opinions with a sophistication I'll never approach. To my new family, I must thank Myrna and Jim Weikengnant for lending their ear through our many troubles adjusting to life in Riverside. I also thank Jeff Taylor for our many opinionated, yet respectful discussions and his encouragement of my scientific endeavors.

The text, figures, and schemes for the following chapters have been reproduced, in part from the following published manuscripts.

Chapter 1:
Essex, L. A.; McSkimming, A.; Thompson, N. B.; Kelty, M. L.; Hill, E. A.; Harman, W. H. $\eta^2$-Arene Binding at High-Spin Fe(I) Enabled by a Sterically Accommodating Tris(Pyrazolyl)Hydroborate Ligand. *Organometallics* **2020**, *39* (13), 2545–2552. https://doi.org/10.1021/acs.organomet.0c00340.

Chapter 4:
Essex, L. A.; Taylor, J. W.; Harman, W. H. Nickel Complexes of Phosphine-Appended Benzannulated Boron Heterocycles. *Tetrahedron* **2019**, *75* (15), 2255–2260. https://doi.org/10.1016/j.tet.2019.02.047.

## ABSTRACT OF THE DISSERTATION

## Low-Valent, High-Spin Iron Chemistry and Late Transition Metal Complexes of Benzannulated Boron Heterocycles

by

Laura Essex

Doctor of Philosophy, Graduate Program in Chemistry
University of California, Riverside, September 2020
Dr. W. Hill Harman, Chairperson

Transition metal catalysis is largely dominated by two electron transformations, often performed by third row, late transition metals. Herein we have largely concentrated on the opposite, using iron in a weak ligand field (via trispyrazolyl borate, Tp ligands) to access low-valent, high-spin species and utilized steric bulk to access new and interesting low coordinate species. Herein we report the first high-spin $\eta^2$-arene metal complexes and their properties. While the arene is bound weakly, spin density is conferred to it upon binding. Using this same strategy at iron, we report a novel C−H activation mechanism by combining our low-valent, high-spin iron center with a bulkly phenoxyl radical. This enabled the activation of $sp^3$, $sp^2$, and sp C−H bonds in 2-butyne, ethylene, and phenylacetylene. In a digression from iron, we've also designed ligands that incorporate boron into the ligand scaffold to stabilize highly reduced metals, allowing us to isolate and characterize the first molecular dianionic platinum compound.

## Table of Contents

## List of Figures

## List of Schemes

## List of Tables

# Chapter 1 : Dihapto Arene Binding at High Spin Fe(I)

## Introduction

Arenes are an important class of ligands in organometallic chemistry,[1–3] serving as spectator ligands or substrates in the functionalization of the arene itself. The hapticity of unsupported arene ligands is determined by the electronic properties of the metal center to which it is bound, according to the 18-electron rule and related concepts. If sterically accessible, $\eta^6$ binding is the norm, as it preserves the aromaticity of the arene. With electron-deficient metal fragments, hexahapto coordination can imbue reactivity with nucleophiles (e.g. group 6 $(CO)_3M$(arene) complexes).[4,5] In some cases, ring-slippage to tetrahapto coordination occurs, as in the reduction of $[(\eta^6\text{-}C_6Me_6)_2Ru]^{2+}$ to $(\eta^6\text{-}C_6Me_6)Ru(\eta^4\text{-}C_6Me_6)$.[6] With some metal fragments, dihapto binding of arenes is observed,[7–11] and in the case of electron-rich, π-basic metal fragments, the metal-arene interaction is driven by strong backbonding (Figure 1-1). This transfer of electron density into the arene π* orbitals perturbs the aromaticity of the ring system and can drive reactivity of the bound arene with electrophiles.[12,13] Owing to the use of strong-field ligands and/or second- and third-row metals, the $\eta^2$-arene complexes reported to date tend to be electronically saturated and low-spin. We have been interested in the chemistry of low-valent Fe fragments supported by trispyrazoylhydroborate (Tp) ligands,[14] which, in the Fe(I) state, bind unsaturated ligands (e.g. $N_2$[15,16] and CO[17]) with strong activation of the substrate via backbonding. Crucially, the metal centers in these complexes populate a high-spin ($S$ = 3/2) ground state despite the coordination of a π-accepting substrate. Low-coordinate TpFe complexes can be prepared with bulky Tp ligands of the "tetrahedral enforcer" variety,[18–21] and their sterically encumbered Fe centers limit the size of accessible fourth ligands. Herein we report the development of a new Tp scaffold which, while bulky enough to allow the preparation of low-coordinate TpFe(I) complexes, contains an open face due to a regiochemical switch where one of the larger substituents is oriented away from the apical pocket This steric accommodation allows for the access of larger ligands to the metal center. Using this weak-field Fe(I) fragment, we have prepared the first examples of high-spin, $\eta^2$-arene/heteroarene adducts and definitively established their spin state via EPR and solution magnetometry.

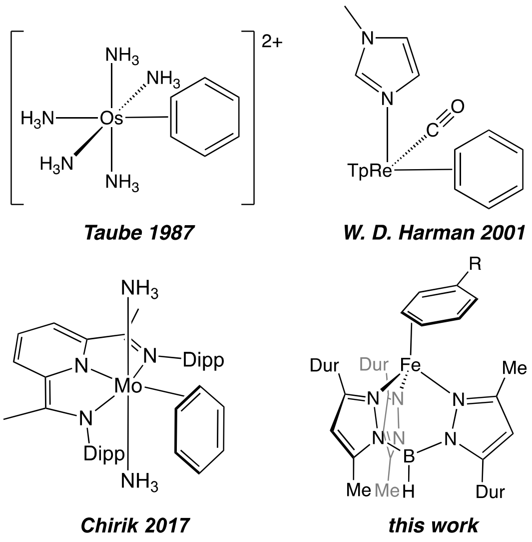

**Taube 1987**

**W. D. Harman 2001**

**Chirik 2017**

**this work**

Figure 1-1. A selection of mononuclear $\eta^2$-arene complexes of $\pi$-basic transition metal fragments (Dur = 2,3,5,6-tetramethylphenyl, Dipp = 2,6-diisopropylphenyl).

## *Results and Discussion*

After discovering that sufficiently bulky Tp ligands could enable access to an unprecedented mononuclear $S = 3/2$ Fe(I) complex of $N_2$,[15] we began to explore other Tp variants in order to find supporting ligands that were less sterically imposing but still capable of supporting low-coordinate, monometallic Fe(I) centers. To this end, we synthesized a Tp ligand derived from the novel pyrazole 5-methyl-3-duryl-1H-pyrazole (**2**, duryl = Dur = 2,3,5,6-tetramethylphenyl). After subjecting **2** to standard Tp synthesis conditions with $NaBH_4$, we isolated a single product whose $^1H$ NMR spectrum was inconsistent with a threefold symmetric Tp scaffold (Scheme 1-1, Figure 1-8). Instead, the solution $^1H$ features two different sets of pyrazole resonances in a 2:1 ratio, consistent with an inversion of the regiochemistry of the B–N bond forming step for one of the pyrazoles to give sodium bis(5-methyl-3-(2,3,5,6-tetramethylphenyl)-1-pyrazolyl)(3-methyl-5-(2,3,5,6-tetramethylphenyl)-1-pyrazolyl)hydroborate ($NaTp^{Me,Dur}$, **3**) in 56% yield. This regiochemistry has been observed in other Tp derivatives and is presumably a consequence of very bulky aryl substituents at the 3-position of the pyrazole.[22–24] Compound **3** is noteworthy, however, for the relative ease of its synthesis.

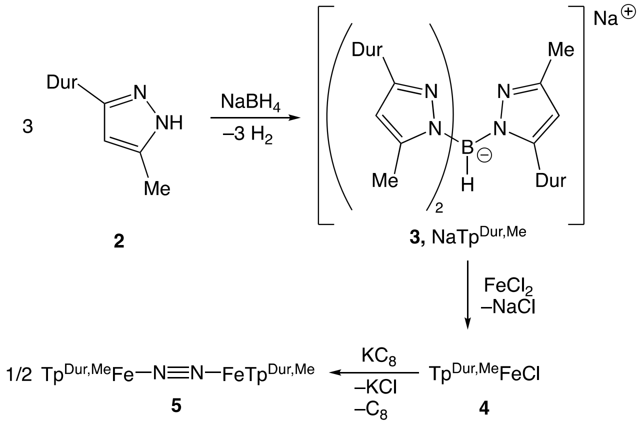

Scheme 1-1. Synthesis of $[Tp^{Dur,Me}]^-$ and Its Iron Complexes

The novel Tp ligand **3** could be metallated with iron(II) chloride to give the paramagnetic complex $Tp^{Me,Dur}FeCl$ (**4**, Scheme 1-1). Single-crystal X-ray diffraction (XRD) confirmed this structural assignment and the unusual regiochemistry of **3**, revealing a pseudotetrahedral Fe(II) center flanked by two duryl substituents and a methyl group (Figure 1-2). A single, irreversible reduction event was observed for **4** at $E_{p,c}$ = –2.97 V vs. Fc/$Fc^+$ by cyclic voltammetry in THF (Figure 1-33) indicating the plausibility of accessing formally Fe(I) complexes with this framework. To wit, reduction of **4** with $KC_8$ affords the formally Fe(I) $N_2$ complex $(Tp^{Me,Dur}Fe)_2(\mu\text{-}N_2)$ (**5**, Scheme 1), which, despite the significant steric bulk presented by the duryl substituents, was shown to exist as a bimetallic complex with a bridging $N_2$ ligand in the solid state by XRD (Figure 1, bottom). While complex **5** is structurally analogous to the complex $(Tp^{Ph,Me}Fe)_2(\mu\text{-}N_2)$ previously reported by our group,[15] the phenyl-substituted analogue exhibits nearly perfect threefold symmetry due to the interdigitation of the phenyl substituents. In contrast, the TpFe units in **5** are strongly canted away from the latent threefold axis, with the methyl group, due to its smaller size, encroaching on the bridging $N_2$ ligand. Complex **5** is dark red both in the solid state and in THF solution. Like its phenyl-substituted analogue, **5** exhibits an intense band at 910 nm in the UV-vis-NIR spectrum, consistent with an intact Fe–$N_2$–Fe unit in solution.[15,25] Unlike its phenyl congener, however, **5** undergoes an immediate and reversible color change to black when dissolved in benzene under $N_2$, accompanied by the disappearance of the NIR feature characteristic of the Fe–$N_2$–Fe unit. Working under argon allows the isolation of this material as a black microcrystalline solid. Despite significant effort, we have been unable to generate single crystals suitable for its structural characterization via XRD. Vibrational spectroscopy provided no indication of a bound $N_2$ ligand, and combustion analysis is consistent with the formulation of this complex as the benzene adduct $Tp^{Dur,Me}Fe(C_6H_6)$ (**6**). Solution magnetometry conducted on **6** by the method of Evans[26,27] gave an effective magnetic moment of 3.9 ± 0.1 $\mu_B$, consistent with a high-spin, monometallic Fe(I) complex. In further support of the high-spin assignment, the X-band EPR spectrum of **6** in 2-methyltetrahydrofuran (2-MeTHF) at 109 K contained a broad feature spanning ~0–500 mT (Figure 1-27), inconsistent with an $S = ½$ complex. Given the rarity of arene complexes featuring high-spin metal centers, we were eager to gain more information on this class of molecules and so turned to alternate arene ligands in order to identify related complexes amenable to structural characterization.

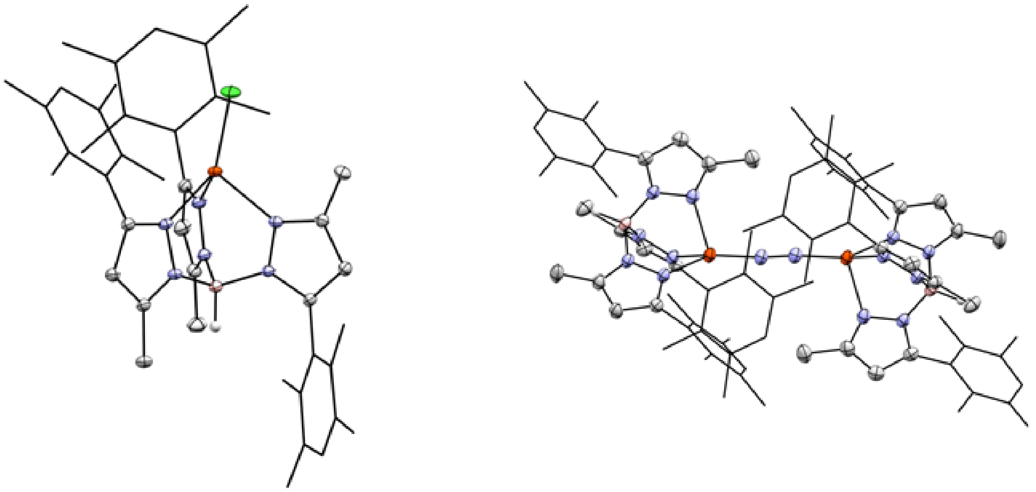

Figure 1-2. Thermal ellipsoid plots (50% probability) of the solid-state structure of $Tp^{Me,Dur}FeCl$ (**4**, left) and $(Tp^{Me,Dur}Fe)_2(\mu\text{-}N_2)$ (**5**, right). Orange, blue, pink, and gray ellipsoids represent Fe, N, B, and C atoms, respectively. Most hydrogen atoms and co-crystallized solvent molecules are omitted for clarity.

Due to its electron deficient character, $PhCF_3$ has been used as a benzene surrogate in systems that bind arenes in a dihapto fashion,[28] with an ~3 kcal/mol greater binding energy reported for a Mo(0) system.[29] Dissolution of **5** in $PhCF_3$ under argon resulted in the quantitative formation of a new purple species (Scheme 1-2.) with a solution magnetic moment ($\mu_{eff} = 3.9 \pm 0.1$ $\mu_B$) and optical properties (Figure 1-23) similar to those of **6**. Slow evaporation of a pentane solution of this material gave single crystals which were shown by XRD to be the dihapto arene complex Tp$^{\mathrm{Dur,Me}}$Fe(3,4-$\eta^2$-PhCF$_3$) (**7**, Figure 1-3). Compound **7** is the first example of a crystallographically characterized $\eta^2$-PhCF$_3$ complex, and its solid-state structure contains two crystallographically independent but chemically equivalent molecules with minor variations in bond distances. The coordinated π bond is elongated significantly ($d_{\mathrm{C–C}}$ = 1.427(4), 1.428(4) Å) compared to free PhCF$_3$,[30] and the uncoordinated portion of the arene exhibits bond lengths consistent with perturbation of the aromaticity of the bound ligand (Figure 1-3, right). Inspection of a space-filling model of **7** suggests that the open face of the Tp$^{\mathrm{Dur,Me}}$ ligand with the flanking methyl group is critical for accommodating arene binding to this otherwise sterically bulky fragment.

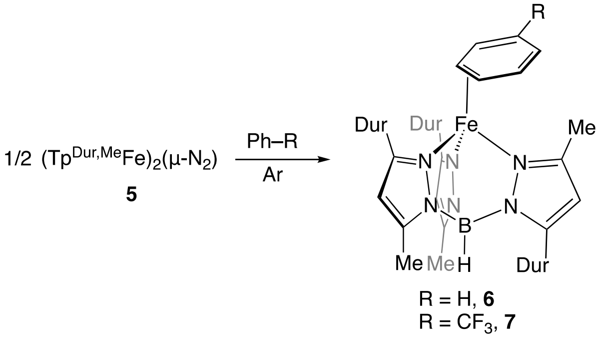

Scheme 1-2. Synthesis of Tp$^{\mathrm{Dur,Me}}$Fe(I) Arene Complexes

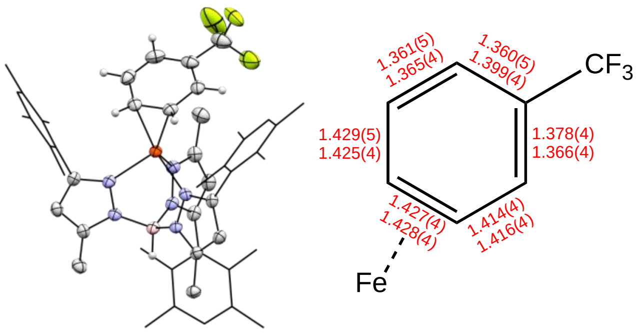

Figure 1-3. Thermal ellipsoid plot (50% probability) of one of independent molecules in the solid-state structure of Tp$^{\mathrm{Me,Dur}}$(3,4-$\eta^2$-PhCF$_3$) (**7**, left) and selected bond lengths for both independent molecules

(right). Bond lengths are given in Å. Orange, blue, pink, and gray ellipsoids represent Fe, N, B, and C atoms, respectively. One disordered $CF_3$ group, co-crystallized solvent molecules, and most hydrogen atoms have been omitted for clarity.

Having confirmed the structure of **7** via single crystal XRD, we were eager to definitively establish its spin-state. Like complex **6**, the X-band EPR spectrum of **7** at 105 K is extremely broad (Figure 1-26). However, a sample of **7** in hexane cooled to 15 K exhibits a well-resolved spectrum with features at $g_{\mathrm{eff}}$ values of 5.8, 2.3, and 1.7, consistent with rhombic $S = 3/2$ complex ($E/D \approx 0.3$) with $g_{\mathrm{iso}} > 2$ (Figure 1-4).[31] The $^{57}$Fe Mossbauer spectrum of **7** contains a quadrupole doublet with an isomer shift of 0.951 mm/s and a quadrupole splitting of 1.011 mm/s. (Figure 1-31). Although Mössbauer data on low-coordinate TpFe complexes are scant, the large isomer shift is consistent with a high-spin assignment.[32,33]

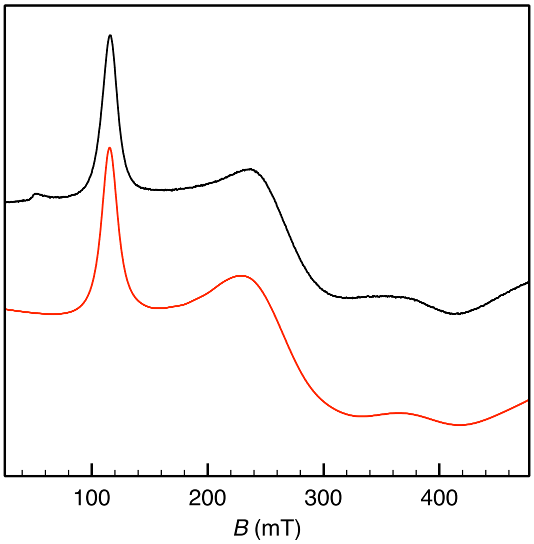

Figure 1-4. X-band EPR spectrum (9.631 GHz) of $Tp^{Me,Dur}Fe(3,4\text{-}\eta^2\text{-}PhCF_3)$ in hexane at 15 K (black) and its simulation (red) with the following parameters: $g$ = [2.4, 2.2, 2.2], $E/D$ = 0.31. See Supporting Information for simulation details.

Density functional theory (DFT) calculations of the model complex $TpFe(3,4\text{-}\eta^2\text{-}PhCF_3)$ were carried out on both the doublet and quartet manifolds in order to gain further insight into the electronic structure of **7** (M06L[34] with a custom Alrichs basis[35] set via ORCA,[36] see SI). Although energy minima featuring dihapto arene coordination could be converged in both spin states (Figure 1-40 and 1-41), the $S = 3/2$ configuration was significantly lower in energy ($\Delta E = 0.0389\ E_h$) and better reproduced the longer Fe–N and Fe–C bond lengths observed by XRD. A spin density plot generated for the high-spin structure of TpFe(3,4-$\eta^2$-PhCF$_3$) (Figure 1-5) shows significant spin delocalization onto the bound arene, with Mulliken spin populations of 3.33 at Fe and –0.13 on each of the two bound carbons. We observed a similar phenomenon in our computational investigation of the related terminal $N_2$ complex Tp$^{Ad,Me}$Fe(N$_2$),[15] and this spin polarization may be a key difference between π-basic fragments with weak ligand fields and more typical strong-field π-bases.[37,38]

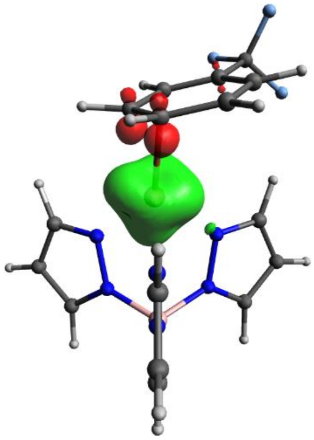

Figure 1-5. Spin-density isosurface (0.01) calculated for the model high-spin complex TpFe($\eta^2$-PhCF$_3$). Green represents positive spin and red represents negative spin. Mulliken spin populations: Fe = 3.33, C1 = −0.13, C2 = −0.13.

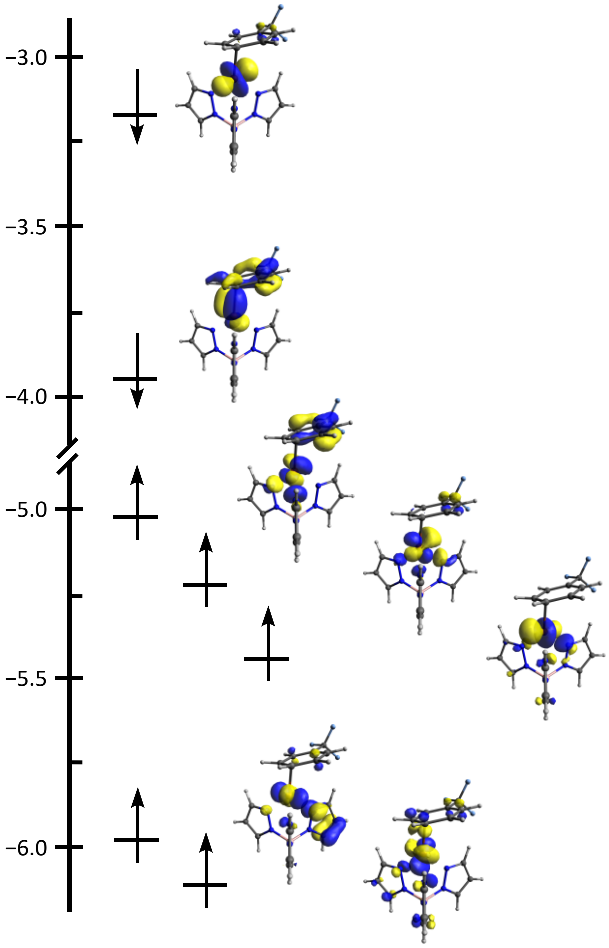

Figure 1-6. Canonical single-electron Kohn−Sham orbitals calculated for TpFe(3,4-$\eta^2$-PhCF$_3$) at an isosurface value of 0.05 (see text for computational details). Orbital energies are in eV.

Having established that **7** is a bona fide high-spin Fe(I) complex of a dihapto arene, we explored the generality of this motif. Treatment of **5** with naphthalene, anthracene, and furan under Ar gave rise to isolable complexes of the form Tp$^{\text{Dur,Me}}$Fe($\eta^2$-L) (Scheme 1-3) where L = naphthalene (**8**), anthracene (**9**), and furan (**10**). Complex **8** can also be synthesized directly from **4** via reduction with K($C_{10}H_8$). Like **7**, compounds **8**–**10** are also $S = 3/2$, with solution magnetic moments ranging from 3.7–3.9 $\mu_B$ and broad X-band EPR spectra spanning hundreds of mT (Figure 1-28, 1-29, and 1-30). Single crystal XRD confirms the dihapto ligand binding in **8–10** (Figure 1-7). These structures feature lengthening of the coordinated C–C bond ($d_{C–C}$ > 1.4 Å) consistent with significant backbonding, and **10** is a rare example of a structurally characterized mononuclear η$^2$-furan complex.[39,40] Although complexes **6** and **7** slowly reform the bridging $N_2$ complex **5** in the presence of $N_2$, **8** and **9** are indefinitely stable in ethereal solvents under the same conditions. The furan complex **10**, however, cannot be prepared except by the rigorous exclusion of $N_2$, and we observed no binding between the Tp$^{Dur,Me}$Fe(I) fragment and N-methylpyrrole. These findings are consistent both with the diminished aromaticity of naphthalene and anthracene relative to benzene as well as the centrality of backbonding to these interactions, weakening the ability of the electron-rich substrates furan and N-methylpyrrole to coordinate.

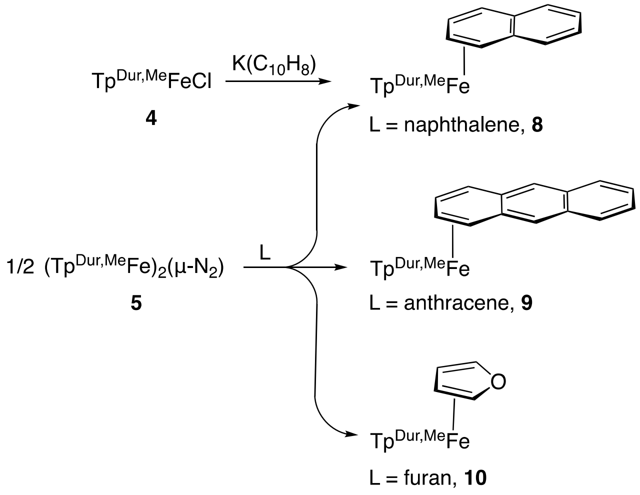

Scheme 1-3. Synthesis of Polycyclic Arene and Heteroarene Complexes of Tp$^{Dur,Me}$Fe(I)

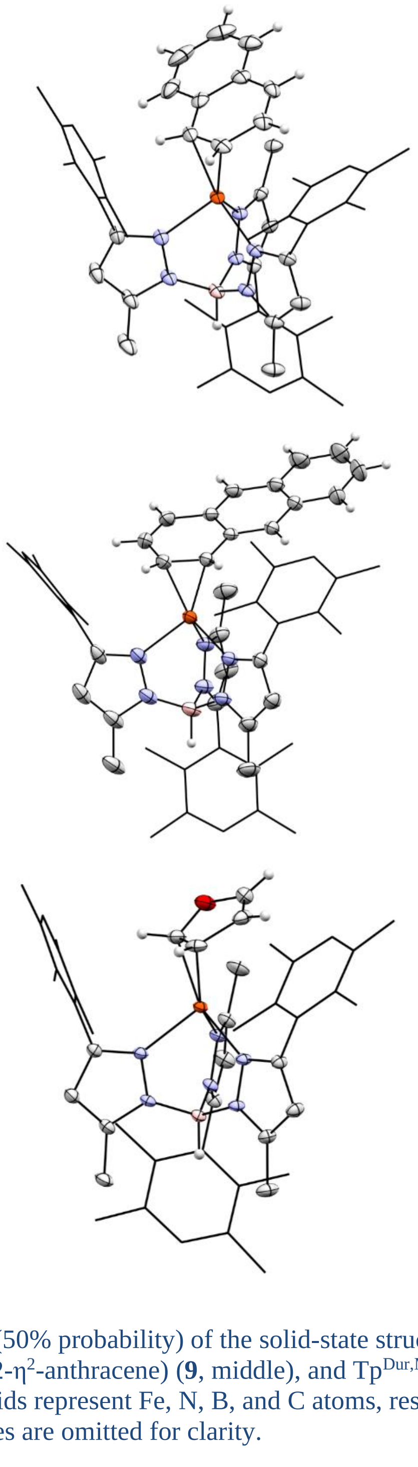

Figure 1-7. Thermal ellipsoid plots (50% probability) of the solid-state structures of Tp$^{\mathrm{Dur,Me}}$Fe(1,2-$\eta^2$-naphthalene) (**8**, top), Tp$^{\mathrm{Dur,Me}}$Fe(1,2-$\eta^2$-anthracene) (**9**, middle), and Tp$^{\mathrm{Dur,Me}}$Fe(1,2-$\eta^2$-furan) (**10**, bottom). Orange, blue, pink, and gray ellipsoids represent Fe, N, B, and C atoms, respectively. Most hydrogen atoms and co-crystallized solvent molecules are omitted for clarity.

## *Conclusions*

We have developed a new, readily synthesized Tp ligand which is bulky enough to support low-coordinate Fe(I) complexes while preserving a binding site that can accommodate large unsaturated ligands. This fragment binds a range of arenes and heteroarenes to give dihapto complexes that populate a high-spin ($S = 3/2$) ground state. These compounds are unusual given the plethora of low-spin Fe(I) complexes featuring hexahapto arene coordination[25,41,42] and the lack of high-spin dihapto arene complexes. DFT calculations suggest the delocalization of unpaired spin onto the bound arene, and, given the utility of dihapto coordination in the functionalization of arenes with electrophiles, we are currently exploring analogous chemistry, with a focus on radical-mediated processes.

## *Experimental Section*

General Considerations: Unless stated otherwise, all compounds were purchased from commercial sources and used without further purification. 2,3,5,6-tetramethylacetophenone was prepared according to a literature procedure.[43] Solvents were dried and deoxygenated by argon sparge followed by passage through an activated alumina column and were stored over 4 Å molecular sieves. All manipulations were performed under an $N_2$ or argon atmosphere either in a glovebox or using standard Schlenk techniques. $^1$H NMR spectra were recorded at 298 K using Bruker 400 MHz instruments. Chemical shifts are referenced to residual solvent peaks, IR spectra were recorded using a Bruker Alpha FT-IR with a universal sampling module collecting at 4 cm$^{-1}$ resolution with 32 scans. EPR X-band spectra collected above 100 K were recorded using a Bruker EMX spectrometer and analyzed using Win-EPR software. EPR spectra collected at 15 K were recorded on a Bruker ELEXSYS E500 spectrometer with an Oxford ESR 900 X-band cryostat and a Bruker Cold-Edge Stinger. UV-Vis spectra were recorded using a Cary Bio 500 spectrometer using a 1 cm path length quartz cuvette with a solvent background subtraction applied. X-ray diffraction studies were performed using a Bruker-AXS diffractometer. Elemental Analyses were performed by Midwest Microlabs. Solution phase effective magnetic moments were obtained via the method described by Evans[**Error! Bookmark not defined.**] and were performed in triplicate. Standard deviations are reported. The Mössbauer spectrum was recorded on a spectrometer from SEE Co. (formerly WEB Research Co.) operating in the constant acceleration mode in a transmission geometry. The sample was kept in an SVT-300 cryostat from Janis (Wilmington, MA), using liquid $N_2$ as a cryogen for 80 K measurements. Data analysis was performed using version 4 of the program WMOSS (www.wmoss.org) and quadrupole doublets were fit to Lorentzian lineshapes.

*Synthesis of 1-(2,3,5,6-tetramethylphenyl)butane-1,3-dione* ***(1).*** A solution of 2,3,5,6-acetophenone (20.0 g, 0.113 mol) in 250 mL of dry THF was refluxed with sodium hydride (6.00 g, 0.250 mol) for 1 hour. The suspension was then cooled to room temperature and ethyl acetate (20.0 mL, 0.203 mol) was added dropwise. Following the addition, the mixture was refluxed again for 6 hours. After cooling to room temperature, the reaction mixture was then quenched with 200 mL water, and then extracted with 200 mL of diethyl ether three times. The aqueous layer was then acidified with 35% hydrochloric acid and extracted again with 200 mL of ether three times. The ether extracts from the acidified aqueous layer were combined, dried over sodium sulfate, and the volatiles removed *in vacuo*. This procedure was repeated three times yielding a combined ~50 g of yellow oil, which was then distilled at 86 °C under vacuum (0.77 mm Hg) to yield a colorless oil which crystallized on cooling to room temperature. Yield: 38 g (51%). $^1$H NMR (400 MHz, $CDCl_3$) δ 6.98 (s, 1H), 5.61 (s, 1H), 2.22 (s, 6H), 2.16 (s, 3H), 2.15 (s, 6H). $^{13}$C NMR (101 MHz, $CDCl_3$) δ 193.6, 189.8, 137.4, 134.1, 132.0, 130.1, 103.1, 25.8, 19.7, 16.3. HRMS (ESI): *m/z* for $C_{14}H_{19}O_2$ $[M+H]^+$ calcd.: 219.1385, found: 219.1375.

*Synthesis of 5-methyl-3-(2,3,5,6-tetramethylphenyl)-1H-pyrazole (**2**).* A solution of **1** (38 g, 0.17 mol) in ethanol was added to a stirring solution of hydrazine monohydrate in ethanol, and the resulting solution brought to reflux. After 16 h, the reaction mixture was partitioned between 400 mL of water and 400 mL of ether. The aqueous layer was extracted with 200 mL of ether three times. The combined ether extracts were washed twice with 100 mL of water. The ether extract was subsequently dried over $Na_2SO_4$, and the volatiles removed *in vacuo*, resulting in a colorless crystalline solid. Yield: 35 g (94 %). $^1$H NMR (400 MHz, $CDCl_3$) δ 10.79 (br s, 1H), 6.99 (s, 1H), 5.91 (s, 1H), 2.23 (s, 6H), 2.21 (s, 3H), 1.95 (s, 6H). $^{13}$C NMR (101 MHz, $CDCl_3$) δ 146.2 (br), 145.4 (br), 133.9, 133.5, 131.6 (br), 131.6, 105.5, 20.0, 16.8, 12.5. HRMS (ESI): *m/z* for $C_{14}H_{19}N_2$ $[M+H]^+$ calcd.: 215.1548, found: 215.1567.

*Synthesis of Sodium bis(5-methyl-3-(2,3,5,6-tetramethylphenyl)-1-pyrazolyl)(3-methyl-5-(2,3,5,6-tetramethylphenyl)-1-pyrazolyl)hydroborate (NaTp$^{Dur,Me}$, **3**).* A hot Schlenk flask was charged with **2** (20.0 g, 93 mmol), evacuated, and then placed under nitrogen. Sodium borohydride (1 g, 26 mmol) was added to the flask under a flow of nitrogen. The flask was sealed with a glass stopper and heated to 303°C for 3 hours. After being allowed to cool to 60°C, and the viscous oil was triturated with acetonitrile, yielding a pure white solid. Yield: 10 g (56%). $^1$H NMR (600 MHz, $C_6D_6$) δ 6.99 (s, 1H), 6.94 (s, 2H), 5.95 (s, 1H), 5.85 (s, 2H), 2.21 (s, 6H), 2.21 – 2.18 (m, 15H), 2.17 (d, 6H), 2.02 (br s, 12H), 1.93 (s, 6H). $^{13}$C NMR (151 MHz, $C_6D_6$) δ 151.0, 149.3, 147.4, 144.6, 137.6, 136.0, 134.4 (br), 134.1, 133.2, 133.0, 131.2, 130.9, 104.9, 104.3, 20.3, 17.3 (br), 17.1, 14.5, 13.1. HRMS (ESI): m/z for $C_{42}H_{54}BN_6$ $[M+2H]^+$ calcd.: 653.4508, found: 653.4644.

*Synthesis of Tp$^{Dur,Me}$FeCl (**4**).* Under a nitrogen atmosphere, **3** (2.00 g, 2.96 mmol) was dissolved in 80 mL of dry THF and combined with anhydrous $FeCl_2$ (0.420 g, 3.31 mmol). The mixture was stirred for 4 hours, filtered through Celite, and concentrated to 10 mL *in vacuo*. The concentrate was layered with hexanes (20 mL), which precipitated colorless microcrystals. These were collected by filtration and washed with ether (5 mL). Yield: 2.2 g (99%). $^1$H NMR (400 MHz, $C_6D_6$) δ 61.31, 58.52, 56.76, 44.97, 11.58, 8.77, 6.47, 6.13, 3.64, 1.46, 0.24, −10.18, −28.37, −30.56. Evans Method ($d_8$-THF): $\mu_B$ 6.8 ± 0.1. FTIR: $\nu_{max}$ cm$^{-1}$ 2542 (B-H). Calc. for $C_{42}H_{52}BClFeN_6$: C 67.89; H 7.05; N 11.31. Found: C 68.06; H 7.03; N 11.31.

*Synthesis of ($Tp^{Dur,Me}Fe)_2(\mu\text{-}N_2)$ (**5**).* To a solution of **4** (0.500 g, 0.673 mmol) in 50 mL of toluene, potassium graphite (0.300 g, 2.22 mmol) was added. The reaction was monitored by NMR until completion (*ca* 6 hours). The suspension was filtered through celite and the filtrate was concentrated to 20 mL *in vacuo*. Layering the filtrate with hexane (40 mL) provided dark red cubic crystals. Yield: 210 mg (43%). $^{1}$H NMR (400 MHz, $d_8$-THF) δ 78.09, 67.24, 66.70, 54.50, 12.02, 6.89, 5.32, 1.28, 0.87, −4.20, −8.84, −9.78, −17.27, −29.15. Evan's Method ($d_8$-THF): $\mu_B$ 6.5 ± 0.1. FTIR: $\nu_{max}$ cm$^{-1}$ 2540 (B-H). Raman: $\nu_{max}$ cm$^{-1}$ 1770 (NN). UV-vis (THF): $\lambda_{max}$ (nm) ($\varepsilon_{max}$ (M$^{-1}$cm$^{-1}$)) 904 (3.5 x 10$^{3}$), 520 (2.9 x 10$^{3}$), 436 (3.4 x 10$^{3}$). Calc. for $C_{84}H_{104}B_2Fe_2N_{14}$: C 69.91; H 7.26; N 13.59. Found: C 69.81; H 7.51; N 13.71.

*$Tp^{Dur,Me}Fe(C_6H_6)$ (**6**).* Under an argon atmosphere, **5** (80 mg, 0.055 mmol) was dissolved in minimal benzene. The solvent was concentrated *in vacuo* to yield analytically pure black microcrystals. Yield: 87 mg (99%). $^{1}$H NMR (400 MHz, $C_6D_6$) δ 44.30, 38.90, 19.37, 11.18, 9.81, 6.58, 6.11, 5.93, 3.16, 2.67, 1.42, −2.64, −7.56, −10.44. $^{1}$H NMR (400 MHz, $d_8$-THF, argon) δ 130.52, 44.52, 38.68, 19.31, 11.26, 10.00, 7.30, 6.66, 6.06, 6.00, 3.32, 2.78, 0.89, −2.68, −7.67, −10.98. Evan's Method ($C_6D_6$): $\mu_B$ 3.9 ± 0.1. UV-Vis (Benzene) $\lambda_{max}$ (nm) ($\varepsilon_{max}$ (M$^{-1}$cm$^{-1}$)) 765 (sh, 5.4 x 10$^{2}$), 579 (1.3 x 10$^{3}$), 384 (sh, 3.2 x 10$^{3}$), 301 (sh, 6.4 x 10$^{3}$). Calc. for $C_{48}H_{58}BFeN_6$: C 73.38; H 7.44; N 10.70. Found: C 73.09; H 7.29; N 10.45.

*Synthesis of Tp$^{Dur,Me}$Fe(3,4-$\eta^2$-PhCF$_3$) (7).* Under an argon atmosphere, **5** (50 mg, 0.035 mmol) was dissolved in trifluorotoluene (0.5 mL), producing a deep purple solution. The volatiles were removed *in vacuo* yielding purple glaze that was dissolved in pentane. Slow evaporation afforded crystals suitable for XRD. Yield: 59 mg (99%). $^1$H NMR δ 56.28, 46.68, 39.52, 22.74, 12.26, 12.03, 7.71, 6.70, 3.87, 2.79, −7.27, −13.44. Evans Method ($C_6D_6$): $\mu_B$ 3.9 ± 0.1. UV-Vis (Trifluorotoluene): $\lambda_{max}$ (nm) ($\varepsilon_{max}$ ($M^{-1}cm^{-1}$)) 752 (sh, 5.1 x $10^2$), 549 (1.6 x $10^3$), 376 (sh, 3.4 x $10^3$), 303 (sh, 7.0 x $10^3$). Calc. for $C_{49}H_{57}BF_3FeN_6$: C 68.94; H 6.73; N 9.84. Found: C 68.69; H 6.74; N 9.69.

*Synthesis of Tp$^{Dur,Me}$Fe(1,2-$\eta^2$-napthalene) (**8**). Method 1:* Potassium naphthalenide・4/3 THF (74 mg, 0.363 mmol) was added to a solution of **4** (170 mg, 0.228 mmol) in toluene (12 mL). The reaction was monitored by NMR until all of the starting material was consumed (~4 hours). The reaction mixture was filtered through celite and concentrated *in vacuo* to 1 mL. Hexanes (4 mL) were added, and the mixture was cooled to −30°C, yielding dark olive-green crystals. Yield: 116 mg (61%). *Method 2:* Solid naphthalene (6 mg, 0.047 mmol) was added to a stirring solution of **5** (25 mg, 0.017 mmol) in toluene (2 mL). The solvent was concentrated *in vacuo* and layered with ether. Cooling to −30 °C overnight produced metallic olive-colored crystals suitable for single-crystal XRD. Yield: 25 mg (86%). $^1$H NMR (400 MHz, $C_6D_6$) δ 121.91, 42.53, 34.52, 27.24, 25.81, 12.41, 12.12, 11.12, 8.82, 7.58, 5.48, 3.84, 3.65, −12.27, −18.70. Evans Method ($d_8$-THF): $\mu_B$ 3.7 ± 0.1. UV-vis (THF): $\lambda_{max}$ (nm) ($\varepsilon_{max}$ ($M^{-1}cm^{-1}$)) 921(sh, 1.6 x $10^2$), 728 (sh, 3.6 x $10^2$), 533 (6.7

x $10^2$), 391 (sh, 1.7 x $10^3$). Calc. for $C_{48}H_{58}BFeN_6$: C 74.73; H 7.24; N 10.06. Found: C 74.47; H 7.40; N 10.77.

*Synthesis of Tp$^{Dur,Me}$Fe(1,2-$\eta^2$-anthracene) (**9**).* A stirring solution of **5** (23 mg, 0.016 mmol) in toluene (2 mL) was treated with solid anthracene (8 mg, 0.05 mmol). The solution turned from dark green to dark plum within seconds. The solvent was concentrated to 1 mL *in vacuo* and layered with hexane (2 mL). Cooling to −19°C produced dark purple crystals suitable for single-crystal XRD. Yield: 27 mg (96%). $^1$H NMR (400 MHz, $C_6D_6$) δ 139.28, 52.41, 41.88, 34.59, 21.52, 15.00, 13.81, 10.96, 10.17, 8.83, 7.65, 5.22, 3.86, 3.71, −12.39, −18.33. Evans Method ($d_8$-THF): $\mu_B$ 3.7 ± 0.2. UV-Vis (THF): $\lambda_{max}$ (nm) ($\varepsilon_{max}$ ($M^{-1}cm^{-1}$)) 700 (sh, 1.3 x $10^3$), 551 (sh, 2.1 x $10^3$), 516 (2.3 x $10^3$), 476 (sh, 2.0 x $10^3$), 402 (sh, 4.7 x $10^3$). Calc. for $C_{56}H_{62}BFeN_6$ (½ × $C_6H_{14}$): C 76.29; H 7.49; N 9.05. Found: C 76.66; H 7.67; N 9.02.

*Synthesis of Tp$^{Dur,Me}$Fe(2,3-$\eta^2$-furan) (**10**).* Under an argon atmosphere, **5** (80 mg, 0.055 mmol) was dissolved in furan (1 mL), producing a deep plum color. The solution was concentrated *in vacuo* to ~250 μL and layered with hexane (2 mL). Cooling to −19°C produced dark purple needles, suitable for XRD. Yield: 86 mg (99%). $^1$H NMR (400 MHz, $d_8$-THF, argon) δ 59.66, 47.57, 36.73, 30.00, 21.76, 9.52, 7.48, 7.19, 6.36, 1.30, 0.89, 0.13, −6.16. Evans Method ($d_8$-THF): $\mu_B$ 3.9 ± 0.1. UV-Vis (THF): $\lambda_{max}$ (nm) ($\varepsilon_{max}$ ($M^{-1}cm^{-1}$)) 800 (p, 5.35 x $10^2$), 561 (p, 1.32 x$10^3$), 371 (sh, 3.18 x $10^3$). Due to the high thermal sensitivity of this compound and despite repeated attempts, satisfactory elemental analysis could not be obtained. Spectra are provided below.

*NMR Spectra*

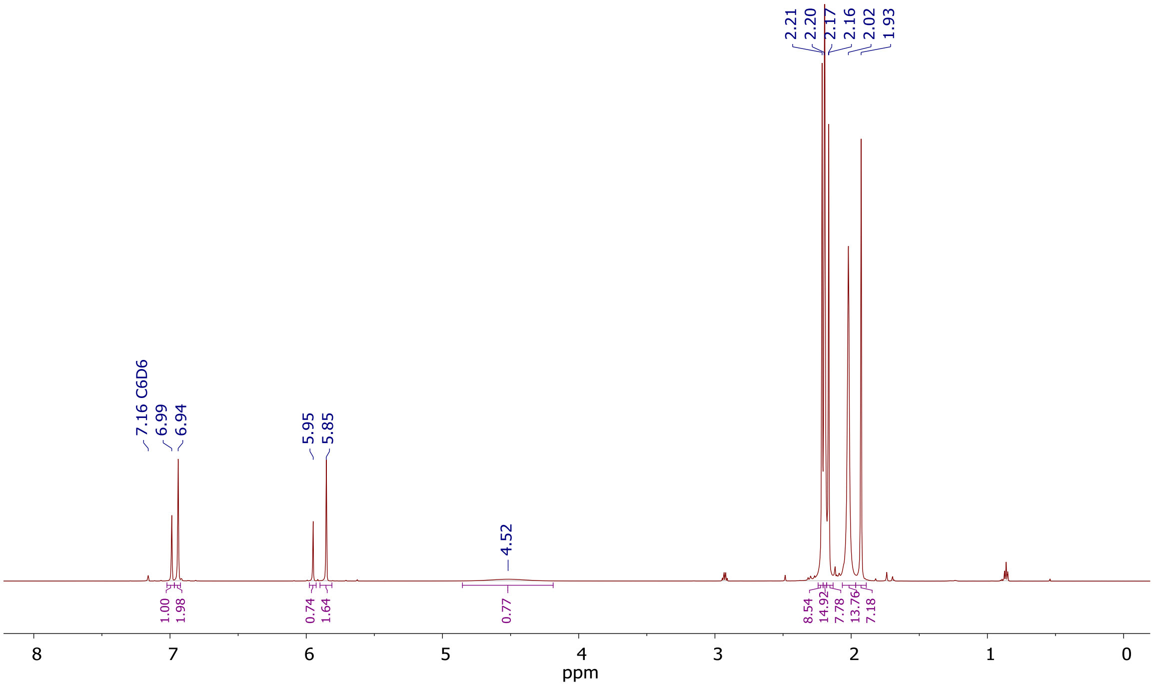

Figure 1-8. $^1$H NMR spectrum of NaTp$^{Dur,Me}$ (**3**) recorded at 400 MHz in $C_6D_6$.

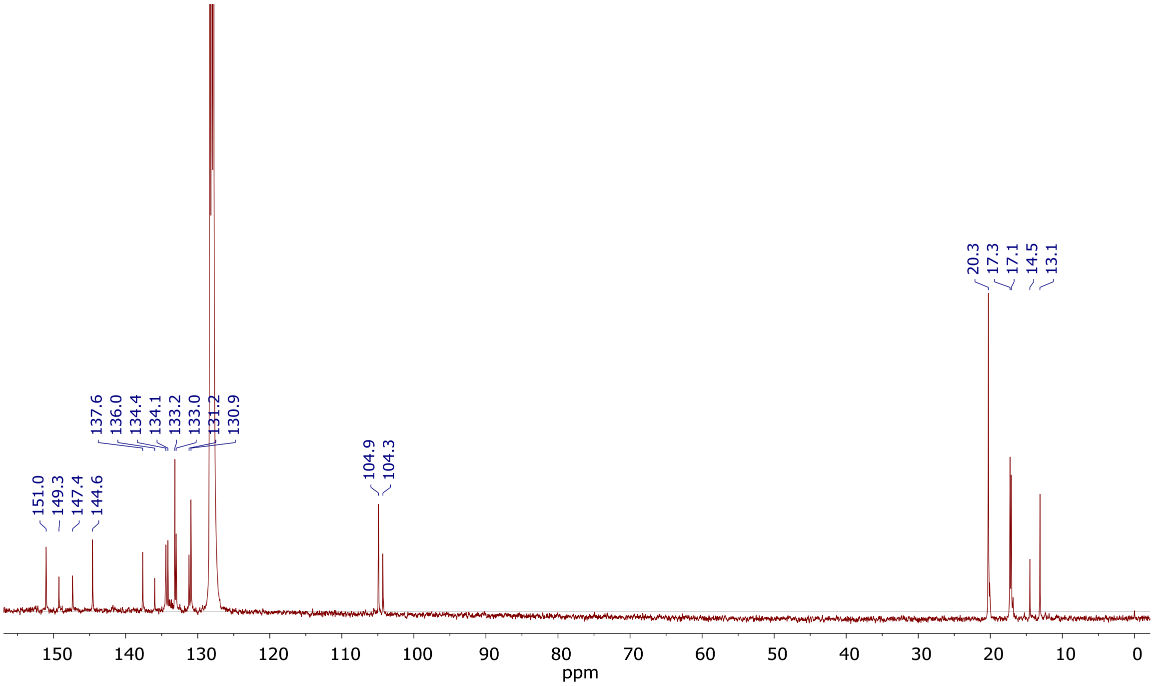

Figure 1-9. $^{13}$C NMR spectrum of NaTp$^{Dur,Me}$ (**3**) recorded at 101 MHz in $C_6D_6$.

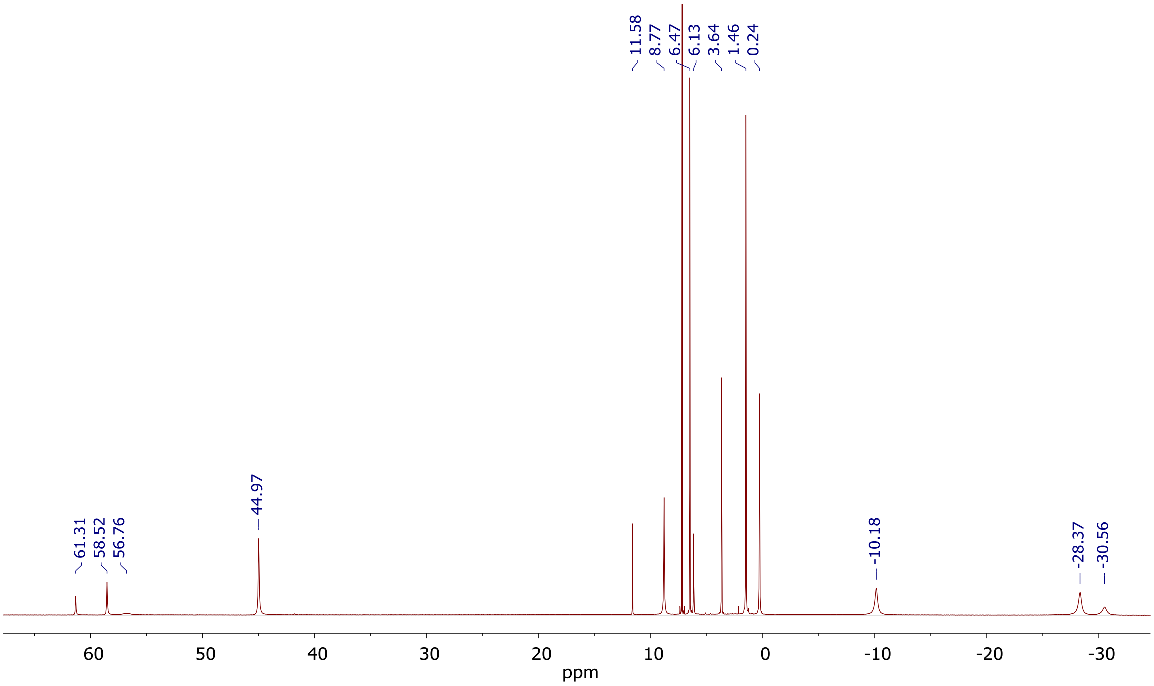

Figure 1-10. $^1$H NMR spectrum of Tp$^{Dur,Me}$FeCl (**4**) recorded at 400 MHz in $C_6D_6$.

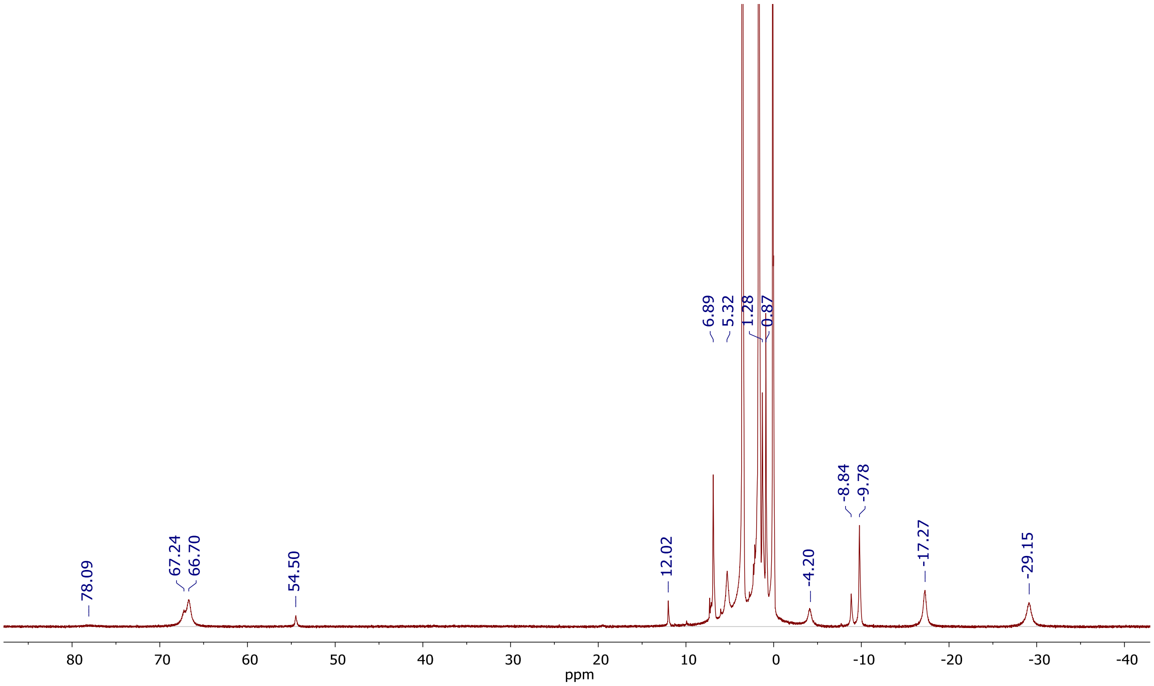

Figure 1-11. $^1$H NMR spectrum of (Tp$^{Dur,Me}$Fe)$_2$(N$_2$) (**5**) recorded at 400 MHz in *d*$_8$-THF.

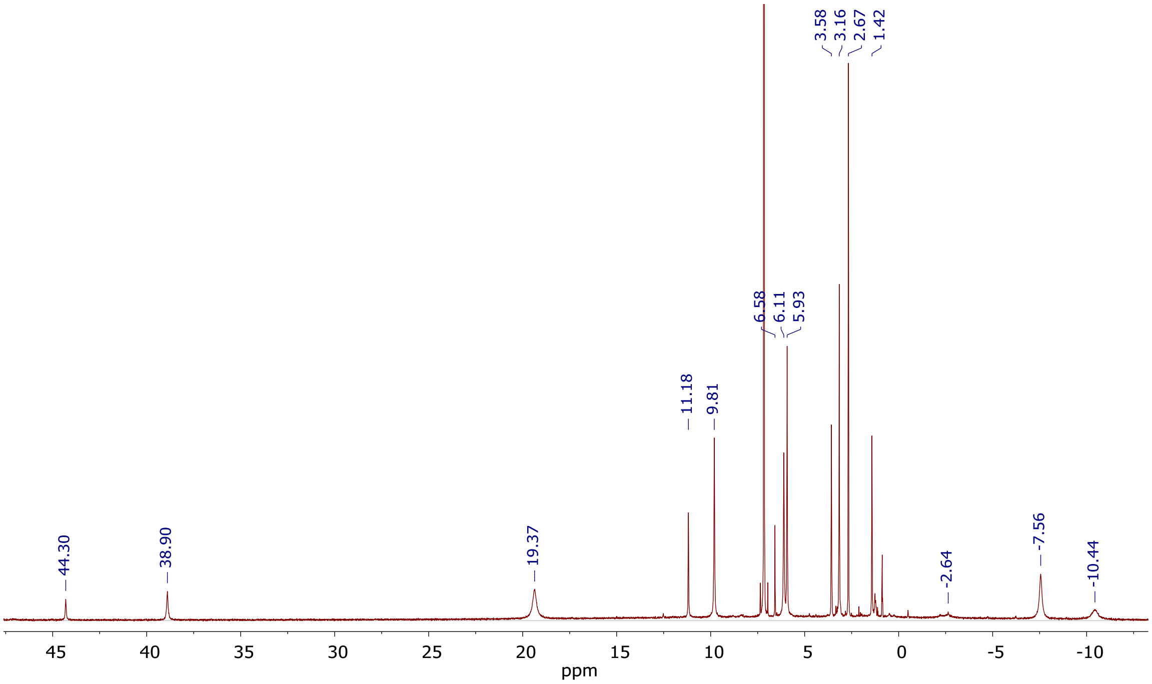

Figure 1-12. ${}^{1}$H NMR spectrum of Tp$^{\mathrm{Dur,Me}}$Fe($C_6D_6$) (**6**) recorded at 400 MHz in $C_6D_6$.

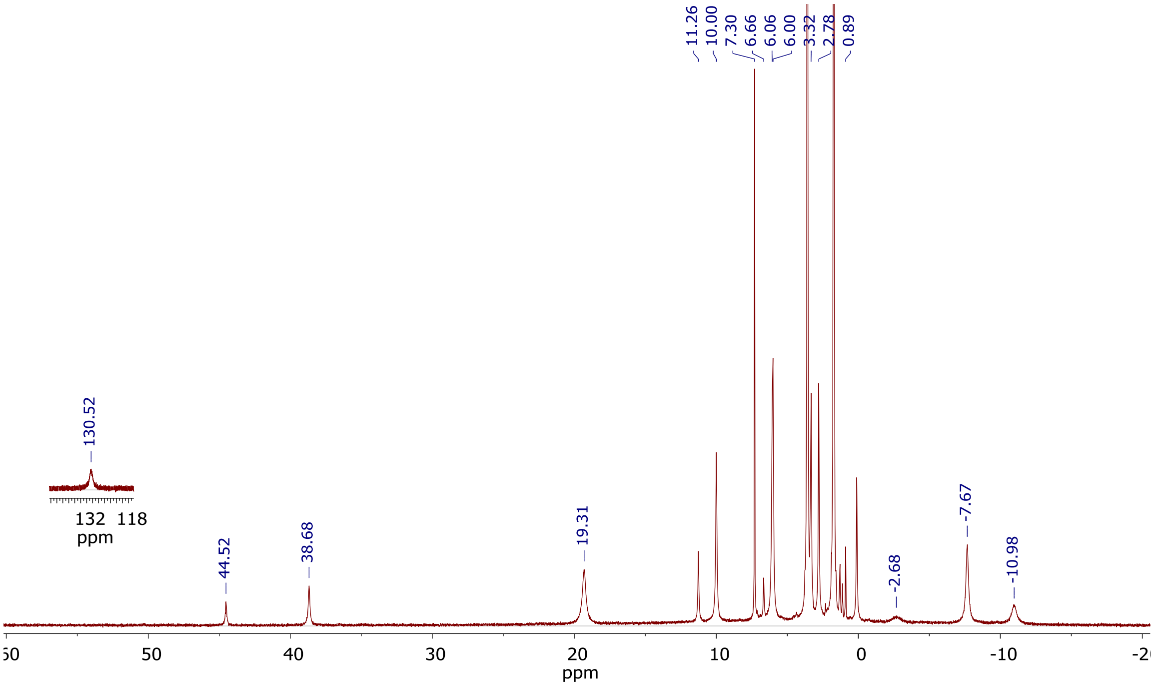

Figure 1-13. ${}^{1}$H NMR spectrum of Tp$^{\mathrm{Dur,Me}}$Fe($C_6H_6$) (**6**) recorded at 400 MHz in $d_8$-THF.

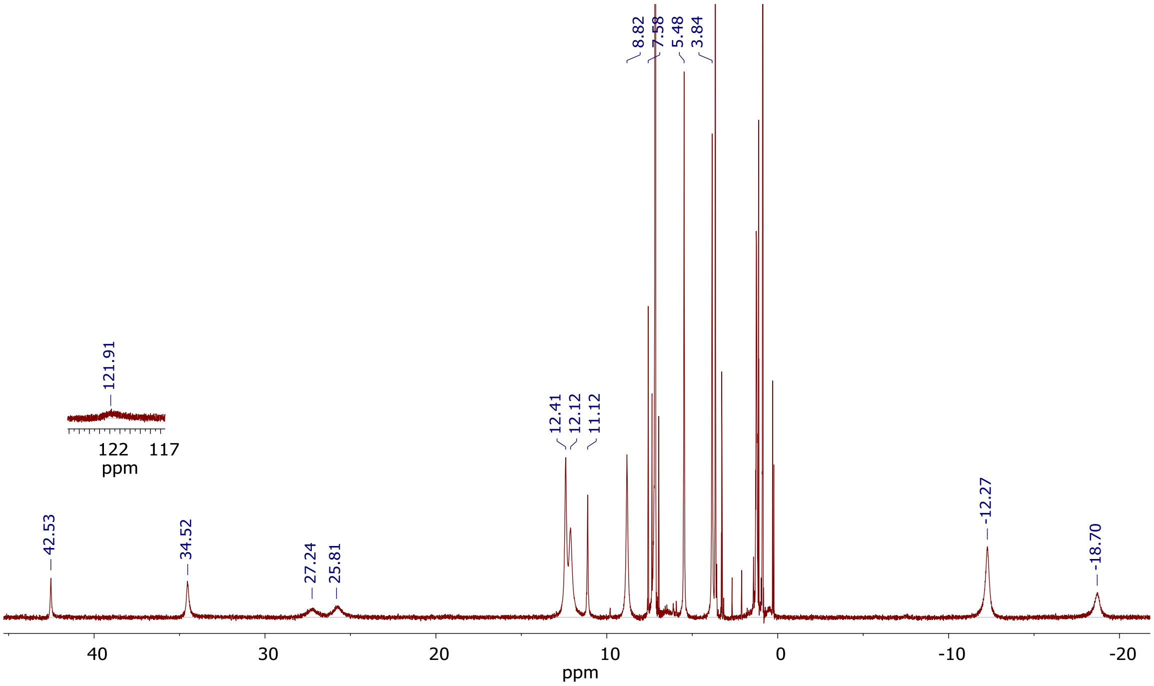

Figure 1-14. $^1$H NMR spectrum of Tp$^{Dur,Me}$Fe(1,2-$\eta^2$-napthalene) (**8**) recorded at 400 MHz in $C_6D_6$.

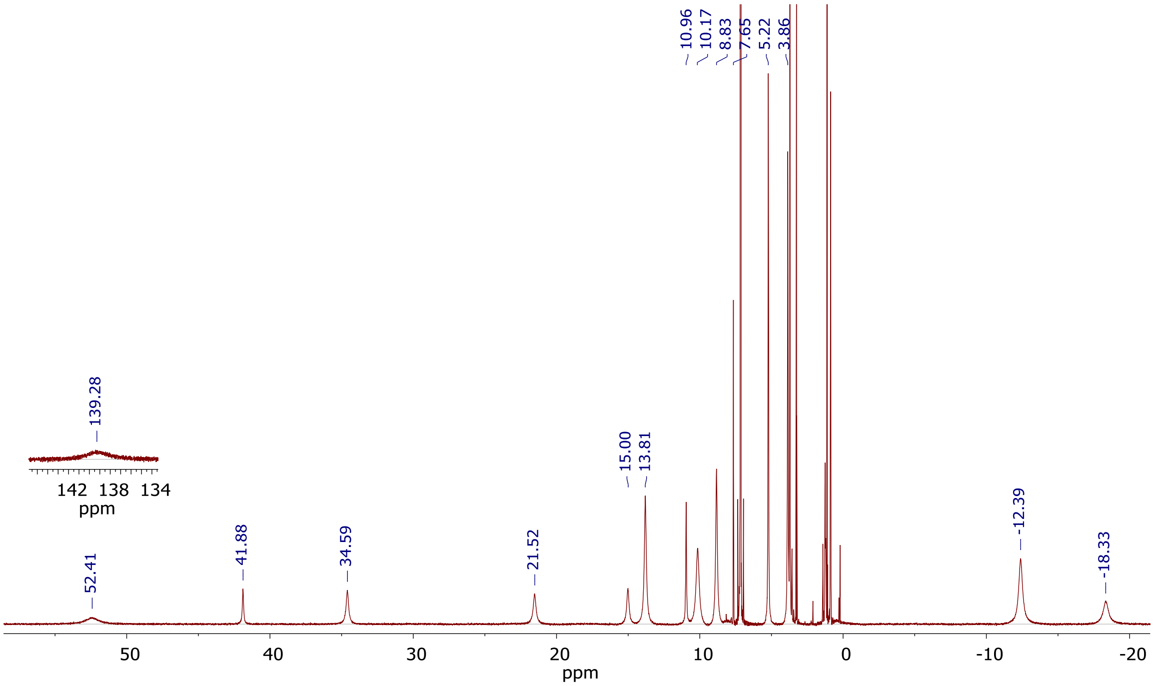

Figure 1-15. $^1$H NMR spectrum of Tp$^{Dur,Me}$Fe(1,2-$\eta^2$-anthracene) (**9**) recorded at 400 MHz in $C_6D_6$.

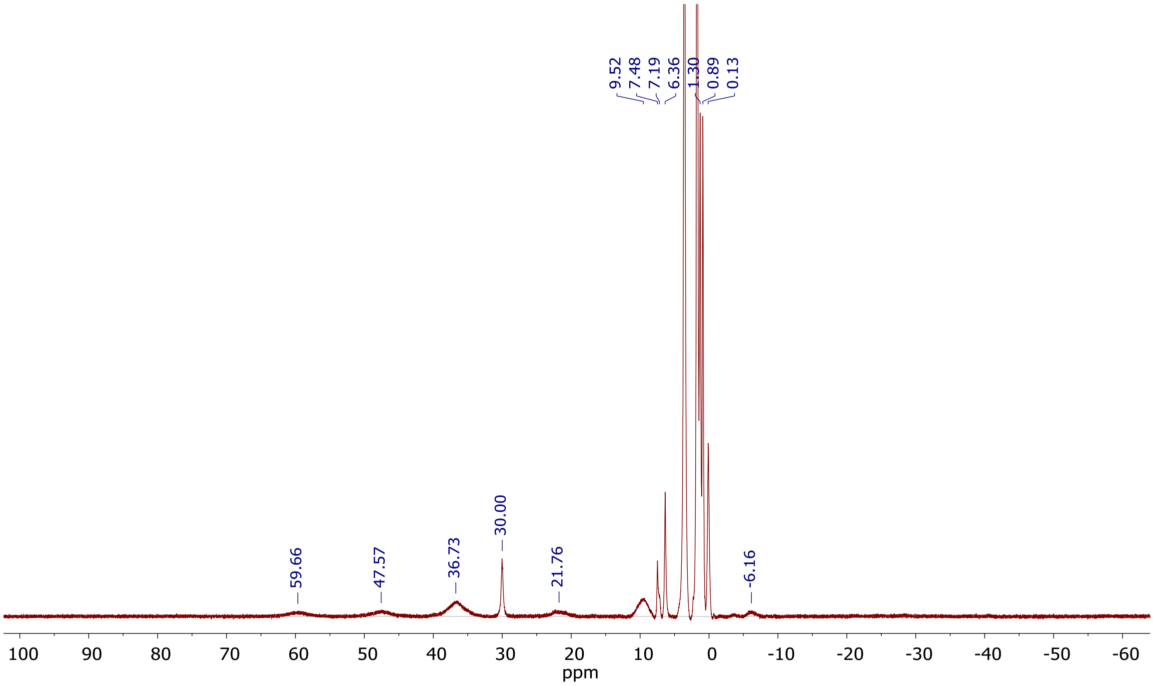

Figure 1-16. $^1$H NMR spectrum of Tp$^{Dur,Me}$Fe(2,3-η$^2$-furan) (**10**) recorded at 400 MHz in *d$_8$*-THF.

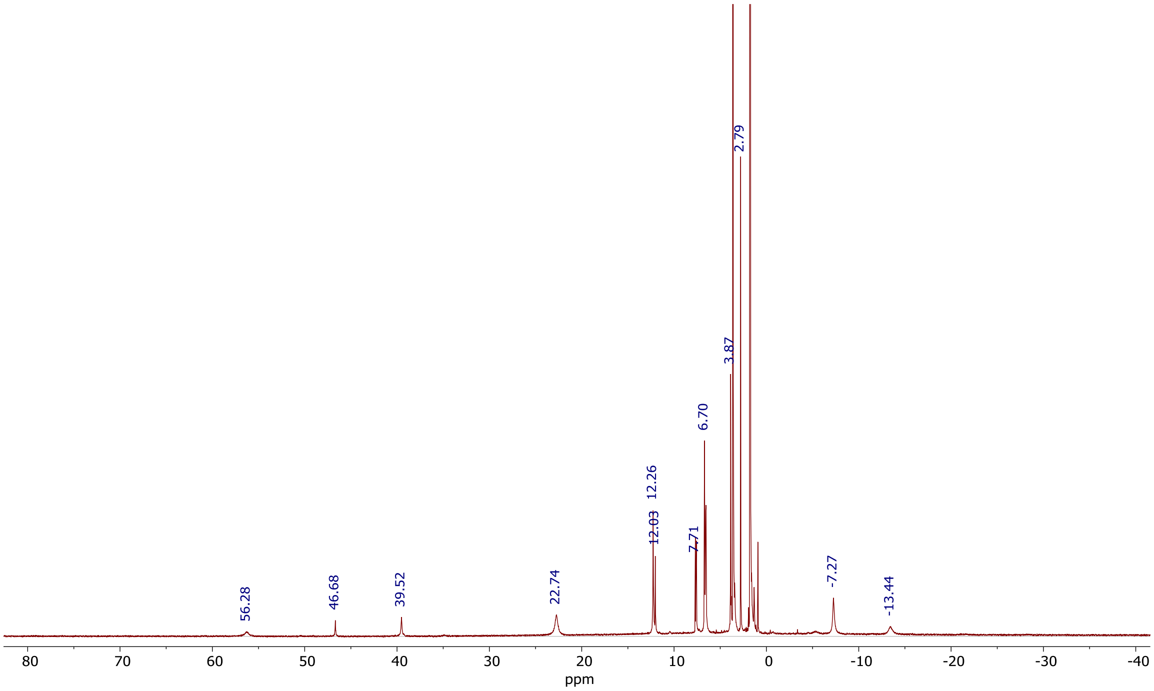

Figure 1-17. $^1$H NMR spectrum of Tp$^{Dur,Me}$Fe(3,4-η$^2$-PhCF$_3$)] recorded at 400 MHz in *d$_8$*-THF.

### *UV-vis-NIR*

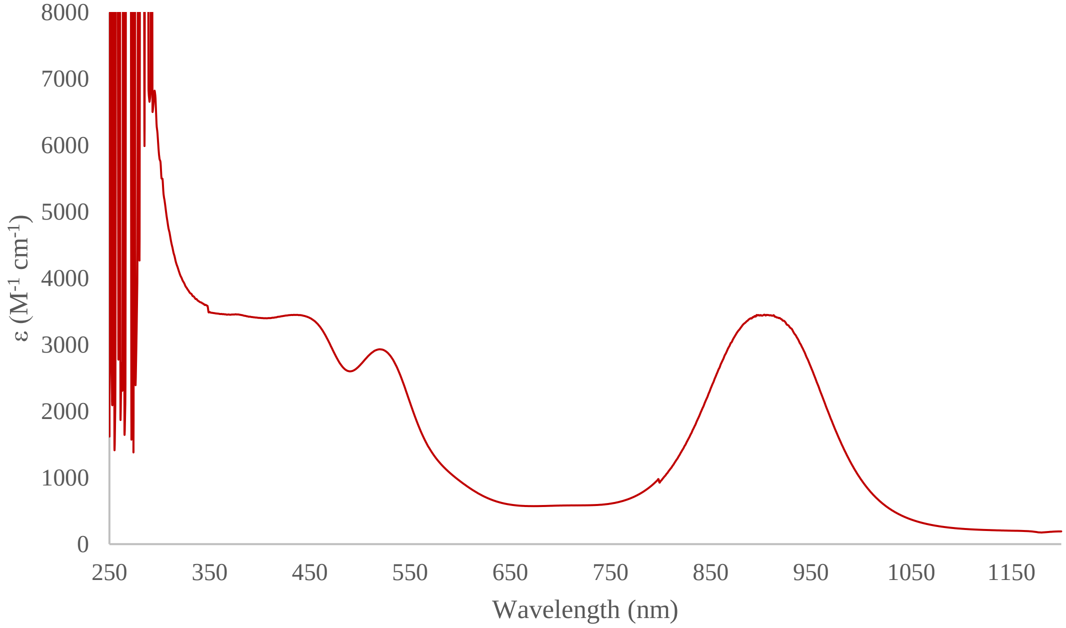

Figure 1-18. UV-vis-NIR spectrum of $(Tp^{Dur,Me}Fe)_2(N_2)$ (**5**) in THF.

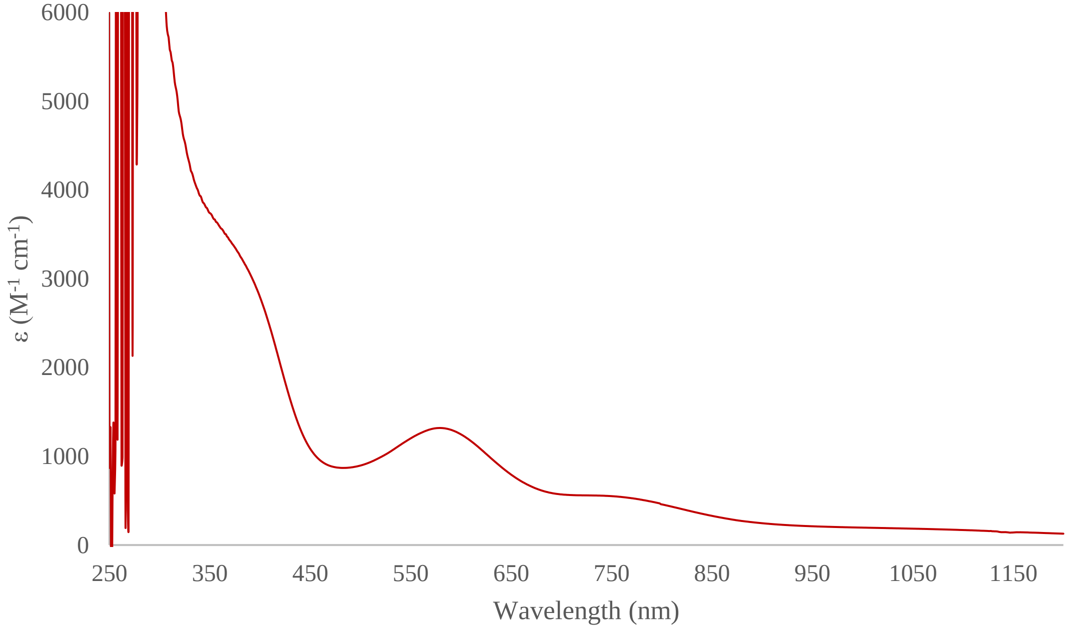

Figure 1-19. UV-vis-NIR spectrum of $Tp^{Dur,Me}Fe(C_6H_6)$ (**6**) in benzene.

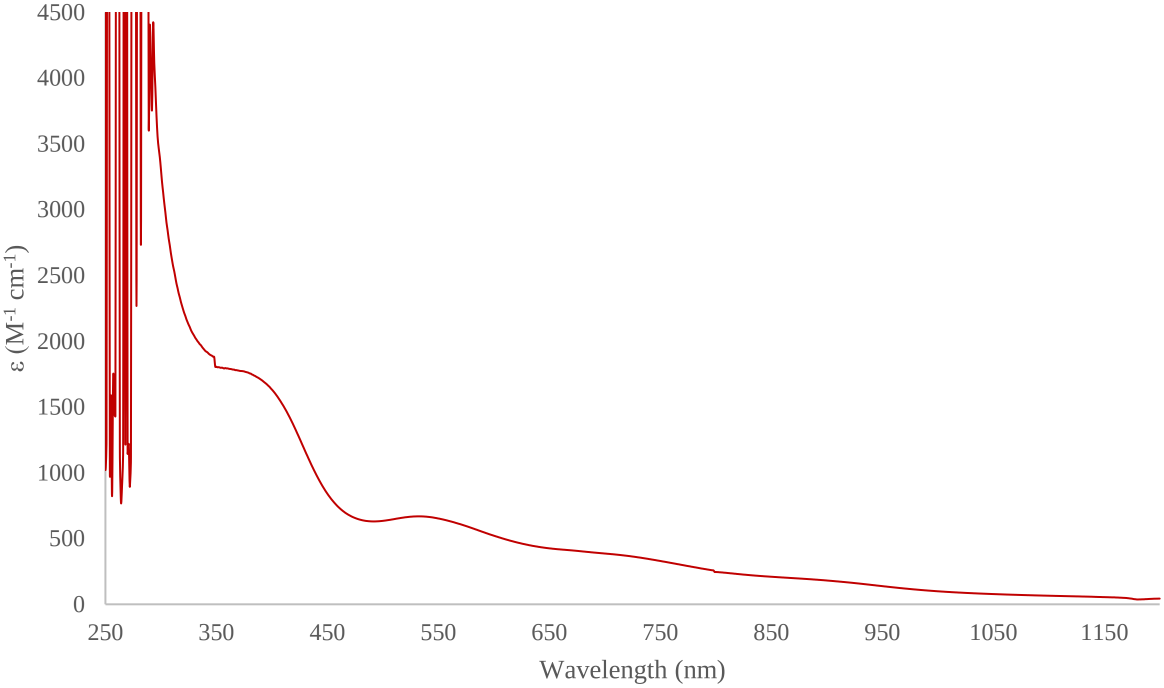

Figure 1-20. UV-vis-NIR spectrum of Tp$^{Dur,Me}$Fe(1,2-η$^2$-napthalene) (**8**) in THF.

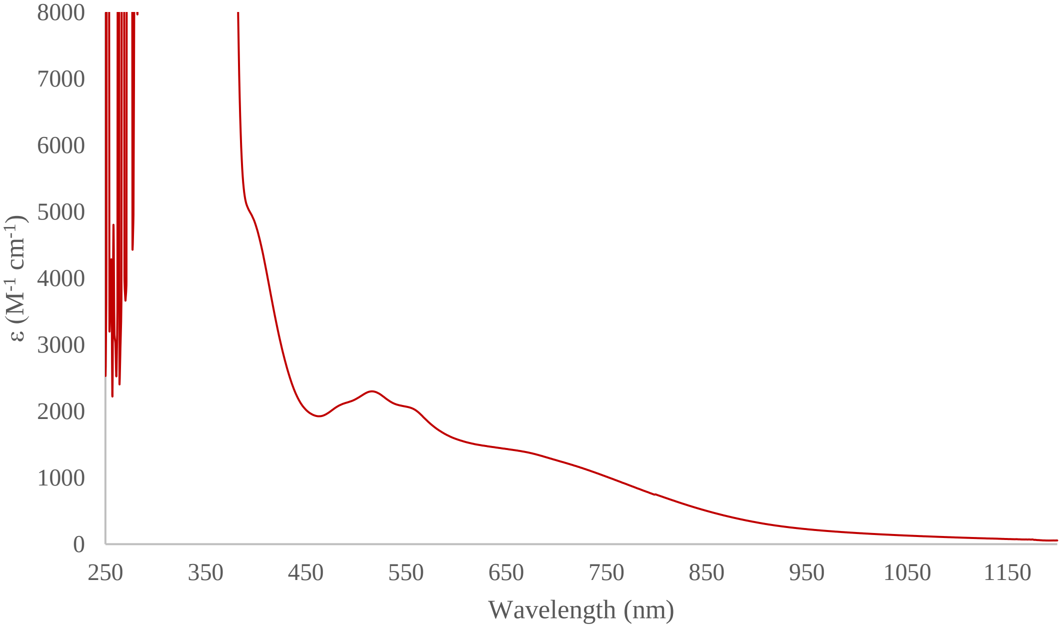

Figure 1-21. UV-vis-NIR spectrum of Tp$^{Dur,Me}$Fe(1,2-η$^2$-anthracene) (**9**) in THF.

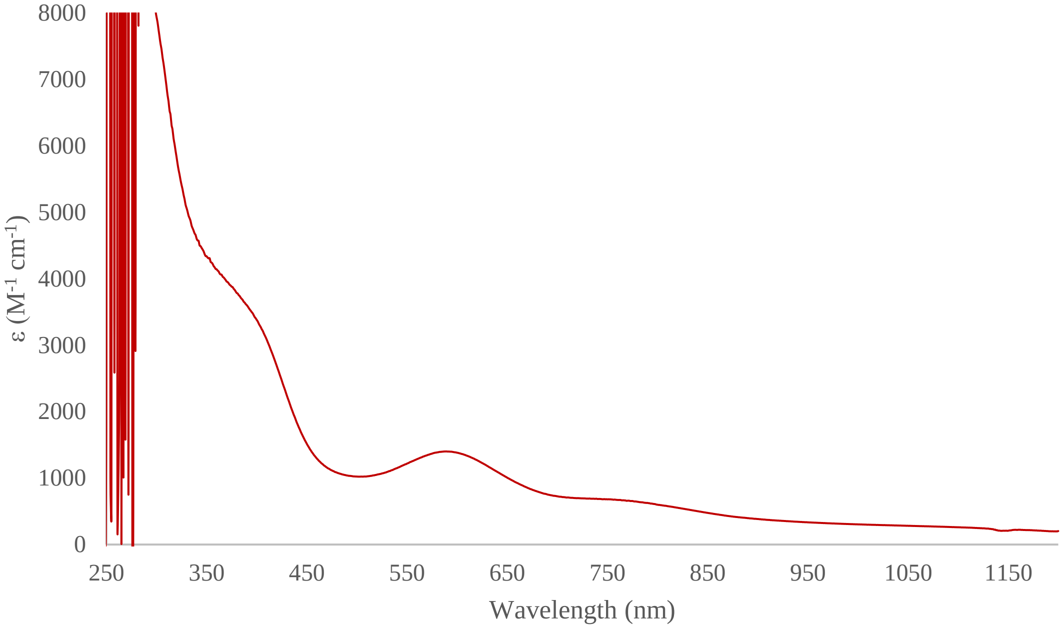

Figure 1-22. UV-vis-NIR spectrum of Tp$^{Dur,Me}$Fe(PhMe) in toluene.

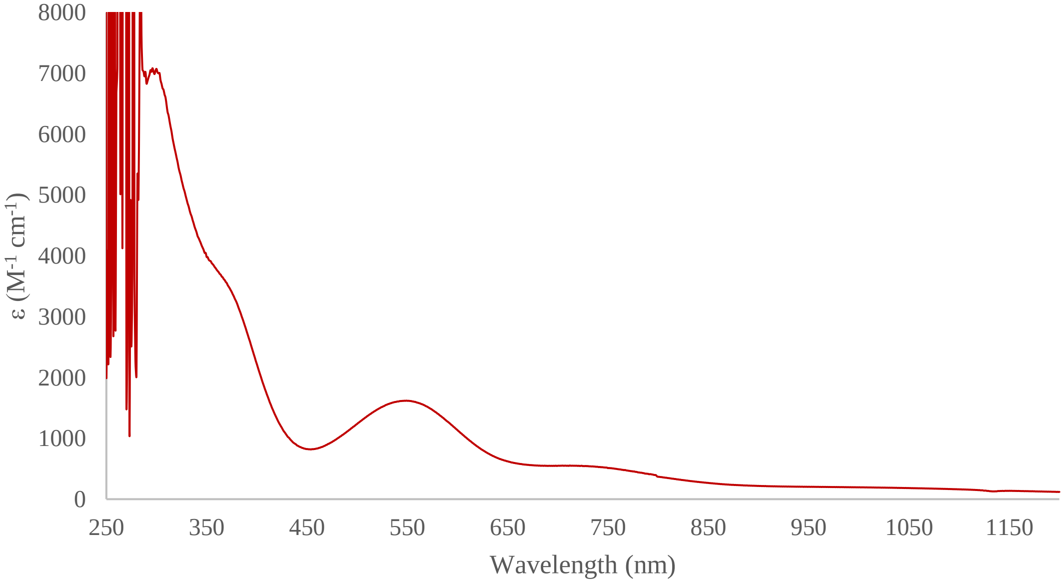

Figure 1-23. UV-vis-NIR spectrum of Tp$^{Dur,Me}$Fe(3,4-η$^2$-PhCF$_3$)] (**7**) in trifluorotoluene.

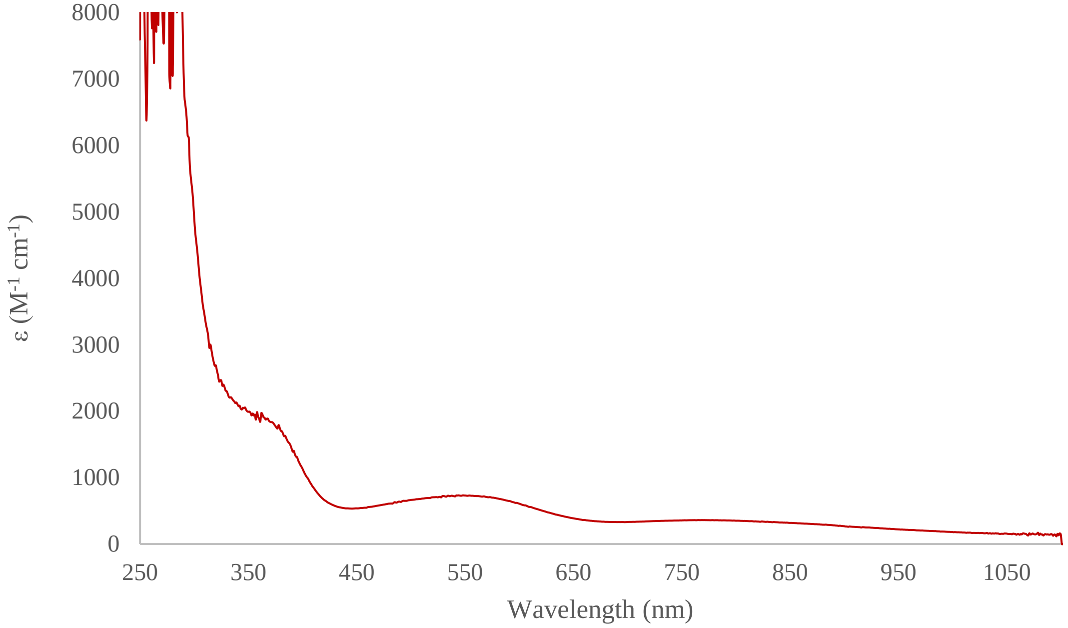

Figure 1-24. UV-vis-NIR spectrum of $\mathrm{Tp^{Dur,Me}Fe(2,3\text{-}\eta^2\text{-}furan)}$ (**10**) in THF.

*EPR*

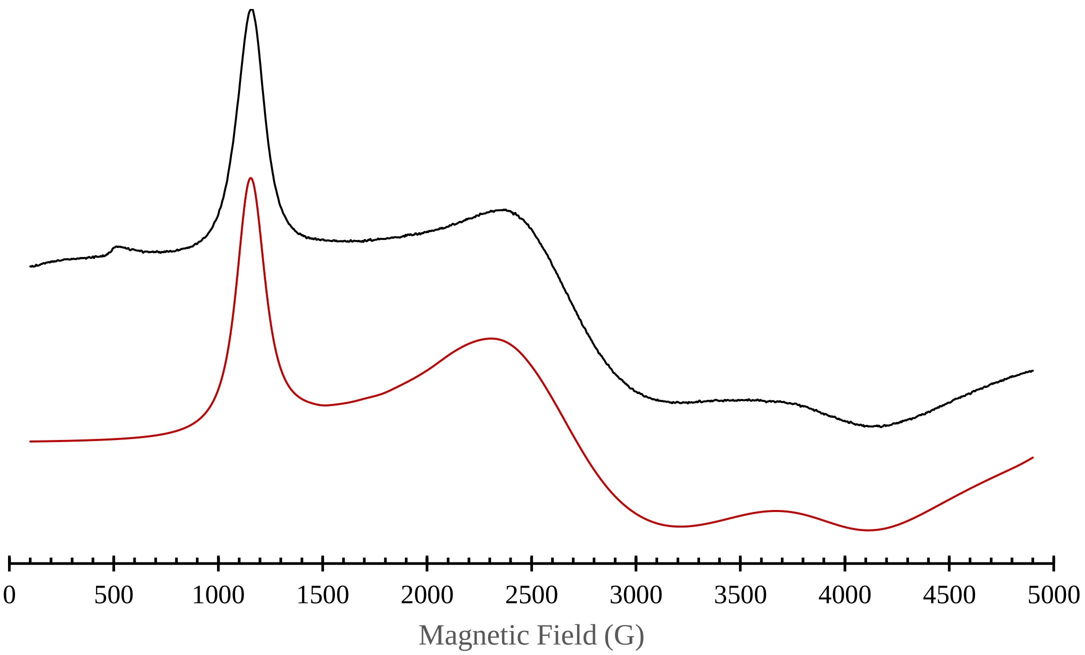

Figure 1-25. X-band EPR spectrum (9.631 GHz) of Tp$^{Dur,Me}$Fe(3,4-η$^2$-PhCF$_3$)] (**7**) in hexane at 15 K (black) and its simulation (**red**). Simulation parameters: $g_1 = 2.4$, $g_2 = 2.2$ $g_3 = 2.2$. $D = 1.04 \times 10^7$ MHz; $E = 3.26 \times 10^6$ MHz; DStrain = $1.1309\times10^6$, EStrain = $8.77\times10^5$; lwpp = 15.878.

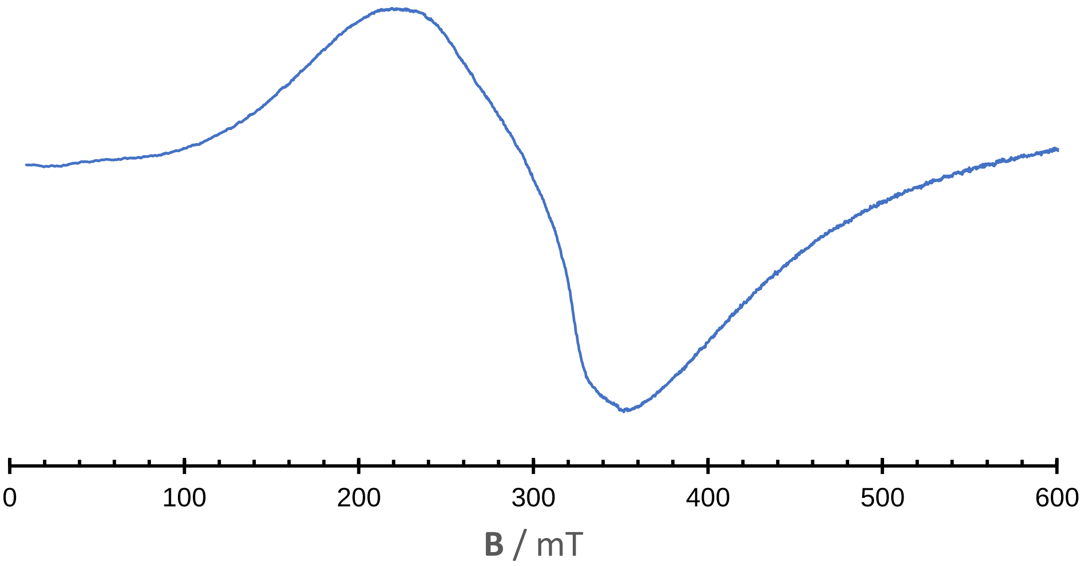

Figure 1-26. X-band EPR spectrum (9.340 GHz) of Tp$^{Dur,Me}$Fe(3,4-η$^2$-PhCF$_3$)] (**7**) in 2-MeTHF at 104 K.

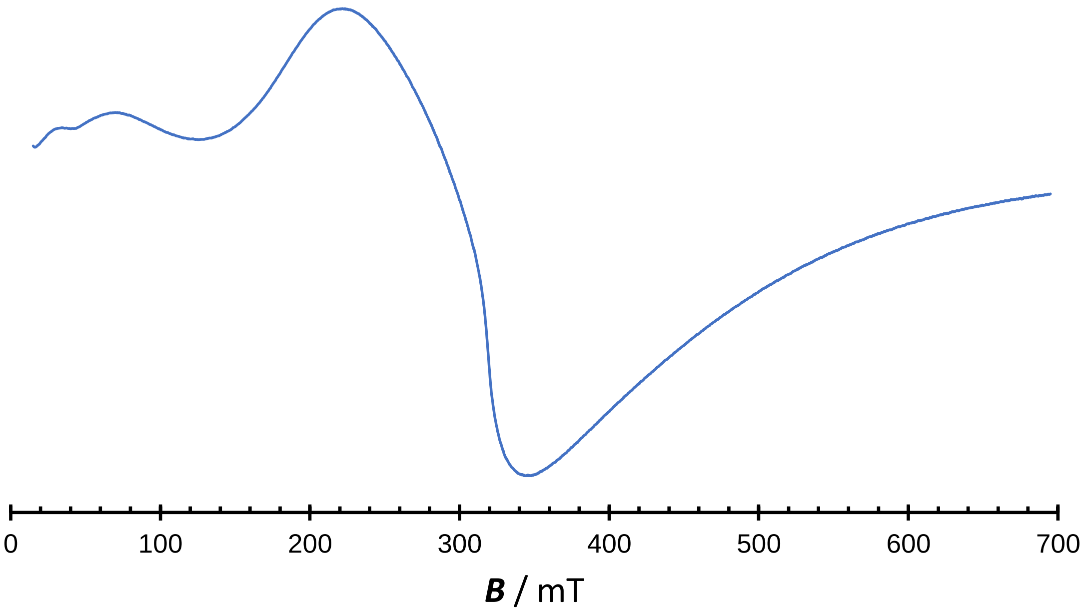

Figure 1-27. X-band EPR spectrum (9.316 GHz) of $Tp^{Dur,Me}Fe(C_6H_6)$ (**6**) in 2-MeTHF at 109 K.

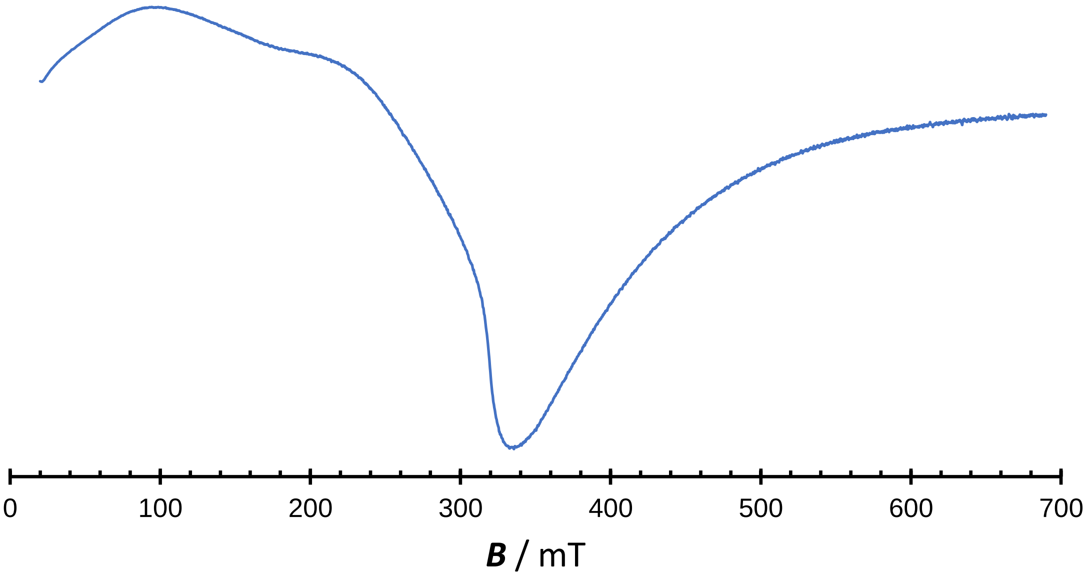

Figure 1-28. X-band EPR spectrum (9.313 GHz) of $Tp^{Dur,Me}Fe(1,2\text{-}\eta^2\text{-napthalene})$ (**8**) in 2-MeTHF at 109 K.

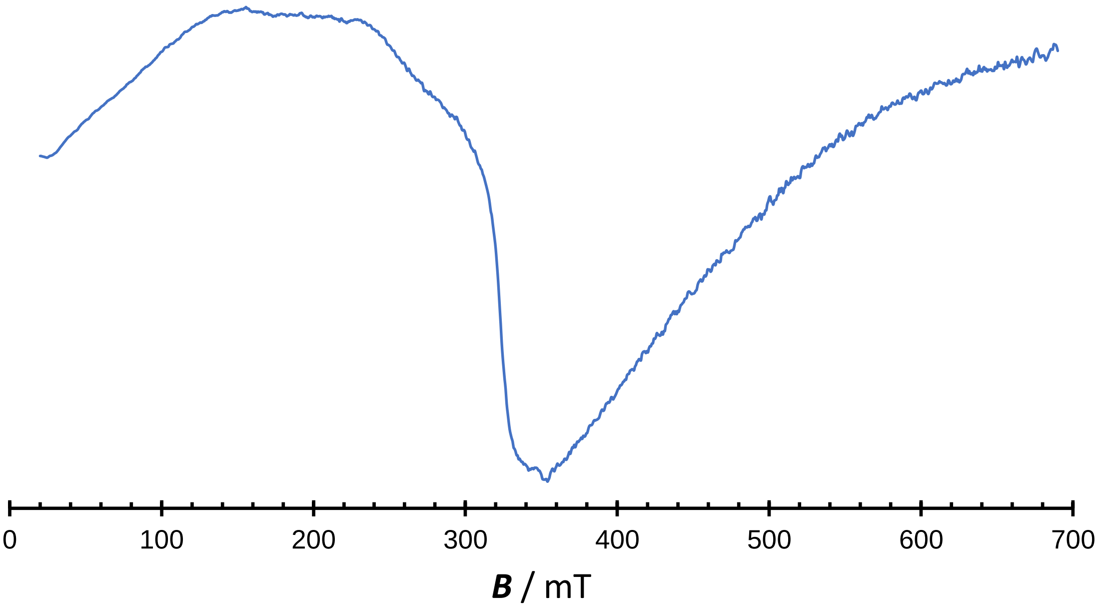

Figure 1-29. X-band EPR spectrum (9.318 GHz) of Tp$^{Dur,Me}$Fe(1,2-η$^2$-anthracene) (**9**) in 2-MeTHF at 104 K.

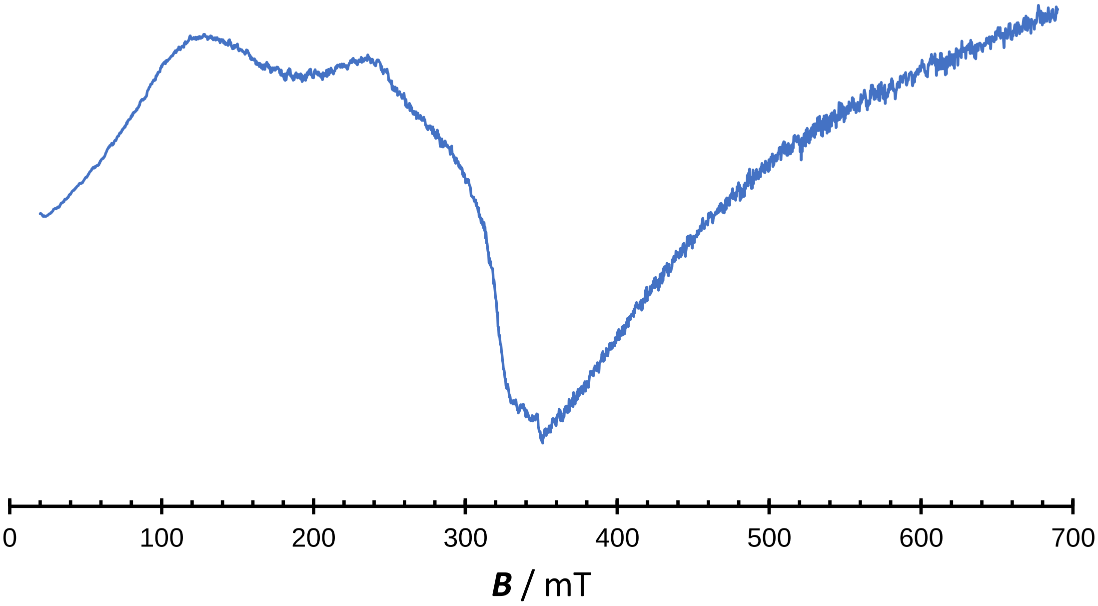

Figure 1-30. X-band EPR spectrum (9.317 GHz) of Tp$^{Dur,Me}$Fe(2,3-η$^2$-furan) (**10**) in 2-MeTHF at 104 K.

### *Mössbauer*

The Mössbauer spectrum was recorded on a spectrometer from SEE Co. (formerly WEB Research Co.) operating in the constant acceleration mode in a transmission geometry. The sample was kept in an SVT-300 cryostat from Janis (Wilmington, MA), using liquid $N_2$ as a cryogen for 80 K measurements. The quoted isomer shift is relative to the centroid of the spectrum of a metallic foil of α-Fe at room temperature. The sample was prepared by dispersing polycrystalline material into Paratone N oil within a Delrin sample cup, and subsequently freezing the dispersion inside the cold well of a $N_2$-filled glovebox chilled to 77 K. The frozen sample was quickly removed from the glovebox and immersed in liquid $N_2$ until mounted in the cryostat. Data analysis was performed using version 4 of the program WMOSS (www.wmoss.org) and quadrupole doublets were fit to Lorentzian lineshapes.[44]

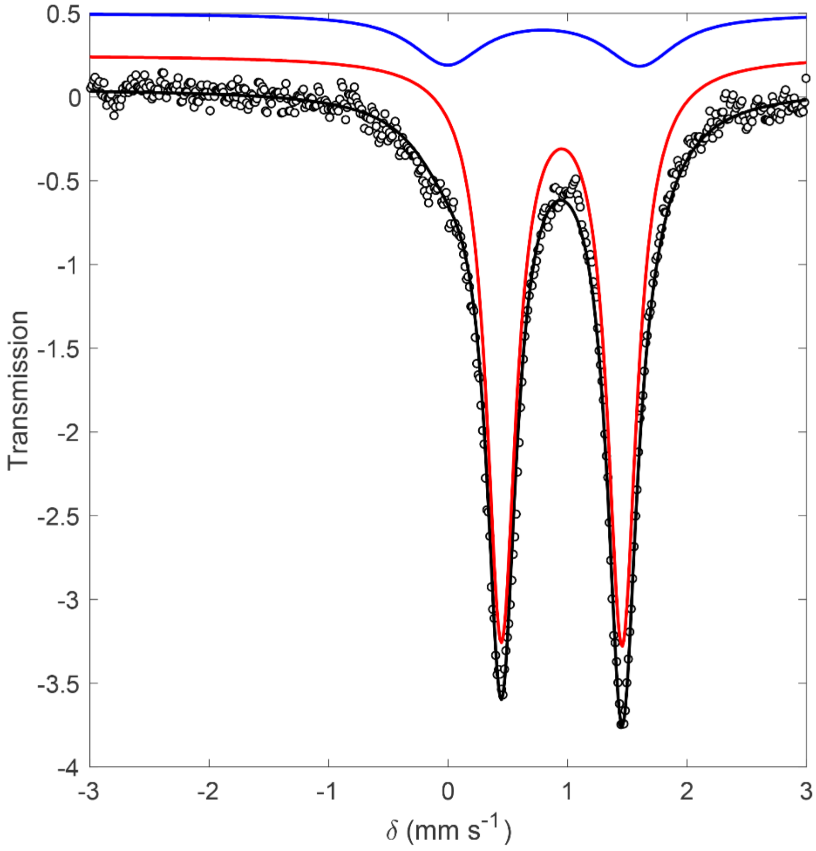

Figure 1-31. Zero-field $^{57}$Fe-Mössbauer spectrum of Tp$^{Dur,Me}$Fe(3,4-$\eta^2$-PhCF$_3$) (**7**) at 80 K and its simulation (**red**) overlaid with another quadrupole doublet (**blue**) to account for broadness in the baseline. Black circles represent experimental data, solid lines are simulations.

Table 1-1. Isomer shifts and quadrupole splittings of the two species in the Mössbauer spectrum above.

| # of site | Doublet | Assignment | Relative intensity | $\delta$ (mm/s) | $\lvert\Delta E_Q\rvert$ (mm/s) | $\Gamma_L$ | $\Gamma_R$ | Reduced $\chi^2$ |
|---|---|---|---|---|---|---|---|---|
| 2 | red | Fe-CF$_3$Ph | 0.911 | 0.951 | 1.011 | 0.301 | 0.301 | 1.025 |
|  | blue | unknown | 0.180 | 0.799 | 1.614 | 0.724 | 0.724 |  |

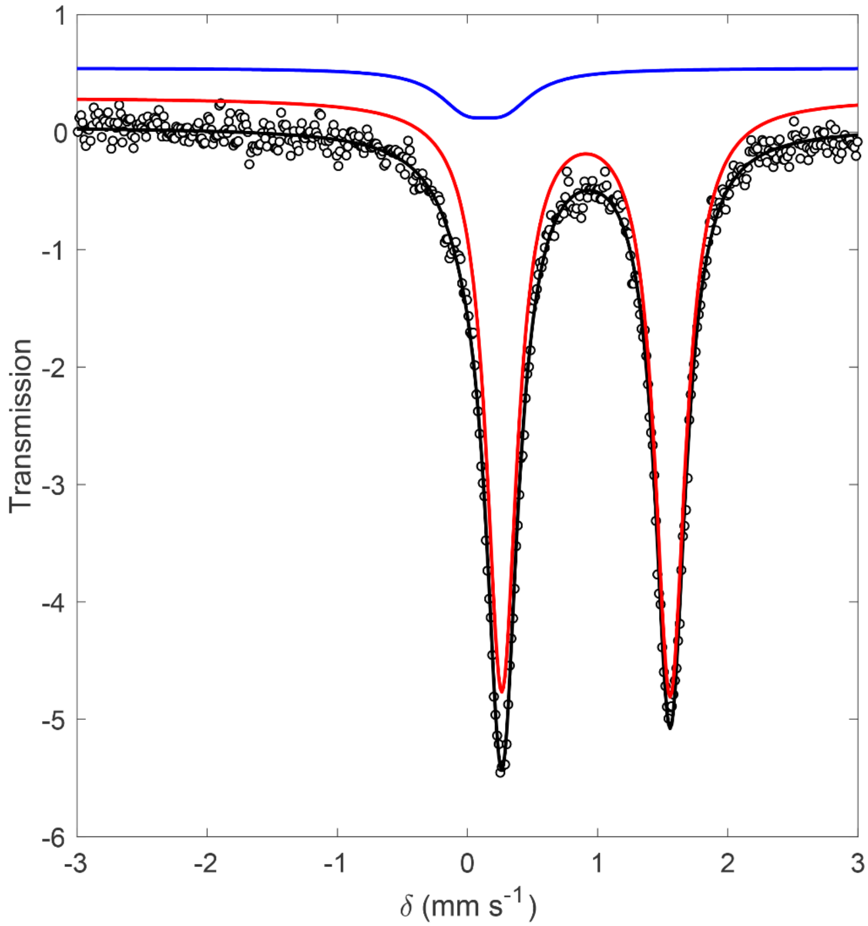

Figure 1-32. Zero-field $^{57}$Fe-Mössbauer spectrum of (Tp$^{Dur,Me}$Fe)$_2$(μ-N$_2$) (**5**) at 80 K and its simulation (**red**) overlaid with another quadrupole doublet (**blue**) to account for broadness in the baseline. Black circles represent experimental data, solid lines are simulations.

Table 1-2. Isomer shifts and quadrupole splittings of the two species in the Mössbauer spectrum above.

| # of site | Doublet | Assignment | Relative intensity | δ (mm/s) | $\lvert\Delta E_Q\rvert$ (mm/s) | $\Gamma_L$ | $\Gamma_R$ | Reduced $\chi^2$ |
|---|---|---|---|---|---|---|---|---|
| 2 | red | Fe-NN-Fe | 0.967 | 0.910 | 1.294 | 0.290 | 0.290 | 0.548 |
| | blue | unknown | 9.43 x $10^{-2}$ | 0.132 | 0.305 | 0.501 | 0.501 | |

### *Cyclic Voltammetry*

Cyclic voltammetry experiments were performed using a Pine AFP1 potentiostat. The cell consisted of a glassy carbon working electrode, a Pt wire auxiliary electrode and a Pt wire pseudo-reference electrode. All potentials are referenced vs. the Fc/Fc$^+$ couple measured as an internal standard.

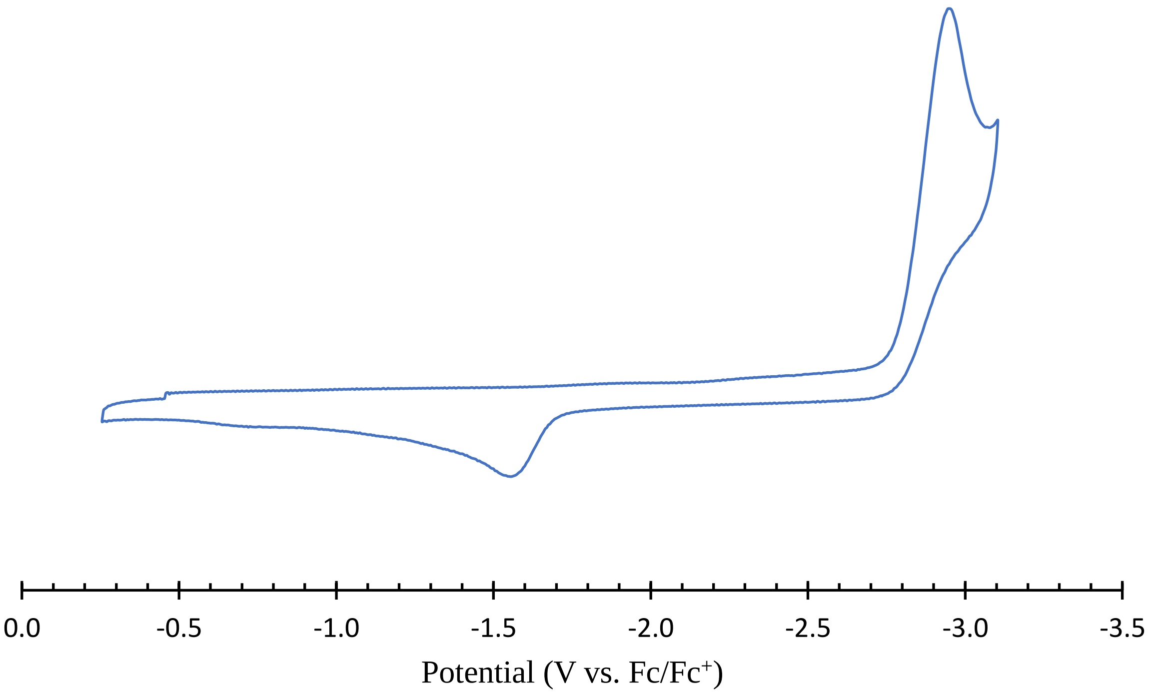

Figure 1-33. Cyclic voltammogram of Tp$^{Dur,Me}$FeCl (**4**) in THF (0.1 M [*n*Bu$_4$N]PF$_6$ as electrolyte; 100 mV/s scan rate).

### *X-Ray Crystallography*

General Considerations: Single crystals were coated with paratone oil and mounted on cryo-loop glass fibers. Diffraction data were collected on a Bruker-AXS Apex II diffractometer with an Apex II CCD detector using Mo $K_\alpha$ radiation ($\lambda$ = 0.71073 Å) from a fine-focus sealed tube source. Data were collected at 100 K by performing 0.5° $\omega$-scans, integrated using SAINT[45], and absorption corrected using SADABS[46]. The structure was solved by direct methods using SHELXT[47] and refined against $F^2$ on all data by full-matrix least squares with SHELXL-2018/3[48] following established refinement strategies.[49] All non-hydrogen atoms were refined anisotropically. Except where noted below, all hydrogen atoms were included into the model at geometrically calculated positions and refined using a riding model. The isotropic displacement parameters of all hydrogen atoms were fixed to 1.2 times the $U$ value of the atoms they are linked to (1.5 times for methyl groups). Crystal and data quality details, as well as a summary of the residual refinement values, are listed in the accompanying table. Relevant details for individual data collections are reported in Tables 1-3 through Table 1-8.

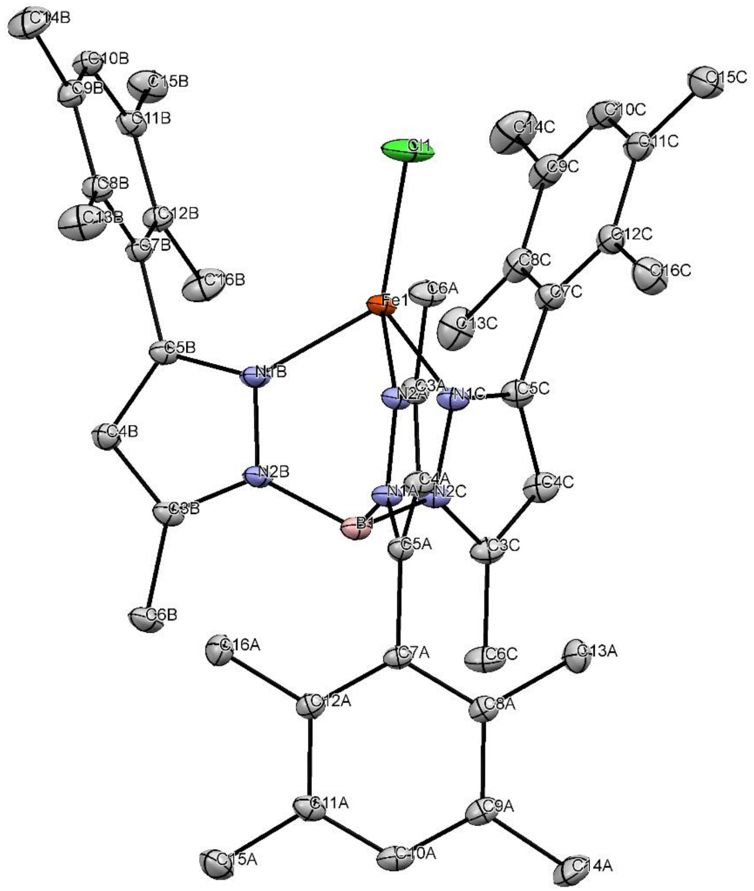

Figure 1-34. Labelled thermal ellipsoid plot (50%) for $Tp^{Dur,Me}FeCl$ (**4**).

Table 1-3. Crystal data and structure refinement for $Tp^{Dur,Me}FeCl$ (**4**).

| | | |
|---|---|---|
| Identification code | hh193LE6_0m | |
| Empirical formula | $C_{42}H_{52}BClFeN_6$ | |
| Formula weight | 743.00 | |
| Temperature | 100(2) K | |
| Wavelength | 0.71073 Å | |
| Crystal system | Monoclinic | |
| Space group | P 21/n | |
| Unit cell dimensions | *a* = 13.0674(3) Å | α= 90°. |
| | *b* = 21.4331(5) Å | β= 96.0852(5)°. |
| | *c* = 14.1351(4) Å | γ = 90°. |
| Volume | 3936.58(17) $Å^3$ | |

| | |
|---|---|
| Z | 4 |
| Density (calculated) | 1.254 mg/m$^3$ |
| Absorption coefficient | 0.489 mm$^{-1}$ |
| F(000) | 1576 |
| Crystal size | 0.441 x 0.272 x 0.199 mm$^3$ |
| θ range for data collection | 1.733 to 30.506°. |
| Index ranges | $-18 \le h \le 18$, $-30 \le k \le 30$, $-20 \le l \le 20$ |
| Reflections collected | 94063 |
| Independent reflections | 12021 [$R_{\mathrm{int}}$ = 0.0275] |
| Completeness to θ = 25.242° | 100.0 % |
| Absorption correction | Semi-empirical from equivalents |
| Refinement method | Full-matrix least-squares on F$^2$ |
| Data / restraints / parameters | 12021 / 0 / 478 |
| Goodness-of-fit on F$^2$ | 1.031 |
| Final *R* indices [$I > 2\sigma_I$] | $R_1$ = 0.0329, $wR_2$ = 0.0861 |
| *R* indices (all data) | $R_1$ = 0.0391, $wR_2$ = 0.0905 |
| Extinction coefficient | n/a |
| Largest diff. peak and hole | 0.503 and −0.512 e/Å$^3$ |

Notes: The hydrogen atom bonded to the B-atom was refined without restraint.

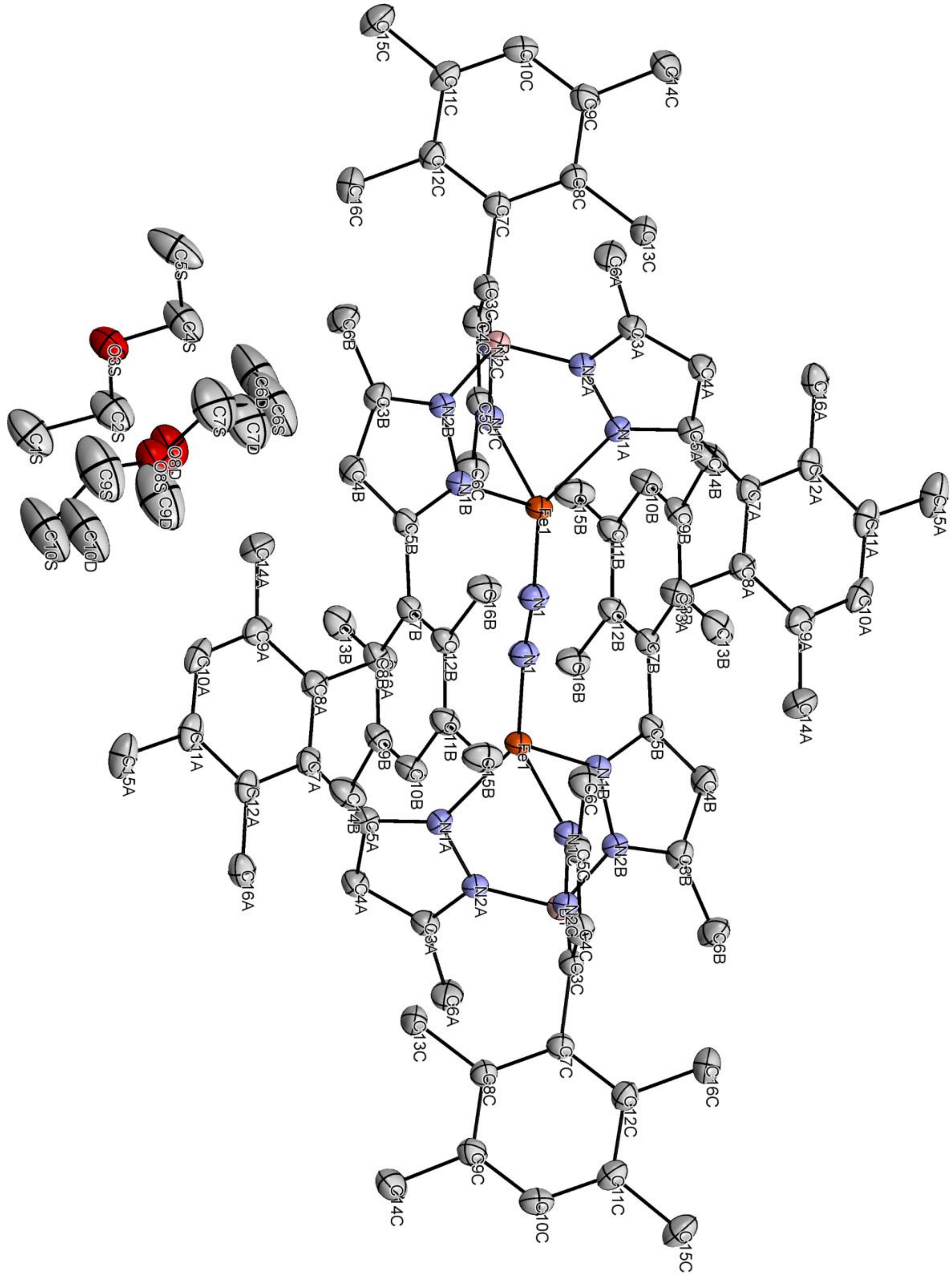

Figure 1-35. Labelled thermal ellipsoid plot (50%) for $(Tp^{Dur,Me}Fe)_2(\mu\text{-}N_2)$ (**5**).

Table 1-4. Crystal data and structure refinement for (Tp$^{Dur,Me}$Fe)$_2$(μ-$N_2$) (**5**).

| | | |
|---|---|---|
| Identification code | hh200LE10_0m | |
| Empirical formula | $C_{100}H_{144}B_2Fe_2N_{14}O_4$ | |
| Formula weight | 1739.60 | |
| Temperature | 100(2) K | |
| Wavelength | 0.71073 Å | |
| Crystal system | Triclinic | |
| Space group | P -1 | |
| Unit cell dimensions | a = 12.1403(7) Å | α = 79.4679(8)°. |
| | b = 13.5553(8) Å | β = 70.9275(8)°. |
| | c = 16.4607(9) Å | γ = 80.4328(8)°. |
| Volume | 2500.4(2) Å$^3$ | |
| Z | 1 | |
| Density (calculated) | 1.155 mg/m$^3$ | |
| Absorption coefficient | 0.345 mm$^{-1}$ | |
| F(000) | 936 | |
| Crystal size | 0.427 x 0.372 x 0.189 mm$^3$ | |
| θ range for data collection | 1.538 to 27.484°. | |
| Index ranges | $-15 \le h \le 15$, $-17 \le k \le 17$, $-21 \le l \le 21$ | |
| Reflections collected | 48459 | |
| Independent reflections | 11473 [$R_{int}$ = 0.0295] | |
| Completeness to θ = 25.242° | 100.0 % | |
| Absorption correction | None | |
| Refinement method | Full-matrix least-squares on $F^2$ | |
| Data / restraints / parameters | 11473 / 165 / 583 | |
| Goodness-of-fit on $F^2$ | 1.032 | |
| Final $R$ indices [$I > 2\sigma_I$] | $R_1$ = 0.0408, $wR_2$ = 0.1067 | |
| $R$ indices (all data) | $R_1$ = 0.0504, $wR_2$ = 0.1132 | |
| Extinction coefficient | n/a | |
| Largest diff. peak and hole | 0.634 and −0.573 e/Å$^3$ | |

Notes: One of the two $C_4H_{10}O$ molecules was modeled with disorder (disordered site occupancy factor ratio was 84%/16%). The close contact of the H14A...H6O atoms is due to this disorder. The H atom bonded to the B atom was refined without restraint.

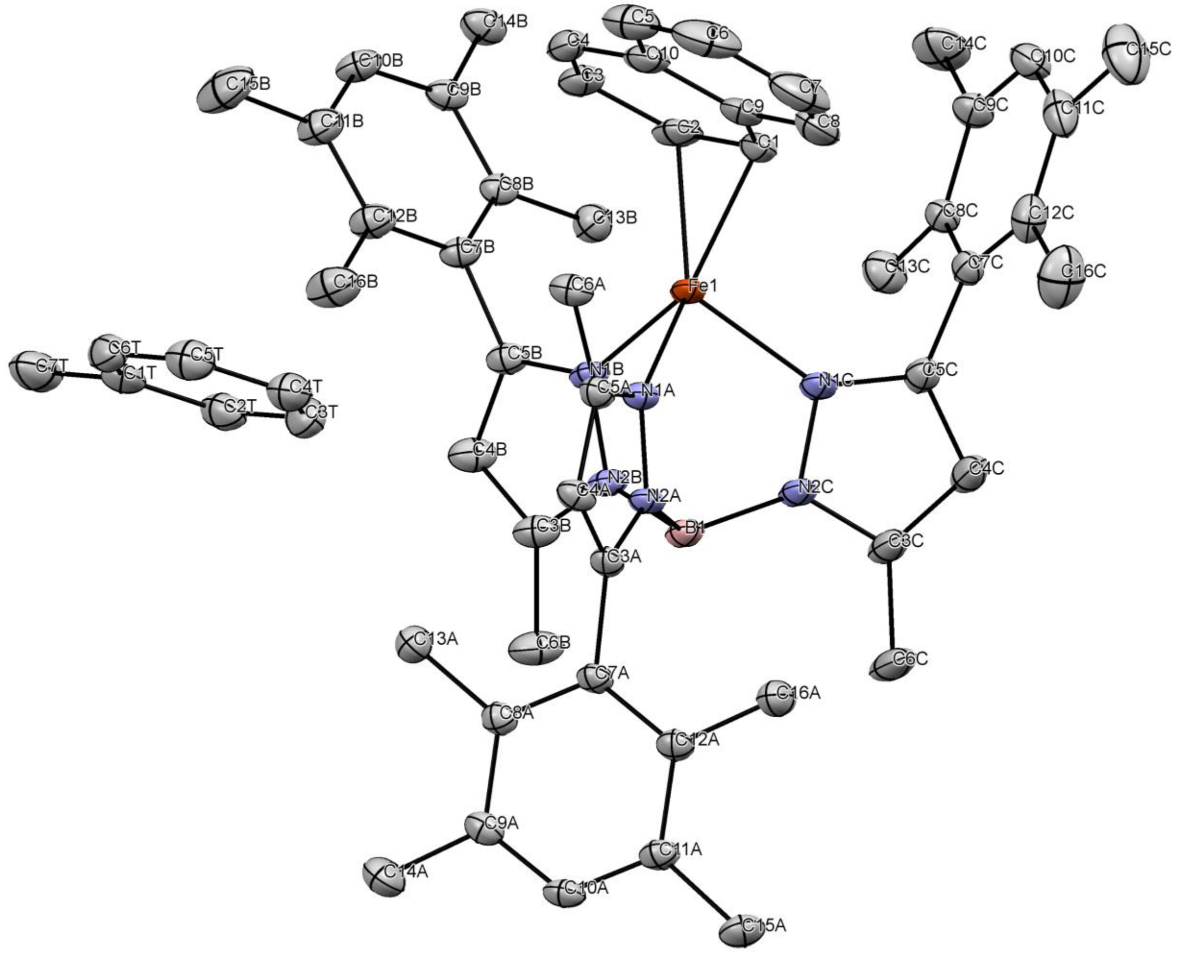

Figure 1-36. Labelled thermal ellipsoid plot (50%) for Tp$^{Dur,Me}$Fe(1,2-η$^2$-napthalene) (**8**).

Table 1-5. Crystal data and structure refinement for Tp$^{Dur,Me}$Fe(1,2-η$^2$-napthalene) (**8**).

| | | |
|---|---|---|
| Identification code | hh173AM61_0m | |
| Empirical formula | $C_{59}H_{68}BFeN_6$ | |
| Formula weight | 927.85 | |
| Temperature | 100(2) K | |
| Wavelength | 0.71073 Å | |
| Crystal system | Triclinic | |
| Space group | P -1 | |
| Unit cell dimensions | a = 11.9115(9) Å | α = 77.2722(12)°. |
| | b = 12.0680(9) Å | β = 89.6965(12)°. |
| | c = 19.7547(15) Å | γ = 67.1206(11)°. |
| Volume | 2541.8(3) Å$^3$ | |
| Z | 2 | |
| Density (calculated) | 1.212 mg/m$^3$ | |
| Absorption coefficient | 0.341 mm$^{-1}$ | |

| | |
|---|---|
| F(000) | 990 |
| Crystal size | 0.388 x 0.248 x 0.038 $mm^3$ |
| θ range for data collection | 1.863 to 28.282°. |
| Index ranges | $-15 \leq h \leq 15, -16 \leq k \leq 16, -26 \leq l \leq 26$ |
| Reflections collected | 52591 |
| Independent reflections | 12606 [$R_{int}$ = 0.0294] |
| Completeness to θ = 25.242° | 100.0 % |
| Absorption correction | Semi-empirical from equivalents |
| Refinement method | Full-matrix least-squares on $F^2$ |
| Data / restraints / parameters | 12606 / 0 / 629 |
| Goodness-of-fit on $F^2$ | 1.033 |
| Final *R* indices [$I > 2\sigma_I$] | $R_1$ = 0.0396, $wR_2$ = 0.0987 |
| *R* indices (all data) | $R_1$ = 0.0527, $wR_2$ = 0.1052 |
| Extinction coefficient | n/a |
| Largest diff. peak and hole | 0.451 and –0.359 e/$Å^3$ |

Notes: H1B, H1 and H2 atoms bonded to B1, C1 and C2, respectively, were refined unrestrained.

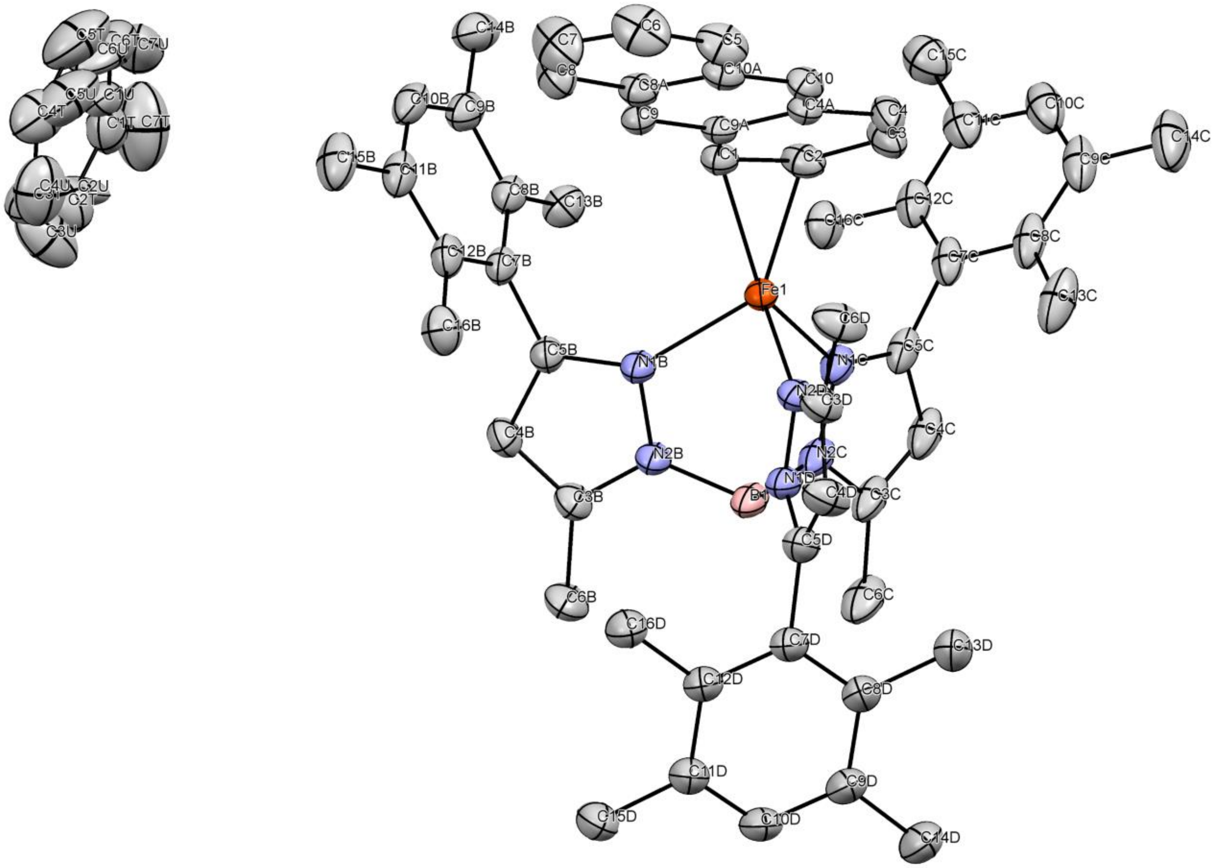

Figure 1-37. Labelled thermal ellipsoid plot (50%) for Tp$^{Dur,Me}$Fe(1,2-η$^2$-anthracene) (**9**).

Table 1-6. Crystal data and structure refinement for Tp$^{Dur,Me}$Fe(1,2-η$^2$-anthracene) (**9**).

| | | |
|---|---|---|
| Identification code | hh252LE29_0m | |
| Empirical formula | $C_{63}H_{70}BFeN_6$ | |
| Formula weight | 977.91 | |
| Temperature | 100(2) K | |
| Wavelength | 0.71073 Å | |
| Crystal system | Monoclinic | |
| Space group | P 21/n | |
| Unit cell dimensions | a = 14.8713(6) Å | α = 90°. |
| | b = 18.9359(8) Å | β = 93.1219(8)°. |
| | c = 18.9480(8) Å | γ = 90°. |
| Volume | 5327.9(4) Å$^3$ | |
| Z | 4 | |
| Density (calculated) | 1.219 mg/m$^3$ | |
| Absorption coefficient | 0.329 mm$^{-1}$ | |
| F(000) | 2084 | |
| Crystal size | 0.442 x 0.197 x 0.115 mm$^3$ | |

| | |
|---|---|
| θ range for data collection | 1.521 to 30.508°. |
| Index ranges | $-21 \leq h \leq 21$, $-27 \leq k \leq 27$, $-27\ l \leq 27$ |
| Reflections collected | 84732 |
| Independent reflections | 16272 [$R_{\text{int}}$ = 0.0547] |
| Completeness to θ = 25.242° | 100.0 % |
| Absorption correction | Semi-empirical from equivalents |
| Refinement method | Full-matrix least-squares on $F^2$ |
| Data / restraints / parameters | 16272 / 252 / 700 |
| Goodness-of-fit on $F^2$ | 1.022 |
| Final $R$ indices [$I > 2\sigma_I$] | $R_1 = 0.0530$, $wR_2 = 0.1233$ |
| $R$ indices (all data) | $R_1 = 0.0907$, $wR_2 = 0.1390$ |
| Extinction coefficient | n/a |
| Largest diff. peak and hole | 0.520 and −0.634 e/Å$^3$ |

Notes: H1B, H1 and H2 atoms bonded to B1, C1 and C2, respectively, were refined unrestrained.

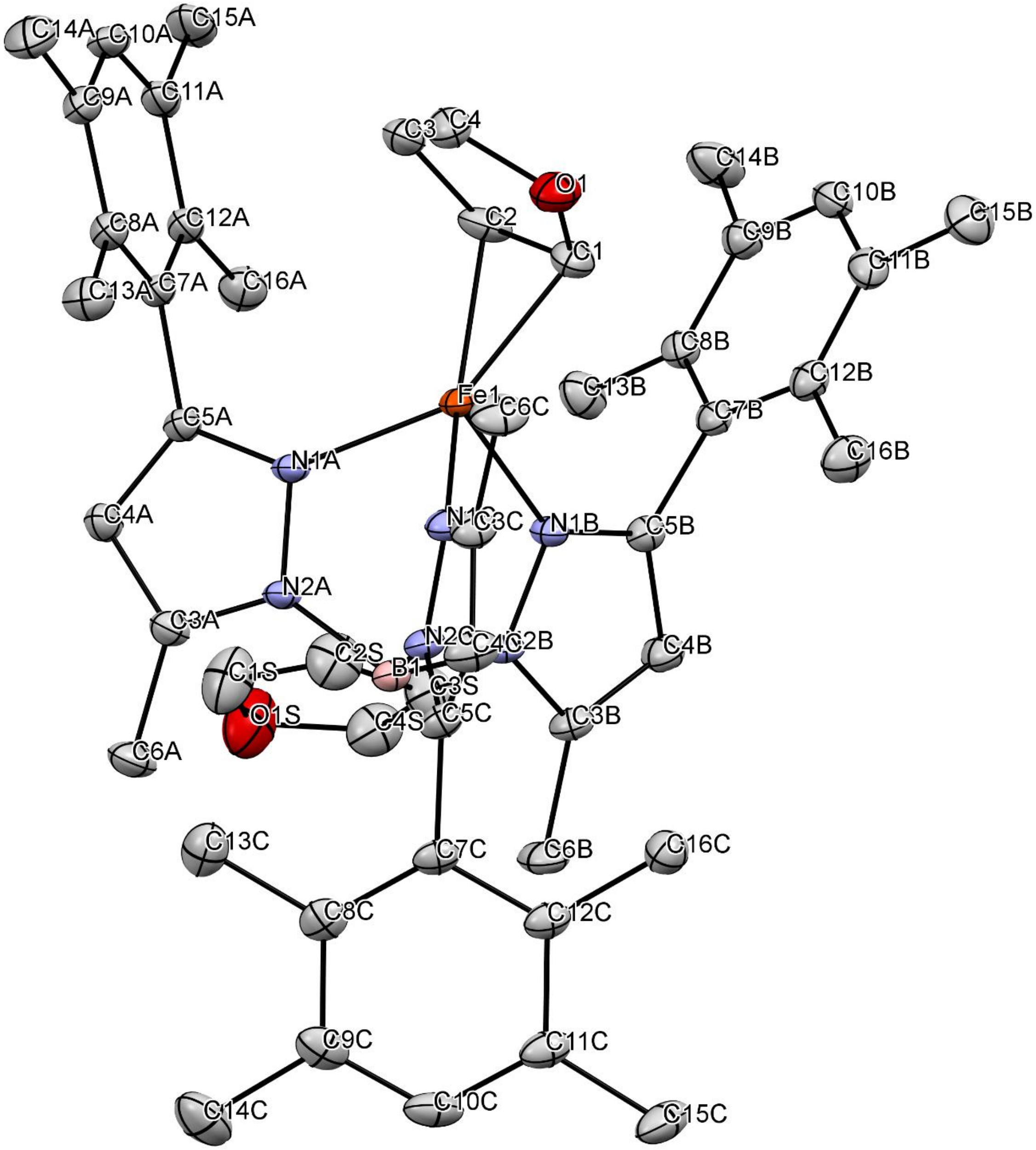

Figure 1-38. Labelled thermal ellipsoid plot (50%) for $\mathrm{Tp^{Dur,Me}Fe}$(2,3-$\eta^2$-furan) (**10**).

Table 1-7. Crystal data and structure refinement for Tp$^{Dur,Me}$Fe(2,3-$\eta^2$-furan) (**10**).

| | | |
|---|---|---|
| Identification code | hh295le_r_sq | |
| Empirical formula | $C_{50}H_{60}BFeN_6O_2$ | |
| Formula weight | 843.70 | |
| Temperature | 100(2) K | |
| Wavelength | 0.71073 Å | |
| Crystal system | Triclinic | |
| Space group | P-1 | |
| Unit cell dimensions | a = 11.9452(4) Å | $\alpha$ = 82.3236(17)°. |
| | b = 12.3931(4) Å | $\beta$ = 75.4079(16)°. |
| | c = 17.4853(6) Å | $\gamma$ = 84.1370(17)°. |
| Volume | 2476.21(14) Å$^3$ | |
| Z | 2 | |
| Density (calculated) | 1.132 mg/m$^3$ | |
| Absorption coefficient | 0.347 mm$^{-1}$ | |
| F(000) | 898 | |
| Crystal color | purple | |
| Crystal size | 0.160 x 0.151 x 0.126 mm$^3$ | |
| Theta range for data collection | 1.662 to 29.575° | |
| Index ranges | $-16 \leq h \leq 16, -17 \leq k \leq 17, -24 \leq l \leq 24$ | |
| Reflections collected | 72958 | |
| Independent reflections | 13884 [$R_{int}$ = 0.0444] | |
| Completeness to $\theta$ = 25.242° | 100.0 % | |
| Absorption correction | Semi-empirical from equivalents | |
| Refinement method | Full-matrix least-squares on F$^2$ | |
| Data / restraints / parameters | 13884 / 7 / 571 | |
| Goodness-of-fit on F$^2$ | 1.037 | |
| Final *R* indices [$I > 2\sigma_I$ = 11128 data] | $R_1$ = 0.0404, $wR_2$ = 0.1017 | |
| *R* indices (all data, 0.72 Å) | $R_1$ = 0.0549, $wR_2$ = 0.1101 | |
| Largest diff. peak and hole | 1.282 and −0.393 e/Å$^3$ | |

Notes: H atoms bonded to B1, C1 and C2 were refined unrestrained. The SQUEEZE program within the PLATON suite was used to address a very poorly-behaved solvent pocket likely containing a mixture of disordered furan and n-hexane molecules; attempts to model this solvent mixture required unreasonably strong restraints in order to maintain sensible geometries.

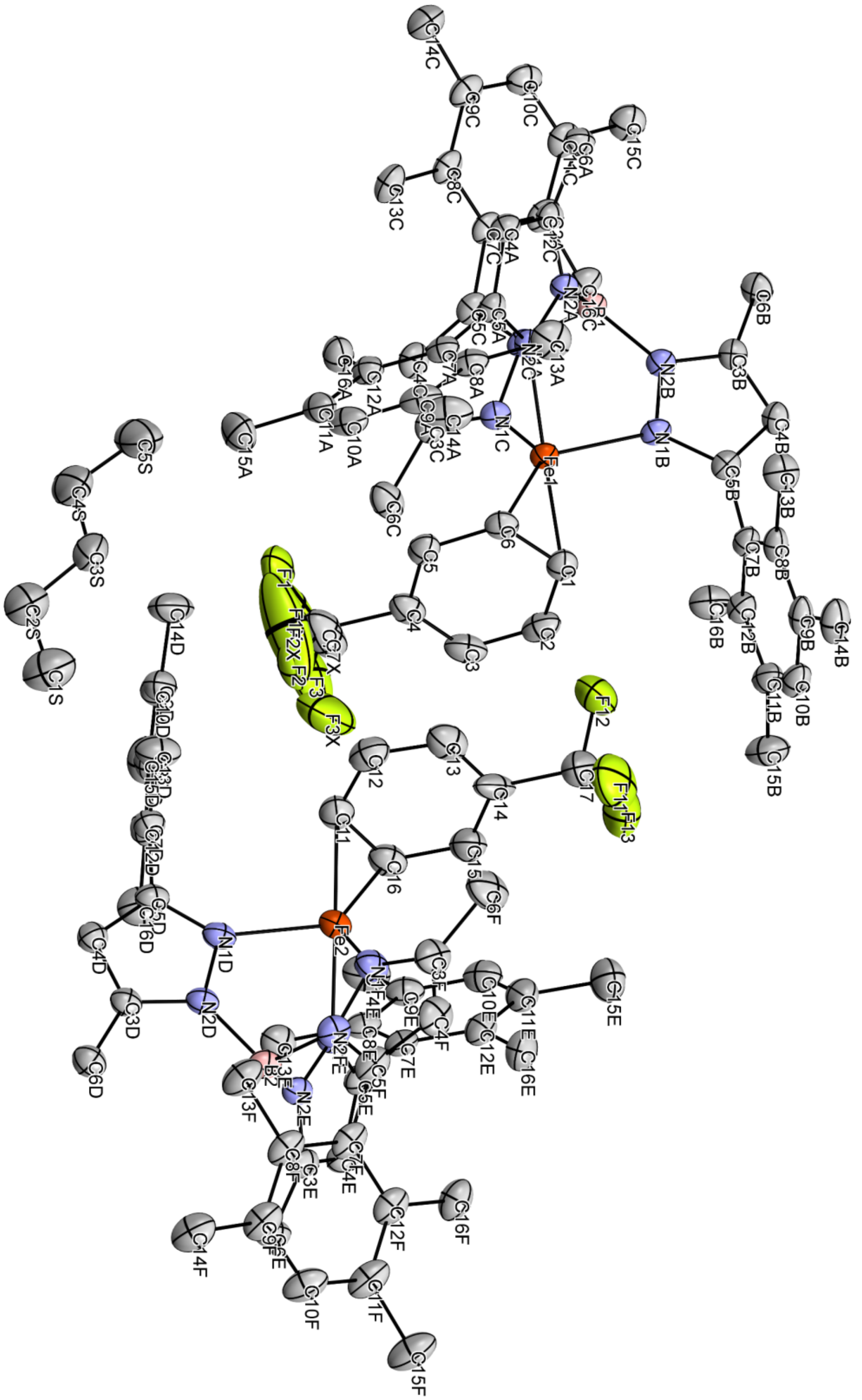

Figure 1-39. Labelled thermal ellipsoid plot (50%) for $\mathrm{Tp^{Dur,Me}Fe(3,4\text{-}\eta^2\text{-}PhCF_3)}$ (**7**).

Table 1-8. Crystal data and structure refinement for $\mathrm{Tp^{Dur,Me}Fe(3,4\text{-}\eta^2\text{-}PhCF_3)}$ (**7**).

| | | |
|---|---|---|
| Identification code | hh309le_r | |
| Empirical formula | $C_{51.50}H_{63}BF_3FeN_6$ | |
| Formula weight | 889.74 | |
| Temperature | 100(2) K | |
| Wavelength | 0.71073 Å | |
| Crystal system | Monoclinic | |
| Space group | $P2_1/c$ | |
| Unit cell dimensions | a = 19.5663(9) Å | $\alpha = 90°$. |
| | b = 21.8594(10) Å | $\beta = 90.623(3)°$. |
| | c = 22.1014(10) Å | $\gamma = 90°$. |
| Volume | 9452.4(7) $Å^3$ | |
| Z | 8 | |
| Density (calculated) | 1.250 $mg/m^3$ | |
| Absorption coefficient | 0.372 $mm^{-1}$ | |
| F(000) | 3776 | |
| Crystal color | brown | |
| Crystal size | 0.207 x 0.183 x 0.103 $mm^3$ | |
| Theta range for data collection | 1.041 to 27.103° | |
| Index ranges | $-25 \le h \le 25$, $-28 \le k \le 27$, $-28 \le l \le 28$ | |
| Reflections collected | 232521 | |
| Independent reflections | 20851 [$R_{\mathrm{int}} = 0.0607$] | |
| Completeness to $\theta = 25.242°$ | 100.0 % | |
| Absorption correction | Semi-empirical from equivalents | |
| Refinement method | Full-matrix least-squares on $F^2$ | |
| Data / restraints / parameters | 20851 / 79 / 1225 | |
| Goodness-of-fit on $F^2$ | 1.034 | |
| Final $R$ indices [$I > 2\sigma_I$ = 15255 data] | $R_1 = 0.0543$, $wR_2 = 0.1313$ | |
| $R$ indices (all data, 0.78 Å) | $R_1 = 0.0819$, $wR_2 = 0.1464$ | |
| Largest diff. peak and hole | 1.543 and −0.888 e/$Å^3$ | |

Notes: H atoms bonded to B1, C1 and C2 were refined unrestrained. One $CF_3$ group exhibited disordered that was modeled over two positions; the disorder ratio was refined freely and converged at 65:35. The disorder was refined with the help of similarity restraints on 1,2- and 1,3- distances as well as rigid-bond restraints on anisotropic displacement parameters. The two carbon atom positions were nearly-overlapping, and their anisotropic displacement parameters were constrained to be equivalent.

### *Computational Procedures and Results*

Density functional theory calculations were performed using the M06L[35] functional as implemented in the ORCA 4.2.1 computational chemistry package[36] with a custom Alrichs-type basis set (DefBas4): for H atoms, TZV(p); for B, C, and N atoms, TZV(2d); for Ni, TZV(2pf). The solid-state X-ray structure coordinates were used as a starting point. Molecular orbitals were visualized with Avogadro 1.2.[50] Successful optimization to a minimum was confirmed by the absence of imaginary frequencies in a subsequent frequency calculation.

Table 1-9. Optimized geometry of TpFe(3,4-η2-PhCF3) (S = 3/2) with Mulliken charge and spin populations.

| | **x** | **y** | **z** | **charge** | **spin** |
|---|---|---|---|---|---|
| Fe | -0.038161 | 15.178623 | 16.219800 | 0.742937 | 3.331330 |
| C | 1.345455 | 16.235460 | 17.322950 | -0.203938 | -0.132816 |
| H | 0.960225 | 16.341953 | 18.343443 | 0.056528 | 0.007034 |
| C | 2.605112 | 15.595331 | 17.114796 | 0.025454 | -0.002837 |
| H | 3.027204 | 14.987051 | 17.919314 | 0.041653 | 0.001550 |
| C | 3.314067 | 15.757178 | 15.943847 | -0.042152 | -0.045988 |
| H | 4.281743 | 15.268175 | 15.811912 | 0.039180 | 0.003389 |
| C | 2.792186 | 16.572920 | 14.906587 | -0.239856 | -0.059332 |
| C | 1.569932 | 17.203181 | 15.064000 | 0.043078 | 0.013191 |
| H | 1.194348 | 17.849050 | 14.267212 | 0.042651 | 0.000451 |
| C | 0.815626 | 17.066130 | 16.262308 | -0.202435 | -0.129575 |
| H | 0.025439 | 17.793961 | 16.478090 | 0.056478 | 0.006067 |
| C | 3.592441 | 16.732106 | 13.658776 | 0.750177 | 0.000809 |
| F | 3.797788 | 15.544779 | 13.038652 | -0.233385 | -0.001449 |
| F | 4.819244 | 17.226679 | 13.906496 | -0.225431 | -0.001250 |
| F | 3.010694 | 17.540525 | 12.763653 | -0.216457 | -0.000309 |
| B | -2.007530 | 12.938234 | 15.516578 | 0.378795 | 0.011410 |
| H | -2.792980 | 12.061715 | 15.249600 | -0.182853 | 0.000039 |
| N | -0.741018 | 13.734239 | 17.563010 | -0.282397 | -0.007812 |
| N | -1.628764 | 12.865328 | 17.020557 | -0.131068 | -0.003900 |
| C | -2.047781 | 11.993296 | 17.960778 | 0.106693 | 0.001486 |
| C | -1.414335 | 12.295988 | 19.155877 | -0.177406 | 0.001956 |
| H | -1.522042 | 11.790440 | 20.110609 | 0.055130 | 0.000480 |
| C | -0.605380 | 13.396647 | 18.848039 | 0.102463 | -0.004256 |
| N | -1.950204 | 15.471710 | 15.407322 | -0.284646 | -0.007512 |
| N | -2.642987 | 14.322657 | 15.212942 | -0.131553 | -0.003189 |
| C | -3.865483 | 14.604616 | 14.717663 | 0.107462 | 0.003400 |
| C | -3.979193 | 15.979251 | 14.580308 | -0.177604 | 0.001434 |
| H | -4.830158 | 16.540888 | 14.207350 | 0.055576 | 0.000524 |
| C | -2.747695 | 16.473131 | 15.027008 | 0.104084 | -0.001636 |
| N | 0.302527 | 13.665360 | 14.795957 | -0.278301 | -0.001062 |

| | | | | | |
|---|---|---|---|---|---|
| N | -0.721666 | 12.784311 | 14.669744 | -0.128240 | -0.002279 |
| C | 1.251682 | 13.279878 | 13.940061 | 0.110199 | 0.007589 |
| C | 0.848801 | 12.133389 | 13.244388 | -0.178118 | -0.000023 |
| H | 1.397573 | 11.586462 | 12.483840 | 0.054801 | 0.000710 |
| C | -0.414937 | 11.855426 | 13.742227 | 0.105633 | 0.009387 |
| H | 0.069294 | 13.960679 | 19.490385 | 0.047246 | 0.000881 |
| H | -2.767165 | 11.218215 | 17.707944 | 0.061234 | 0.000465 |
| H | -1.119507 | 11.061979 | 13.504239 | 0.058910 | -0.000175 |
| H | -2.396869 | 17.501976 | 15.090801 | 0.048610 | 0.000753 |
| H | -4.565506 | 13.802761 | 14.495875 | 0.061484 | 0.000357 |
| H | 2.176145 | 13.849458 | 13.860782 | 0.059382 | 0.000710 |

**Final Single Point Energy:** −2534.200570978395 $E_h$

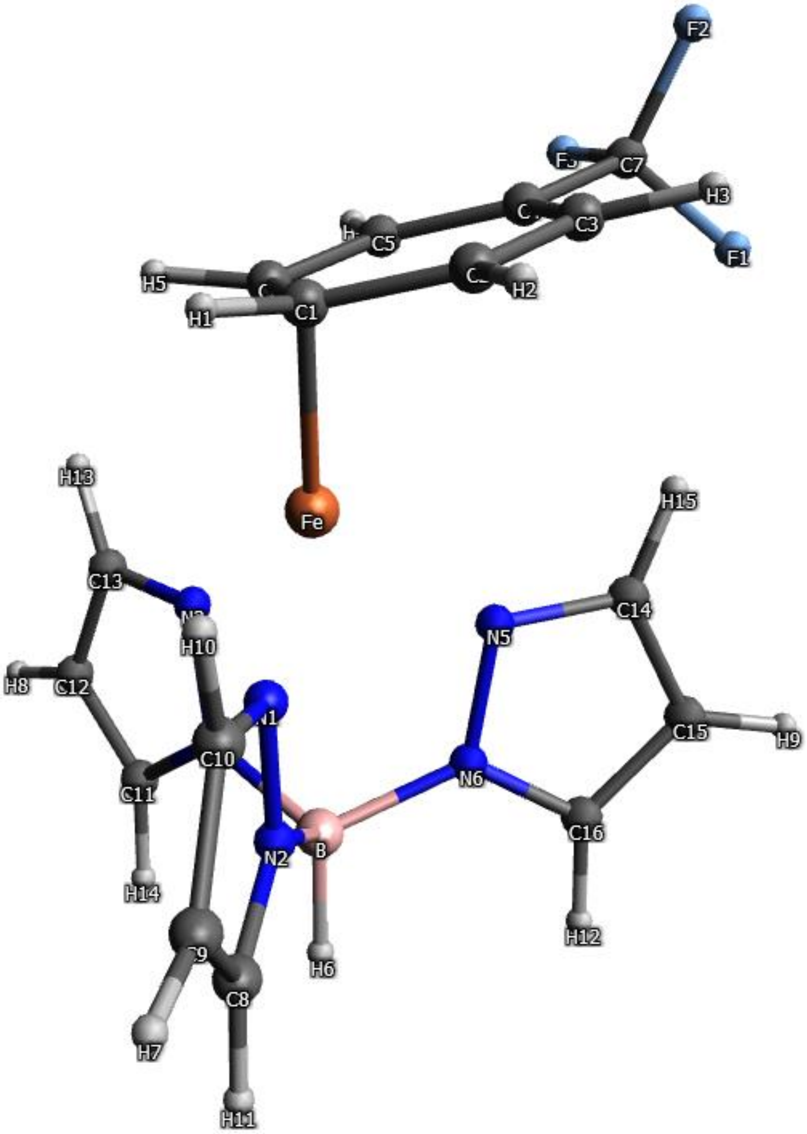

Figure 1-40. Optimized geometry of TpFe(3,4-$\eta^2$-PhCF$_3$) ($S$ = 3/2).

Table 1-10. Optimized geometry of TpFe(3,4-$\eta^2$-PhCF$_3$) ($S$ = 1/2).

| | x | y | z | charge | spin |
|---|---|---|---|---|---|
| Fe | -0.003079 | 15.109430 | 16.165040 | 0.678613 | 0.856050 |
| C | 1.283671 | 16.170874 | 17.353164 | -0.190414 | 0.013684 |
| H | 0.908529 | 16.237725 | 18.380105 | 0.052827 | -0.003446 |
| C | 2.562039 | 15.571307 | 17.128092 | 0.032829 | -0.003056 |
| H | 3.006261 | 14.965120 | 17.922187 | 0.043503 | 0.000026 |
| C | 3.246824 | 15.752874 | 15.950276 | -0.050364 | 0.085204 |
| H | 4.219735 | 15.281393 | 15.795147 | 0.040937 | -0.005817 |
| C | 2.701604 | 16.590989 | 14.933068 | -0.246383 | 0.074409 |
| C | 1.489893 | 17.220488 | 15.125956 | 0.049589 | 0.003914 |
| H | 1.108076 | 17.897291 | 14.358227 | 0.043617 | -0.000144 |
| C | 0.734866 | 17.022241 | 16.318137 | -0.193753 | 0.004438 |
| H | -0.066455 | 17.731845 | 16.549999 | 0.054106 | -0.002837 |
| C | 3.490474 | 16.786420 | 13.682844 | 0.752099 | -0.003580 |
| F | 3.698219 | 15.614536 | 13.036757 | -0.232872 | 0.002096 |
| F | 4.714803 | 17.284782 | 13.933936 | -0.224761 | 0.001790 |
| F | 2.895440 | 17.610698 | 12.811959 | -0.215411 | 0.000289 |
| B | -2.031017 | 12.928138 | 15.523168 | 0.360192 | -0.000504 |
| H | -2.838073 | 12.066705 | 15.273300 | -0.178994 | -0.000123 |
| N | -0.697927 | 13.736445 | 17.500572 | -0.262636 | 0.013217 |
| N | -1.625727 | 12.875459 | 17.017401 | -0.123651 | -0.001146 |
| C | -2.018398 | 12.028043 | 17.990467 | 0.104078 | -0.006408 |
| C | -1.331302 | 12.345727 | 19.151834 | -0.175799 | 0.003155 |
| H | -1.409928 | 11.864109 | 20.121800 | 0.053967 | 0.000007 |
| C | -0.514267 | 13.422904 | 18.786601 | 0.100981 | -0.011105 |
| N | -1.855081 | 15.436127 | 15.374225 | -0.264730 | 0.013419 |
| N | -2.613420 | 14.326960 | 15.199648 | -0.124263 | -0.001136 |
| C | -3.810772 | 14.665415 | 14.679306 | 0.104545 | -0.005737 |
| C | -3.842980 | 16.041268 | 14.512136 | -0.176225 | 0.002988 |
| H | -4.656750 | 16.642792 | 14.118555 | 0.054369 | 0.000044 |
| C | -2.589008 | 16.473648 | 14.961294 | 0.103068 | -0.010256 |
| N | 0.280232 | 13.606705 | 14.800387 | -0.273615 | -0.047343 |
| N | -0.749220 | 12.736506 | 14.672782 | -0.123801 | 0.000792 |
| C | 1.235274 | 13.214216 | 13.952488 | 0.111721 | 0.019987 |
| C | 0.825512 | 12.068499 | 13.259669 | -0.177336 | -0.002606 |
| H | 1.375398 | 11.514601 | 12.504991 | 0.055924 | 0.000420 |
| C | -0.443464 | 11.801806 | 13.750891 | 0.105496 | 0.009757 |
| H | 0.198263 | 13.985451 | 19.387769 | 0.045242 | 0.000704 |
| H | -2.758927 | 11.259104 | 17.783941 | 0.060018 | 0.000995 |
| H | -1.153167 | 11.013370 | 13.512215 | 0.059869 | -0.001772 |
| H | -2.178893 | 17.481405 | 15.004494 | 0.046101 | 0.000645 |
| H | -4.552788 | 13.900302 | 14.464039 | 0.060060 | 0.000952 |
| H | 2.163694 | 13.777417 | 13.876853 | 0.061259 | -0.001963 |

**Final Single Point Energy:** −2534.161680239700 $E_h$

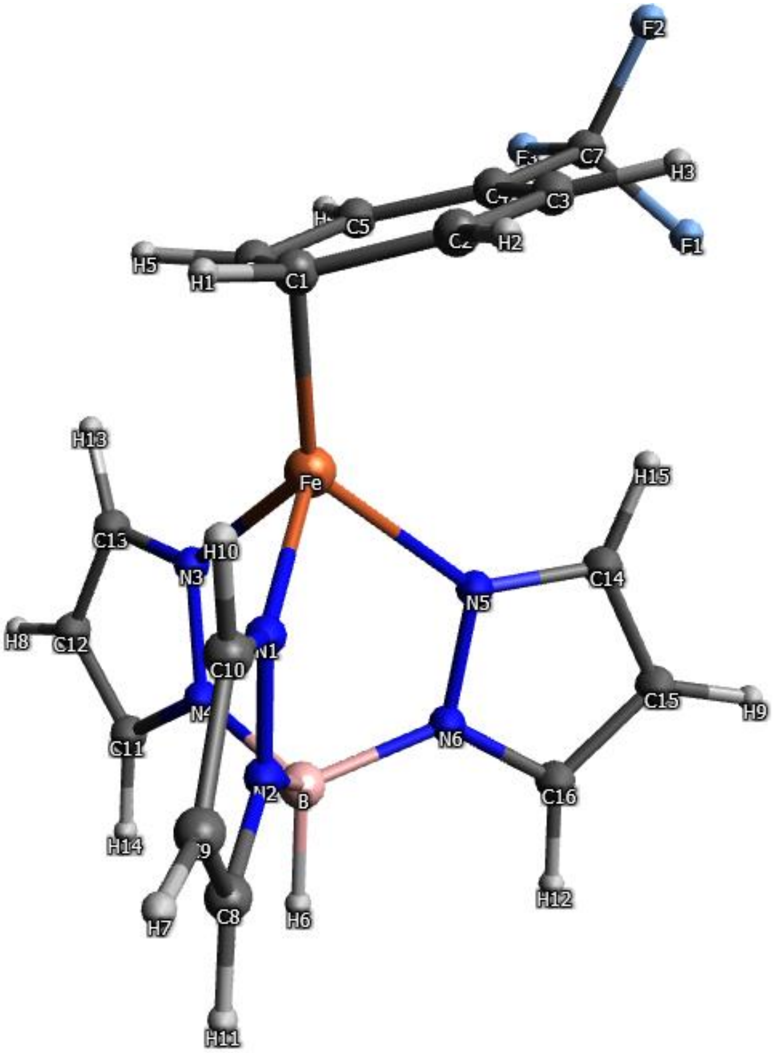

Figure 1-41. Optimized geometry of TpFe(3,4-$\eta^2$-PhCF$_3$) ($S$ = ½).

## References

(1) Muetterties, E. L.; Bleeke, J. R.; Wucherer, E. J.; Albright, T. A. Structural, Stereochemical, and Electronic Features of Arene-Metal Complexes. *Chem. Rev.* **1982**, *82* (5), 499–525. https://doi.org/10.1021/cr00051a002.

(2) Hubig, S. M.; Lindeman, S. V; Kochi, J. K. Charge-Transfer Bonding in Metal–Arene Coordination. *Coord. Chem. Rev.* **2000**, *200–202*, 831–873. https://doi.org/10.1016/S0010-8545(00)00322-2.

(3) Pampaloni, G. Aromatic Hydrocarbons as Ligands. Recent Advances in the Synthesis, the Reactivity and the Applications of Bis(H6-Arene) Complexes. *Coordination Chemistry Reviews*. Elsevier March 1, 2010, pp 402–419. https://doi.org/10.1016/j.ccr.2009.05.014.

(4) Nicholls, B.; Whiting, M. C. The Organic Chemistry of the Transition Elements. Part I. Tricarbonylchromium Derivatives of Aromatic Compounds. *J. Chem. Soc.* **1959**, No. 0, 551–556. https://doi.org/10.1039/jr9590000551.

(5) Semmelhack, M. F.; Chlenov, A. (Arene)Cr(CO)3 Complexes: Aromatic Nucleophilic Substitution. In *Top. Organomet. Chem.*; Springer, Berlin, Heidelberg, 2004; pp 43–69. https://doi.org/10.1007/b94491.

(6) Huttner, G.; Lange, S. Transition Metal Complexes of Cyclic π-Ligands. IV. The Crystal and Molecular Structure of Bis(Hexamethylbenzene)Ruthenium(0), a Complex Containing a Bent Tetrahapto Benzene Nucleus. *Acta Crystallogr. Sect. B Struct. Crystallogr. Cryst. Chem.* **1972**, *28* (7), 2049–2060. https://doi.org/10.1107/s0567740872005515.

(7) Brauer, D. J.; Krueger, C. Bonding of Aromatic Hydrocarbons to Nickel(0). Structure of Bis(Tricyclohexylphosphine)(1,2-.Eta.2-Anthracene)Nickel(0)-Toluene. *Inorg. Chem.* **1977**, *16* (4), 884–891. https://doi.org/10.1021/ic50170a033.

(8) Harman, W. D.; Taube, H. Reactivity of Pentaammineosmium(II) with Benzene. *J. Am. Chem. Soc.* **1987**, *109* (6), 1883–1885. https://doi.org/10.1021/ja00240a061.

(9) Meiere, S. H.; Brooks, B. C.; Gunnoe, T. B.; Sabat, M.; Harman, W. D. A Promising New Dearomatization Agent: Crystal Structure, Synthesis, and Exchange Reactions of the Versatile Complex TpRe(CO)(1-Methylimidazole)(H2-Benzene) (Tp = Hydridotris(Pyrazolyl)Borate). *Organometallics* **2001**, *20* (6), 1038–1040. https://doi.org/10.1021/om000900o.

(10) Graham, P. M.; Meiere, S. H.; Sabat, M.; Harman, W. D. Dearomatization of Benzene, Deamidization of N,N-Dimethylformamide, and a Versatile New Tungsten π Base. *Organometallics* **2003**, *22* (22), 4364–4366.

https://doi.org/10.1021/om030560h.

(11) Margulieux, G. W.; Bezdek, M. J.; Turner, Z. R.; Chirik, P. J. Ammonia Activation, H $_2$ Evolution and Nitride Formation from a Molybdenum Complex with a Chemically and Redox Noninnocent Ligand. *J. Am. Chem. Soc.* **2017**, *139* (17), 6110–6113. https://doi.org/10.1021/jacs.7b03070.

(12) Harman, W. D. The Activation of Aromatic Molecules with Pentaammineosmium(II). *Chem. Rev.* **1997**, *97* (6), 1953–1978. https://doi.org/10.1021/cr940316n.

(13) Liebov, B. K.; Harman, W. D. Group 6 Dihapto-Coordinate Dearomatization Agents for Organic Synthesis. *Chem. Rev.* **2017**, *117* (22), 13721–13755. https://doi.org/10.1021/acs.chemrev.7b00480.

(14) Trofimenko, S. Recent Advances in Poly(Pyrazolyl)Borate (Scorpionate) Chemistry. *Chem. Rev.* **1993**, *93* (3), 943–980. https://doi.org/10.1021/cr00019a006.

(15) McSkimming, A.; Harman, W. H. A Terminal N2 Complex of High-Spin Iron(I) in a Weak, Trigonal Ligand Field. *J. Am. Chem. Soc.* **2015**, *137* (28), 8940–8943. https://doi.org/10.1021/jacs.5b06337.

(16) Cummins, D. C.; Yap, G. P. A.; Theopold, K. H. Scorpionates of the “Tetrahedral Enforcer” Variety as Ancillary Ligands for Dinitrogen Complexes of First Row Transition Metals (Cr-Co). *Eur. J. Inorg. Chem.* **2016**, *2016* (15–16), 2349–2356. https://doi.org/10.1002/ejic.201501326.

(17) Kisko, J. L.; Hascall, T.; Parkin, G. The Synthesis, Structure, and Reactivity of Phenyl Tris(3-Tert- Butylpyrazolyl)Borato Iron Methyl, [PhTp(Bu1)]FeMe: Isolation of a Four- Coordinate Monovalent Iron Carbonyl Complex, [PhTp(Bu1)]FeCO [10]. *J. Am. Chem. Soc.* **1998**, *120* (40), 10561–10562. https://doi.org/10.1021/ja982323p.

(18) Shirasawa, N.; Akita, M.; Hikichi, S.; Moro-Oka, Y. Thermally Stable Coordinatively Unsaturated Alkyl Complexes Resistant to β-Hydride Elimination: Tp(IPr)M-CH2CH3 (M = Co,Fe). *Chem. Commun.* **1999**, No. 5, 417–418. https://doi.org/10.1039/a809441a.

(19) Brunker, T. J.; Hascall, T.; Cowley, A. R.; Rees, L. H.; O’Hare, D. Variable Coordination Modes of Hydrotris(3-Isopropyl-4-Bromopyrazolyl)Borate (Tp′) in Fe(II), Mn(II), Cr(II), and Cr(III) Complexes: Formation of MTp′Cl (M = Fe and Mn), Structural Isomerism in CrTp′2, and the Observation of Tp′- as an Uncoordinated Anion. *Inorg. Chem.* **2001**, *40* (13), 3170–3176. https://doi.org/10.1021/ic010125k.

(20) Nobuhiko Shirasawa; Trieu Thi Nguyet, 1; Shiro Hikichi; Yoshihiko Moro-oka, and; Akita*, M. Tetrahedral, Highly Coordinatively Unsaturated 14e (Fe) and 15e (Co) Hydrocarbyl Complexes Bearing Hydrotris(Pyrazolyl)Borato Ligands (TpR‘), TpR‘M−R (M = Fe, Co, Ni). **2001**. https://doi.org/10.1021/OM0103106.

(21) Jové, F. A.; Pariya, C.; Scoblete, M.; Yap, G. P. A.; Theopold, K. H. A Family of Four-Coordinate Iron(II) Complexes Bearing the Sterically Hindered Tris(Pyrazolyl)Borato Ligand TptBu,Me. *Chem. - A Eur. J.* **2011**, *17* (4), 1310–1318. https://doi.org/10.1002/chem.201001792.

(22) Rheingold, A. L.; White, C. B.; Trofimenko, S. Hydrotris(3-Mesitylpyrazol-1-Yl)Borate and Hydrobis(3-Mesitylpyrazol-1-Yl)(5-Mesitylpyrazol-1-Yl)Borate: Symmetric and Asymmetric Ligands with Rotationally Restricted Aryl Substituents. *Inorg. Chem.* **1993**, *32* (16), 3471–3477. https://doi.org/10.1021/ic00068a015.

(23) Yap, G. P. A.; Jove, F.; Urbano, J.; Alvarez, E.; Trofimenko, S.; Díaz-Requejo, M. M.; Pérez, P. J. Unusual Polybrominated Polypyrazolylborates and Their Copper(I) Complexes: Synthesis, Characterization, and Catalytic Activity. *Inorg. Chem.* **2007**, *46* (3), 780–787. https://doi.org/10.1021/ic061714z.

(24) van Dijkman, T. F.; Siegler, M. A.; Bouwman, E. Highly Tunable Fluorinated Trispyrazolylborates [HB(3-CF $_3$ -5-{4-RPh}pz) $_3$ ] $^-$ (R = NO $_2$ , CF $_3$ , Cl, F, H, OMe and NMe $_2$ ) and Their Copper( i ) Complexes. *Dalt. Trans.* **2015**, *44* (48), 21109–21123. https://doi.org/10.1039/C5DT04006J.

(25) Smith, J. M.; Sadique, A. R.; Cundari, T. R.; Rodgers, K. R.; Lukat-Rodgers, G.; Lachicotte, R. J.; Flaschenriem, C. J.; Vela, J.; Holland, P. L. Studies of Low-Coordinate Iron Dinitrogen Complexes. *J. Am. Chem. Soc.* **2006**, *128* (3), 756–769. https://doi.org/10.1021/ja052707x.

(26) Deutsch, J. L.; Poling, S. M. The Determination of Paramagnetic Susceptibility by NMR: A Physical Chemistry Experiment. *J. Chem. Educ.* **1969**, *46* (3), 167. https://doi.org/10.1021/ed046p167.

(27) Schubert, E. M. Utilizing the Evans Method with a Superconducting NMR Spectrometer in the Undergraduate Laboratory. *J. Chem. Educ.* **1992**, *69* (1), 62. https://doi.org/10.1021/ed069p62.1.

(28) Kevin D. Welch; Daniel P. Harrison; Edward C. Lis, J. .; Weijun Liu; Rebecca J. Salomon, and; Harman*, W. D.; Myers, W. H. Large-Scale Syntheses of Several Synthons to the Dearomatization Agent {TpW(NO)(PMe3)} and Convenient Spectroscopic Tools for Product Analysis. **2007**. https://doi.org/10.1021/OM070034G.

(29) Myers, J. T.; Smith, J. A.; Dakermanji, S. J.; Wilde, J. H.; Wilson, K. B.;

Shivokevich, P. J.; Harman, W. D. Molybdenum(0) Dihapto-Coordination of Benzene and Trifluorotoluene: The Stabilizing and Chemo-Directing Influence of a CF $_3$ Group. *J. Am. Chem. Soc.* **2017**, jacs.7b05009. https://doi.org/10.1021/jacs.7b05009.

(30) Six Structures Were Found in the Cambridge Structural Database Containing Well-Ordered Molecules of Free PhCF3 (Version 5.41, March 2020). Among These, the C–C Bonds Ranged from 1.36 to 1.40 Å, with Average Cipso–Cortho, Cortho-Cmeta, and Cmeta-Cpara Dist.

(31) Hagen, W. R. EPR Spectroscopy of Iron—Sulfur Proteins. *Adv. Inorg. Chem.* **1992**, *38* (C), 165–222. https://doi.org/10.1016/S0898-8838(08)60064-1.

(32) Reger, D. L.; Gardinier, J. R.; Elgin, J. D.; Smith, M. D.; Hautot, D.; Long, G. J.; Grandjean, F. Structure-Function Correlations in Iron(II) Tris(Pyrazolyl)Borate Spin-State Crossover Complexes. *Inorg. Chem.* **2006**, *45* (22), 8862–8875. https://doi.org/10.1021/ic0607437.

(33) McWilliams, S. F.; Brennan-Wydra, E.; MacLeod, K. C.; Holland, P. L. Density Functional Calculations for Prediction of $^{57}$ Fe Mössbauer Isomer Shifts and Quadrupole Splittings in β-Diketiminate Complexes. *ACS Omega* **2017**, *2* (6), 2594–2606. https://doi.org/10.1021/acsomega.7b00595.

(34) Zhao, Y.; Truhlar, D. G. A New Local Density Functional for Main-Group Thermochemistry, Transition Metal Bonding, Thermochemical Kinetics, and Noncovalent Interactions. *J. Chem. Phys.* **2006**, *125* (19), 194101. https://doi.org/10.1063/1.2370993.

(35) Weigend, F.; Ahlrichs, R. Balanced Basis Sets of Split Valence, Triple Zeta Valence and Quadruple Zeta Valence Quality for H to Rn: Design and Assessment of Accuracy. *Phys. Chem. Chem. Phys.* **2005**, *7* (18), 3297–3305. https://doi.org/10.1039/b508541a.

(36) Neese, F. Orca 4.2.1. *Wiley Interdiscip. Rev. Comput. Mol. Sci.* **2012**, *2*, 73.

(37) Hoyt, J. M.; Sylvester, K. T.; Semproni, S. P.; Chirik, P. J. Synthesis and Electronic Structure of Bis(Imino)Pyridine Iron Metallacyclic Intermediates in Iron-Catalyzed Cyclization Reactions. *J. Am. Chem. Soc.* **2013**, *135* (12), 4862–4877. https://doi.org/10.1021/ja400895j.

(38) Joannou, M. V.; Darmon, J. M.; Bezdek, M. J.; Chirik, P. J. Exploring C(Sp3)–C(Sp3) Reductive Elimination from an Isolable Iron Metallacycle. *Polyhedron* **2019**, *159*, 308–317. https://doi.org/10.1016/j.poly.2018.11.047.

(39) Chen, H.; Hodges, L. M.; Liu, R.; Stevens, W. C.; Sabat, M.; Harman, W. D.

Dearomatization of Furan: Structure of an H2-Furan Complex and a Survey of Its Reactivity. *J. Am. Chem. Soc.* **1994**, *116* (12), 5499–5500. https://doi.org/10.1021/ja00091a076.

(40) Meiere, S. H.; Brooks, B. C.; Gunnoe, T. B.; Carrig, E. H.; Sabat, M.; Harman, W. D. Dihapto Coordination of Aromatic Molecules by the Asymmetric π-Bases {TpRe(CO)(L)} (Tp = Hydridotris(Pyrazolyl)Borate; L = TBuNC, PMe3, Pyridine, 1-Methylimidazole, or NH3). *Organometallics* **2001**, *20* (17), 3661–3671. https://doi.org/10.1021/om010227i.

(41) Hamon, J. R.; Astruc, D.; Michaud, P. Syntheses, Characterizations, and Stereoelectronic Stabilization of Organometallic Electron Reservoirs: The 19-Electron D7 Redox Catalysts H5-C5R5FeI-H6-C6R6. *J. Am. Chem. Soc.* **1981**, *103* (4), 758–766. https://doi.org/10.1021/ja00394a006.

(42) Hickey, A. K.; Lee, W. T.; Chen, C. H.; Pink, M.; Smith, J. M. A Bidentate Carbene Ligand Stabilizes a Low-Coordinate Iron(0) Carbonyl Complex. *Organometallics* **2016**, *35* (17), 3069–3073. https://doi.org/10.1021/acs.organomet.6b00599.

(43) Ahdreou, A. D.; Bulbulian, R. V.; Gore, P. H. Friedel-Crafts Acetylation of Durene,Isodurene and Prehnitene. *Tetrahedron* **1980**, *36* (14), 2101–2104. https://doi.org/10.1016/0040-4020(80)80098-6.

(44) *Prisecaru, VMOSS4 Mössbauer Spectral Analysis Software, Www.Vmoss.Org, 2009-2016.*

(45) *SAINT, Version 8.34, Bruker (2012)*; Bruker AXS Inc.: Madison, Wisconsin, USA.

(46) *SADABS, Version 2012/1, Bruker (2012)*; Bruker AXS Inc.: Madison, Wisconsin, USA.

(47) Sheldrick, G. M. SHELXT - Integrated Space-Group and Crystal-Structure Determination. *Acta Crystallogr. Sect. A* **2015**, *71* (1), 3–8. https://doi.org/10.1107/S2053273314026370.

(48) Sheldrick, G. M. Crystal Structure Refinement with SHELXL. *Acta Crystallogr. Sect. C* **2015**, *71* (1), 3–8. https://doi.org/10.1107/S2053229614024218.

(49) Muller, P. Practical Suggestions for Better Crystal Structures. *Crystallogr. Rev.* **2009**, *15* (1), 57–83. https://doi.org/10.1080/08893110802547240.

(50) Hanwell, M. D.; Curtis, D. E.; Lonie, D. C.; Vandermeersch, T.; Zurek, E.; Hutchison, G. R. Avogadro 1.2. *J. Cheminform.* **2012**, *4*, 17.

# Chapter 2 : Activation of $sp^3$, $sp^2$, and sp C-H Bonds at High Spin Fe(I)

## *Introduction*

In biological systems, C-H functionalization is achieved using metalloenzymes of first-row transition metals (i.e. Mn, Fe, Co, Ni, and Cu).[1,2] However, in homogenous catalysis, few examples using these metals for that purpose have been observed. With iron, C-H activation is usually limited to substrates with coordinating functional groups to facilitate C-H activation via a cyclometalated species.[3–5] In the absence of directing groups, the activation of hydrocarbon substrates typically employs UV-irradiation to initiate radical pathways.[6–8]

From an organometallic perspective, ligands that dissociate as stable radical species are very rare. This was first reported in iron β-diketiminato complexes of trityl and ketyl radicals.[9] Both of these bound radicals are easily displaced by π-acids benzophenone and phenylacetylene to generate an Fe(I) species and the corresponding free radical. DFT calculations suggested that little radical character resides on the bound radical due to extensive mixing of metal and ligand orbitals. In contrast, a new 3-coordinate iron(I) PNP complex reacts with benzophenone to form a ketyl complex with distinct radical character on the bound ligand.[10] This is exemplified by end-on binding as opposed to side-on of the ketyl unit. Dissociation of neither benzophenone or ketyl radical was observed upon heating at 100°C for days, and unfortunately reactivity of this complex with π-acids was not described (Scheme 2-1).

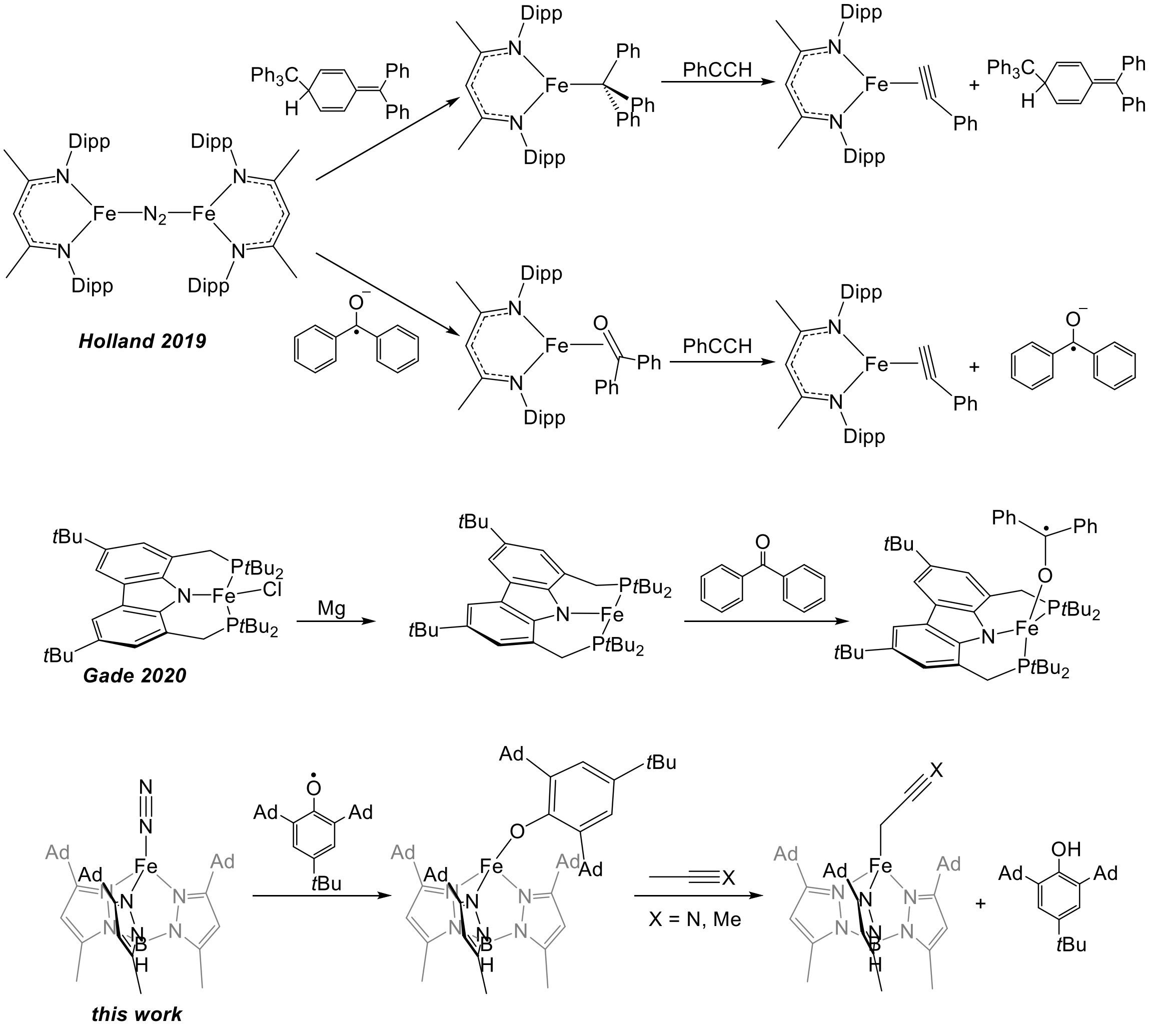

Scheme 2-1. Previously reported masked[9] and unmasked[10] radicals of iron, and the reactivity of the masked radical reported herein.

While our previously reported adamantyl-substituted trispyrazolylborate $Tp^{Ad}FeCl$ reduces to form the corresponding terminal $N_2$ species and not a naked Fe(I) fragment, we did note in our spin density calculations that there was significant single-electron character on the bound $N_2$.[11] Using the substantial steric bulk of this Tp ligand inspired us to explore its reactivity with a similarly bulky, stable free radical and explore how this species would interact with π-acids.

## *Results and Discussion*

Finding suitable π-acids to accommodate the extreme steric bulk of the adamantyl-substituted trispyrazolylborate ($Tp^{Me,Ad}$)$FeN_2$ was challenging. Substitution of dinitrogen with ethylene takes nearly 6 hours for completion under 4 atm of ethylene. This substitution takes 10 seconds for completion with our less bulky durene-substituted $(Tp^{Me,Dr}Fe)_2(\mu\text{-}N_2)$ (Figure 2-40). Addition of propene under similar conditions failed to produce any substitution at all. Single crystal X-Ray crystallography (XRD) of the ethylene complex **1** revealed two different structures (Figure 2-1). Both with the bound ethylene tipped downwards 12-14° away from the axis along the B-H bond. (Table 2-1).

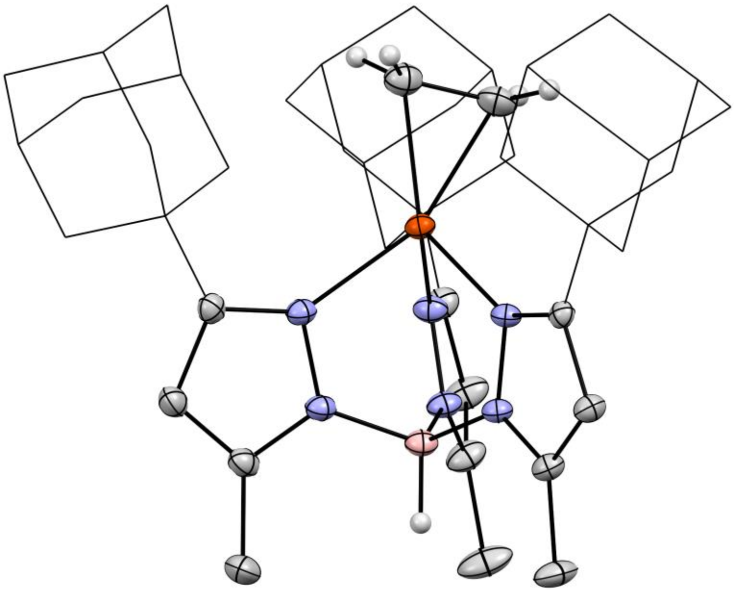

Figure 2-1. Thermal ellipsoid plots (50% probability) of the solid-state structure of $Tp^{Me,Ad}Fe(C_2H_4)$ (**1**). Orange, blue, pink, and gray ellipsoids represent Fe, N, B, and C atoms, respectively. Most hydrogen atoms and co-crystallized solvent molecules are omitted for clarity.

Table 2-1. Selected bond angles for $Tp^{Me,Ad}Fe(C_2H_4)$ (**1**).

|  | C–C [Å] | Fe–$C_1$ [Å] | Fe–$C_2$ [Å] | Angle B–Fe–$C_2$ [°] |
|---|---|---|---|---|
| A | 1.412(3) | 2.074(2) | 2.071(2) | 148.29(6) |

| | | | | |
|---|---|---|---|---|
| B | 1.385(2) | 2.058(2) | 2.072(2) | 146.05(6) |

Solution magnetomety on **1** by the method of Evans[12,13] gave an effective magnetic moment of 4.0 ± 0.2 $\mu_B$, confirming its assignment as high spin. X-band electron paramagnetic resonance (EPR) of the durene analogue $Tp^{Me,Dr}Fe(C_2H_4)$ **3** in 2-MeTHF at 15K exhibits a broad rhombic spectrum consistent with an $S = 3/2$ ($E/D \approx 0.3$) (Figure 2-28). Thus it was assumed that **1** would be very similar. We attempted to displace the bound ethylene with 2,6-adamantyl-4-tertbutylphenoxyl radical, however we surprisingly generated a high yield (70%) of the vinyl species $Tp^{Me,Dr}Fe$(vinyl) **2** instead (Scheme 2-2). Single crystal XRD on **2** revealed an Fe−C bond length of 2.046(1) Å, typical of Tp iron(II) alkyls.[14,15] As expected, the vinyl C-C bond length was ~ 0.1 Å shorter than the previously reported C-C bond length of the $Tp^{tBu,tBu}Fe$(ethyl) (1.327(2) and 1.441(5) Å, respectively).[16] The C-C bond length is most comparable to the previously reported pyridine(diimine)iron(vinyl)(acetate) at 1.323(2) Å.[17] To wit, this is the only TpFe vinyl species crystallographically characterized to date.

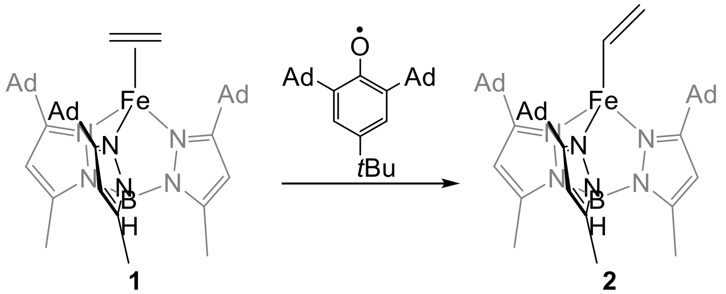

Scheme 2-2. C-H Activation of ethylene

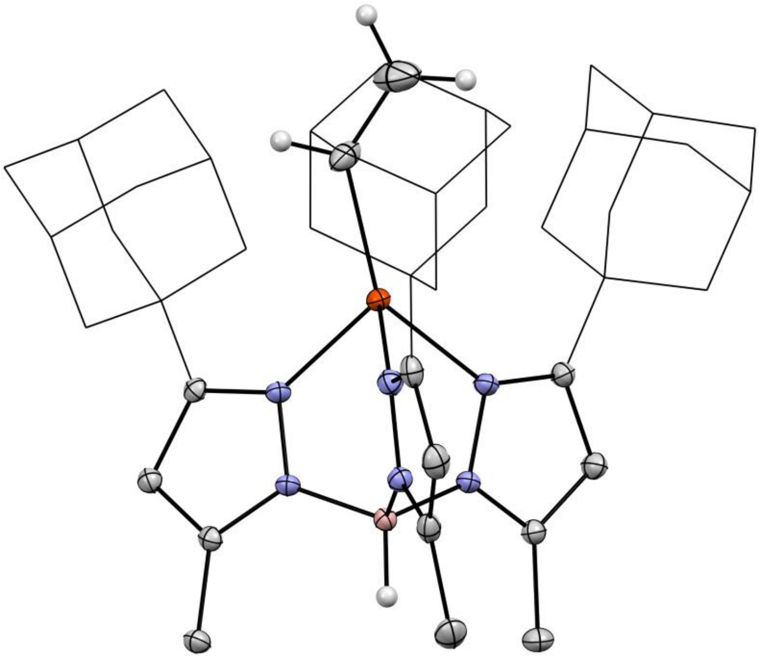

Figure 2-2. Thermal ellipsoid plots (50% probability) of the solid-state structure of Tp$^{Me,Dr}$Fe(vinyl) (**2**). Orange, blue, pink, and gray ellipsoids represent Fe, N, B, and C atoms, respectively. Most hydrogen atoms and co-crystallized solvent molecules are omitted for clarity.

We conducted the analogous experiment using our less bulky durene-substituted Tp$^{Me,Dr}$Fe($C_2H_4$) **3**, however we exclusively generated the iron phenoxide **4**. (Scheme 2-3).

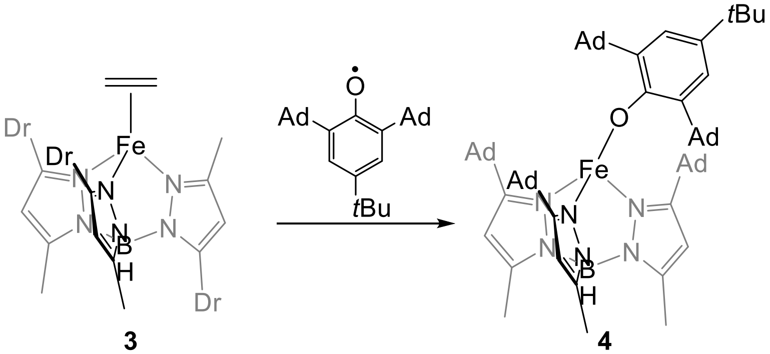

**3** **4**

Scheme 2-3. Ethylene substitution at Tp$^{Me,Dr}$Fe

This difference of reactivity with varying steric bulk suggested that dissociation of the bound phenoxyl radical was occuring in **1** but not **3**. We thus prepared the alkoxide

$\mathrm{Tp^{Me,Dr}Fe(OPhAd_2)}$ **5** (Scheme 2-4) and placed it under 4 atm of ethylene. However, no reaction took place after several days at room temperature. If heated, **5** was largely decomposed by adventitious water.

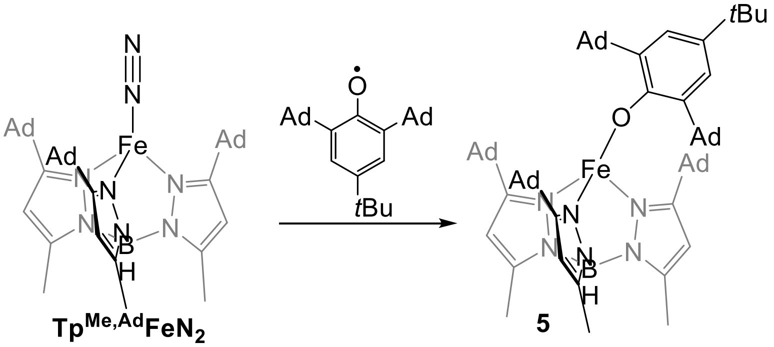

Scheme 2-4. Preparation of $\mathrm{Tp^{Me,Dr}Fe(OPhAd_2)}$ **5**

We speculated that the weak binding affinity of ethylene was insufficient to displace the radical, so we moved towards more π-acidic, triply-bonded substrates. Substitution of the bound $N_2$ with these substrates was remarkably more facile. Addition of acetonitrile or 2-butyne to $\mathrm{Tp^{Me,Ad}FeN_2}$ produced the corresponding $\eta^2$ species **6** and **8** within seconds. Acetonitrile produced the side-on species as previously observed with Fe(I) β-diketiminato complexes.[18] In both complexes, X-Ray crystallography revealed an elongation of the triple bond and deviation from sp linearity (Figure 2-3, Table 2-3). Close Fe-C contacts (< 1.99 Å) indicated stronger backbonding interactions than observed in **1**.

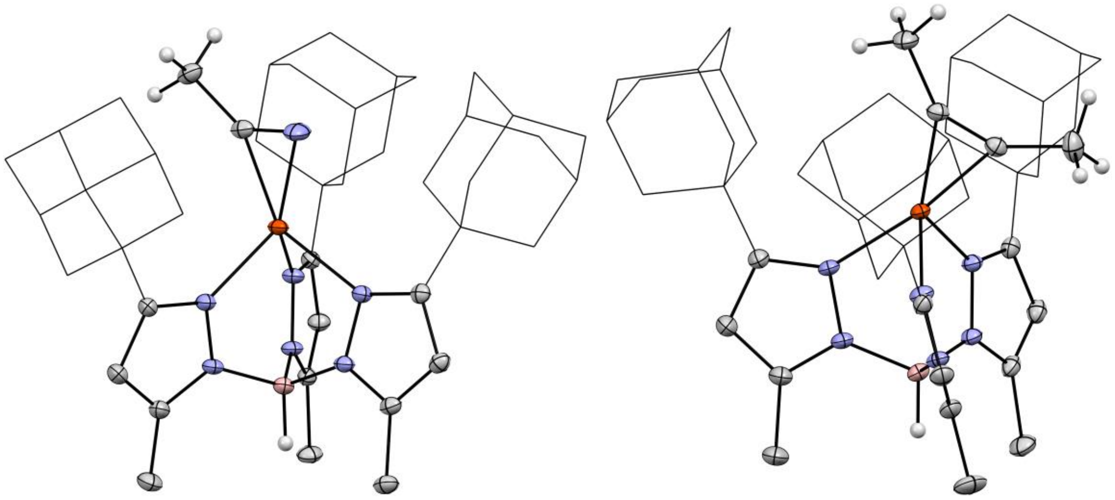

Figure 2-3. Thermal ellipsoid plots (50% probability) of the solid-state structure of $Tp^{Me,Ad}$Fe(MeCN) **6** and $Tp^{Me,Ad}$Fe(2-butyne) **8.** Orange, blue, pink, and gray ellipsoids represent Fe, N, B, and C atoms, respectively. Most hydrogen atoms and co-crystallized solvent molecules are omitted for clarity.

Table 2-2. Selected bond angles for 6, 7, and 12.

| compound | $C_1$/N−$C_2$ [Å] | Fe−$C_1$/N [Å] | Fe−$C_2$ [Å] | Angle $C_1$/N−$C_2$−$C_3$ [°] |
|---|---|---|---|---|
| $Tp^{Me,Ad}$Fe(MeCN) **6** | 1.208(3) | 1.943(1) | 1.980(1) | 137.4(2) |
| $Tp^{Me,Ad}$Fe(2-butyne) **8** | 1.269(2) | 1.981(2) | 1.973(2) | 142.8(2), 147.0(2) |
| $Tp^{Me,Ad}$Fe(PhCCH) **12** | 1.249(2) | 1.972(2) | 1.987(2) | 145.4(2) |

With $Tp^{Me,Ad}$Fe(MeCN) **6** and $Tp^{Me,Ad}$Fe(2-butyne) **8** in hand, we tested their reactivity for H-atom abstraction with 2,6-bis(adamantyl)-4-tert-butylphenoxyl radical ($Ad_2$PhO). C-H activation of the bound acetonitrile and butyne is rapid at −80°C producing the corresponding **7** and **9** complexes. (Figure 2-4).

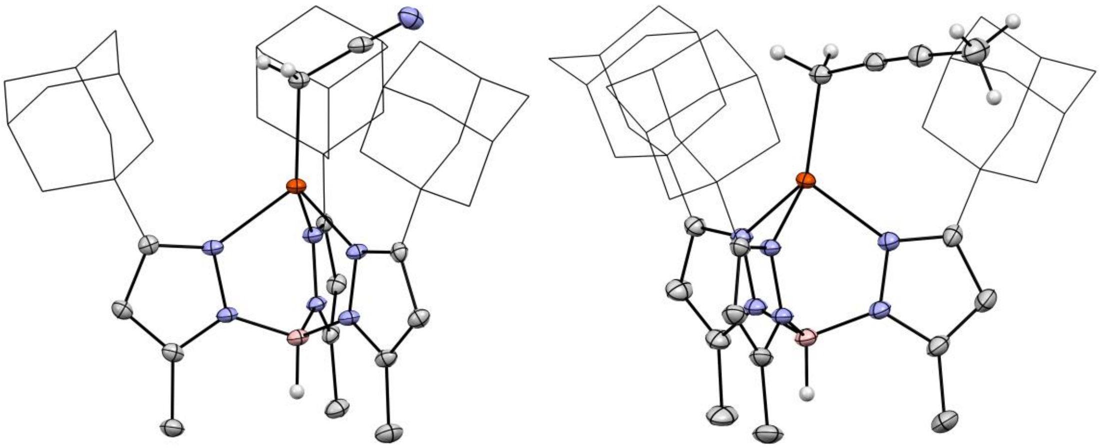

Figure 2-4. Thermal ellipsoid plots (50% probability) of the solid-state structure of $\mathrm{Tp^{Me,Ad}Fe(CH_2CN)}$ **7** and $\mathrm{Tp^{Me,Ad}Fe(CH_2CCCH_3)}$ **9**. Orange, blue, pink, and gray ellipsoids represent Fe, N, B, and C atoms, respectively. Most hydrogen atoms and co-crystallized solvent molecules are omitted for clarity.

Concerned that the iron center was simply reducing the radical to the phenoxide, then deprotonating the bound substrate, we prepared two different phenoxide complexes of varying steric bulk to see if we could discern a trend. To our surprise, we were unable to prepare any 4-tert-butylphenoxide complex $\mathrm{Tp^{Me,Ad}Fe(OPh}$*t*Bu) **11** by salt metathesis with $\mathrm{Tp^{Me,Ad}FeCl}$ and lithium 4-(tert-butyl)phenolate. Instead, we had to prepare the $\mathrm{Tp^{Me,Ad}Fe}$(methyl) **10** and react it with 4-tert-butylphenol which produces the desired product quantitatively. Note, this new route proved entirely ineffective for generating the $\mathrm{Tp^{Me,Ad}Fe(OPhAd_2)}$ **5**, which can only be produced by combining equal molar quantities of $\mathrm{Tp^{Me,Ad}FeN_2}$ and free radical $\mathrm{Ad_2PhO}$. With increasing steric bulk, X-Ray crystallography revealed elongated Fe-O bond lengths and steep deviations from the ideal tetrahedral geometry. (Figure 2-5, Table 2-3). While no iron phenoxides of 2,6-diadamanyl phenol have been structurally characterized to date, there are a handful of examples of the analogous 2,4,6-tri-tert-butyl phenoxide complexes, which have Fe–O bond lengths from

1.811–1.814 Å.[19,20] The Fe–O bond lengths of unsubstituted Fe(II) phenoxides are typically longer from 1.867–1.884 Å.[21,22]

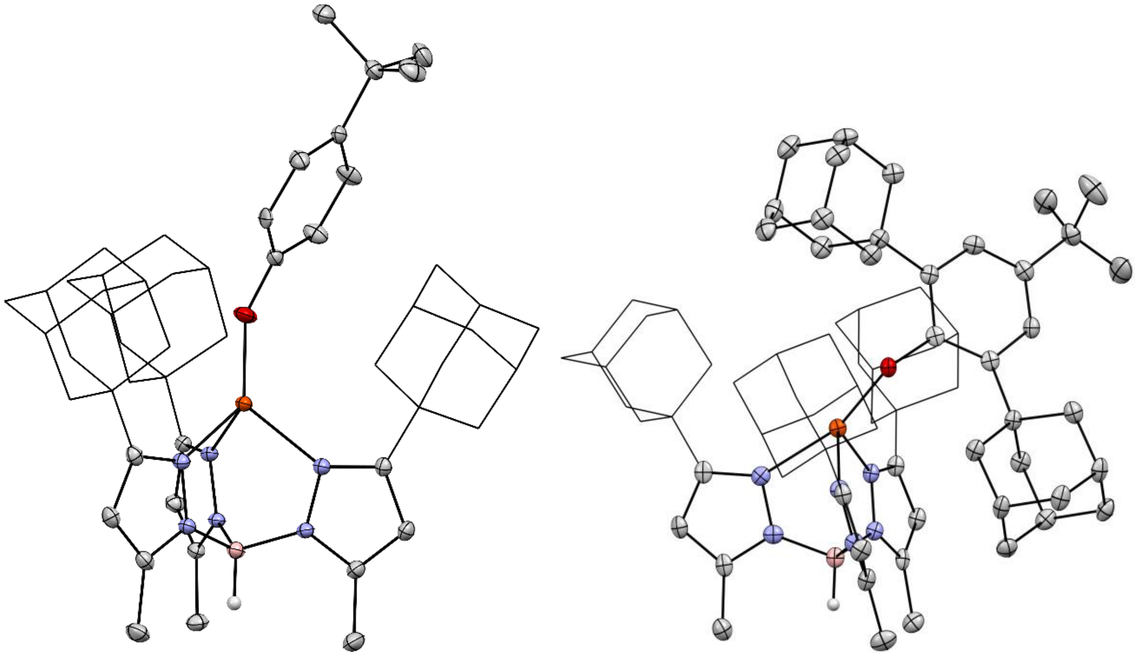

Figure 2-5. Thermal ellipsoid plots (50% probability) of the solid-state structure of **11** and **5**. Orange, red, blue, pink, and gray ellipsoids represent Fe, O, N, B, and C atoms, respectively. Most hydrogen atoms and co-crystallized solvent molecules are omitted for clarity.

Table 2-3. Selected bonds and angles for **11** and **5**.

| | Fe–O [Å] | Angle B–Fe–O [°] |
|---|---|---|
| Tp$^{\text{Me,Ad}}$Fe(OPhtBu) **11** | 1.851(8) | 167.1(3) |
| Tp$^{\text{Me,Ad}}$Fe(OPhAd$_2$) **5** | 1.906(2) | 141.03(9) |

With Tp$^{\text{Me,Ad}}$Fe(OPhAd$_2$) **5** and Tp$^{\text{Me,Ad}}$Fe(OPhtBu) **11** in hand, we tested their reactivity towards phenylacetylene. Curiously, only **5** produced the C-H activation product **12** (Figure 2-6). Even with extended heating of **11** in a large excess of phenylacetylene, no reaction was observed.

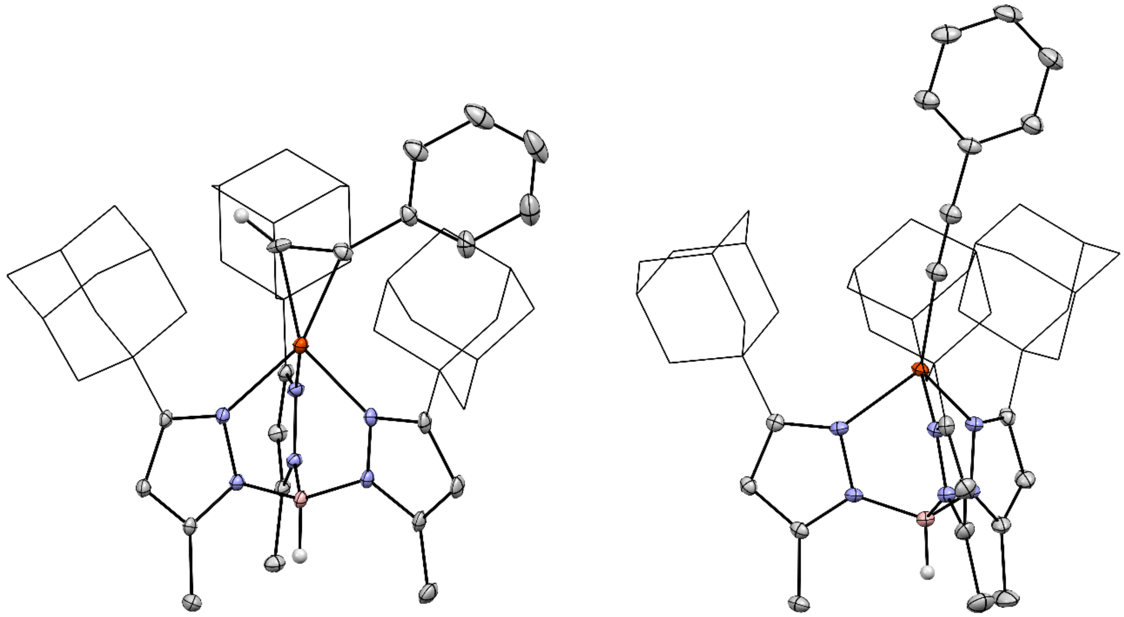

Figure 2-6. Thermal ellipsoid plots (50% probability) of the solid-state structure of **12** and **13**. Orange, blue, pink, and gray ellipsoids represent Fe, N, B, and C atoms, respectively. Most hydrogen atoms and co-crystallized solvent molecules are omitted for clarity.

From these studies, we couldn’t rule out that the C-H activations are occurring from the homolysis of the Fe-O bond, generating a stable organic radical and an iron(I) fragment with a high affinity for π-bonds. Once the alkene or alkyne is bound to iron, a rapid H-atom abstraction may occur to generate the Fe(II) alkyl and a new O-H bond. If indeed these reactions are proceeding through a free radical, this could be easily observed by EPR. Indeed, room-temperature X-Band EPR of high purity $Tp^{Me,Ad}Fe(OPhAd_2)$ **5** reveals a trace amount of the corresponding free radical in solution. (Figure 2-7).

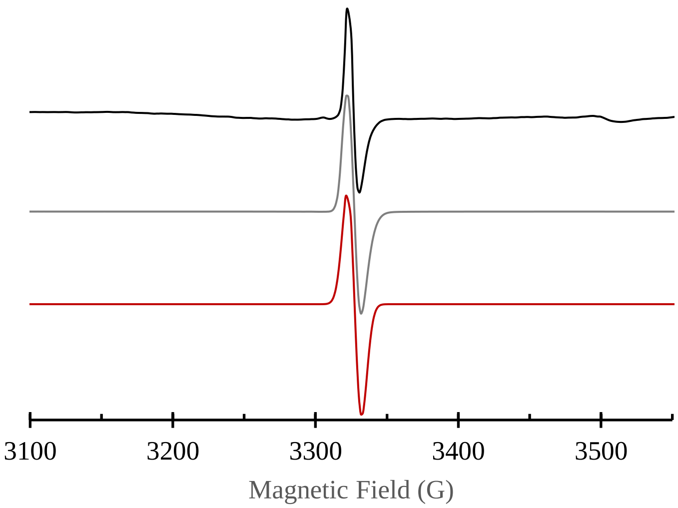

Figure 2-7. X-Band EPR spectra at 291K of $\text{Tp}^{\text{Me,Ad}}\text{Fe(OPhAd}_2)$ **5** (top, black) at 9.312 GHz, free radical $\text{Ad}_2\text{PhO}$ (middle, gray) at 9.318 GHz, and simulation (bottom, red). Simulation parameters: g = 2.004, lw = 1.00.

We attempted to quantify this dissociation using UV-Vis. At room temperature we estimated 0.18% dissociation. However upon heating the UV cell in either THF or toluene, the quantity of free radical generated increased, irreversibly. Efforts to isolate the iron-containing decomposition product have thus far been unsuccessful. We also attempted to trap this Fe(I) fragment by heating $\text{Tp}^{\text{Me,Ad}}\text{Fe(OPhAd}_2)$ **5** with CO, however no reaction was observed.

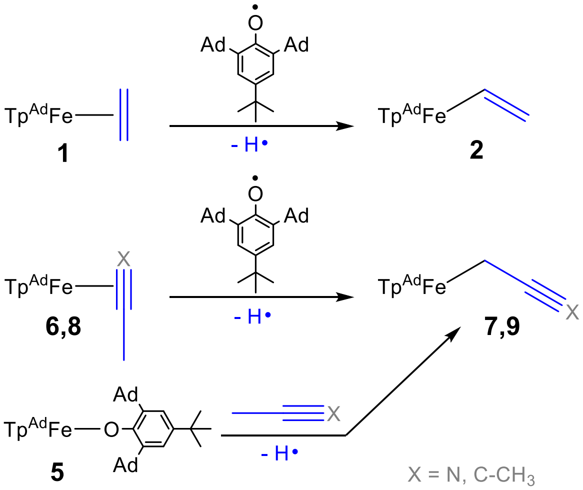

Scheme 2-5. C-H Activation of ethylene, acetonitrile, and butyne.

## *Conclusion*

Herein we have described an TpFe(I) radical pair that cooperatively cleaves sp, $sp^2$, and $sp^3$ C-H bonds. We've established the requirement for extreme steric bulk around the iron center as demonstrated by the reactivity differences between $Tp^{Me,Dr}Fe(C_2H_2)$ **3** and $Tp^{Me,Ad}Fe(C_2H_2)$ **1**. We've described the importance for the phenol having a stable radical form, as simple phenoxides are unable to do this chemistry. This was especially evident in $Tp^{Me,Ad}Fe(OPhtBu)$ **11** being incapable of cleaving the acidic C-H bond of phenylacetylene. We have also characterized the dissociation of the radical by EPR and UV-Vis, however this process is irreversible and such intermediates have thus far evaded characterization due to their high sensitivity. Our results thus far are consistent with a frustrated iron-radical pair that homolyzes in the presence of π-acidic alkynes but not alkenes or carbon monoxide. The precise mechanism for how the formally Fe(II) phenoxide species interacts with the alkyne substrate is unclear. The preference for such high steric bulk makes a concerted process less likely, however it is also possible that van der Waals dispersive forces play a significant role within the adamanyl-lined pocket.[23] Kinetic studies to further elucidate the mechanism are underway.

## *Experimental Section*

General Considerations: Unless stated otherwise, all compounds were purchased from commercial sources and used without further purification. Solvents were dried and deoxygenated by argon sparge followed by passage through an activated alumina column and were stored over 4 Å molecular sieves. All manipulations were performed under an $N_2$ atmosphere either in a glovebox or using standard Schlenk techniques. $Tp^{Me,Ad}FeCl$,[11] $Tp^{Me,Dr}FeCl$, $[Tp^{Me,Ad}Fe(N_2)]$, and $Ad_2PhO$[24,25] were synthesized according to literature procedures. $^1H$ NMR spectra were recorded at 298 K using Bruker 400 MHz instruments. Chemical shifts are referenced to residual solvent peaks, IR spectra were recorded using a Bruker Alpha FT-IR with a universal sampling module collecting at 4 $cm^{-1}$ resolution with 32 scans. EPR X-band spectra were recorded using a Bruker EMX spectrometer and analyzed using Win-EPR software. UV-Vis spectra were recorded using a Cary Bio 500 spectrometer using a 1 cm path length quartz cuvette with a solvent background subtraction applied. X-ray diffraction studies were performed using a Bruker-AXS diffractometer. Cyclic Voltammetry experiments were performed using a Pine AFP1 potentiostat. The cell consisted of a glassy carbon working electrode, a Pt wire auxiliary electrode and a Pt wire pseudo-reference electrode. All potentials are referenced vs. the $Fc/Fc^+$ couple measured as an internal standard. Elemental Analyses were performed by Midwest Microlab.

Solution phase effective magnetic moments were obtained via the method described by Evans[3] and were performed in triplicate. Standard deviations are reported.

### $Tp^{Me,Ad}Fe(PhCCH)$ **(12)**

Phenylacetylene (20 μL, 0.182 mmol) was added to a solution of $[Tp^{Me,Ad}Fe(N_2)]$ (45 mg, 0.062 mmol) in toluene (4 mL), producing a deep green solution. The volatiles were removed *in vacuo* and the resultant crystalline solid was dissolved in minimal THF and layered with hexane. Cooling this solution to −19 °C overnight yielded hunter green crystals suitable for XRD. Overall yield: 50 mg (99%). $^1H$ NMR ($C_6D_6$): δ70.26, 29.95, 26.30, 0.78, 0.39, −2.11, −5.23, −15.46, −16.47, −29.05. Evans Method ($C_6D_6$): $\mu_B$ 3.8±0.1. UV-Vis (THF): $\lambda_{max}$ nm ($\varepsilon_{max}$ $M^{-1}$ $cm^{-1}$) 662 (sh, $2.2 \times 10^2$), 511 (sh, $2.6 \times 10^2$), 419 (p, $8.2 \times 10^2$). Calc. for $C_{49}H_{62}BFeN_6$: C: 73.41; H: 7.80; N: 10.48. Found: C: 73.83; H: 7.79; N: 9.94.

### $Tp^{Me,Ad}Fe(CCPh)$ **(13)**

A solution of radical (either TEMPO or $Ad_2PhO$, 0.025 mmol) in ether (1 mL) was added to a suspension of $[Tp^{Me,Ad}Fe(PhCCH)]$ (20 mg, 0.025 mmol) in ether (2 mL) at −80°C. After 1 hour, the cooling bath was removed and the reaction was allowed to gradually warm up to room temperature (~ 3h). The volatiles were removed *in vacuo* to affording a colorless precipitate. This was extracted with toluene, filtered, and concentrated to (~80 μL). Layering this with ether and cooling to −19°C produced colorless crystals overnight. Overall yield: 15 mg (75%). $^1H$ NMR ($C_6D_6$): δ 57.41, 39.58, 38.46, 34.54, 5.55, 4.84, 2.96, −10.07, −13.59, −22.28. Evans Method ($C_6D_6$): $\mu_B$ 5.2±0.1. Calc. for $C_{49}H_{61}BFeN_6$ (1 × $C_4H_{10}O$): C: 72.77; H: 8.18; N: 9.61. Found: C: 72.64; H: 8.37; N: 9.30.

### $Tp^{Me,Ad}Fe(C_2H_4)$ **(1)**

A solution of $[Tp^{Me,Ad}Fe(N_2)]$ (100 mg, 0.137 mmol) in toluene (20 mL) was degassed *via* 3 freeze-pump-thaw-cycles and placed under an atmosphere of ethylene while briefly cooling with liquid $N_2$. After stirring for 4 hours the volatiles were removed *in vacuo* to afford a brown crystalline solid. The product was suspended in ether (12 mL) and collected by filtration. Cooling the mother liquor to −35 °C gave a second crop of crystalline material. Overall yield: 91 mg (91 %). $^1$H NMR ($C_6D_6$): δ 32.09, 26.78, 20.86, 3.48, 2.94, 2.15, −6.32. Evans Method ($C_6D_6$): $\mu_B$ 4.0±0.2. UV-Vis (THF): $\lambda_{max}$ nm ($\varepsilon_{max}$ $M^{-1}$ $cm^{-1}$) 820 (sh, $9.2 \times 10^1$), 494 (p, $2.9 \times 10^2$), 352 ($6.4 \times 10^2$). Calc. for $C_{44}H_{62}BFeN_6$ (1 × $C_4H_{10}O$): C: 70.67; H: 8.90; N: 10.30. Found: C: 70.37; H: 8.67; N: 10.12.

### $Tp^{Me,Ad}Fe$(vinyl) **(2)**

A solution of $Ad_2PhO$ (60.0 mg, 0.143 mmol) in ether (1 mL) was added to a suspension of $[Tp^{Me,Ad}Fe$(ethylene)] (94.5 mg, 0.129 mmol) in ether (2 mL) at −80°C. After 1 hour, the cooling bath was removed and the reaction was allowed to gradually warm up to room temperature (~ 3h). The volatiles were removed *in vacuo* to affording a colorless precipitate. This was washed with cold pentane (3×2 mL), then dissolved in toluene (4 mL). The toluene solution was filtered then concentrated in vacuo to 1 mL and layered with hexane (5 mL). This produced colorless crystals upon cooling to −19°C overnight.

Overall yield: 66.6 mg (70.6%). $^1$H NMR ($C_6D_6$): δ 56.73, 51.64, 39.33, 4.30, 2.13, 1.75, −26.30. Evans Method ($C_6D_6$): $\mu_B$ 4.6±0.2. Calc. for $C_{44}H_{61}BFeN_6$ (½ × $C_7H_8$): C: 72.52; H: 8.33; N: 10.68. Found: C: 72.83; H: 8.54; N: 10.81.

Tp$^{Me,Ad}$Fe(MeCN) **(6)**

Acetonitrile (~100 μL, 2 mmol) was added to a solution of [Tp$^{Me,Ad}$Fe($N_2$)] (27 mg, 0.037 mmol) in toluene (2 mL), producing an army-green solution. The volatiles were removed *in vacuo* and the resultant crystalline solid was dissolved in minimal THF and layered with hexane. Cooling this solution to −19 °C overnight yielded dichroic orange-green crystals suitable for XRD. Overall yield: 25 mg (91%). $^1$H NMR ($C_6D_6$): δ 53.30, 28.93, 24.47, 2.64, 1.98, 0.21, −17.28, −31.31. Evans Method ($C_6D_6$): $\mu_B$ 3.9±0.1. UV-Vis (THF): $\lambda_{max}$ nm ($\varepsilon_{max}$ $M^{-1}$ $cm^{-1}$) 714 (p, $2.2 \times 10^2$), 474 (p, $3.0 \times 10^2$), 336 (sh, $1.5 \times 10^3$). Calc. for $C_{43}H_{59}BFeN_7$: C: 69.73; H: 8.03; N: 13.24. Found: C: 69.46; H: 8.39; N: 12.96.

Tp$^{Me,Ad}$Fe($CH_2CN$) **(7)**

A solution of $Ad_2PhO$ (16, 0.038 mmol) in ether (1 mL) was added to a suspension of [Tp$^{Me,Ad}$Fe(MeCN)] (27 mg, 0.036 mmol) in ether (2 mL) at −80°C. After 1 hour, the cooling bath was removed and the reaction was allowed to gradually warm up to room temperature (~ 3h). The volatiles were removed *in vacuo* to affording a colorless precipitate. This was extracted with toluene, filtered, and concentrated to (~200 μL). Layering this orange filtrate with hexane and cooling to −19°C produced colorless needles overnight. If ether/hexane is used instead, crystalline orange plates form instead. Although the crystals have different colors and forms, the chemical identity was identical by XRD. Overall yield: 19 mg (70%). $^1$H NMR ($C_6D_6$): δ 60.75, 54.92, 41.97, 39.58, 37.57, 12.30, 4.33, 4.16, 4.06, 3.82, 3.13, 1.57, −8.04, −12.84. Evans Method ($C_6D_6$): $\mu_B$ 5.4±0.1. UV-Vis (THF): $\lambda_{max}$ nm ($\varepsilon_{max}$ M$^{-1}$ cm$^{-1}$) 521 (p, $3.6 \times 10^2$), 437 (p, $5.2 \times 10^2$), 373 (p, $5.7 \times 10^2$). Calc. for $C_{43}H_{58}BFeN_7$ (½ × $C_6H_{12}$): C: 70.45; H: 8.32; N: 12.64. Found: C: 70.25; H: 8.28; N: 11.46.

Tp$^{Me,Ad}$Fe(butyne) **(8)**

2-Butyne (~200 μL, 3 mmol) was added to a solution of [Tp$^{Me,Ad}$Fe($N_2$)] (35 mg, 0.048 mmol) in toluene (2 mL), producing a deep hunter green solution. The volatiles were removed *in vacuo* and the resultant crystalline solid was dissolved in minimal THF and layered with pentane. Cooling this solution to −19 °C overnight yielded hunter green crystals suitable for XRD. Overall yield: 30 mg (83%). $^1$H NMR ($C_6D_6$): δ 79.39, 33.00, 31.70, 17.34, 1.54, −4.38, −6.33, −49.74. Evans Method ($C_6D_6$): $\mu_B$ 3.8±0.1. UV-Vis (THF): $\lambda_{max}$ nm ($\varepsilon_{max}$ M$^{-1}$ cm$^{-1}$) 616 (p, $3.0 \times 10^2$), 450 (p, $4.3 \times 10^2$), 337 (sh, $1.4 \times 10^3$). Calc. for $C_{45}H_{62}BFeN_6$ (1 × $C_5H_{12}$): C: 72.72; H: 9.03; N: 10.18. Found: C: 72.19; H: 8.73; N: 10.27.

Tp$^{Me,Ad}$Fe($CH_2CCCH_3$) **(9)**

A solution of $Ad_2PhO$ (14 mg, 0.033 mmol) in ether (1 mL) was added to a suspension of [Tp$^{Me,Ad}$Fe(butyne)] (24 mg, 0.032 mmol) in ether (2 mL) at −80°C. After 1 hour, the cooling bath was removed and the reaction was allowed to gradually warm up to room temperature (~ 3h). The volatiles were removed *in vacuo* to affording a colorless precipitate. This was extracted with toluene, filtered, and concentrated to (~200 μL). Layering this with hexane and cooling to −19°C produced colorless crystals overnight. Overall yield: 19 mg (79%). $^1$H NMR ($C_6D_6$): δ 126.43, 64.93, 51.31, 39.76, 3.48, 1.55, 1.31, −28.98. Evans Method ($C_6D_6$): $\mu_B$ 6.2±0.2. Calc. for $C_{45}H_{61}BFeN_6$ (½($C_6H_{14}$ + $C_7H_8$)): C: 73.48; H: 8.62; N: 9.98. Found: C: 73.35; H: 8.42; N: 9.75.

### Tp$^{Me,Ad}$Fe(methyl) **(10)**

A solution of [Tp$^{Me,Ad}$FeCl] (104 mg, 0.139 mmol) in THF (16 mL) was chilled to −78°C. Methyllithium was added (50 μL, 0.155 mmol, 3.1M in DME) turning the colorless solution a very pale yellow color. The reaction was allowed to stir at −78°C for 30 minutes, then the bath was removed for another 30 min. After which time, the solvent was removed *in vacuo* leaving a white powder. This was brought into the glovebox and redissolved in minimal THF and layered with ether, which provided colorless crystals upon cooling to −19°C overnight. These were collected and dried *in vacuo*. Overall yield: 62 mg (62%). $^1$H NMR ($C_6D_6$): δ 84.18, 48.76, 43.23, 4.77, 4.00, 1.10, −45.30. Evans Method ($C_6D_6$): $\mu_B$ 4.6±0.1. Calc. for $C_{42}H_{59}BFeN_6$ (1 × $C_6H_{10}O$): C: 70.05; H: 8.82; N: 10.66. Found: C: 70.06; H: 8.71; N: 10.43.

### Tp$^{Me,Ad}$Fe(OPh*t*Bu) **(11)**

4-tert-butylphenol (8 mg, 0.053 mmol) was added to a solution of [Tp$^{Me,Ad}$Fe(methyl)] (26 mg , 0.036 mmol) in toluene (3 mL) at room temperature. The solution was swirled until bubbling ceased. Volatiles were removed *in vacuo* producing a colorless powder. The product was suspended in hexane (4 mL) and collected by filtration. This was rinsed with hexane (3 x 1 mL). Dissolving the solid in minimal toluene and layering with hexane produced colorless crystals at −19°C. Overall yield: 30 mg (97%). $^1$H NMR ($C_6D_6$): δ 67.84, 66.60, 58.98, 40.23, 11.28, 2.20, 1.09, 0.06, −5.88, −22.69. Evans Method ($C_6D_6$): $\mu_B$ 4.3±0.1. Calc. for $C_{51}H_{69}BFeN_6$ (1 × $C_6H_{14}$): C: 73.22; H: 8.95; N: 8.99. Found: C: 72.83; H: 9.25; N: 8.74.

Tp$^{Me,Ad}$Fe(OPhAd$_2$) **(5)**

A solution of OPhAd2 (15 mg, 0.036 mmol) in toluene (~1 mL) was added to a solution of [Tp$^{Me,Ad}$Fe($N_2$)] (26 mg, 0.036 mmol) in toluene (2 mL). After stirring for 10 minutes at room temperature, the volatiles were removed *in vacuo* to afford an orange glaze. Pentane (1 mL) was added to dissolve the glaze and subsequently removed *in vacuo,* twice. Another 1 mL portion of pentane was added producing an orange-yellow solution. This was filtered, then concentrated to half the volume. Upon cooling to −19°C overnight, this solution produced yellow crystals. Crystals are very soluble and highly air and water sensitive.

Overall yield: 12 mg (30%). $^1$H NMR ($C_6D_6$): δ 67.11, 63.76, 60.63, 50.77, 40.92, 26.52, 17.12, 14.22, 4.35, 2.20, 1.76, −4.28, −4.92, −6.97, −7.36, −9.44, −10.28, −13.94, −21.87. Evans Method ($C_6D_6$): $\mu_B$ 5.1±0.1. UV-Vis (THF): $\lambda_{max}$ nm ($\varepsilon_{max}$ $M^{-1}$ $cm^{-1}$) 908 (p, 1.4 ×

$10^2$), 395 (p, 1.2 × $10^3$), 340 (1.5 × $10^3$). Calc. for $C_{71}H_{97}BFeN_6O$: C: 76.33; H: 8.75; N: 7.52. Found: C: 75.95; H: 8.95; N: 7.52.

$Tp^{Me,Dr}Fe(C_2H_4)$ **(3)**

A solution of [$Tp^{Me,Dr}Fe(N_2)$] (110 mg, 0.076) in toluene (10 mL) was degassed *via* 3 freeze-pump-thaw-cycles and placed under an atmosphere of ethylene. An immediate color change from dark red to deep green occurred. After stirring for 10 minutes, the volatiles were removed *in vacuo* to afford an hunter green crystalline solid. The product was suspended in ether (X mL) was collected by filtration. Overall yield: 100 mg (89%).

$^1$H NMR ($C_6D_6$): δ 33.21, 32.02, 26.25, 19.33, 7.83, 7.32, 4.07, 3.33, 1.78, 1.40, −4.24, −5.72, −8.65. Evans Method ($C_6D_6$): $\mu_B$ 3.9±0.1. UV-Vis (THF): $\lambda_{max}$ nm ($\varepsilon_{max}$ $M^{-1}$ $cm^{-1}$) 802 (sh, 1.3 × $10^2$), 630 (p, 1.6 × $10^2$), 435 (sh, 4.0 × $10^2$), 360 (sh, 1.2 × $10^3$). Calc. for $C_{44}H_{56}BFeN_6$ (⅓ x $C_5H_{12}$): C: 72.20; H: 7.96; N: 11.06. Found: C: 72.05; H: 8.02; N: 11.03.

## *NMR Spectra*

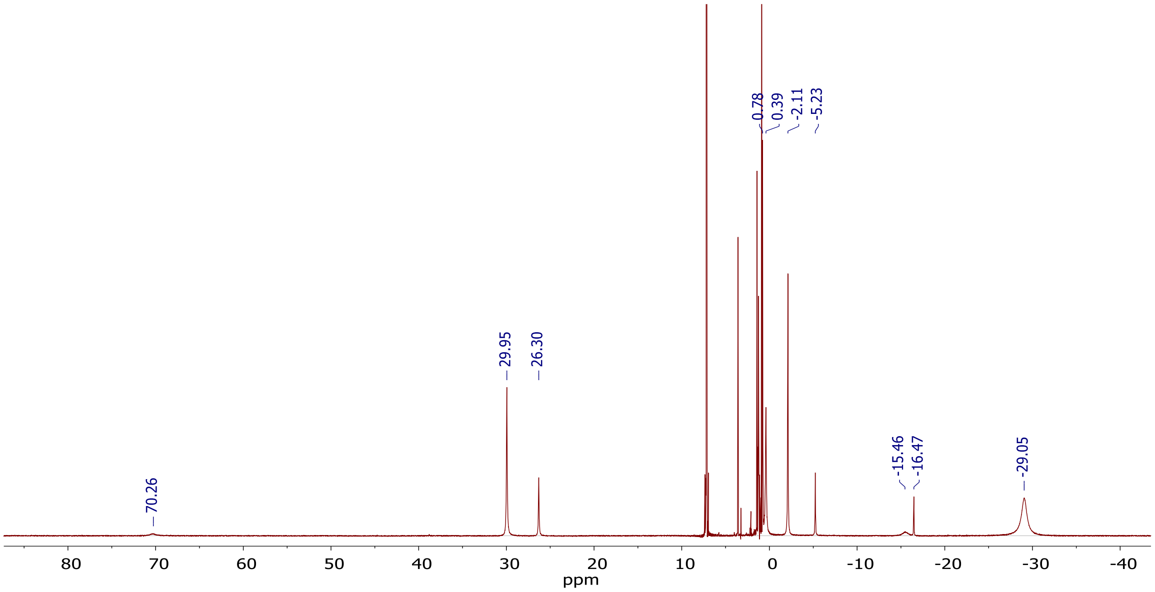

Figure 2-8**.** $^1$H NMR spectrum of Tp$^{Me, Ad}$Fe(PhCCH) (**12**) recorded at 400 MHz in $C_6D_6$.

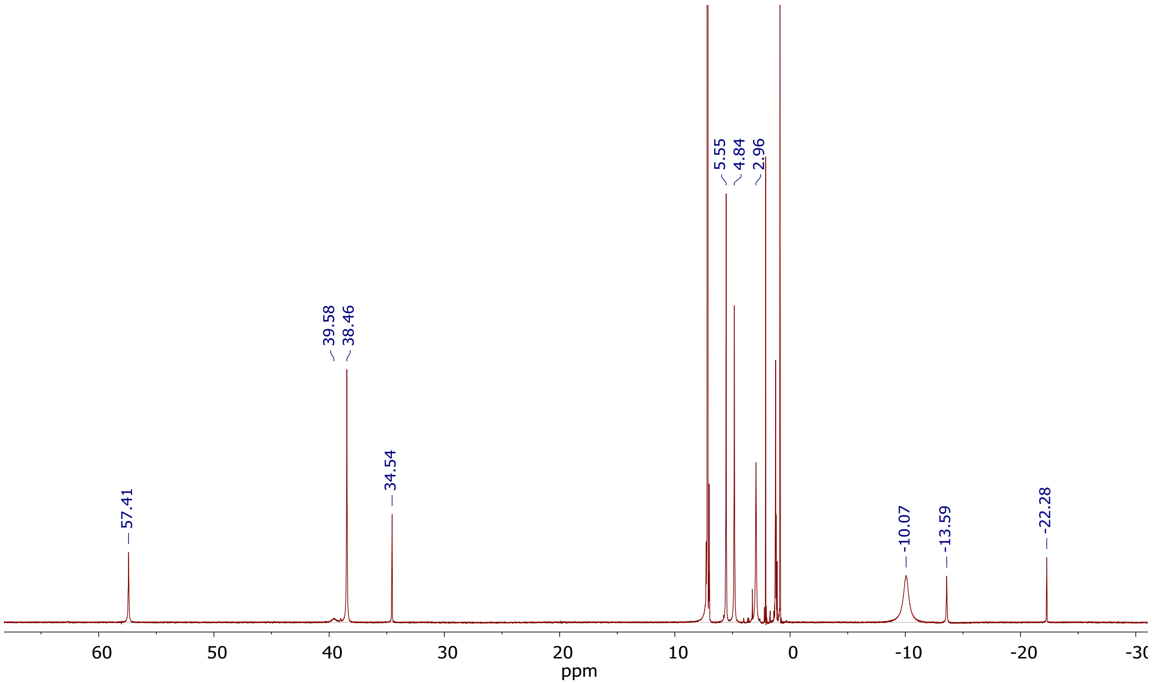

Figure 2-9. $^1$H NMR spectrum of Tp$^{Me, Ad}$Fe(CCPh) (**13**) recorded at 600 MHz in $C_6D_6$.

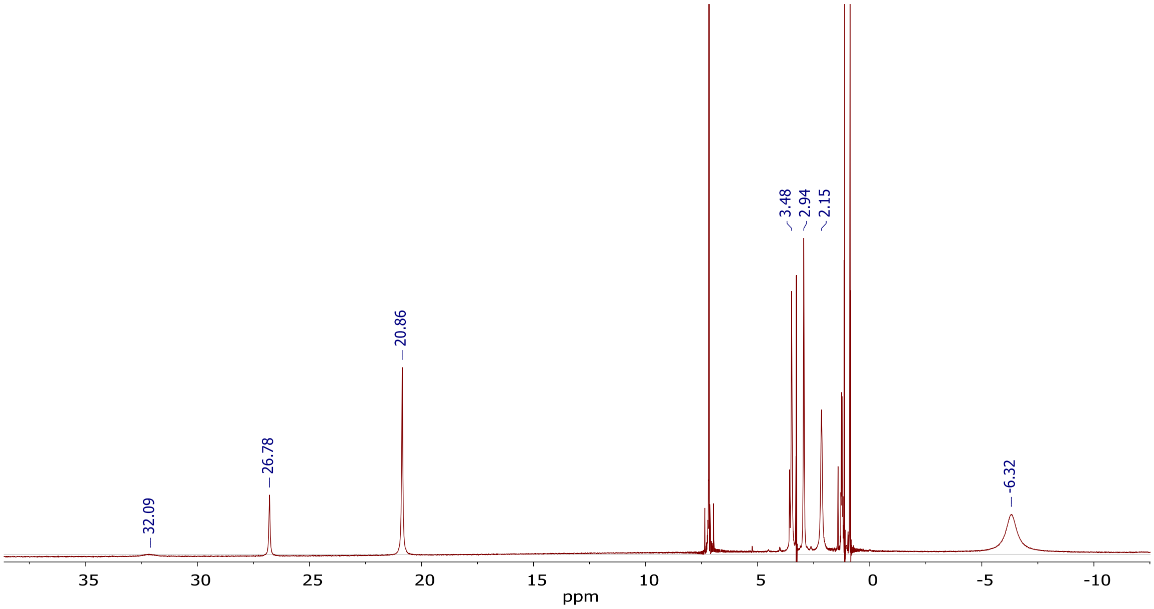

Figure 2-10. $^1$H NMR spectrum of Tp$^{Me,Ad}$Fe($C_2H_4$) (**1**) recorded at 400 MHz in $C_6D_6$.

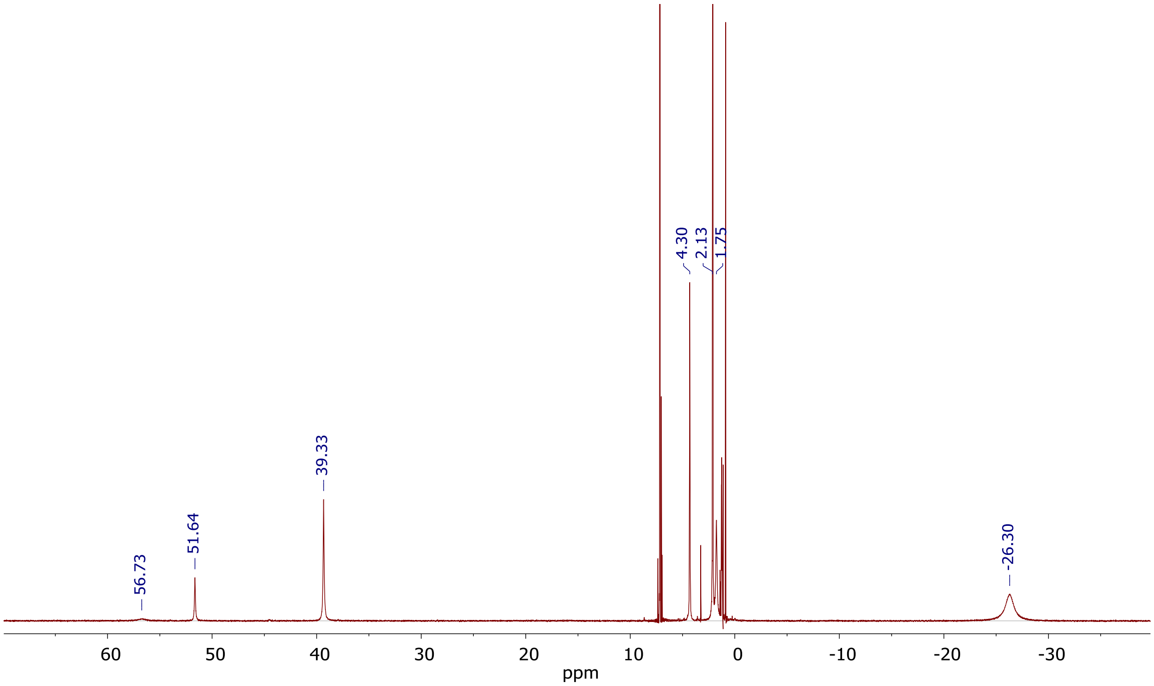

Figure 2-11. $^1$H NMR spectrum of Tp$^{Me,Ad}$Fe(vinyl) (**2**) recorded at 400 MHz in $C_6D_6$.

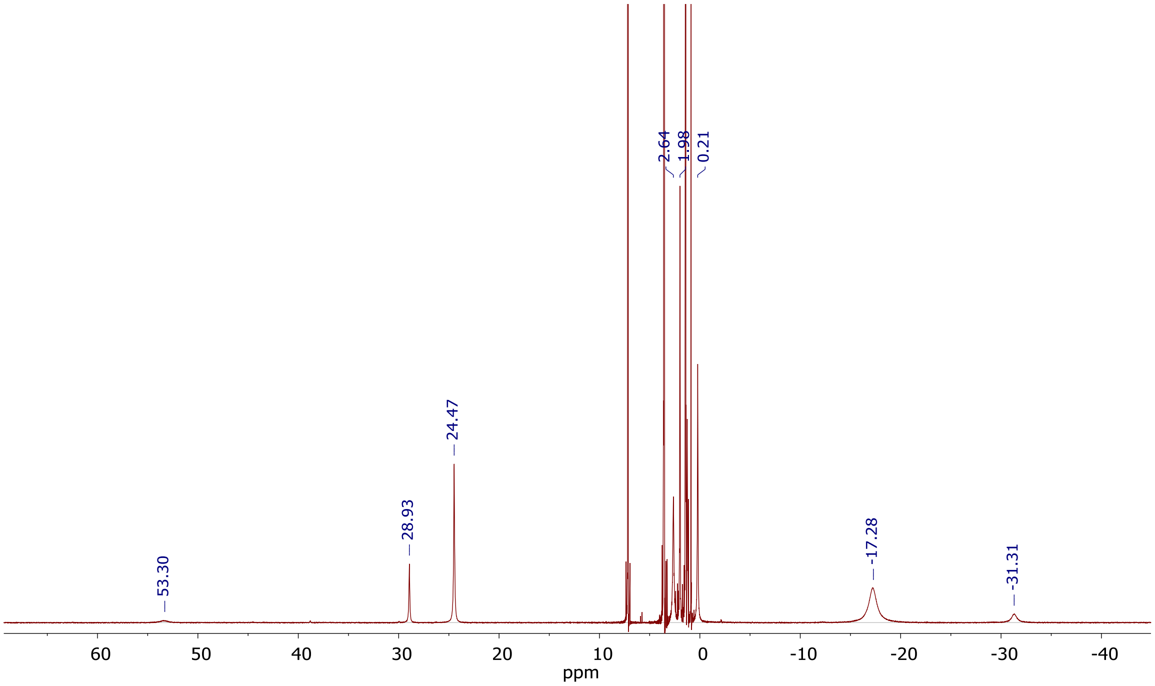

Figure 2-12. $^1$H NMR spectrum of Tp$^{Me,Ad}$Fe(MeCN) (**6**) recorded at 400 MHz in a 10%THF solution of $C_6D_6$.

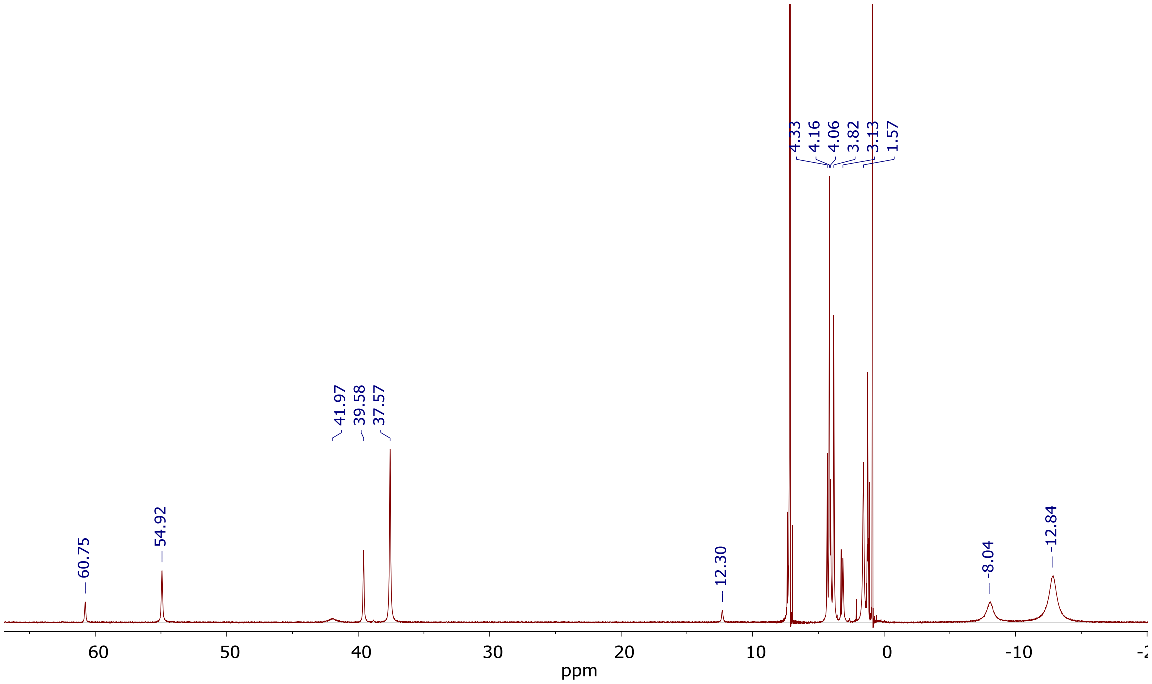

Figure 2-13. $^1$H NMR spectrum of Tp$^{Me,Ad}$Fe($CH_2CN$) (**7**) recorded at 400 MHz in $C_6D_6$.

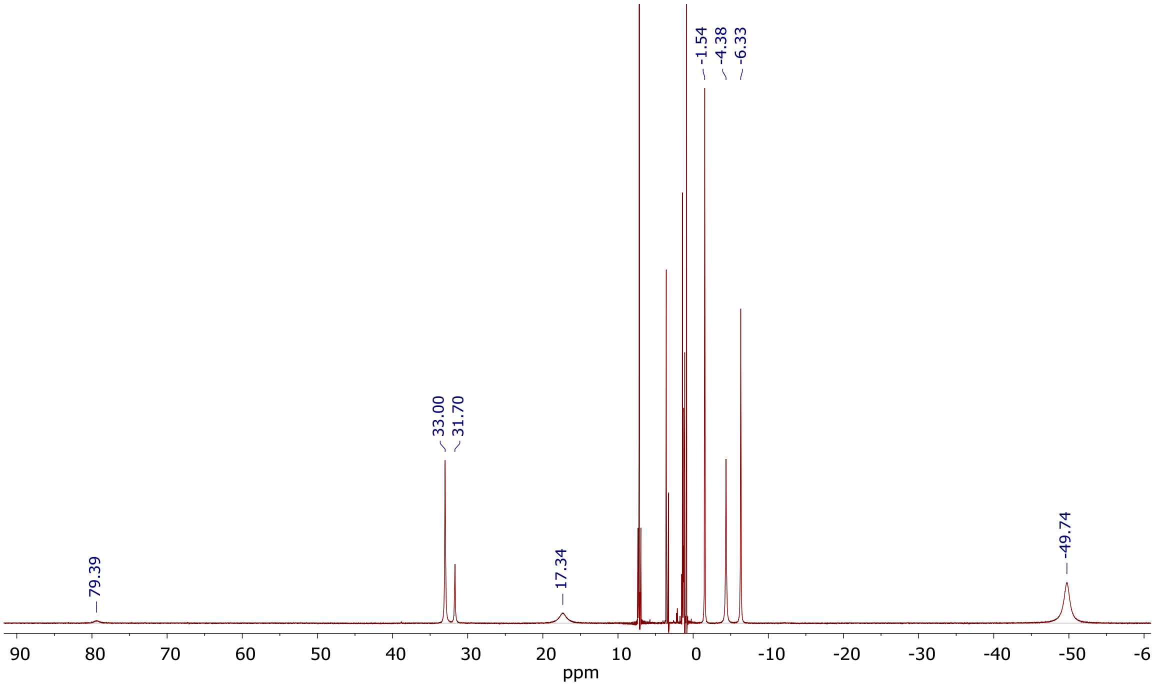

Figure 2-14. $^1$H NMR spectrum of Tp$^{Me,Ad}$Fe(2-butyne) (**8**) recorded at 400 MHz in $C_6D_6$.

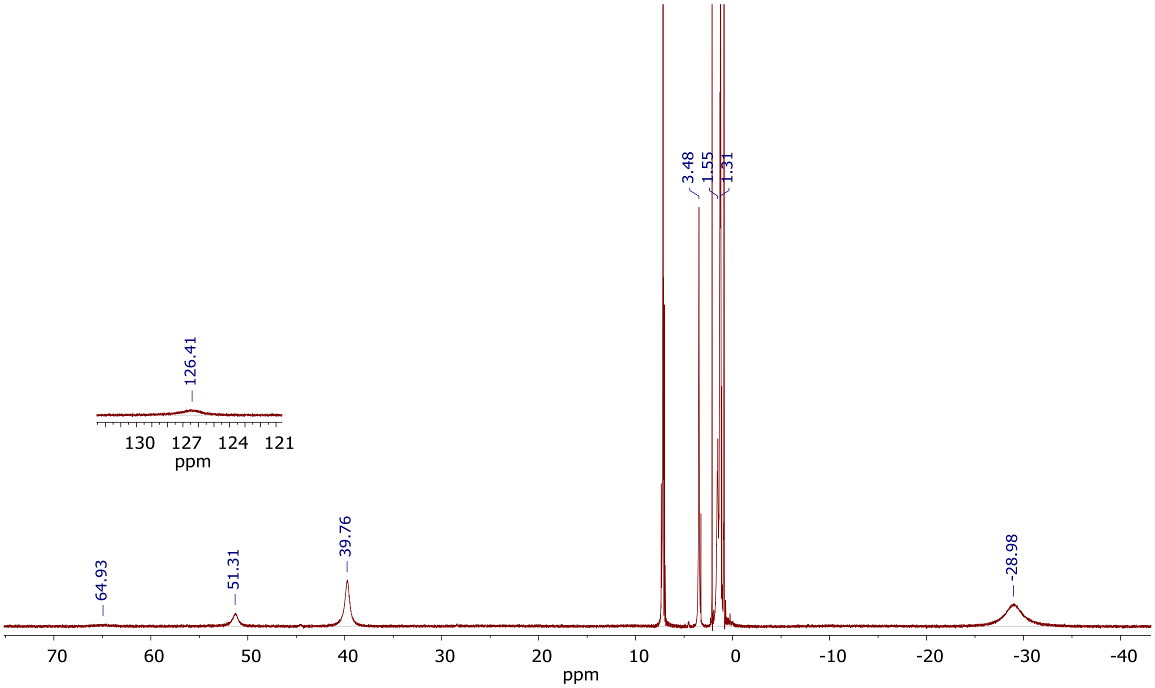

Figure 2-15. $^1$H NMR spectrum of Tp$^{Me,Ad}$Fe($CH_2CCCH_3$) (**9**) recorded at 400 MHz in $C_6D_6$.

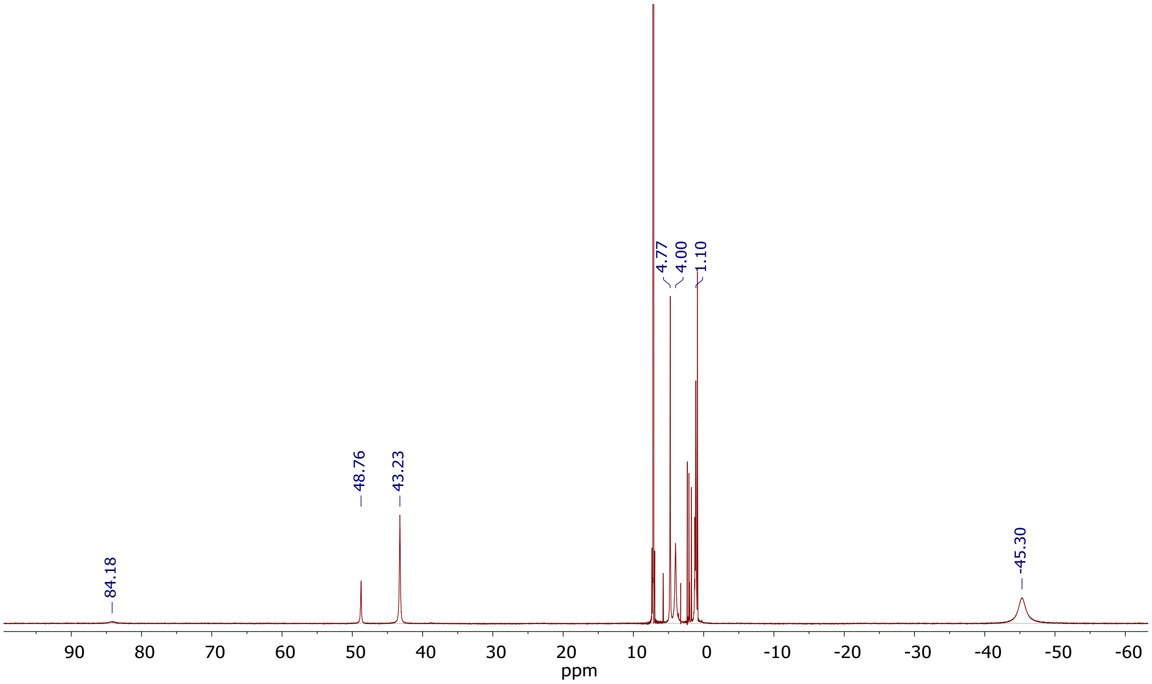

Figure 2-16. $^1$H NMR spectrum of Tp$^{Me,Ad}$Fe(methyl) (**10**) recorded at 400 MHz in $C_6D_6$.

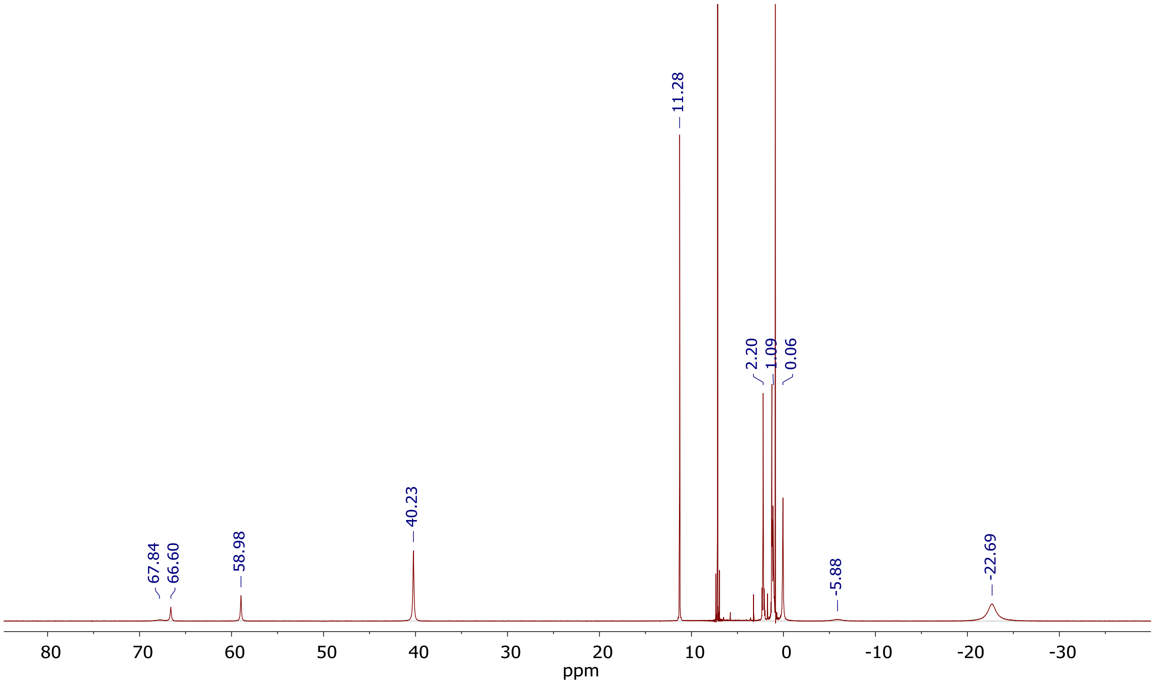

Figure 2-17. $^1$H NMR spectrum of Tp$^{Me,Ad}$Fe(OPh*t*Bu) (**11**) recorded at 400 MHz in $C_6D_6$.

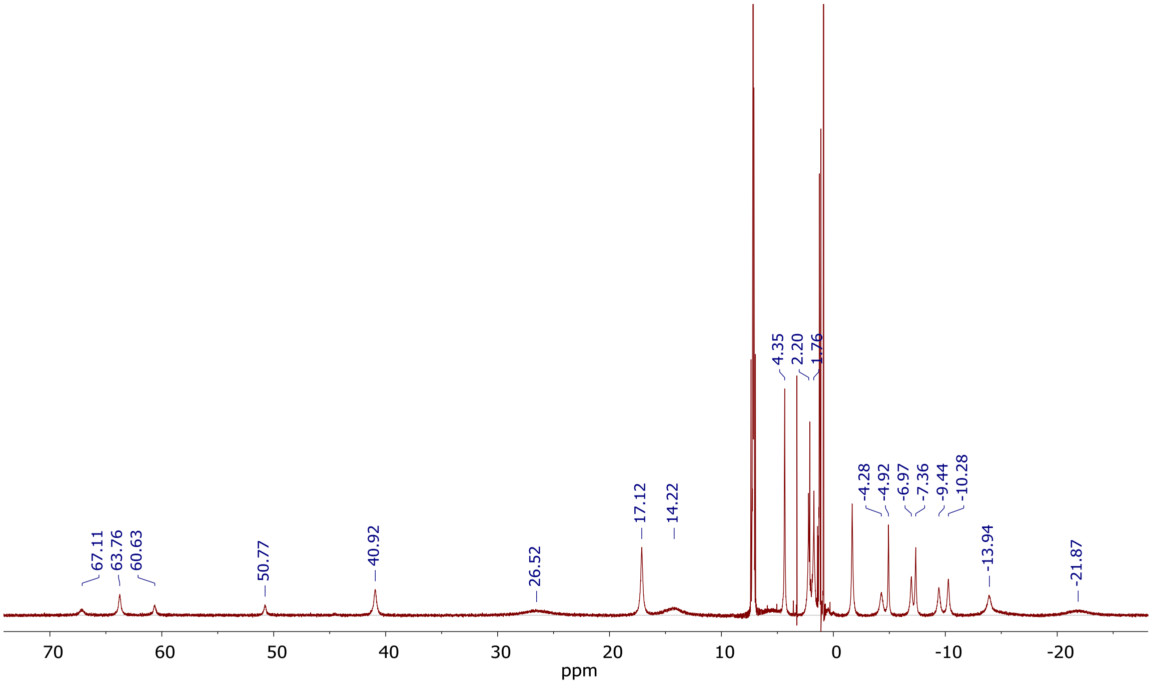

Figure 2-18. $^1$H NMR spectrum of Tp$^{Me,Ad}$Fe(OPhAd$_2$) (**5**) recorded at 400 MHz in $C_6D_6$.

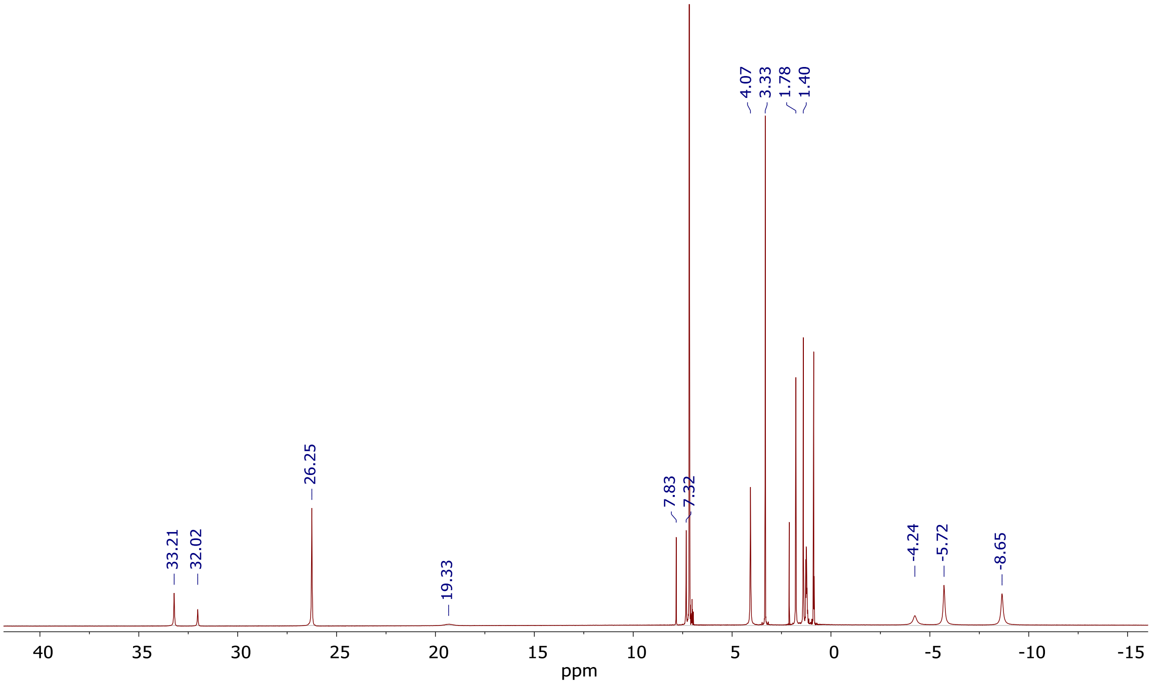

Figure 2-19. $^1$H NMR spectrum of Tp$^{Me,Dr}$Fe($C_2H_4$) (**3**) recorded at 400 MHz in $C_6D_6$.

*UV-Vis*

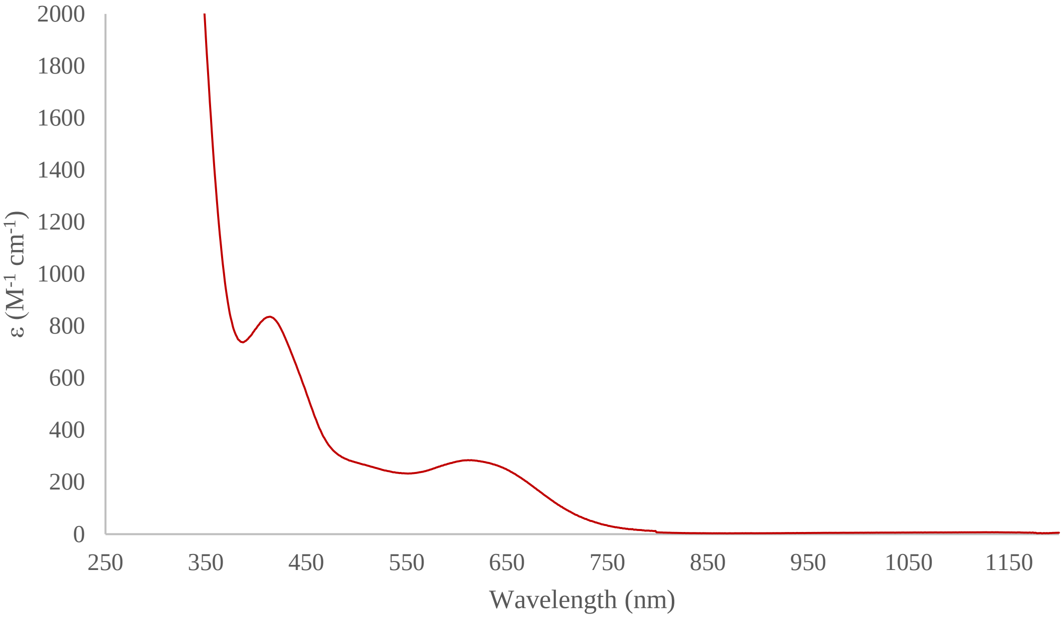

Figure 2-20. UV-Vis-NIR spectrum of Tp$^{Me,Ad}$Fe(PhCCH) (**12**) in THF.

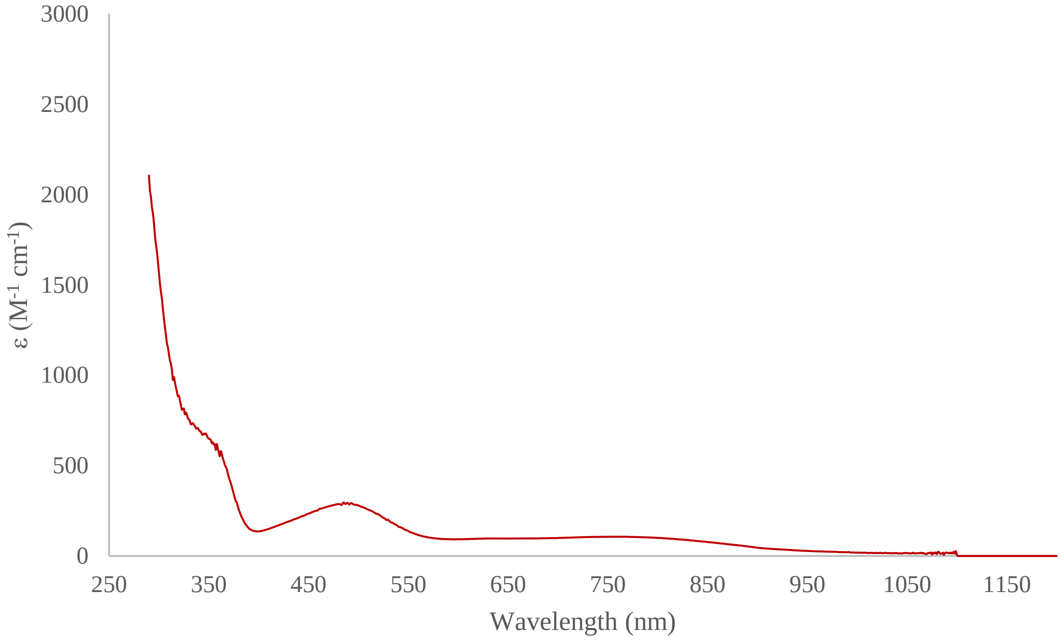

Figure2-21. UV-Vis-NIR spectrum of Tp$^{Me,Ad}$Fe($C_2H_4$) (**1**) in THF.

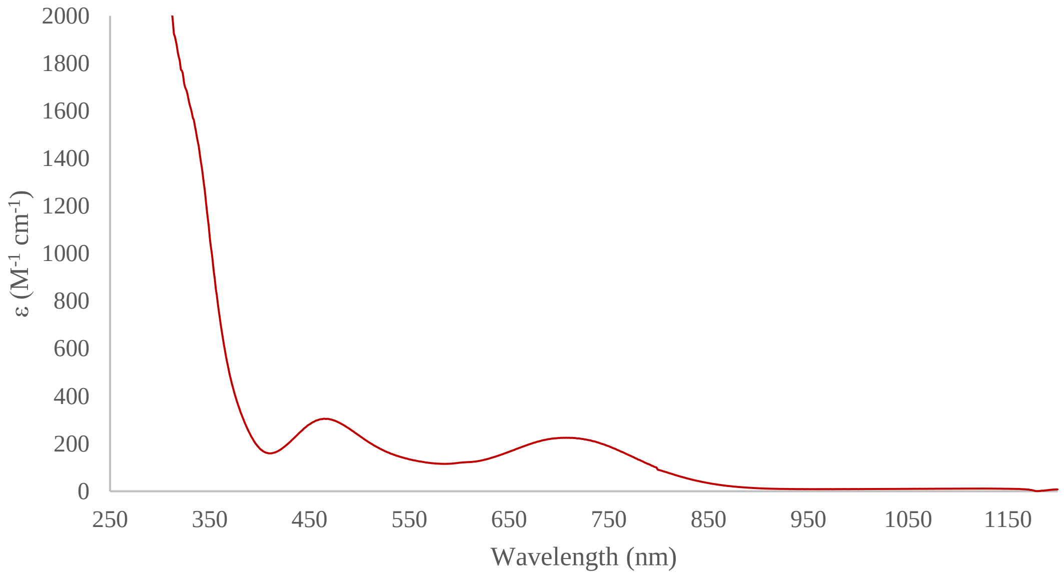

Figure 2-22. UV-Vis-NIR spectrum of Tp$^{Me,Ad}$Fe(MeCN) (**6**) in THF.

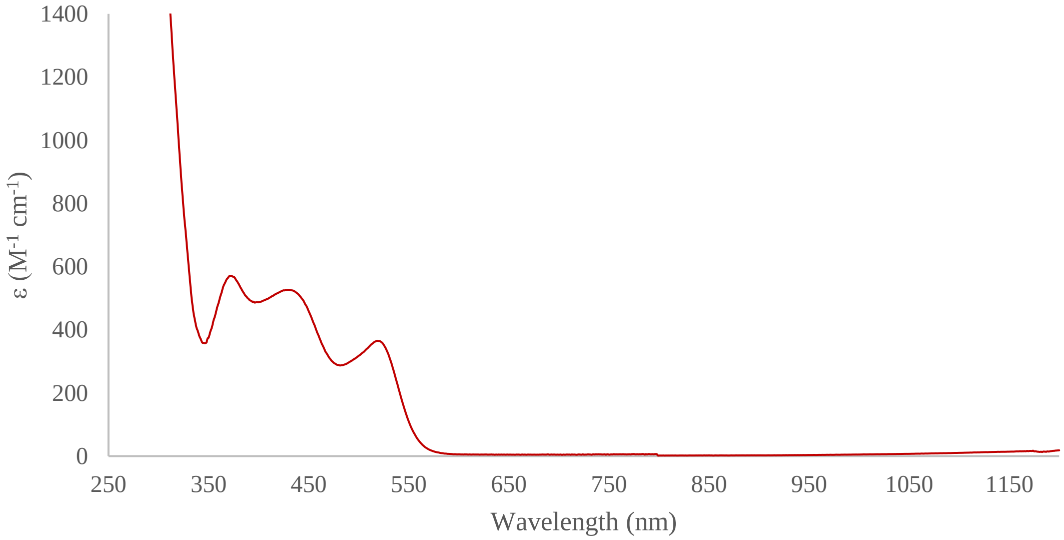

Figure 2-23. UV-Vis-NIR spectrum of Tp$^{Me,Ad}$Fe($CH_2CN$) (**7**) in THF.

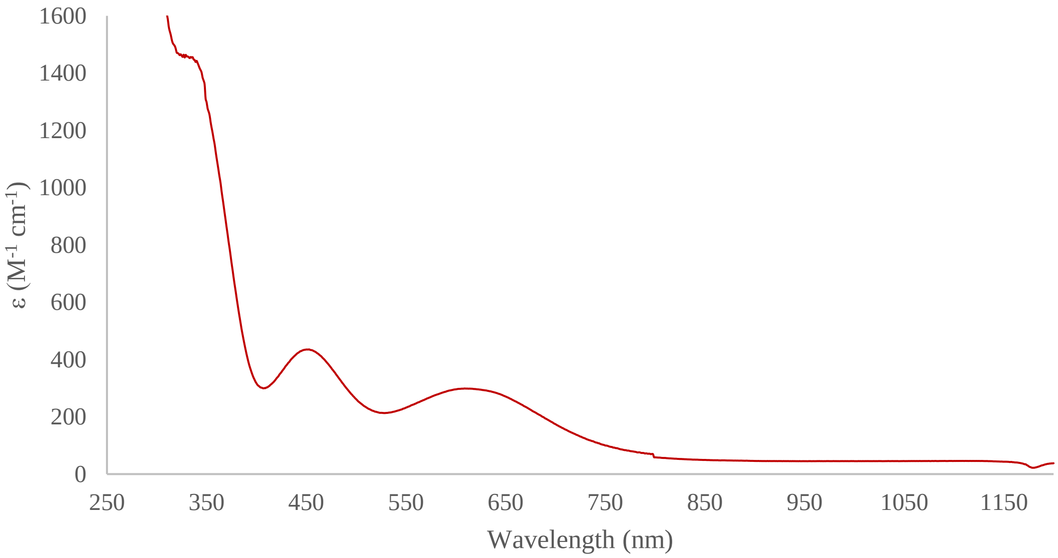

Figure 2-24. UV-Vis-NIR spectrum of Tp$^{Me,Ad}$Fe(2-butyne) (**8**) in THF.

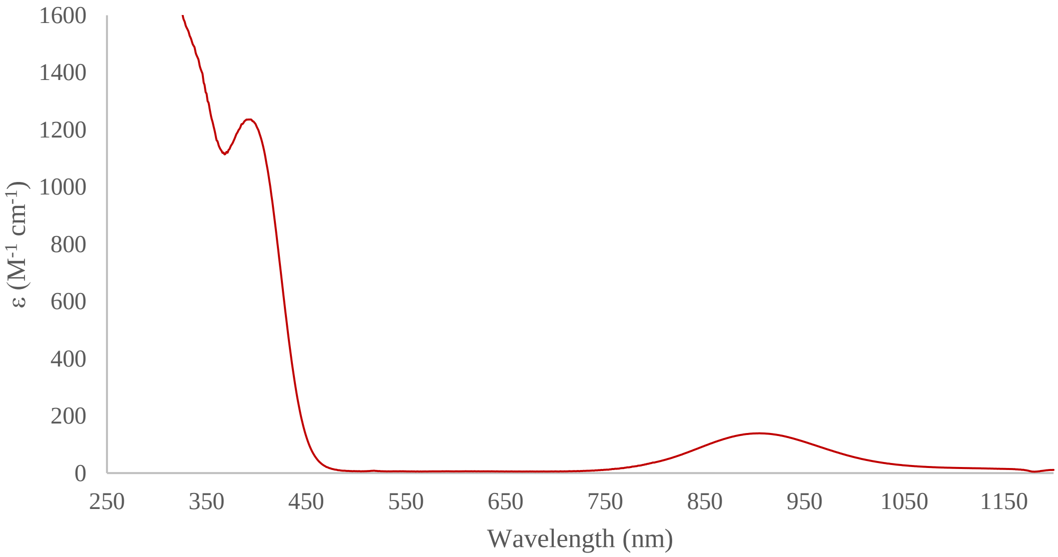

Figure 2-25. UV-Vis-NIR spectrum of Tp$^{Me,Ad}$Fe(OPhAd$_2$) (**5**) in THF.

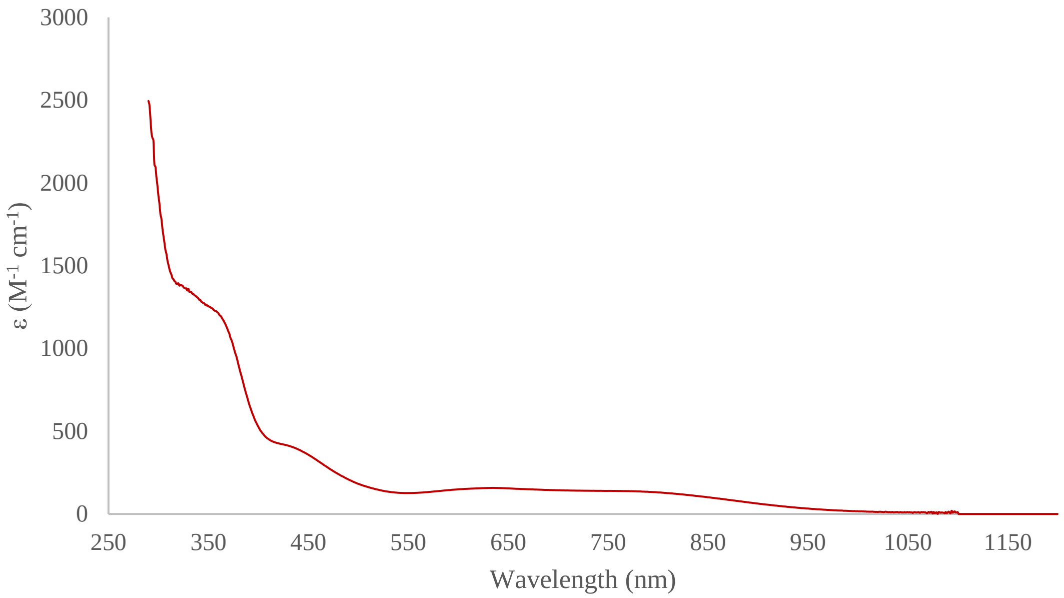

Figure 2-26. UV-Vis-NIR spectrum of Tp$^{Me,Dr}$Fe($C_2H_4$) (**3**) in THF.

*EPR*

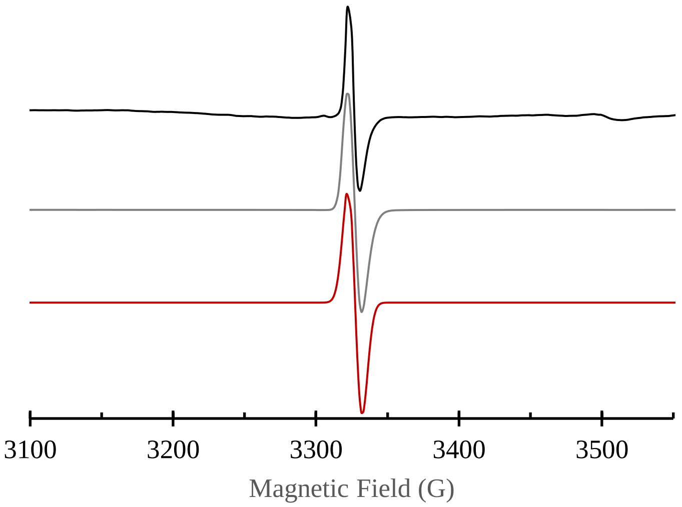

Figure 2-27. X-Band EPR spectra at 291K of $Tp^{Me,Ad}Fe(OPhAd_2)$ **5** (top, black) at 9.312 GHz, free radical $Ad_2PhO$ (middle, gray) at 9.318 GHz, and simulation (bottom, red). Simulation parameters: g = 2.004, lw = 1.00.

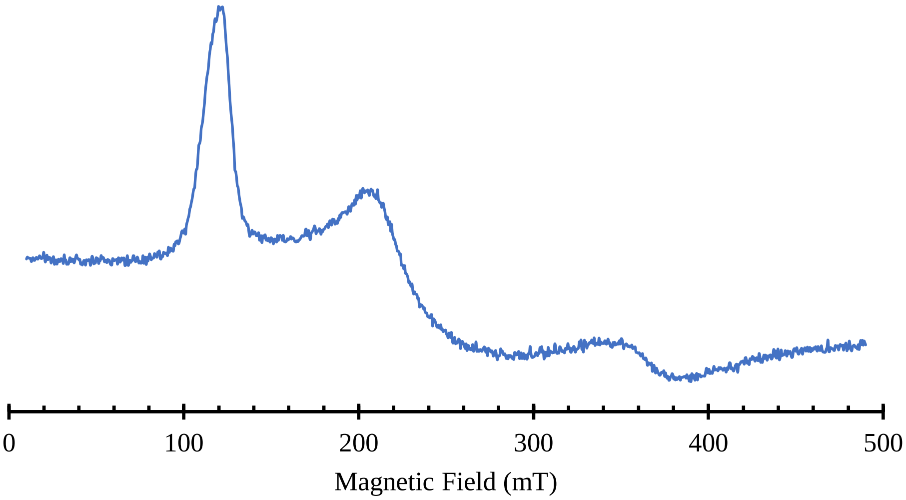

Figure 2-28. X-band EPR spectrum (9.630 GHz) of **[($Tp^{Me,Dr}$Fe(ethylene)]** in 2-MeTHF at 15 K (**black**) and its simulated spectrum (**red**).

### *X-Ray Crystallography*

**General Considerations**. Single crystals were coated with paratone oil and mounted on cryo-loop glass fibers. X-ray intensity data were collected at 100(2) K on a Bruker APEX2[26] platform-CCD X-ray diffractometer system using fine-focus Mo $K_\alpha$ radiation ($\lambda$ = 0.71073 Å, 50kV/30mA power). The CCD detector was placed at 5.0600 cm from the crystal. Frames were integrated using the Bruker SAINT software package[27] and using a narrow-frame integration algorithm. Absorption corrections were applied to the raw intensity data using the SADABS program.[28] The Bruker SHELXTL software package[29] was used for phase determination and structure refinement. Atomic coordinates, isotropic and anisotropic displacement parameters of all the non-hydrogen atoms were refined by means of a full matrix least-squares procedure on $F^2$. The H-atoms were included in the refinement in calculated positions riding on the atoms to which they were attached. Relevant details for individual data collections are reported in Table 2-4 through Table 2-13.

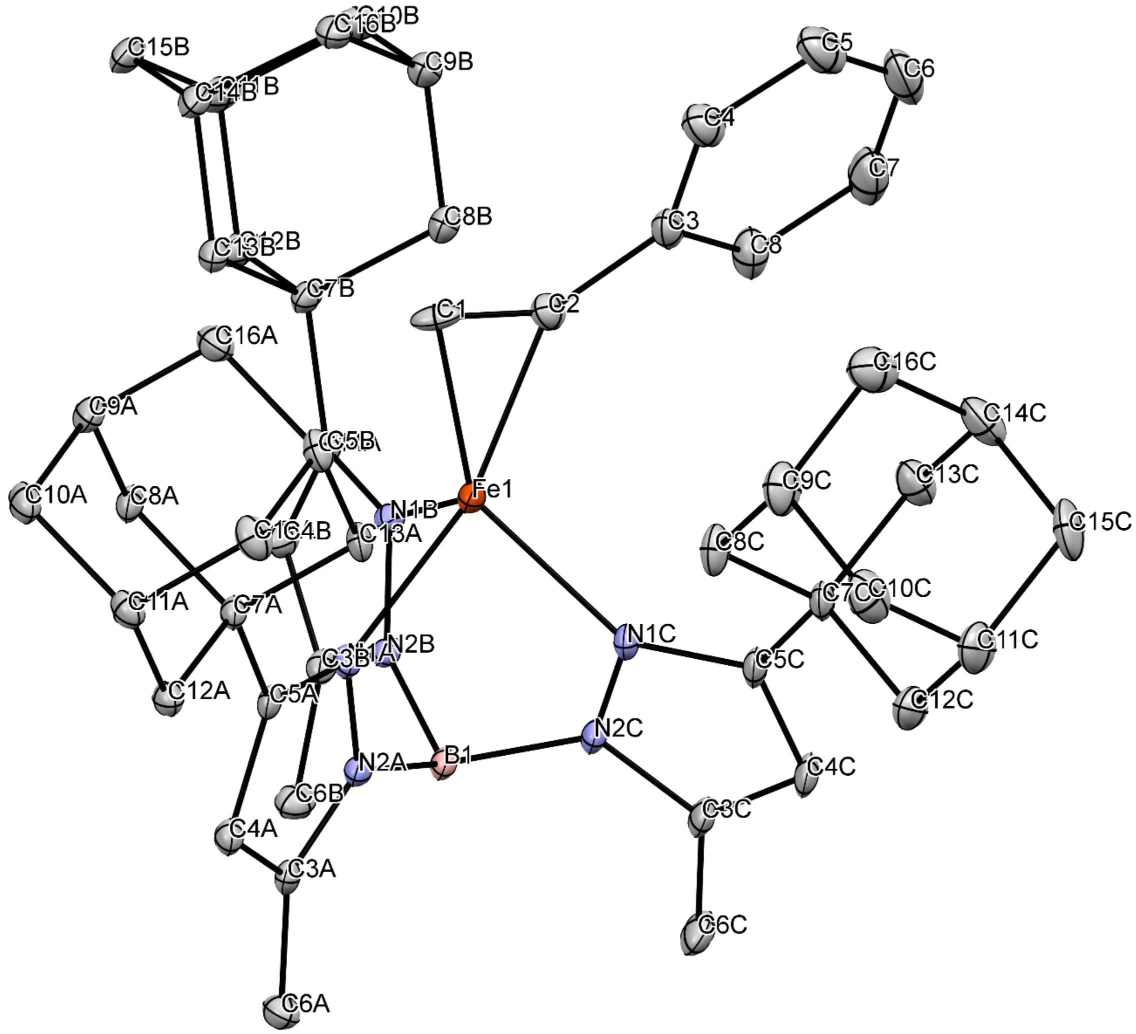

Figure 2-29. Labelled thermal ellipsoid plot (50%) for Tp$^{Me,Ad}$Fe(PhCCH) (**12**).

Table 2-4. Crystal data and structure refinement for Tp$^{Me,Ad}$Fe(PhCCH) (**12**).

| | | |
|---|---|---|
| Identification code | hh288le | |
| Empirical formula | $C_{50}H_{64}BFeN_6$ | |
| Formula weight | 815.73 | |
| Temperature | 100(2) K | |
| Wavelength | 0.71073 Å | |
| Crystal system | Triclinic | |
| Space group | P-1 | |
| Unit cell dimensions | a = 11.4506(7) Å | α = 80.882(3)°. |
| | b = 13.6241(8) Å | β = 87.335(3)°. |
| | c = 14.3430(8) Å | γ = 70.633(3)°. |
| Volume | 2084.2(2) Å$^3$ | |
| Z | 2 | |

| | |
|---|---|
| Density (calculated) | 1.300 mg/m$^3$ |
| Absorption coefficient | 0.406 mm$^{-1}$ |
| F(000) | 874 |
| Crystal color | green |
| Crystal size | 0.321 x 0.228 x 0.112 mm$^3$ |
| $\theta$ range for data collection | 1.603 to 30.998° |
| Index ranges | $-16 \le h \le 16$, $-19 \le k \le 19$, $-20 \le l \le 20$ |
| Reflections collected | 80037 |
| Independent reflections | 13261 [$R_{\text{int}}$ = 0.0788] |
| Completeness to $\theta$ = 25.242° | 100.0 % |
| Absorption correction | Semi-empirical from equivalents |
| Refinement method | Full-matrix least-squares on F$^2$ |
| Data / restraints / parameters | 13261 / 2 / 532 |
| Goodness-of-fit on F$^2$ | 1.041 |
| Final $R$ indices [$I > 2\sigma_I$ = 10856 data] | $R_1$ = 0.0478, $wR_2$ = 0.1222 |
| $R$ indices (all data, ? Å) | $R_1$ = 0.0618, $wR_2$ = 0.1327 |
| Extinction coefficient | n/a |
| Largest diff. peak and hole | 1.331 and −0.952 e/Å$^3$ |

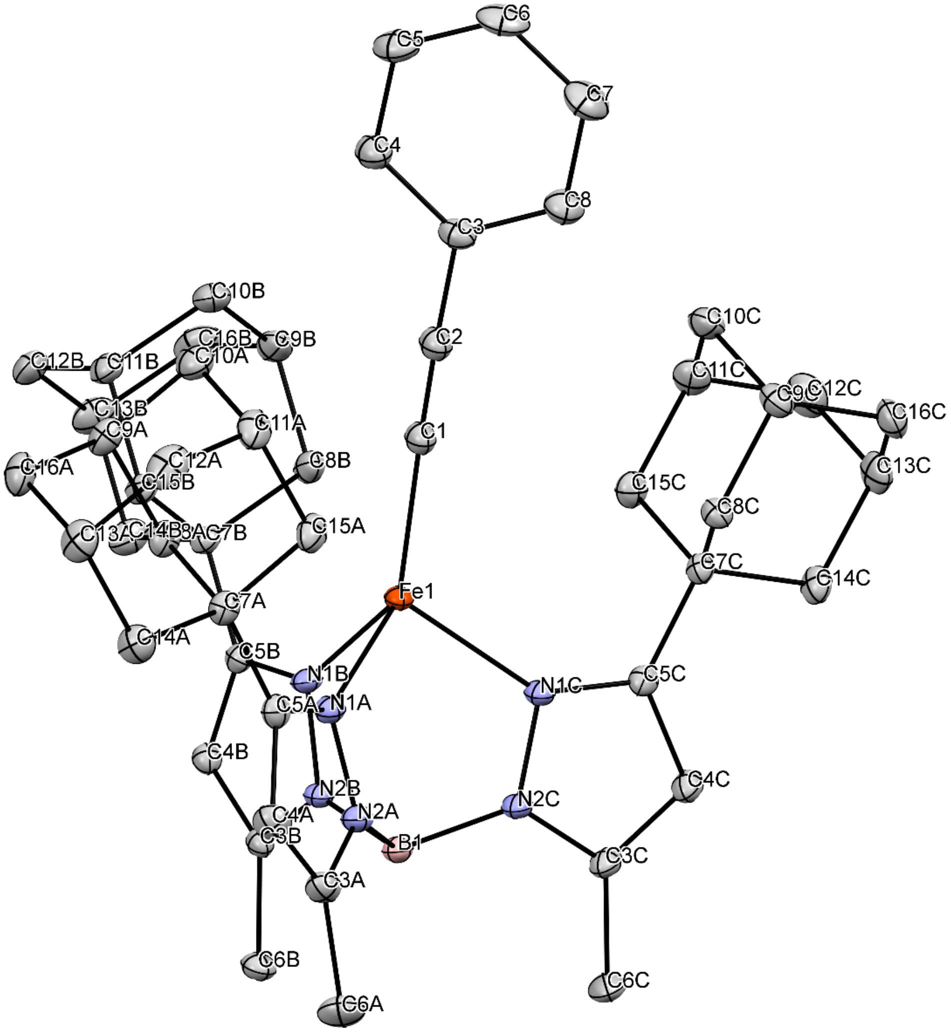

Figure 2-30. Labelled thermal ellipsoid plot (50%) for Tp$^{Me,Ad}$Fe(CCPh) (**13**).

Table 2-5. Crystal data and structure refinement for Tp$^{Me,Ad}$Fe(CCPh) (**13**).

| | | |
|---|---|---|
| Identification code | hh235LE22_0m | |
| Empirical formula | $C_{50}H_{63}BFeN_6$ | |
| Formula weight | 814.72 | |
| Temperature | 100(2) K | |
| Wavelength | 0.71073 Å | |
| Crystal system | Triclinic | |
| Space group | P -1 | |
| Unit cell dimensions | a = 12.2097(3) Å | α = 104.2153(5)°. |
| | b = 14.2547(4) Å | β = 100.8771(5)°. |
| | c = 14.2667(4) Å | γ= 109.9922(5)°. |
| Volume | 2158.28(10) Å$^3$ | |
| Z | 2 | |

| | |
|---|---|
| Density (calculated) | 1.254 $\mathrm{mg/m^3}$ |
| Absorption coefficient | 0.392 $\mathrm{mm^{-1}}$ |
| F(000) | 872 |
| Crystal size | 0.545 x 0.391 x 0.266 $\mathrm{mm^3}$ |
| θ range for data collection | 1.614 to 28.280°. |
| Index ranges | $-16 \leq h \leq 16$, $-18 \leq k \leq 18$, $-19 \leq l \leq 19$ |
| Reflections collected | 44888 |
| Independent reflections | 10685 [$R_{\mathrm{int}}$ = 0.0188] |
| Completeness to θ = 25.242° | 100.0 % |
| Absorption correction | Semi-empirical from equivalents |
| Refinement method | Full-matrix least-squares on $F^2$ |
| Data / restraints / parameters | 10685 / 0 / 529 |
| Goodness-of-fit on $F^2$ | 1.026 |
| Final *R* indices [$I > 2\sigma_I$] | $R_1 = 0.0304$, $wR_2 = 0.0769$ |
| *R* indices (all data) | $R_1 = 0.0339$, $wR_2 = 0.0792$ |
| Extinction coefficient | n/a |
| Largest diff. peak and hole | 0.409 and −0.276 e/$\mathrm{Å^3}$ |

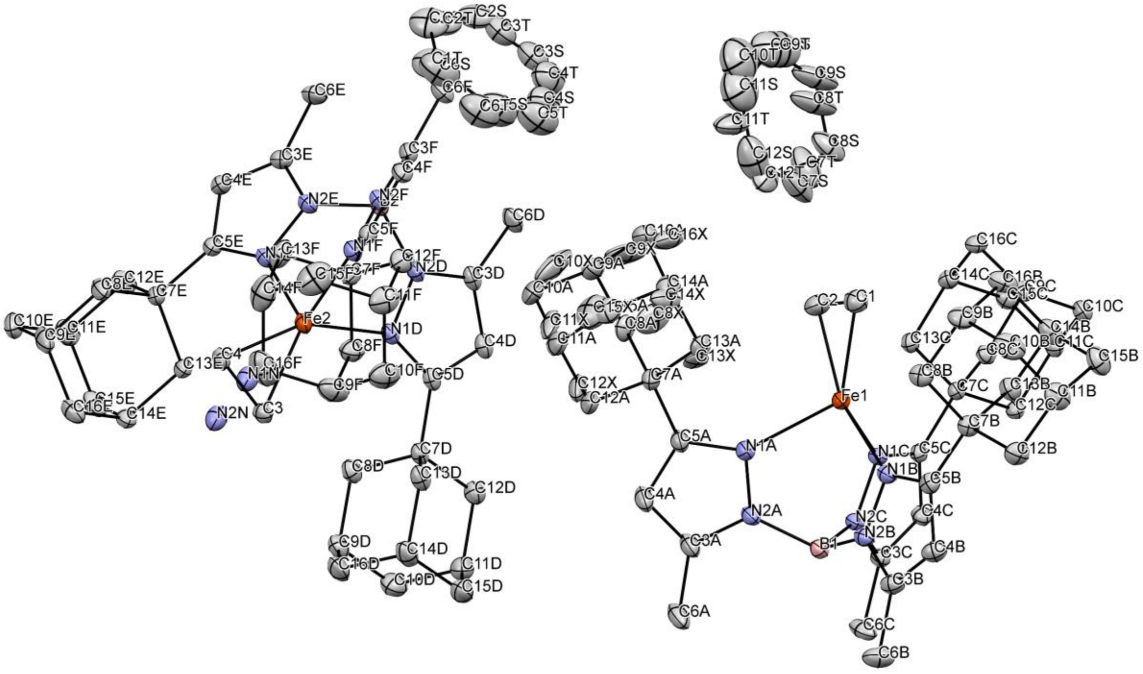

Figure 2-31. Labelled thermal ellipsoid plot (50%) for $\mathrm{Tp^{Me,Ad}Fe(C_2H_4)}$ (**1**).

Table 2-6. Crystal data and structure refinement for $\mathrm{[Tp^{Me,Ad}Fe(C_2H_4)}$ (**1**).

| | |
|---|---|
| Identification code | hh129AM44_0m |
| Empirical formula | $\mathrm{C_{99.70}\,H_{135.40}\,B_2\,Fe_2\,N_{12.30}}$ |

|  |  |  |
|---|---|---|
| Formula weight | 1639.51 |  |
| Temperature | 100(2) K |  |
| Wavelength | 0.71073 Å |  |
| Crystal system | Triclinic |  |
| Space group | P -1 |  |
| Unit cell dimensions | $a$ = 11.3926(4) Å | $\alpha$ = 72.6599(6)°. |
|  | $b$ = 17.9010(7) Å | $\beta$ = 75.9780(6)°. |
|  | $c$ = 23.0224(9) Å | $\gamma$ = 80.8836(6)°. |
| Volume | 4329.3(3) $Å^3$ |  |
| Z | 2 |  |
| Density (calculated) | 1.258 $mg/m^3$ |  |
| Absorption coefficient | 0.391 $mm^{-1}$ |  |
| F(000) | 1763 |  |
| Crystal size | 0.471 x 0.311 x 0.047 $mm^3$ |  |
| $\theta$ range for data collection | 1.716 to 28.282°. |  |
| Index ranges | $-15 \leq h \leq 15$, $-23 \leq k \leq 23$, $-30 \leq l \leq 30$ |  |
| Reflections collected | 110635 |  |
| Independent reflections | 21472 [$R_{int}$ = 0.0286] |  |
| Completeness to $\theta$ = 25.242° | 100.0 % |  |
| Absorption correction | Semi-empirical from equivalents |  |
| Refinement method | Full-matrix least-squares on $F^2$ |  |
| Data / restraints / parameters | 21472 / 121 / 1184 |  |
| Goodness-of-fit on $F^2$ | 1.027 |  |
| Final $R$ indices [$I > 2\sigma_I$] | $R_1$ = 0.0372, $wR_2$ = 0.0893 |  |
| $R$ indices (all data) | $R_1$ = 0.0471, $wR_2$ = 0.0941 |  |
| Extinction coefficient | n/a |  |
| Largest diff. peak and hole | 0.617 and −0.531 e/$Å^3$ |  |

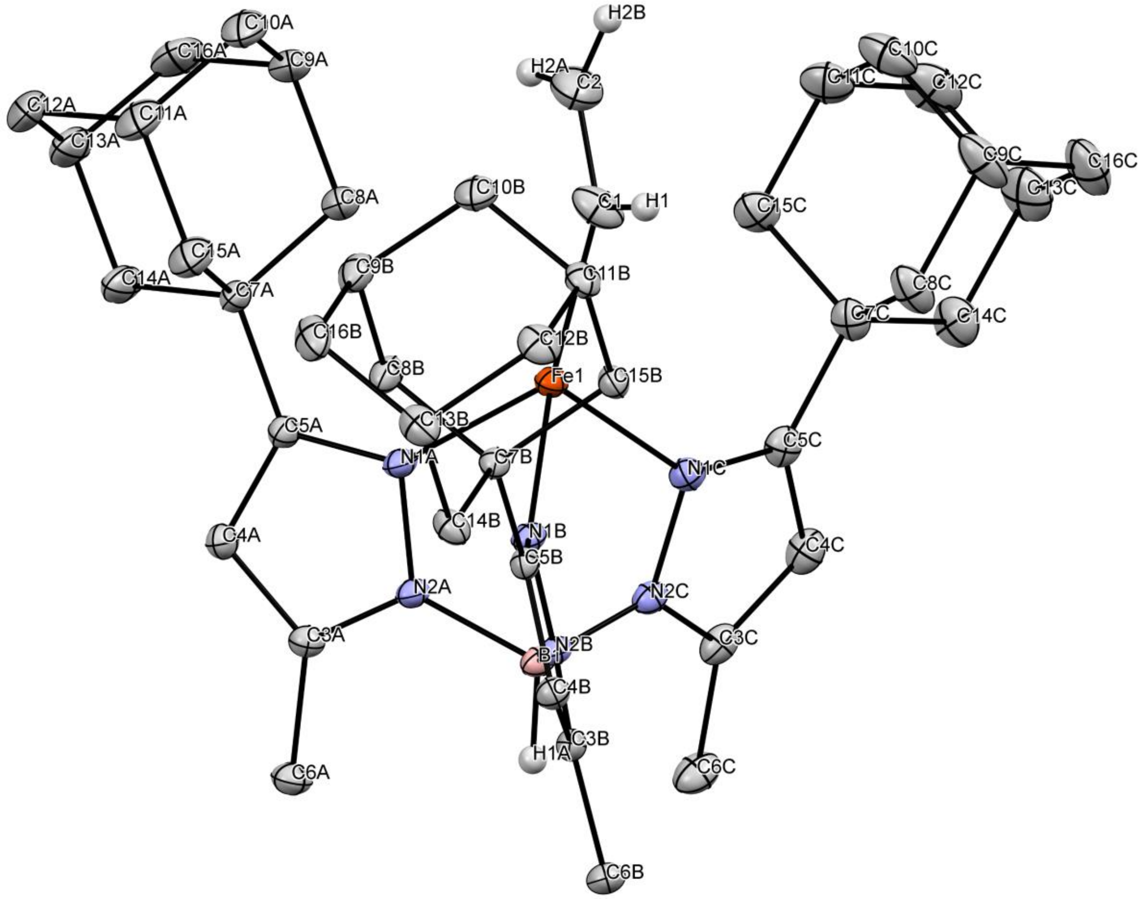

Figure 2-32. Labelled thermal ellipsoid plot (50%) for Tp$^{Me,Ad}$Fe(vinyl) (**2**).

Table 2-7. Crystal data and structure refinement for Tp$^{Me,Ad}$Fe(vinyl) (**2**).

| | | |
|---|---|---|
| Identification code | hh138AM48_0m | |
| Empirical formula | $C_{44}H_{61}BFeN_6$ | |
| Formula weight | 740.64 | |
| Temperature | 100(2) K | |
| Wavelength | 0.71073 Å | |
| Crystal system | Monoclinic | |
| Space group | P 21/c | |
| Unit cell dimensions | a = 11.2710(7) Å | α = 90°. |
| | b = 14.2252(8) Å | β = 98.7927(9)°. |
| | c = 24.5745(14) Å | γ = 90°. |
| Volume | 3893.8(4) Å$^3$ | |
| Z | 4 | |
| Density (calculated) | 1.263 mg/m$^3$ | |
| Absorption coefficient | 0.427 mm$^{-1}$ | |
| F(000) | 1592 | |

| | |
|---|---|
| Crystal size | 0.449 x 0.409 x 0.161 mm$^3$ |
| θ range for data collection | 1.677 to 30.508°. |
| Index ranges | $-16 \leq h \leq 16$, $-20 \leq k \leq 20$, $-35 \leq l \leq 35$ |
| Reflections collected | 89831 |
| Independent reflections | 11883 [$R_{\mathrm{int}} = 0.0350$] |
| Completeness to θ = 25.242° | 100.0 % |
| Absorption correction | Semi-empirical from equivalents |
| Refinement method | Full-matrix least-squares on F$^2$ |
| Data / restraints / parameters | 11883 / 0 / 478 |
| Goodness-of-fit on F$^2$ | 1.033 |
| Final R indices [$I > 2\sigma_I$] | $R_1 = 0.0340$, $wR_2 = 0.0860$ |
| $R$ indices (all data) | $R_1 = 0.0424$, $wR_2 = 0.0913$ |
| Extinction coefficient | n/a |
| Largest diff. peak and hole | 0.980 and −0.441 e/Å$^3$ |

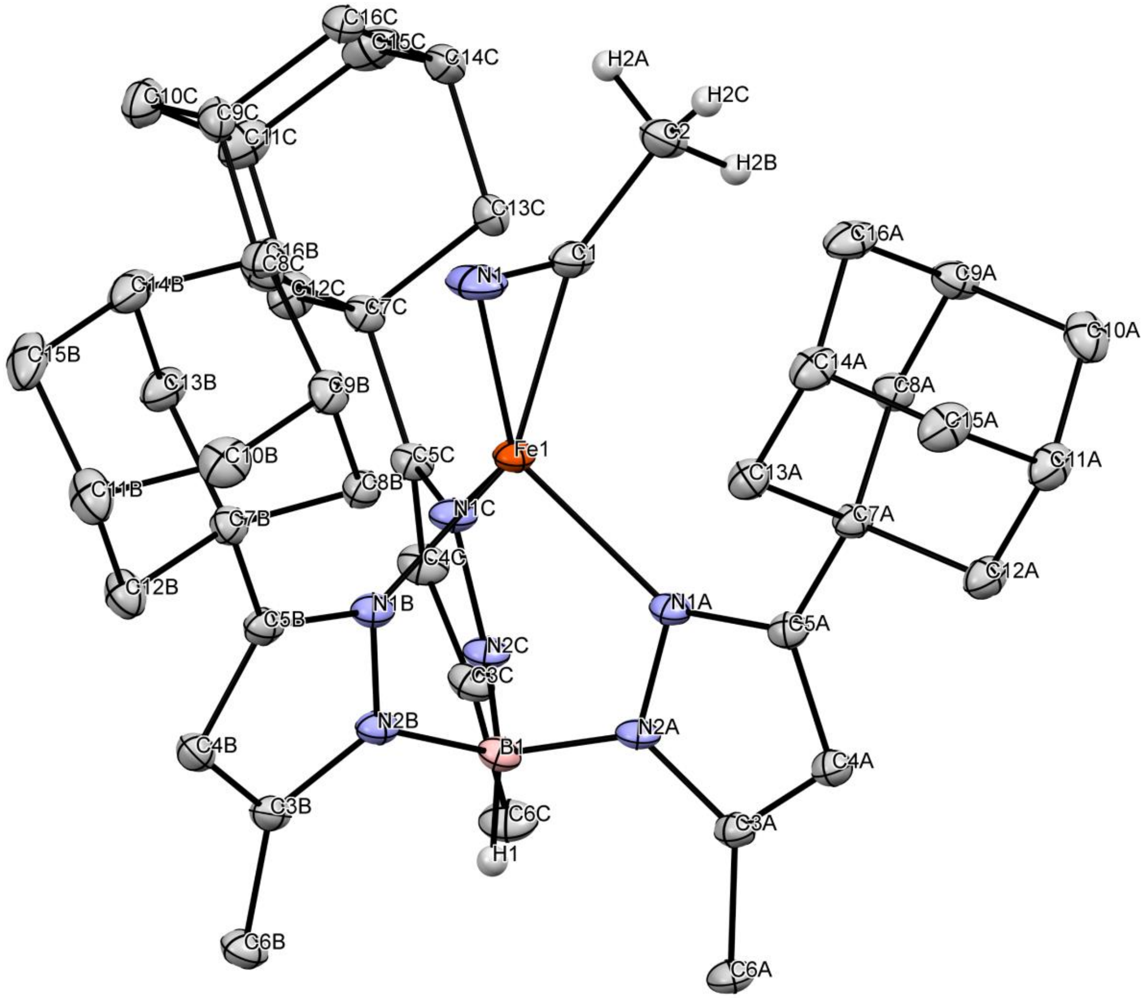

Figure 2-33. Labelled thermal ellipsoid plot (50%) for Tp$^{Me,Ad}$Fe(MeCN) (**6**).

Table 2-8. Crystal data and structure refinement for Tp$^{Me,Ad}$Fe(MeCN) (**6**).

| | | |
|---|---|---|
| Identification code | hh327le | |
| Empirical formula | $C_{44}H_{61}BFeN_7$ | |
| Formula weight | 754.65 | |
| Temperature | 100(2) K | |
| Wavelength | 0.71073 Å | |
| Crystal system | Triclinic | |
| Space group | P-1 | |
| Unit cell dimensions | a = 12.6129(4) Å | $\alpha$ = 78.3399(13)°. |
| | b = 12.6543(3) Å | $\beta$ = 64.6205(13)°. |
| | c = 13.8613(4) Å | $\gamma$ = 88.6530(15)°. |
| Volume | 1952.61(10) Å$^3$ | |
| Z | 2 | |
| Density (calculated) | 1.284 mg/m$^3$ | |
| Absorption coefficient | 0.428 mm$^{-1}$ | |
| F(000) | 810 | |
| Crystal color | green | |
| Crystal size | 0.162 x 0.122 x 0.102 mm$^3$ | |
| $\theta$ range for data collection | 1.647 to 30.508° | |
| Index ranges | $-18 \leq h \leq 18, -18 \leq k \leq 18, -19 \leq l \leq 19$ | |
| Reflections collected | 77062 | |
| Independent reflections | 11884 [$R_{int}$ = 0.0814] | |
| Completeness to $\theta$ = 25.242° | 100.0 % | |
| Absorption correction | Semi-empirical from equivalents | |
| Refinement method | Full-matrix least-squares on $F^2$ | |
| Data / restraints / parameters | 11884 / 1 / 484 | |
| Goodness-of-fit on $F^2$ | 1.024 | |
| Final *R* indices [$I > 2\sigma_I$= 8839 data] | R1 = 0.0434, wR2 = 0.0916 | |
| *R* indices (all data, 0.70 Å) | R1 = 0.0680, wR2 = 0.1030 | |
| Largest diff. peak and hole | 0.445 and −0.444 e/Å$^3$ | |

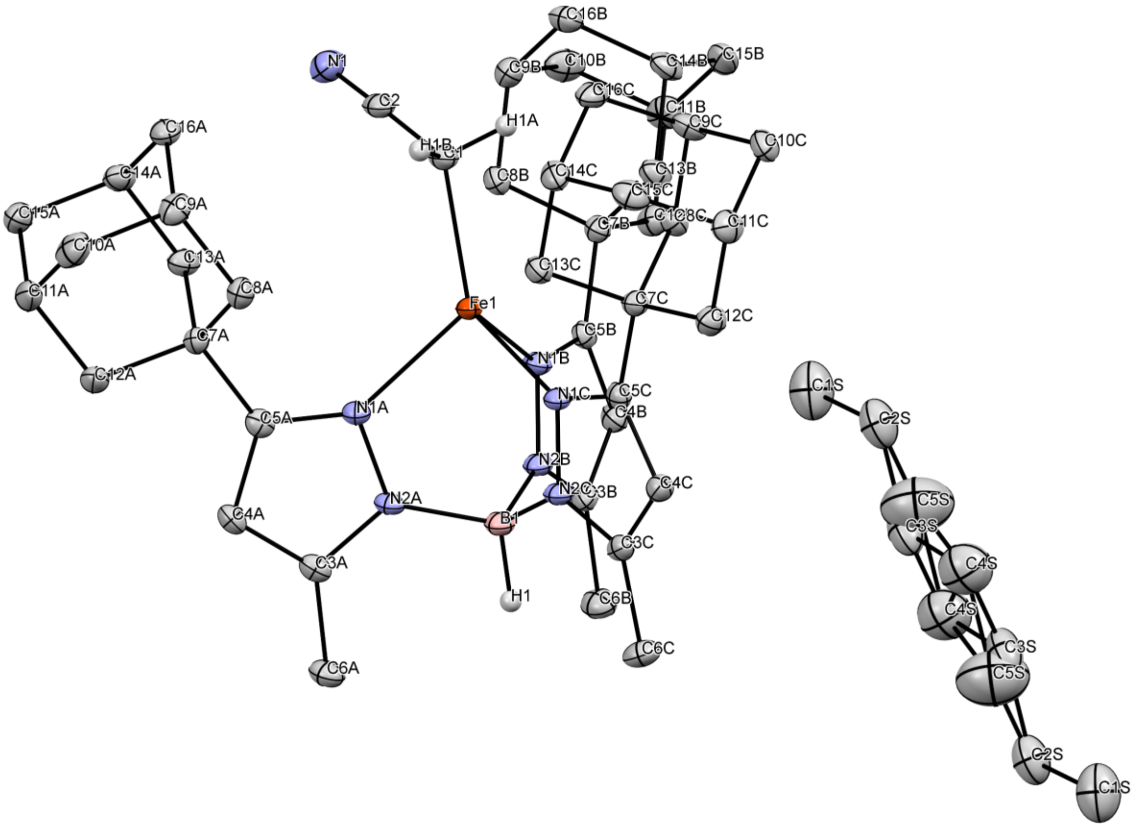

Figure 2-34. Labelled thermal ellipsoid plot (50%) for Tp$^{Me,Ad}$Fe(CH$_2$CN) (**7**).

Table 2-9. Crystal data and structure refinement for Tp$^{Me,Ad}$Fe(CH$_2$CN) (**7**).

| | | |
|---|---|---|
| Identification code | hh328le | |
| Empirical formula | $C_{46.50}H_{66}BFeN_7$ | |
| Formula weight | 789.72 | |
| Temperature | 100(2) K | |
| Wavelength | 0.71073 Å | |
| Crystal system | Monoclinic | |
| Space group | P2₁/c | |
| Unit cell dimensions | a = 11.7381(3) Å | α = 90°. |
| | b = 17.6544(5) Å | β = 105.6388(15)°. |
| | c = 21.1400(6) Å | γ = 90°. |
| Volume | 4218.6(2) Å$^3$ | |
| Z | 4 | |
| Density (calculated) | 1.243 mg/m$^3$ | |
| Absorption coefficient | 0.399 mm$^{-1}$ | |
| F(000) | 1700 | |
| Crystal color | colourless | |
| Crystal size | 0.280 x 0.047 x 0.044 mm$^3$ | |

| | |
|---|---|
| θ range for data collection | 1.802 to 26.370° |
| Index ranges | $-14 \leq h \leq 14$, $-22 \leq k \leq 22$, $-26 \leq l \leq 26$ |
| Reflections collected | 118020 |
| Independent reflections | 8649 [$R_{\text{int}} = 0.0977$] |
| Completeness to θ = 25.242° | 100.0 % |
| Absorption correction | Semi-empirical from equivalents |
| Refinement method | Full-matrix least-squares on $F^2$ |
| Data / restraints / parameters | 8649 / 3 / 535 |
| Goodness-of-fit on $F^2$ | 1.007 |
| Final *R* indices [$I > 2\sigma_I = 6532$ data] | $R_1 = 0.0363$, $wR_2 = 0.0772$ |
| *R* indices (all data, 0.80 Å) | $R_1 = 0.0597$, $wR_2 = 0.0872$ |
| Largest diff. peak and hole | 0.272 and −0.377 e/Å$^3$ |

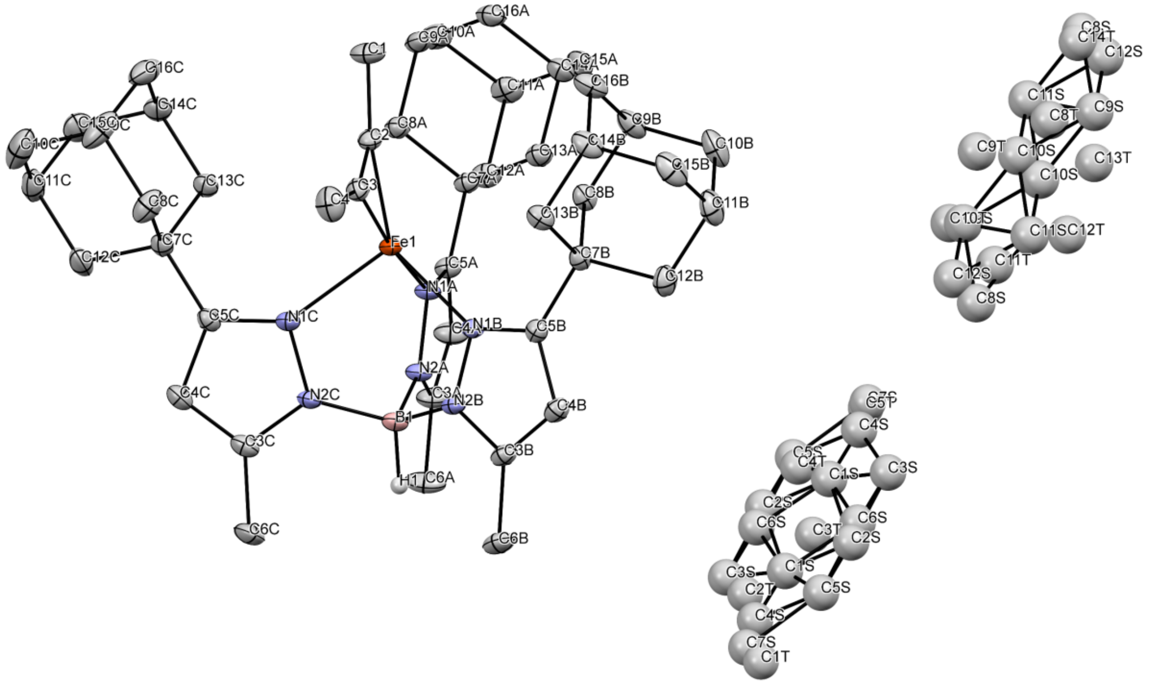

Figure 2-35. Labelled thermal ellipsoid plot (50%) for Tp$^{\text{Me,Ad}}$Fe(2-butyne) (**8**).

Table 2-10. Crystal data and structure refinement for Tp$^{\text{Me,Ad}}$Fe(2-butyne) (**8**).

| | |
|---|---|
| Identification code | hh334le |
| Empirical formula | $C_{51.96}H_{74.09}BFeN_6$ |
| Formula weight | 849.37 |
| Temperature | 100(2) K |
| Wavelength | 0.71073 Å |

|  |  |  |
|---|---|---|
| Crystal system | Triclinic |  |
| Space group | P-1 |  |
| Unit cell dimensions | a = 10.9234(2) Å | $\alpha$ = 112.9654(9)°. |
|  | b = 15.1313(3) Å | $\beta$ = 99.7092(9)°. |
|  | c = 15.6446(3) Å | $\gamma$ = 98.1137(10)°. |
| Volume | 2284.94(8) Å$^3$ |  |
| Z | 2 |  |
| Density (calculated) | 1.235 mg/m$^3$ |  |
| Absorption coefficient | 0.373 mm$^{-1}$ |  |
| F(000) | 918 |  |
| Crystal color | green |  |
| Crystal size | 0.215 x 0.177 x 0.072 mm$^3$ |  |
| $\theta$ range for data collection | 1.588 to 29.130° |  |
| Index ranges | $-14 \le h \le 14$, $-20 \le k \le 20$, $-21 \le l \le 21$ |  |
| Reflections collected | 71166 |  |
| Independent reflections | 12271 [$R_{\mathrm{int}}$ = 0.0463] |  |
| Completeness to $\theta$ = 25.242° | 100.0 % |  |
| Absorption correction | Semi-empirical from equivalents |  |
| Refinement method | Full-matrix least-squares on F$^2$ |  |
| Data / restraints / parameters | 12271 / 1 / 525 |  |
| Goodness-of-fit on F$^2$ | 1.032 |  |
| Final *R* indices [$I > 2\sigma_I$ = 10111 data] | $R_1$ = 0.0411, $wR_2$ = 0.0968 |  |
| *R* indices (all data, 0.73 Å) | $R_1$ = 0.0544, $wR_2$ = 0.1041 |  |
| Largest diff. peak and hole | 0.943 and -0.650 e/Å$^3$ |  |

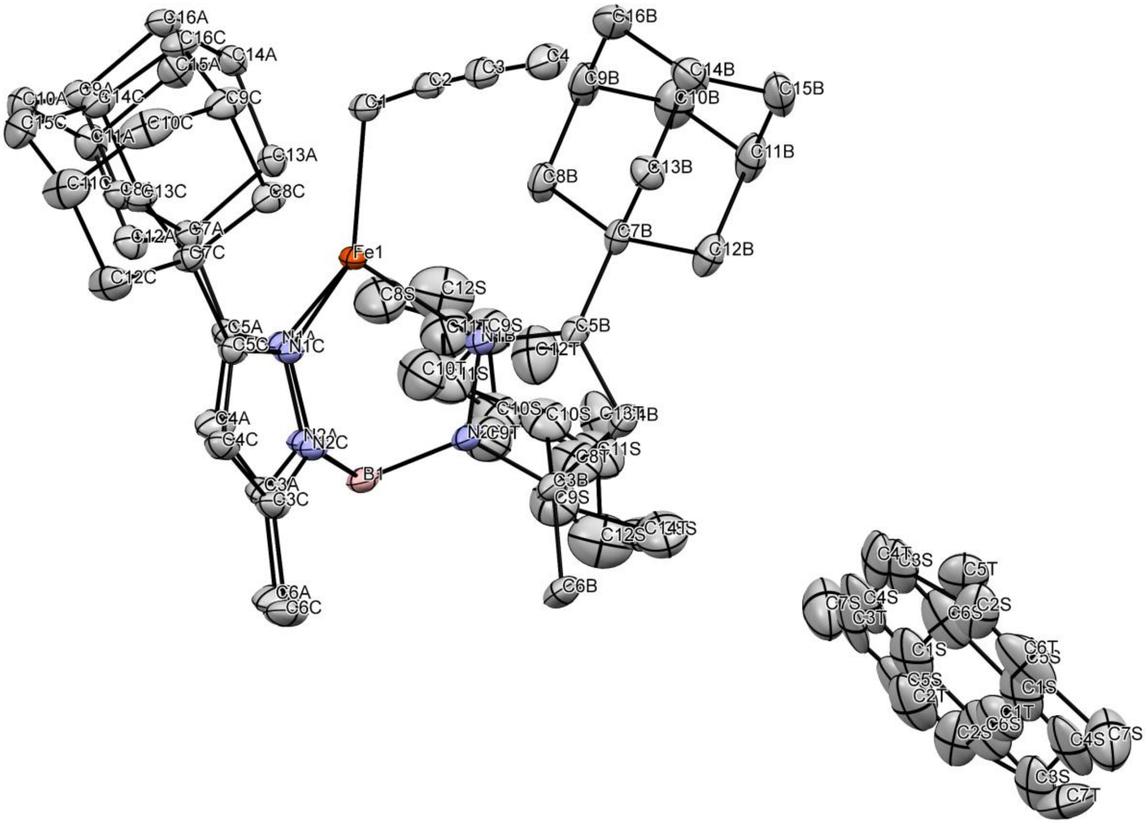

Figure 2-36. Labelled thermal ellipsoid plot (50%) for Tp$^{Me,Ad}$Fe(CH2butyne) (**9**).

Table 2-11. Crystal data and structure refinement for Tp$^{Me,Ad}$Fe(CH2butyne) (**9**).

| | | |
|---|---|---|
| Identification code | hh333le_r | |
| Empirical formula | $C_{52.29}H_{72.41}BFeN_6$ | |
| Formula weight | 851.77 | |
| Temperature | 100(2) K | |
| Wavelength | 0.71073 Å | |
| Crystal system | Triclinic | |
| Space group | P-1 | |
| Unit cell dimensions | a = 10.5699(2) Å | α = 115.6253(8)°. |
| | b = 14.9829(3) Å | β = 100.2432(9)°. |
| | c = 16.6020(3) Å | γ = 96.3457(9)°. |
| Volume | 2280.18(8) $Å^3$ | |
| Z | 2 | |
| Density (calculated) | 1.241 $mg/m^3$ | |
| Absorption coefficient | 0.374 $mm^{-1}$ | |
| F(000) | 918 | |
| Crystal color | brown | |
| Crystal size | 0.313 x 0.223 x 0.110 $mm^3$ | |

| | |
|---|---|
| $\theta$ range for data collection | 1.542 to 30.998° |
| Index ranges | $-15 \leq h \leq 15$, $-21 \leq k \leq 21$, $-24 \leq l \leq 24$ |
| Reflections collected | 88266 |
| Independent reflections | 14495 [$R_{\mathrm{int}} = 0.0419$] |
| Completeness to $\theta = 25.242°$ | 100.0 % |
| Absorption correction | Semi-empirical from equivalents |
| Refinement method | Full-matrix least-squares on $F^2$ |
| Data / restraints / parameters | 14495 / 549 / 691 |
| Goodness-of-fit on $F^2$ | 1.032 |
| Final $R$ indices [$I > 2\sigma_I = 12035$ data] | $R_1 = 0.0376$, $wR_2 = 0.0930$ |
| $R$ indices (all data, 0.69 Å) | $R_1 = 0.0485$, $wR_2 = 0.0999$ |
| Largest diff. peak and hole | 0.469 and −0.305 e/Å$^3$ |

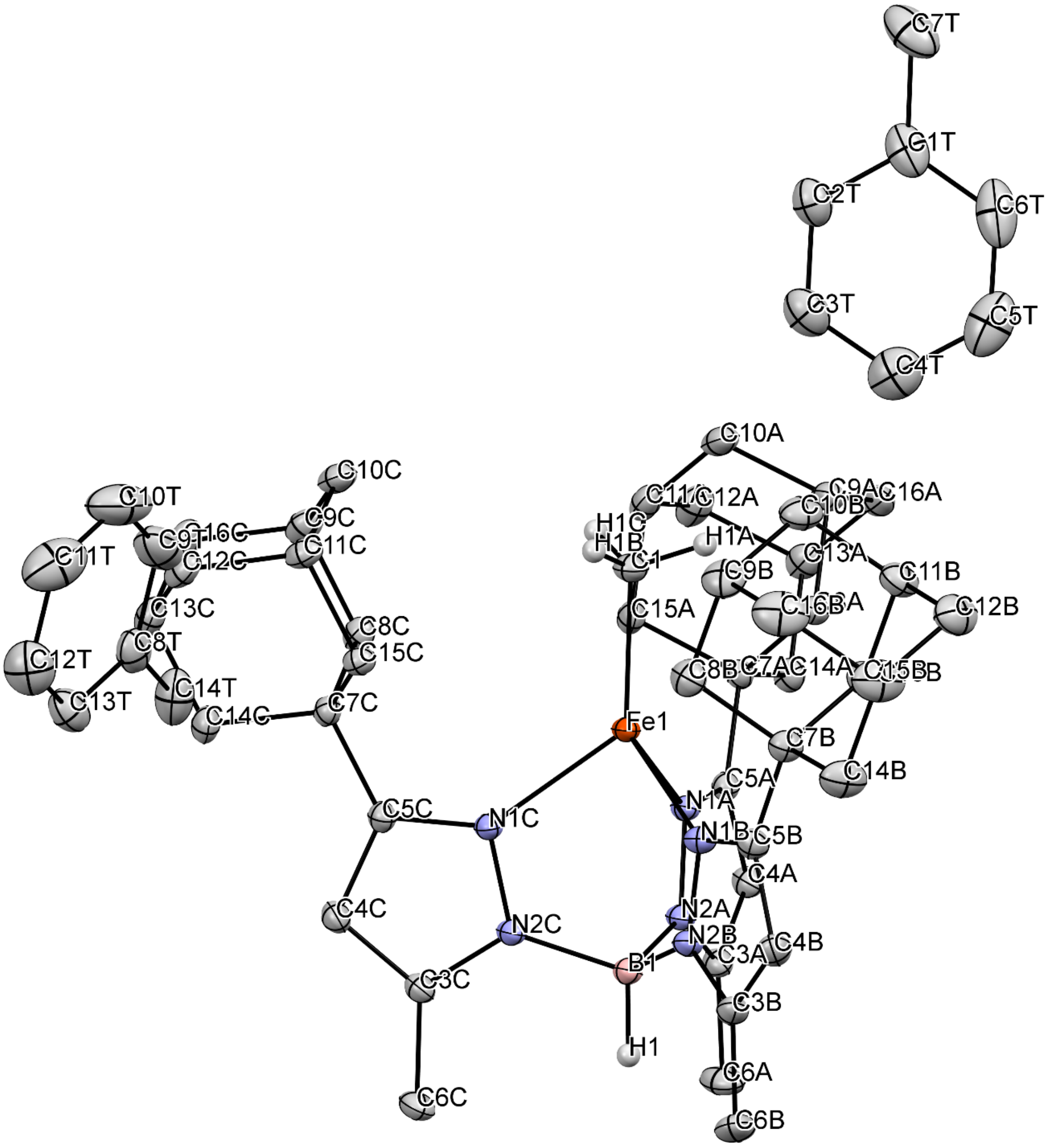

Figure 2-37. Labelled thermal ellipsoid plot (50%) for Tp$^{Me,Ad}$Fe(Me) (**10**).

Table 2-12. Crystal data and structure refinement for Tp$^{Me,Ad}$Fe(Me) (**10**).

| | |
|---|---|
| Identification code | hh260LE33_0m |
| Empirical formula | $C_{57}H_{77}BFeN_6$ |
| Formula weight | 912.90 |
| Temperature | 100(2) K |
| Wavelength | 0.71073 Å |
| Crystal system | Monoclinic |

|  |  |  |
|---|---|---|
| Space group | P 21/n |  |
| Unit cell dimensions | a = 11.5144(5) Å | $\alpha$ = 90°. |
|  | b = 18.2775(7) Å | $\beta$ = 91.8309(6)°. |
|  | c = 23.3949(9) Å | $\gamma$ = 90°. |
| Volume | 4921.0(3) Å$^3$ |  |
| Z | 4 |  |
| Density (calculated) | 1.232 mg/m$^3$ |  |
| Absorption coefficient | 0.351 mm$^{-1}$ |  |
| F(000) | 1968 |  |
| Crystal size | 0.392 x 0.299 x 0.164 mm$^3$ |  |
| $\theta$ range for data collection | 1.414 to 30.507°. |  |
| Index ranges | $-16 \leq h \leq 16$, $-26 \leq k \leq 26$, $-33 \leq l \leq 33$ |  |
| Reflections collected | 116873 |  |
| Independent reflections | 15017 [$R_{\text{int}}$ = 0.0212] |  |
| Completeness to $\theta$ = 25.242° | 99.9 % |  |
| Absorption correction | Semi-empirical from equivalents |  |
| Refinement method | Full-matrix least-squares on F$^2$ |  |
| Data / restraints / parameters | 15017 / 0 / 595 |  |
| Goodness-of-fit on F$^2$ | 1.017 |  |
| Final *R* indices [$I > 2\sigma_I$] | $R_1$ = 0.0353, $wR_2$ = 0.0958 |  |
| *R* indices (all data) | $R_1$ = 0.0421, $wR_2$ = 0.1011 |  |
| Extinction coefficient | n/a |  |
| Largest diff. peak and hole | 0.472 and −0.328 e/Å$^3$ |  |

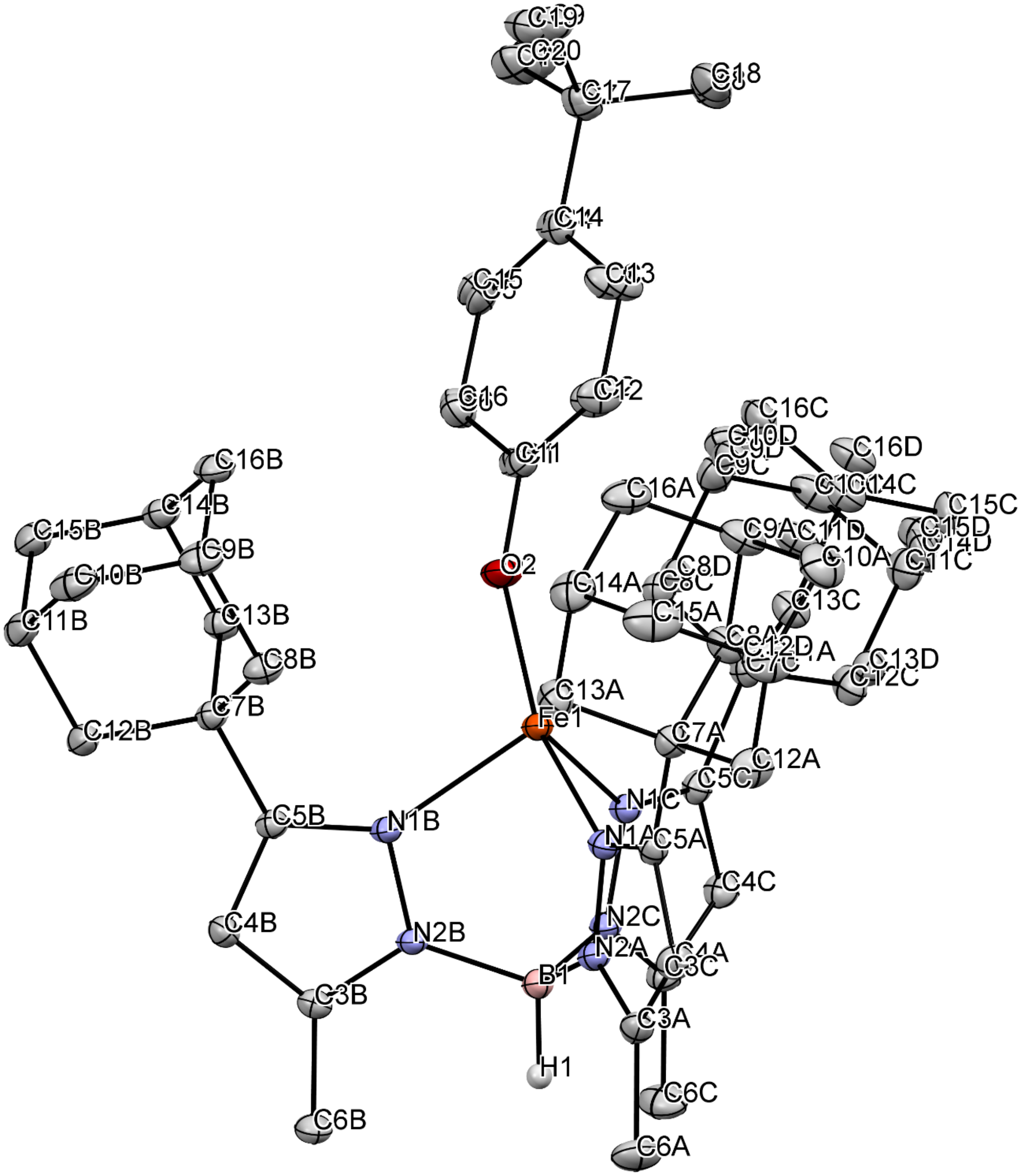

Figure 2-38. Labelled thermal ellipsoid plot (50%) for Tp$^{Me,Ad}$Fe(OPh*t*Bu) (**11**).

Table 2-13. Crystal data and structure refinement for Tp$^{Me,Ad}$Fe(OPh*t*Bu) (**11**).

| | |
|---|---|
| Identification code | hh325le_sq |
| Empirical formula | $C_{52}H_{71}BFeN_6O$ |
| Formula weight | 862.80 |
| Temperature | 100(2) K |

| | | |
|---|---|---|
| Wavelength | 0.71073 Å | |
| Crystal system | Monoclinic | |
| Space group | $P2_1/n$ | |
| Unit cell dimensions | a = 13.8994(3) Å | α = 90°. |
| | b = 19.3362(5) Å | β = 100.7562(12)°. |
| | c = 19.3716(5) Å | γ = 90°. |
| Volume | 5114.9(2) $Å^3$ | |
| Z | 4 | |
| Density (calculated) | 1.120 $mg/m^3$ | |
| Absorption coefficient | 0.335 $mm^{-1}$ | |
| F(000) | 1856 | |
| Crystal color | colourless | |
| Crystal size | 0.110 x 0.108 x 0.079 $mm^3$ | |
| θ range for data collection | 1.665 to 29.130° | |
| Index ranges | $-19 \le h \le 19$, $-26 \le k \le 26$, $-26 \le l \le 26$ | |
| Reflections collected | 120612 | |
| Independent reflections | 13765 [$R_{\mathrm{int}}$ = 0.0810] | |
| Completeness to θ = 25.242° | 100.0 % | |
| Absorption correction | Semi-empirical from equivalents | |
| Refinement method | Full-matrix least-squares on $F^2$ | |
| Data / restraints / parameters | 13765 / 679 / 681 | |
| Goodness-of-fit on $F^2$ | 1.017 | |
| Final *R* indices [$I > 2\sigma_I$ = 10072 data] | $R_1$ = 0.0408, $wR_2$ = 0.0962 | |
| *R* indices (all data, 0.73 Å) | $R_1$ = 0.0658, $wR_2$ = 0.1070 | |
| Largest diff. peak and hole | 0.379 and −0.412 $e/Å^3$ | |

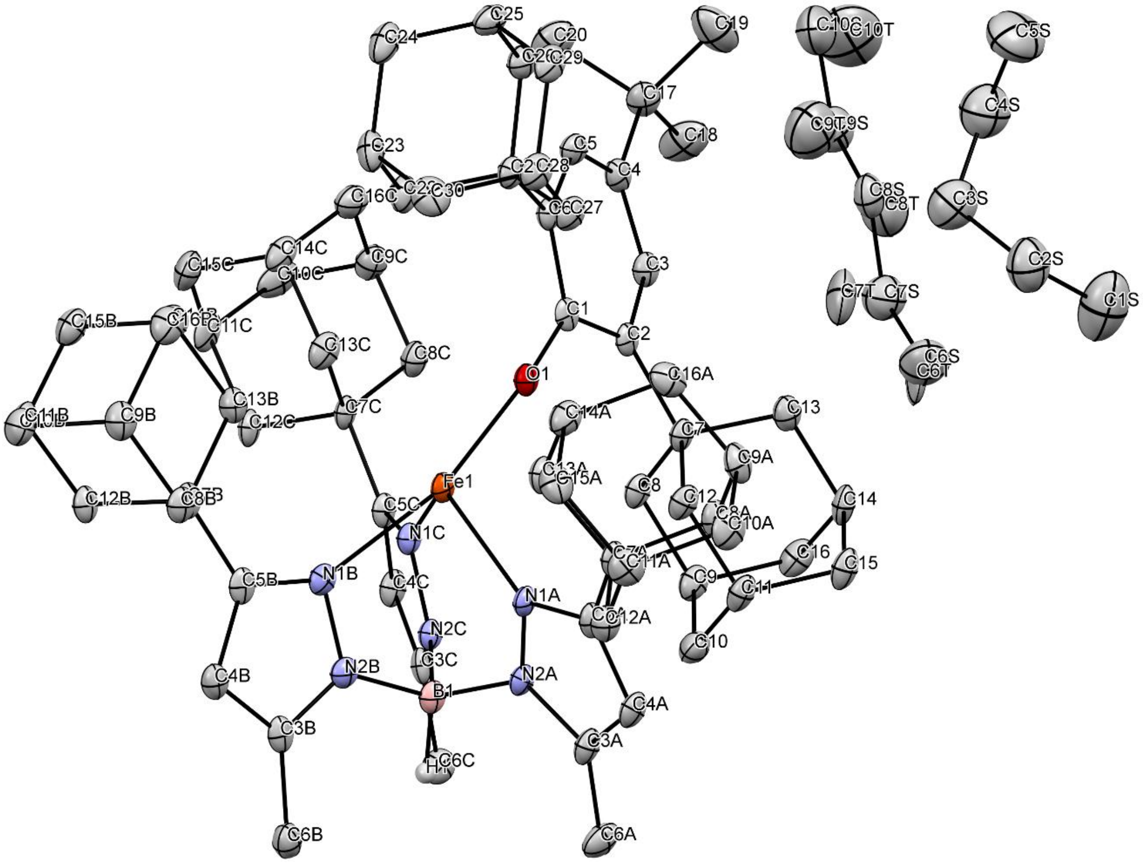

Figure 2-39. Labelled thermal ellipsoid plot (50%) for Tp$^{Me,Ad}$Fe(OPhAd$_2$) (**5**).

Table 2-14. Crystal data and structure refinement for Tp$^{Me,Ad}$Fe(OPhAd$_2$) (**5**).

| | | |
|---|---|---|
| Identification code | hh322le | |
| Empirical formula | $C_{82}H_{123}BFeN_6O$ | |
| Formula weight | 1275.52 | |
| Temperature | 100(2) K | |
| Wavelength | 0.71073 Å | |
| Crystal system | Monoclinic | |
| Space group | $P2_1/c$ | |
| Unit cell dimensions | a = 15.7572(5) Å | α = 90°. |
| | b = 15.2367(5) Å | β = 93.3247(17)°. |
| | c = 29.2794(9) Å | γ = 90°. |
| Volume | 7017.8(4) Å$^3$ | |
| Z | 4 | |
| Density (calculated) | 1.207 mg/m$^3$ | |
| Absorption coefficient | 0.266 mm$^{-1}$ | |
| F(000) | 2784 | |
| Crystal color | colourless | |

| | |
|---|---|
| Crystal size | 0.254 x 0.236 x 0.058 $mm^3$ |
| θ range for data collection | 0.697 to 27.101° |
| Index ranges | $-20 \le h \le 20$, $-19 \le k \le 19$, $-37 \le l \le 37$ |
| Reflections collected | 106324 |
| Independent reflections | 15469 [$R_{int}$ = 0.0903] |
| Completeness to θ = 25.242° | 100.0 % |
| Absorption correction | Semi-empirical from equivalents |
| Refinement method | Full-matrix least-squares on $F^2$ |
| Data / restraints / parameters | 15469 / 263 / 878 |
| Goodness-of-fit on $F^2$ | 1.098 |
| Final *R* indices [$I > 2\sigma_I$ = 10577 data] | $R_1$ = 0.0694, $wR_2$ = 0.1513 |
| *R* indices (all data, 0.78 Å) | $R_1$ = 0.1118, $wR_2$ = 0.1688 |
| Largest diff. peak and hole | 0.734 and −0.575 e/$Å^3$ |

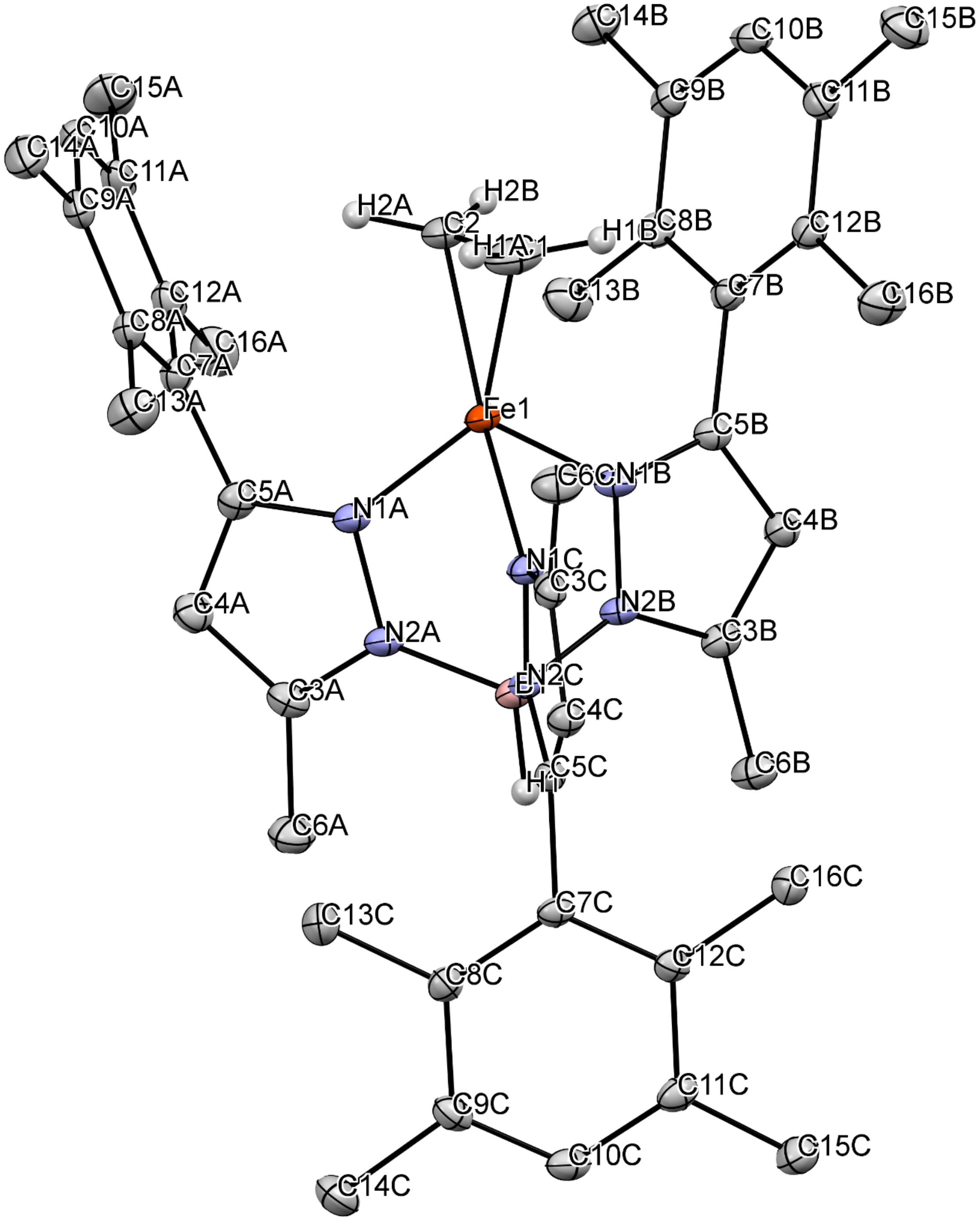

Figure 2-40. Labelled thermal ellipsoid plot (50%) for $Tp^{Me,Dr}Fe(C_2H_4)$ (**3**).

Table 2-15. Crystal data and structure refinement for $Tp^{Me,Dr}Fe(C_2H_4)$ (**3**).

| | |
|---|---|
| Identification code | hh323le |

| | | |
|---|---|---|
| Empirical formula | $C_{44}H_{56}BFeN_6$ | |
| Formula weight | 735.60 | |
| Temperature | 100(2) K | |
| Wavelength | 0.71073 Å | |
| Crystal system | Monoclinic | |
| Space group | $P2_1/n$ | |
| Unit cell dimensions | a = 13.1060(3) Å | α = 90°. |
| | b = 21.6201(5) Å | β = 95.8838(14)°. |
| | c = 14.0719(3) Å | γ = 90°. |
| Volume | 3966.31(15) $Å^3$ | |
| Z | 4 | |
| Density (calculated) | 1.232 $mg/m^3$ | |
| Absorption coefficient | 0.419 $mm^{-1}$ | |
| F(000) | 1572 | |
| Crystal color | green | |
| Crystal size | 0.108 x 0.095 x 0.034 $mm^3$ | |
| θ range for data collection | 1.733 to 28.279° | |
| Index ranges | $-17 \le h \le 17$, $-28 \le k \le 28$, $-18 \le l \le 18$ | |
| Reflections collected | 73235 | |
| Independent reflections | 9853 [$R_{int}$ = 0.0757] | |
| Completeness to θ = 25.242° | 100.0 % | |
| Absorption correction | Semi-empirical from equivalents | |
| Refinement method | Full-matrix least-squares on $F^2$ | |
| Data / restraints / parameters | 9853 / 5 / 499 | |
| Goodness-of-fit on $F^2$ | 1.010 | |
| Final *R* indices [$I > 2\sigma_I$ = 7359 data] | $R_1 = 0.0408$, $wR_2 = 0.0855$ | |
| *R* indices (all data, 0.75 Å) | $R_1 = 0.0662$, $wR_2 = 0.0960$ | |
| Largest diff. peak and hole | 0.343 and −0.393 $e/Å^3$ | |

## *References*

(1) Ortiz De Montellano, P. R. Hydrocarbon Hydroxylation by Cytochrome P450 Enzymes. *Chem. Rev.* **2010**, *110* (2), 932–948. https://doi.org/10.1021/cr9002193.

(2) Meunier, B.; de Visser, S. P.; Shaik, S. Mechanism of Oxidation Reactions Catalyzed by Cytochrome P450 Enzymes. *Chem. Rev.* **2004**, *104* (9), 3947–3980. https://doi.org/10.1021/CR020443G.

(3) Klein, H.-F.; Camadanli, S.; Beck, R.; Leukel, D.; Flörke, U. Cyclometalation of Substrates Containing Imine and Pyridyl Anchoring Groups by Iron and Cobalt Complexes. *Angew. Chemie Int. Ed.* **2005**, *44* (6), 975–977. https://doi.org/10.1002/anie.200460978.

(4) Yoshikai, N.; Mieczkowski, A.; Matsumoto, A.; Ilies, L.; Nakamura, E. Iron-Catalyzed C−C Bond Formation at α-Position of Aliphatic Amines via C−H Bond Activation through 1,5-Hydrogen Transfer. *J. Am. Chem. Soc.* **2010**, *132* (16), 5568–5569. https://doi.org/10.1021/ja100651t.

(5) Shang, R.; Ilies, L.; Matsumoto, A.; Nakamura, E. β-Arylation of Carboxamides via Iron-Catalyzed C(Sp3)-H Bond Activation. *J. Am. Chem. Soc.* **2013**, *135* (16), 6030–6032. https://doi.org/10.1021/ja402806f.

(6) Baker, M. V.; Field, L. D. Reaction of Carbon-Hydrogen Bonds in Alkanes with Bis(Diphosphine) Complexes of Iron. *J. Am. Chem. Soc.* **1987**, *109* (9), 2825–2826. https://doi.org/10.1021/ja00243a046.

(7) Jones, W. D.; Foster, G. P.; Putinas, J. M. The Catalytic Activation and Functionalization of Carbon-Hydrogen Bonds. Aldimine Formation by the Insertion of Isonitriles into Aromatic Carbon-Hydrogen Bonds. *J. Am. Chem. Soc.* **1987**, *109* (16), 5047–5048. https://doi.org/10.1021/ja00250a060.

(8) Waltz, K. M.; He, X.; Muhoro, C.; Hartwig, J. F. Hydrocarbon Functionalization by Transition Metal Boryls. *J. Am. Chem. Soc.* **1995**, *117* (45), 11357–11358. https://doi.org/10.1021/ja00150a041.

(9) MacLeod, K. C.; Dimucci, I. M.; Zovinka, E. P.; McWilliams, S. F.; Mercado, B. Q.; Lancaster, K. M.; Holland, P. L. Masked Radicals: Iron Complexes of Trityl, Benzophenone, and Phenylacetylene. *Organometallics* **2019**, *38* (21), 4224–4232. https://doi.org/10.1021/acs.organomet.9b00534.

(10) Ott, J. C.; Wadepohl, H.; Gade, L. H. Opening up the Valence Shell: A T-Shaped Iron(I) Metalloradical and Its Potential for Atom Abstraction. *Angew. Chemie - Int. Ed.* **2020**, *59* (24), 9448–9452. https://doi.org/10.1002/anie.202003118.

(11) McSkimming, A.; Harman, W. H. A Terminal N2 Complex of High-Spin Iron(I) in a Weak, Trigonal Ligand Field. *J. Am. Chem. Soc.* **2015**, *137* (28), 8940–8943. https://doi.org/10.1021/jacs.5b06337.

(12) Deutsch, J. L.; Poling, S. M. The Determination of Paramagnetic Susceptibility by NMR: A Physical Chemistry Experiment. *J. Chem. Educ.* **1969**, *46* (3), 167. https://doi.org/10.1021/ed046p167.

(13) Schubert, E. M. Utilizing the Evans Method with a Superconducting NMR Spectrometer in the Undergraduate Laboratory. *J. Chem. Educ.* **1992**, *69* (1), 62. https://doi.org/10.1021/ed069p62.1.

(14) Jové, F. A.; Pariya, C.; Scoblete, M.; Yap, G. P. A.; Theopold, K. H. A Family of Four-Coordinate Iron(II) Complexes Bearing the Sterically Hindered Tris(Pyrazolyl)Borato Ligand TptBu,Me. *Chem. - A Eur. J.* **2011**, *17* (4), 1310–1318. https://doi.org/10.1002/chem.201001792.

(15) Nobuhiko Shirasawa; Trieu Thi Nguyet, 1; Shiro Hikichi; Yoshihiko Moro-oka, and; Akita*, M. Tetrahedral, Highly Coordinatively Unsaturated 14e (Fe) and 15e (Co) Hydrocarbyl Complexes Bearing Hydrotris(Pyrazolyl)Borato Ligands (TpR‘), TpR‘M−R (M = Fe, Co, Ni). **2001**. https://doi.org/10.1021/OM0103106.

(16) Kisko, J. L.; Hascall, T.; Parkin, G. The Synthesis, Structure, and Reactivity of Phenyl Tris(3-Tert- Butylpyrazolyl)Borato Iron Methyl, [PhTp(Bu1)]FeMe: Isolation of a Four- Coordinate Monovalent Iron Carbonyl Complex, [PhTp(Bu1)]FeCO [10]. *J. Am. Chem. Soc.* **1998**, *120* (40), 10561–10562. https://doi.org/10.1021/ja982323p.

(17) Trovitch, R. J.; Lobkovsky, E.; Bouwkamp, M. W.; Chirik, P. J. Carbon-Oxygen Bond Cleavage by Bis(Imino)Pyridine Iron Compounds: Catalyst Deactivation Pathways and Observation of Acyl C-O Bond Cleavage in Esters. *Organometallics* **2008**, *27* (23), 6264–6278. https://doi.org/10.1021/om8005596.

(18) Cowley, R. E.; Christian, G. J.; Brennessel, W. W.; Neese, F.; Holland, P. L. A Reduced (β-Diketiminato)Iron Complex with End-On and Side-On Nitriles: Strong Backbonding or Ligand Non-Innocence? *Eur. J. Inorg. Chem.* **2012**, *2012* (3), 479–483. https://doi.org/10.1002/ejic.201100787.

(19) MacLeod, K. C.; McWilliams, S. F.; Mercado, B. Q.; Holland, P. L.; Smil, V.; Jenkinson, D. S.; Schlögl, R.; Burgess, B. K.; Lowe, D. J.; Hoffman, B. M.; et al. Stepwise N–H Bond Formation from N2-Derived Iron Nitride, Imide and Amide Intermediates to Ammonia. *Chem. Sci.* **2016**, *277*, 76–81. https://doi.org/10.1039/C6SC00423G.

(20) Walter, M. D.; White, P. S. Reactivity Studies on [Cp′FeI]2: Monomeric Amido,

Phenoxo, and Alkyl Complexes. *Inorg. Chem.* **2012**, *51* (21), 11860–11872. https://doi.org/10.1021/ic301770f.

(21) Nesbit, M. A.; Suess, D. L. M.; Peters, J. C. E–H Bond Activations and Hydrosilylation Catalysis with Iron and Cobalt Metalloboranes. *Organometallics* **2015**, *34* (19), 4741–4752. https://doi.org/10.1021/acs.organomet.5b00530.

(22) Iovan, D. A.; Wilding, M. J. T.; Baek, Y.; Hennessy, E. T.; Betley, T. A. Diastereoselective C−H Bond Amination for Disubstituted Pyrrolidines. *Angew. Chemie Int. Ed.* **2017**, *56* (49), 15599–15602. https://doi.org/10.1002/anie.201708519.

(23) Fokin, A. A.; Chernish, L. V.; Gunchenko, P. A.; Tikhonchuk, E. Y.; Hausmann, H.; Serafin, M.; Dahl, J. E. P.; Carlson, R. M. K.; Schreiner, P. R. Stable Alkanes Containing Very Long Carbon–Carbon Bonds. *J. Am. Chem. Soc.* **2012**, *134* (33), 13641–13650. https://doi.org/10.1021/ja302258q.

(24) Watanabe, T.; Ishida, Y.; Matsuo, T.; Kawaguchi, H. Syntheses and Structures of Zirconium(Iv) Complexes Supported by 2,6-Di-Adamantylaryloxide Ligands and Formation of Arene-Bridged Dizirconium Complexes with an Inverse Sandwich Structure. *Dalt. Trans.* **2010**, *39* (2), 484–491. https://doi.org/10.1039/B911082H.

(25) Varlamov, V. T.; Denisov, E. T.; Chatgilialoglu, C. Reactivity of Tris(Trimethylsilyl)Silane toward Diarylaminyl Radicals. *J. Org. Chem.* **2001**, *66* (19), 6317–6322. https://doi.org/10.1021/jo010408u.

(26) Bruker. APEX 2. Bruker AXS Inc.: Madison, Wisconsin, USA 2014.

(27) *SAINT, Version 8.34, Bruker (2012)*; Bruker AXS Inc.: Madison, Wisconsin, USA.

(28) *SADABS, Version 2012/1, Bruker (2012)*; Bruker AXS Inc.: Madison, Wisconsin, USA.

(29) Bruker. SHELXTL. Bruker AXS Inc.: Madison, Wisconsin, USA 2013.

# Chapter 3 : A Molecular Platinide

## *Introduction*

The two transition metals with the highest electron affinity are gold (2.31 eV) and platinum (2.13 eV).[1] Both metals have been observed as stable monatomic metal anions in the gas phase.[2] This increased stability is due to relativistic effects that grow concomitantly with atomic number, contracting the s and p orbitals while expanding the d and f orbitals.[3] This effect becomes especially prominent in the 6th period, so much so that both Pt and Au have a greater electron affinity than sulfur (2.08 eV) which routinely forms dianions. Since the isolation of the 12-valence-electron species $[NMe_4][Au^-]$[4] we were able to generate a stable boroauride using our $B_2P_2$ ligand scaffold.[5] This ligand features *trans*-disposed phosphine donors straddling a 9,10-diboraanthracene (DBA) core. Unlike its predecessor which is only stable in liquid ammonia, $AuB_2P_2$ can reversibly interconvert between Au(0) and Au(−1) oxidation states using the stabilizing acceptor interactions of the boraanthracene core. Given our success with gold and the existence of the Pt(−2) species as $Cs_2Pt$ in the solid state,[6] we wondered if we could similarly access molecular Pt(−1) and Pt(−2) complexes using $B_2P_2$.

## *Results and Discussion*

$B_2P_2$ was prepared as previously described.[5] Metallation with (1,5-cyclooctadiene)platinum(II) chloride, bis(triphenylphosphine)platinum(II) chloride, and bis(benzonitrile)platinum(II) chloride all resulted in intractable mixtures. Metallation with tris(norbornene)platinum(0) produced a bright orange precipitant, which degraded into complex mixtures upon dissolving in THF or DCM. Metallation with tetrakis(triphenylphosphine)platinum(0) did yield some of the desired material (<40%), however obtaining high-purity material from this mixture was impractical. We finally settled on metallation with ethylenebis(triphenylphosphine)platinum(0) from which we were able to produce a 50% yield of **1** in high purity as yellow crystals.

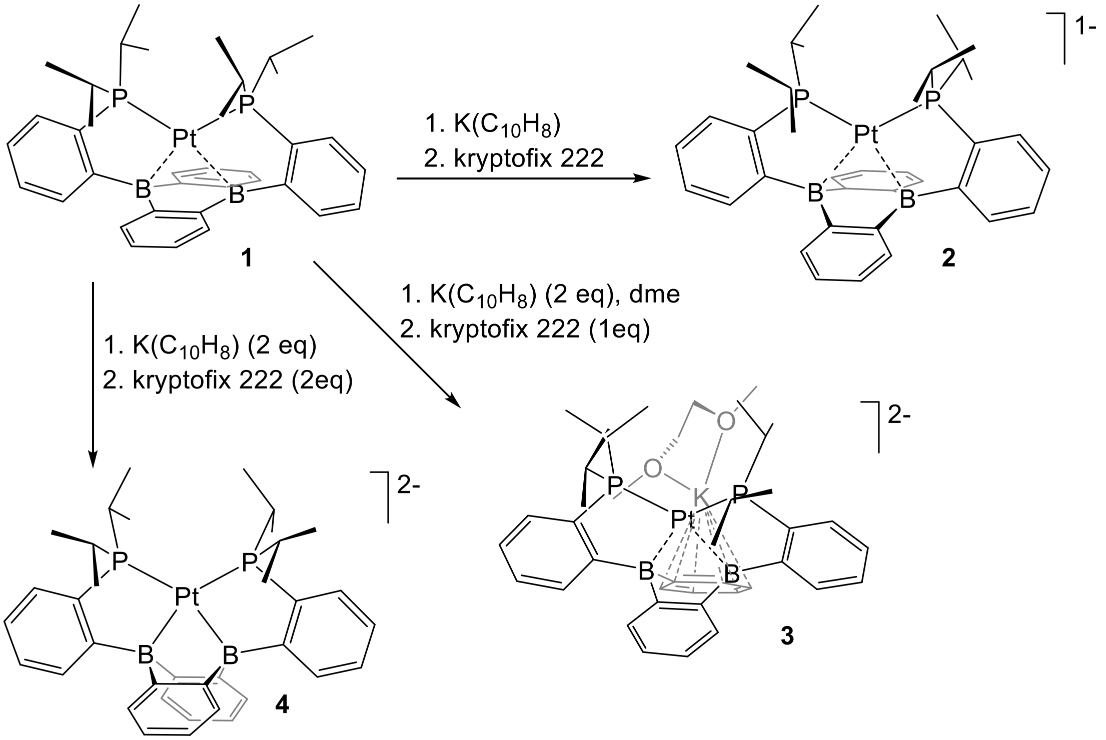

Scheme 3-1. Synthesis of reduced $PtB_2P_2$ complexes.

$^{31}$P-NMR shows a single resonance at 44.0 ppm with distinctive $^{195}$Pt coupling ($^1J_{P,Pt}$ = 4997 Hz) consistent with $C_2$ symmetry in solution (Figure 3-11). $^{195}$Pt signal at −5456 ppm is similar, albeit further upfield than other boron-ligated Pt(0) species reported (Scheme 3-2, Table 3-1). The broad $^{11}$B resonance at 29 ppm is shifted just 5 ppm downfield of the free ligand. These modest platinum-boron interactions are further substantiated by single crystal X-ray diffraction (XRD) revealing planar borons (Σ∡ C-B-

C = 359.7°) with distant contacts to Pt ($d_{\text{Pt–B}}$ = 2.321(2) Å). The platinum-phosphine bond lengths in **1** are also quite typical ($d_{\text{Pt–P}}$ = 2.2901(5), 2.2874(5) Å) (Figure 3-1).

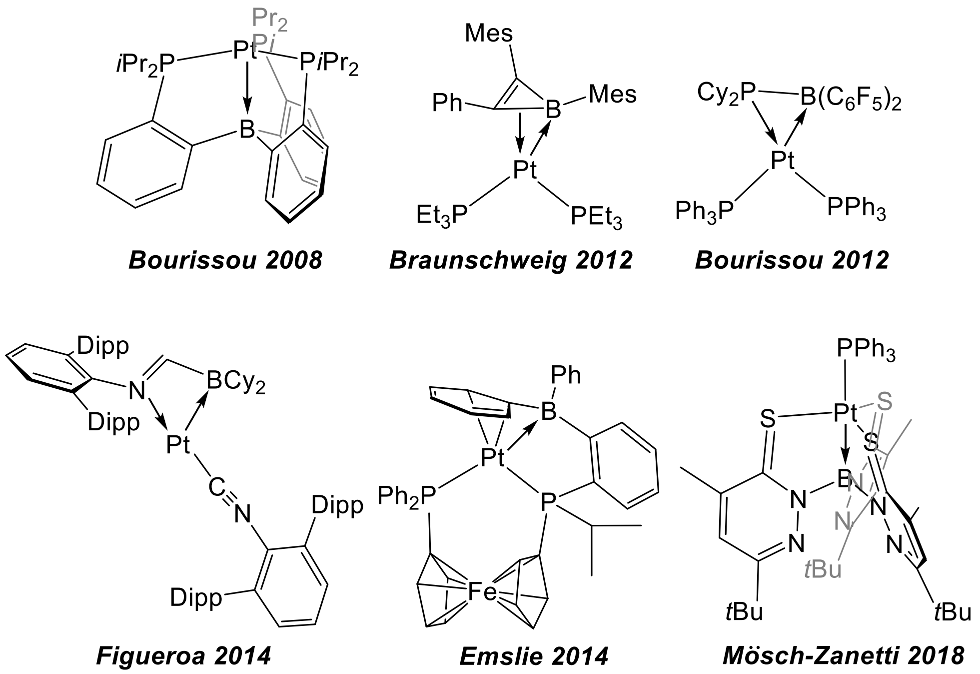

***Bourissou 2008*** ***Braunschweig 2012*** ***Bourissou 2012***

***Figueroa 2014*** ***Emslie 2014*** ***Mösch-Zanetti 2018***

Scheme 3-2. Examples of boron-containing Pt(0) complexes.[7–12]

Table 3-1. Bond lengths and NMR characterization of some Pt(0) complexes.

| **Reference** | **$^{195}$Pt ppm ($J$ = Hz)** | **$^{11}$B ppm ($J$ = Hz)** | **$^{31}$P ppm ($J$ = Hz)** | **Pt−B (Å)** | **Pt−P (Å)** |
|---|---|---|---|---|---|
| Bourissou 2008[7] | N.R. | 18 | 79 ($J$ = 3578) | 2.223 | 2.296* |
| Braunschweig 2012[8] | −4764 | 40 | 15 ($J$ = 2112),<br>11 ($J$ = 3188). | 2.108 | 2.308* |
| Bourissou 2012[9] | N.R. | −20<br>($J$ = 42) | 31 ($J$ = 3750, 230, 13),<br>21 (broad m, $J$ =2160). | 2.234 | 2.311* |
| Figueroa 2014[10] | N.R. | 18 | n/a | 2.313 | n/a |
| Emslie 2014[11] | −4934 | 21 | 51 ($J$ = 5651, 56),<br>28 ($J$ = 4183, 56). | 2.291 | 2.268* |
| Mösch-Zanetti 2018[12] | N.R. | 23 | 16 | 2.092 | 2.364 |
| this paper | −5456 | 29 | 45 ($J$ = 4997) | 2.329* | 2.289* |

*averaged; N.R = not reported.

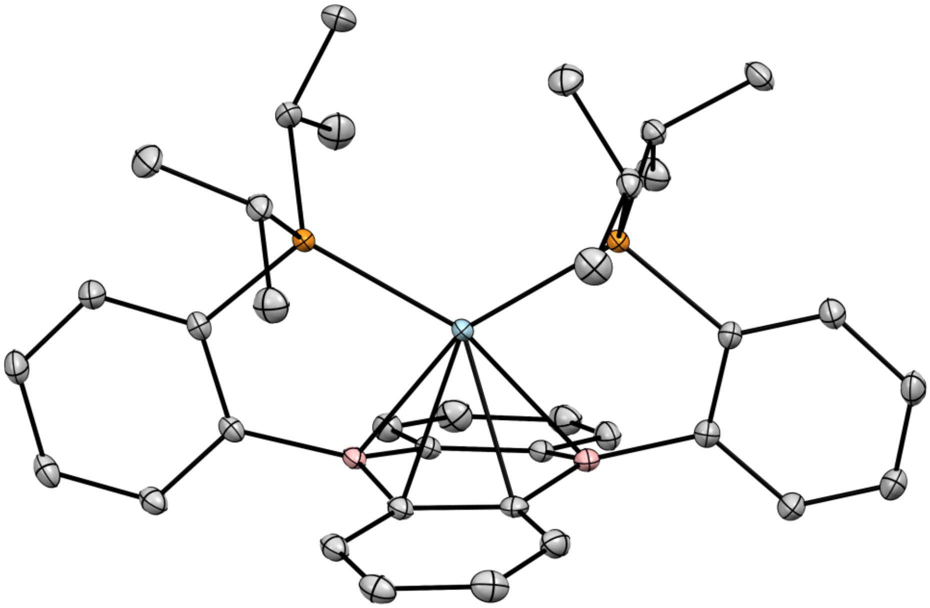

Figure 3-1. Thermal ellipsoid plots (50% probability) of the solid-state structure of PtB2P2 (**1**). Light blue, pink, orange, and gray ellipsoids represent Pt, B, P, and C atoms, respectively. Hydrogen atoms and co-crystallized solvent molecules are omitted for clarity.

Cyclic voltammetry (CV) on **1** (0.1M [$NBu_4$][$PF_6$] in THF, 100 mV/s scan rate) revealed two reversible reduction events at −2.67 and −2.96 V vs. Fc/Fc$^+$ (Fc = $(C_5H_5)_2Fe$, Figure 3-2). In contrast, the nickel analogue **NiB$_2$P$_2$** we previously reported[13] displays only one reduction event at −2.84 V within this solvent window. The free ligand **B$_2$P$_2$,** however is easier to reduce than either of these with two reversible reductions at −2.15 V and −2.67 V. The nearly 200 mV positive shift in potential of **1** over its nickel analogue, implies the platinum is not an innocent bystander.

A quasi-reversible oxidation event at +0.6 was also detected, however attempts to access the Pt(II) species directly from dichloro(1,5-cyclooctadiene)platinum(II) and dichlorbis(triphenylphosphine)platinum(II) resulted in intractable mixtures.

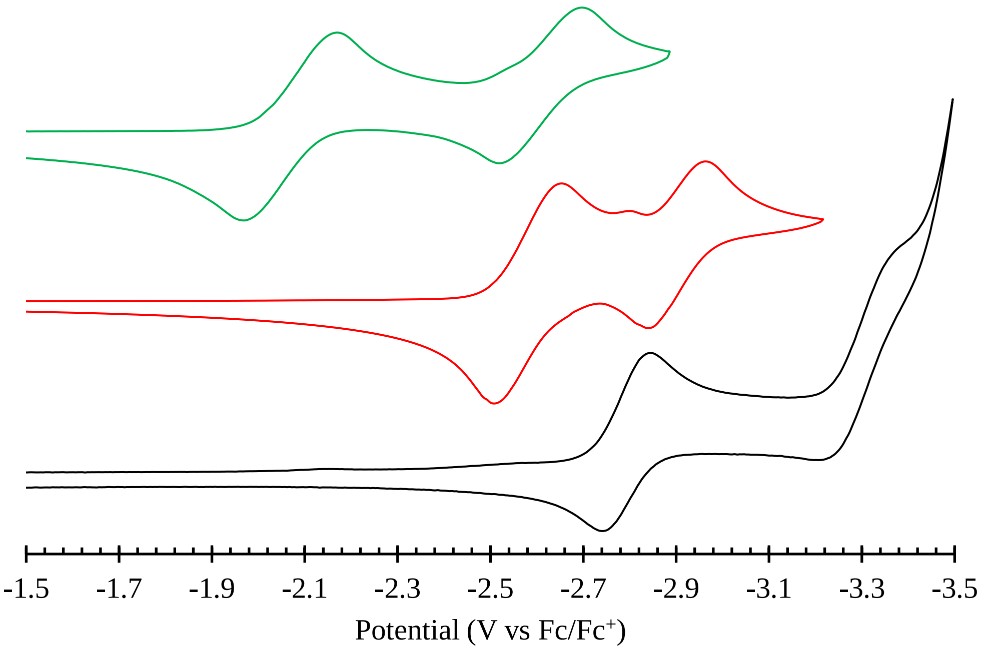

Figure 3-2. Cyclic voltammogram of **$B_2P_2$** (green), **$PtB_2P_2$** (red), **$NiB_2P_2$** (black)[13] in THF (0.1 M $[nBu_4N]PF_6$ as electrolyte; 100 mV/s scan rate).

To better understand platinum's role through these redox processes, we sought to isolate the 1-electron and 2-electron reduction products. Chemical reduction using 1 equivalent of potassium naphthalenide and 1 equivalent of kryptofix 222 provided the 1-electron reduced species as a mauve-red solid crystalline solid. XRD revealed a canted, half-butterfly structure with the platinum interacting with one of the boranthracene rings more than the other, leaning 73.6° towards one side and 119.2° away from the other (Figure 3-3, Figure 3-4). The Pt-P bonds ($d_{Pt-P}$ = 2.2505(3), 2.2988(5) Å) and Pt-B bonds ($d_{Pt-B}$ = 2.331(1), 2.317(1) Å) are also more assymetric and slightly tighter than **1**. The break from planarity at boron however remains subtle ($\Sigma\measuredangle$ C-B-C = 357.1, 355.5°).

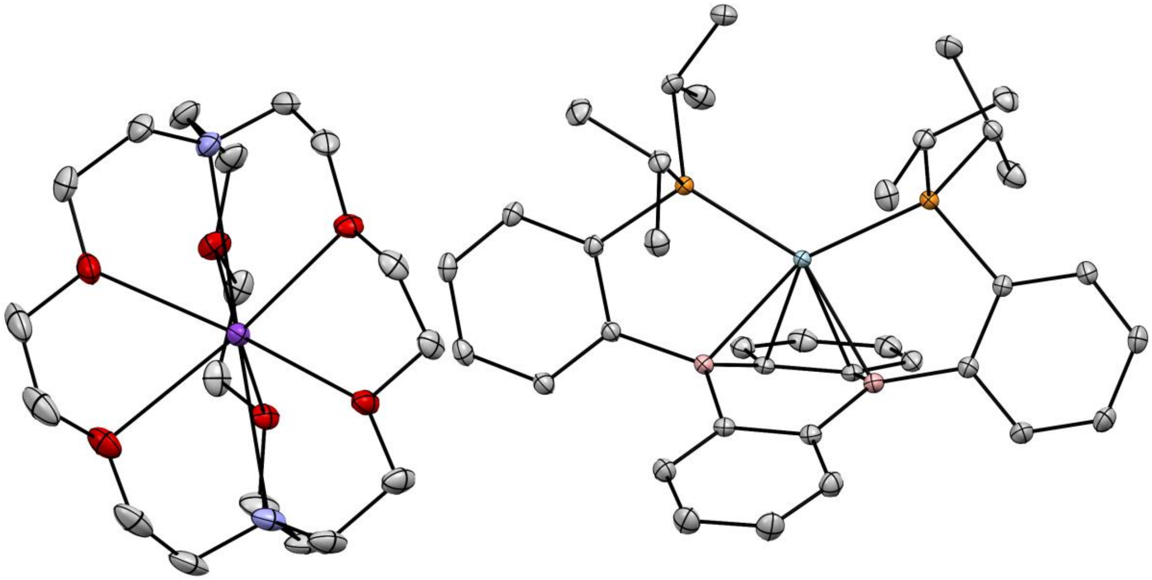

Figure 3-3. Thermal ellipsoid plots (50% probability) of the solid-state structure of [$K^+$krypt]$PtB_2P_2$ (**2**). Light blue, pink, orange, red, purple, lavender, and gray ellipsoids represent Pt, B, P, O, K, N, and C atoms, respectively. Hydrogen atoms and co-crystallized solvent molecules are omitted for clarity.

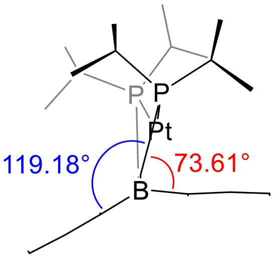

Figure 3-4. Side-on view of [$K^+$krypt]$PtB_2P_2$ (**2**).

X-band electron paramagnetic resonance (EPR) spectrum of **2** in fluid toluene revealed an isotropic signal centered at g ~ 2, which appeared to be a mixture of two slightly different spin systems in a 0.64:0.36 ratio in solution (Figure 3-5). Both spin systems have $^{195}$Pt ($I = ½$, $A_{iso}(^{195}Pt) = 2099, 2647$ MHz) and $^{31}$P ($I = ½$, $A_{iso}(^{31}P) = 65, 45$ MHz) hyperfine interactions. These two different spin systems could be explained by a mixture of $\eta^2$ and $\eta^4$ Pt species at room temperature. However upon cooling, the spectrum became more complex and we were unable to simulate a satisfory result (Figure 3-29).

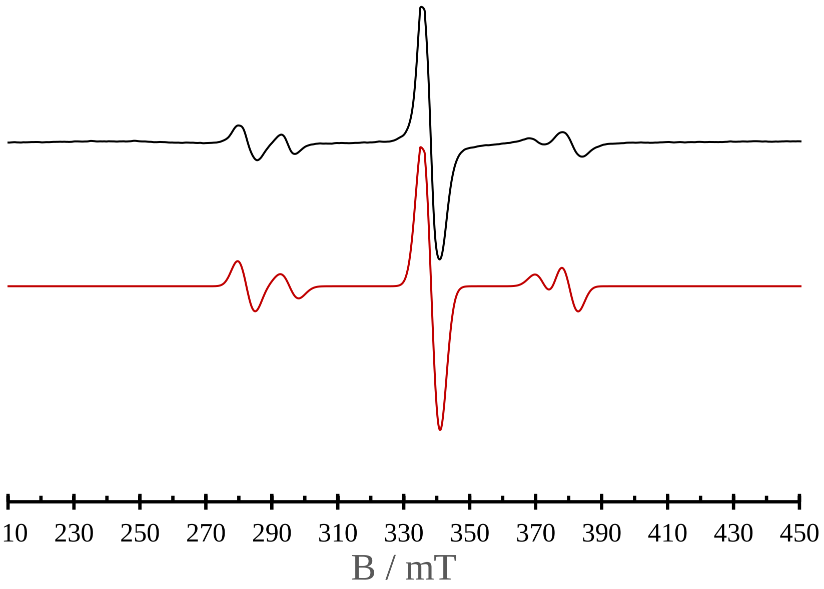

Figure 3-5. X-band EPR spectrum (9.318 GHz) of [$K^+$krypt]$PtB_2P_2$ **(2)** in toluene at 298 K (black) and its simulated spectrum (red). The simulated spectra was produced by a combination of two spin-systems (S = ½) in a 0.64:0.36 ratio. Simulation parameters: spin-system 1: g = 1.968, A[Pt] = 2647 MHz, A[P] = 65 MHz, weight = 0.64, lw = 4.7; spin-system 2: g = 1.968, A[Pt] = 2099 MHz, A[P] = 48 MHz, weight = 0.36, lw = 5.8.

Chemical reduction of **1** using 2 equivalents of potassium naphthalenide produced a soluble unchelated platinum dianion that could be isolated as an amorphous brown powder. Upon reduction, the $^{31}P$ NMR signal was shifted significantly downfield from 44.0 ppm ($J_{Pt-P}$ = 4997 Hz) in complex **1** to 85.1 ppm ($J_{Pt-P}$ = 1198 Hz). The $^{11}B$ signal shifted in the opposite direction from 29.2 ppm in complex **1** to 6.2 ppm with apparant coupling to platinum ($J_{Pt-B}$ = 284 Hz). (Figure 3-17, Figure 3-18). Unfortunately, we were unable to detect any $^{195}Pt$ signal from +1386 through −8394 ppm using a saturated $C_6D_6$ sample collecting 1024 scans per ~700 ppm block (Figure 3-6), or by using $^{195}$Pt-$^{1}$H HMBC with the methylene protons of the isopropyl groups.

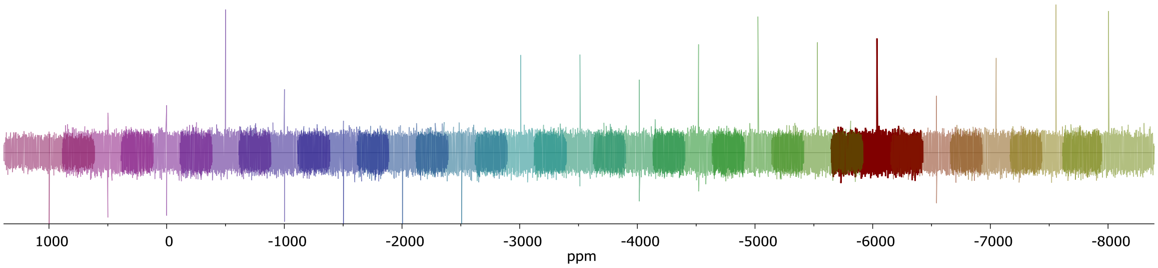

Figure 3-6. $^{195}$Pt NMR window: only artifacts detected.

To obtain crystalline material we added 1 equivalent of kryptofix 222 and excess of DME providing the 2-electron reduced species **3** as an auburn-red crystalline solid. The preliminary solid state structure of **3** features a significantly puckered diboraanthracene ring with short Pt–B contacts of ~2.5 Å. The reduced stability and solubility of this complex in solution resulted in lower resolution NMR characterization, however the chemical shifts are very comparable to what we observed in absence of the cryptand ($^{31}$P $\delta$ = 81 ppm, $^{11}$B $\delta$ = 8 ppm). No $^{195}$Pt coupling was resolved in either the $^{31}$P or the $^{11}$B spectrum.

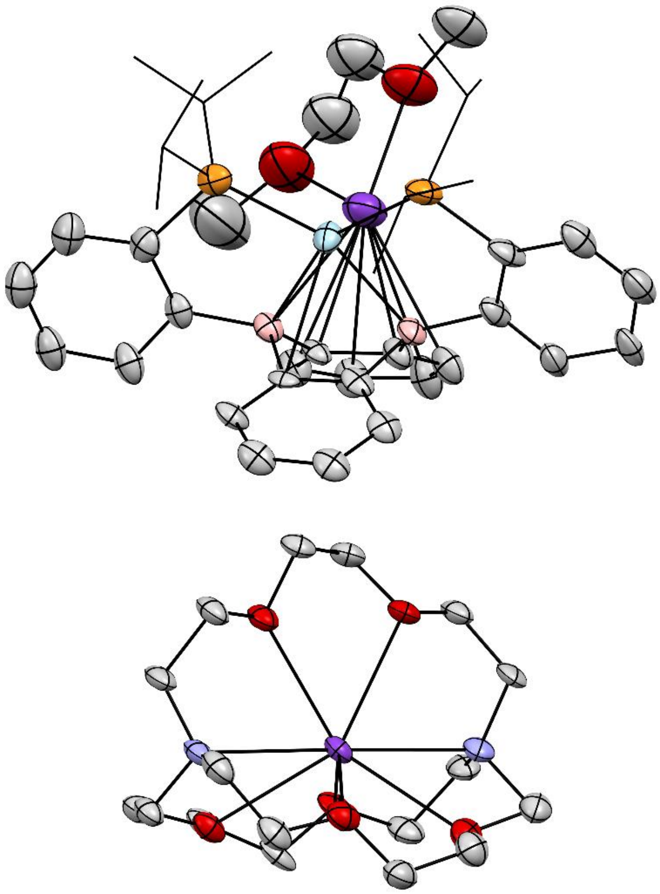

Figure 3-7. Thermal ellipsoid plots (50% probability) of the solid-state structure of [$K^+$ krypt, $K^+$ dme]$PtB_2P_2$ (**3**). Light blue, pink, orange, red, purple, lavender, and gray ellipsoids represent Pt, B, P, O, K, N, and C atoms, respectively. Hydrogen atoms and co-crystallized solvent molecules are omitted for clarity.

The doubly kryptofix 222-chelated species can also be produced by simply adding two equivalents of kryptofix 222, generating **4** as auburn-red crystals. The decreased solubility and sensitivity of this compound limited the solvent choices available for recrystallization. The complete solution to this XRD structure is still in progress (Figure 3-8). Furthermore, this complex has limited stability in solution resulting in low resolution characterization by NMR. The $^{31}P$ and $^{11}B$ shifts were nearly identical to **3** at $\delta = 81$ ppm and 6 ppm, respectively.

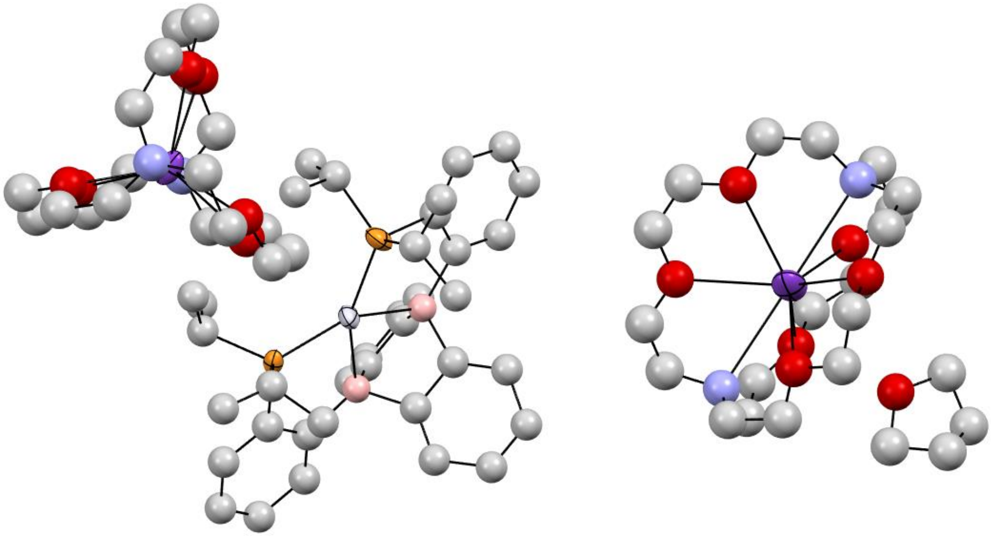

Figure 3-8. Thermal ellipsoid plots (50% probability) of the solid-state structure of [$K^+{}_2$krypt$_2$]Pt$B_2P_2$ (**4**). Light blue, pink, orange, red, purple, lavender, and gray ellipsoids represent Pt, B, P, O, K, N, and C atoms, respectively. Hydrogen atoms and co-crystallized solvent molecules are omitted for clarity.

## *Conclusion*

Herein we were able to isolate and characterize the first molecular Pt(−1) and Pt(−2) species using a redox-active ligand scaffold. While the boroaanthracene core acts as an electron reservoir, significant radical character is placed on the platinum center as indicated by EPR. Upon further reduction to a formally Pt(−2) species, complex **4** can be described as either having two two-center, two-electron (2c-2e) bonds or as a single three-center, two-electron (3c-2e) bond. Using the isolobal analogy of borohydride, we favor the latter explanation as platinum is more electronegative than hydrogen ($\chi_{Pt} = 2.28$, $\chi_H = 2.20$ on the Pauling Scale). However, DFT calculations to further clarify the bonding in **2** and **4** are currently underway.

### *Experimental Section*

General Considerations: Unless stated otherwise, all compounds were purchased from commercial sources and used without further purification. Solvents were dried and deoxygenated by argon sparge followed by passage through an activated alumina column and were stored over 4 Å molecular sieves. All manipulations were performed under an $N_2$ atmosphere either in a glovebox or using standard Schlenk techniques. $B_2P_2$ was synthesized according to literature procedures.[5] $^1H$ NMR spectra were recorded at 298 K using Bruker 400 and 600 MHz instruments. Chemical shifts are referenced to residual solvent peaks, IR spectra were recorded using a Bruker Alpha FT-IR with a universal sampling module collecting at 4 $cm^{-1}$ resolution with 32 scans. EPR X-band spectra were recorded using a Bruker EMX spectrometer and analyzed using Win-EPR software. UV-Vis spectra were recorded using a Cary Bio 500 spectrometer using a 1 cm path length quartz cuvette with a solvent background subtraction applied. X-ray diffraction studies were performed using a Bruker-AXS diffractometer. Cyclic Voltammetry experiments were performed using a Pine AFP1 potentiostat. The cell consisted of a glassy carbon working electrode, a Pt wire auxiliary electrode and a Pt wire pseudo-reference electrode. All potentials are referenced vs. the $Fc/Fc^+$ couple measured as an internal standard. Elemental Analyses were performed by Midwest Microlab. Solution phase effective magnetic moments were obtained via the method described by Evans[14,15] and were performed in triplicate. Standard deviations are reported.

**$PtB_2P_2$ (1).**

$B_2P_2$ (365 mg, 0.651 mmol), Pt(ethylene)($PPh_3$)$_2$ (487 mg, 0.651 mmol), and 15 mL of toluene were combined in a schlenk flask. The flask was open to $N_2$ and heated for 50°C for 3 days. The resulting yellow suspension was filtered to remove trace particulates. The filtrate was concentrated *in vacuo* to 2 mL. Pentane (4 mL) was added, precipitating a pale yellow amorphous solid. The solid was removed by filtration. Another 4 mL of pentane was added to this new filtrate, producing yellow microcrystals. These crystals were removed by filtration. This third filtrate was then allowed to stand at room temp for 16 hours, producing large, orange, elongated hexagons. The hexagonal crystals were rinsed with pentane and recrystalized with toluene/hexane to obtain EA purity material. Overall yield: 240 mg (49%). $^1$H NMR (600 MHz, $C_6D_6$): δ 8.14 (d, $J$ = 7.3 Hz, 2H), 7.55 (dd, $J$ = 5.9, 3.3 Hz, 4H), 7.50 (t, $J$ = 7.4 Hz, 2H), 7.34 (t, $J$ = 6.6 Hz, 2H), 7.24 (t, $J$ = 7.7 Hz, 2H), 7.03 (dd, $J$ = 6.1, 3.2 Hz, 4H), 2.10 (h, $J$ = 13.9 Hz, 2H), 2.08 (h, $J$ = 13.5 Hz, 2H), 0.71 (d, $J$ = 6.8 Hz, 6H), 0.69 (d, $J$ = 7.1 Hz, 6H), 0.59 (d, $J$ = 7.4 Hz, 6H), 0.57 (d, $J$ = 7.2 Hz, 6H). $^{13}$C NMR (151 MHz, $C_6D_6$) δ 159.7, 147.5 (d, $J$ = 24.7 Hz), 147.3 (d, $J$ = 24.9 Hz), 132.7 (t, $J$ = 12.3 Hz), 132.3, 131.6 (t*, $J$ = 13.1 Hz), 130.3, 126.3, 125.3 (t*, $J$ = 3.6 Hz), 28.6 (t, $J$ = 12.7 Hz), 28.6 (dt, $J$ = 77.8, 12.8 Hz), 19.4, 18.5 (t, $J$ = 24.7 Hz). $^{31}$P NMR (162 MHz, $C_6D_6$) δ 44.0 (s), 44.0 (d, $J$ = 4997 Hz). $^{11}$B NMR (128 MHz, $C_6D_6$) δ 29.20. $^{195}$Pt NMR (128 MHz, $C_6D_6$) δ −5456 (t, $J$ = 4997 Hz). UV-Vis (THF): $\lambda_{max}$ nm ($\varepsilon_{max}$ M$^{-1}$ cm$^{-1}$) 404 (sh, 1.7 × 10$^3$). Calc. for $C_{36}H_{44}B_2P_2Pt$: C: 57.24; H: 5.87. Found: C: 57.16; H: 5.88.

**Kkrypt [$PtB_2P_2$] (2).**

$PtB_2P_2$ (64 mg, 0.085 mmol), potassium naphthalenide · ½ THF (20 mg, 0.098 mmol), and 4 mL of toluene were combined in a vial at room temp. The suspension was stirred for 30 minutes and then promptly filtered. The solvent was removed *in vacuo*, producing a dark amber glaze. The glaze was washed with pentane (3×2 mL), then extracted with ether (5 mL). The ether extract was filtered directly into a vial containing kryptofix 222 (47 mg, 0.125 mmol), crashing out a dull eggplant precipitant. This solid was washed with ether (3×2 mL), then toluene (3×2 mL). The solid was extracted with THF (5 mL), concentrated *in vacuo* to 1 mL, and layered with ether (1 mL), and allowed to cool at −19°C overnight, producing deep red-purple crystals. Overall yield: 71 mg (72%). $^1$H NMR ($d_8$-THF): only residual solvent peaks. Evans Method (THF): $\mu_B$ 2.8 ± 0.2. UV-Vis (THF): $\lambda_{max}$ nm ($\varepsilon_{max}$ $M^{-1}$ $cm^{-1}$) 691 (sh, $3.4 \times 10^2$), 517 (sh, $7.6 \times 10^2$), 417 (p, $2.3 \times 10^1$). Calc. for $C_{54}H_{80}B_2KN_2O_6P_2Pt$: C: 55.39; H: 6.89; N: 2.39. Found: C: 55.58; H: 6.75; N: 2.55.

**Kkrypt Kdme[$PtB_2P_2$] (3).**

$PtB_2P_2$ (16 mg, 0.021 mmol), potassium naphthalenide · ½ THF (9.2 mg, 0.045 mmol), and 2 mL of toluene were combined in a vial at room temp. The suspension was stirred for 30 minutes and then promptly filtered. The solvent was removed *in vacuo*, producing a dark amber glaze. The glaze was taken up into ether (1 mL), then crashed back out as an amorphous solid using pentane (5 mL). This brown solid was collected and washed with pentane (2 x 3 mL). The amorphous solid was redissolved in minimal DME and filtered directly into a vial containing kryptofix 222 (21 mg, 0.056 mmol) dissolved in ether (1 mL) and DME (0.5 m), producing a black-blue precipitate. This solid was washed with ether (3×2 mL). Minimal THF was added to the solid to redissolve it (0.5 mL), on standing crystals formed. This material can be recrystallized with with THF/ether. Overall yield: 23 mg (83%).

**$[PtB_2P_2]^{2-}$ ("brown solid")**

$^1$H NMR (600 MHz, $C_6D_6$): δ7.96 (s, 2H), 7.78 (s, 2H), 7.56 (s, 2H), 7.38 (s, 2H), 6.63 (s, 4H), 6.42 (s, 4H), 2.34 (s, 4H), 1.03 (s, 12H), 0.84 (s, 12H). $^{13}$C NMR (151 MHz, $C_6D_6$) δ 176.29, 170.99, 147.91, 133.49, 130.98, 124.31, 123.28, 120.90, 27.51, 21.02, 20.38. $^{31}$P NMR (243 MHz, $C_6D_6$) δ 85.14 (s), 85.14 (d, *J* = 1197.6 Hz). $^{11}$B NMR (192 MHz, $C_6D_6$) δ 6.18 (s), 6.18 (d, *J* = 284.2 Hz).

**After completing prep with kryptofix:**

$^1$H NMR (600 MHz, $C_6D_6$) δ 8.22 (d, *J* = 7.2 Hz, 2H), 7.70 (d, *J* = 7.5 Hz, 2H), 7.59 (t, *J* = 7.1 Hz, 2H), 7.32 (t, *J* = 7.6 Hz, 2H), 6.75 (s, 4H), 6.43 (s, 4H), 3.53 (s, 4H), 3.09 (s, 6H), 3.01 (s, 6H), 2.56 (s, 2H), 2.47 (s, 2H), 2.05 (s, 6H), 1.39 (s, 6H), 1.31 – 1.27 (m, 6H), 1.24 – 1.17 (m, 12H), 1.08 – 1.00 (m, 6H). $^{31}$P NMR (243 MHz, $C_6D_6$) δ 81.34. $^{11}$B NMR (192 MHz, $C_6D_6$) δ 8.02. Calc. for $C_{58}H_{90}B_2K_2N_2O_8P_2Pt$: C: 53.58; H: 6.98; N: 2.15. Found: C: 53.94; H: 7.01; N: 2.42.

**$K_2$ krypt$_2$ $[PtB_2P_2]$ (4).**

$PtB_2P_2$ (20 mg, 0.026 mmol), potassium naphthalenide · ½ THF (12.5 mg, 0.061 mmol), and 2 mL of toluene were combined in a vial at room temp. The suspension was stirred for 30 minutes and then promptly filtered. The solvent was removed *in vacuo*, producing a dark amber glaze. The glaze was taken up into ether (1 mL), then crashed back out as an amorphous solid using pentane (5 mL). This brown solid was collected and washed with pentane (2 x 3 mL). The amorphous solid was redissolved in ether and filtered directly into a vial containing kryptofix 222 (21 mg, 0.056 mmol) dissolved in ether (1 mL) and DME (0.5 m), producing a black-blue precipitate. This solid was washed with ether (3×2 mL). Minimal THF was added to the solid to redissolve it (0.5 mL), on standing crystals formed. This material can be recrystallized with with THF/ether. Overall yield: 33 mg (78%). $^{31}$P NMR (243 MHz, *d₈*-THF) δ 81.03. $^{11}$B NMR (192 MHz, *d₈*-THF) δ 5.96. UV-Vis (THF): $\lambda_{max}$ nm ($\varepsilon_{max}$ M$^{-1}$ cm$^{-1}$) 693 (sh, $4.1 \times 10^2$), 515 (sh, $1.1 \times 10^3$), 430 (p, $1.4 \times 10^3$). Calc. for $C_{72}H_{116}B_2K_2O_{12}P_2Pt$: (½ × $C_6H_{14}$): C: 55.03; H: 7.54; N: 3.38. Found: C: 55.01; H: 6.87; N: 3.13.

## *NMR Spectra*

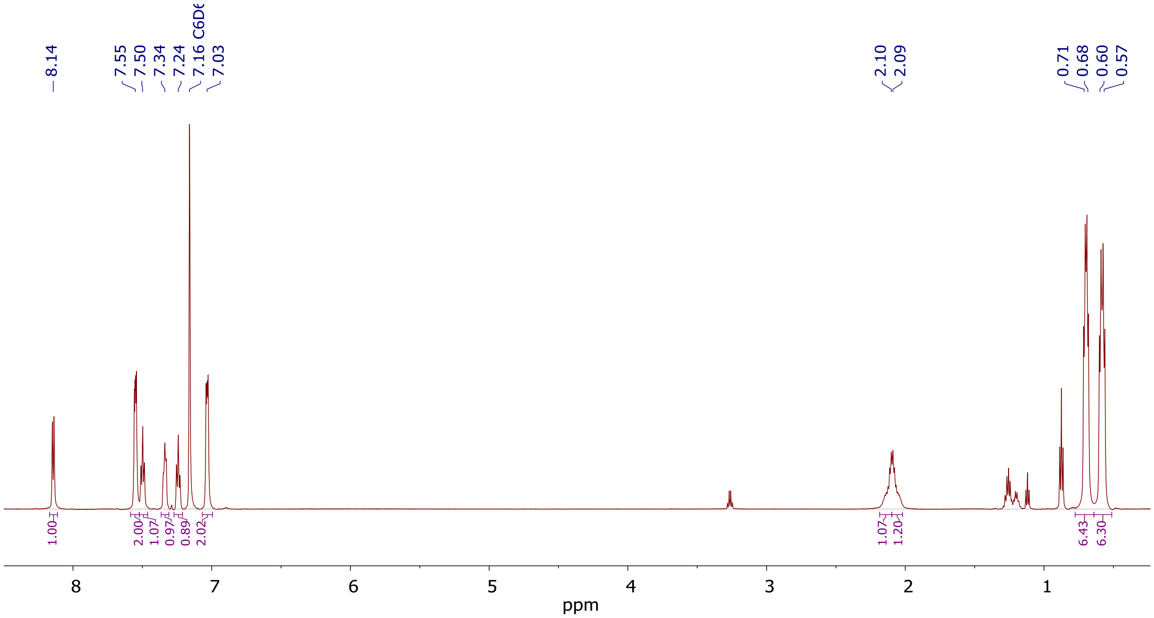

Figure 3-9. $^1$H NMR spectrum of **PtB$_2$P$_2$** recorded at 600 MHz in $C_6D_6$.

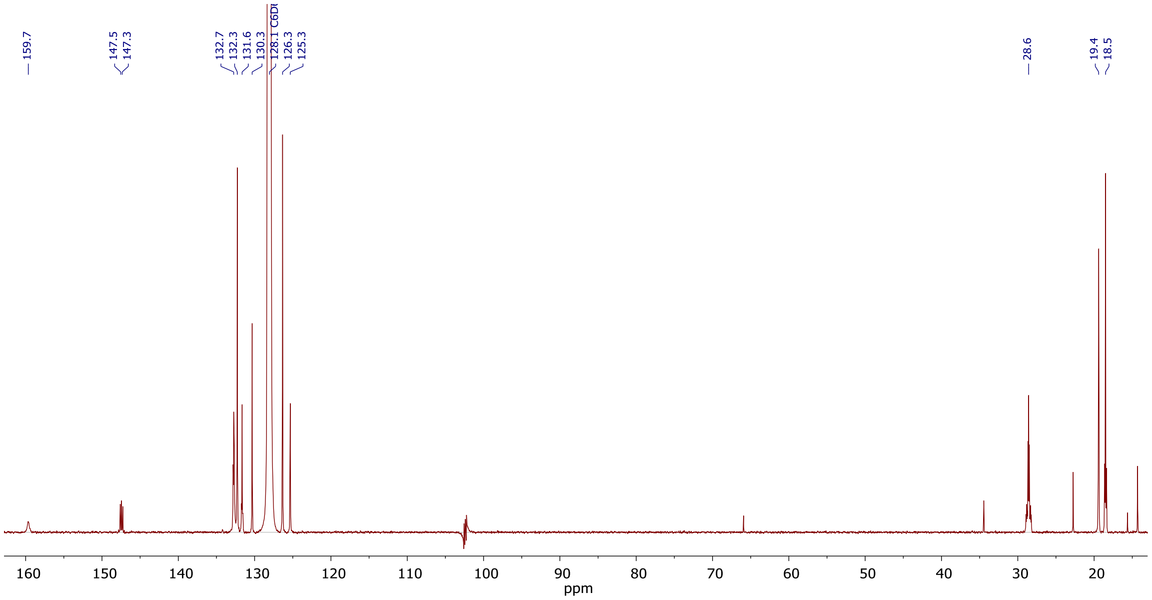

Figure 3-10. $^{13}$C NMR spectrum of **PtB2P2** recorded at 151 MHz in $C_6D_6$.

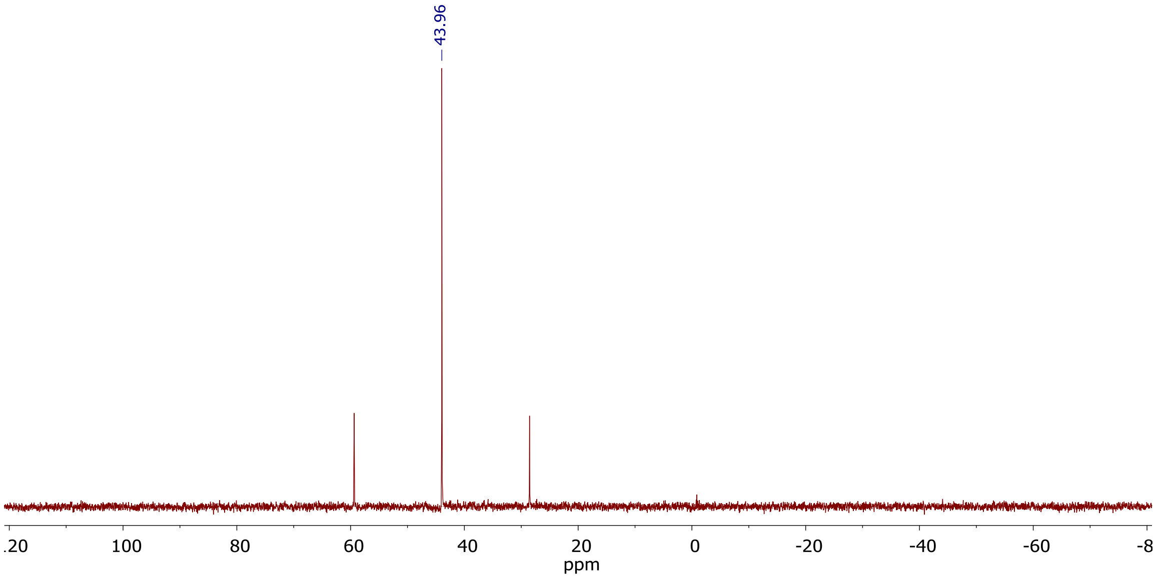

Figure 3-11. $^{31}$P NMR spectrum of **PtB2P2** recorded at 243 MHz in $C_6D_6$.

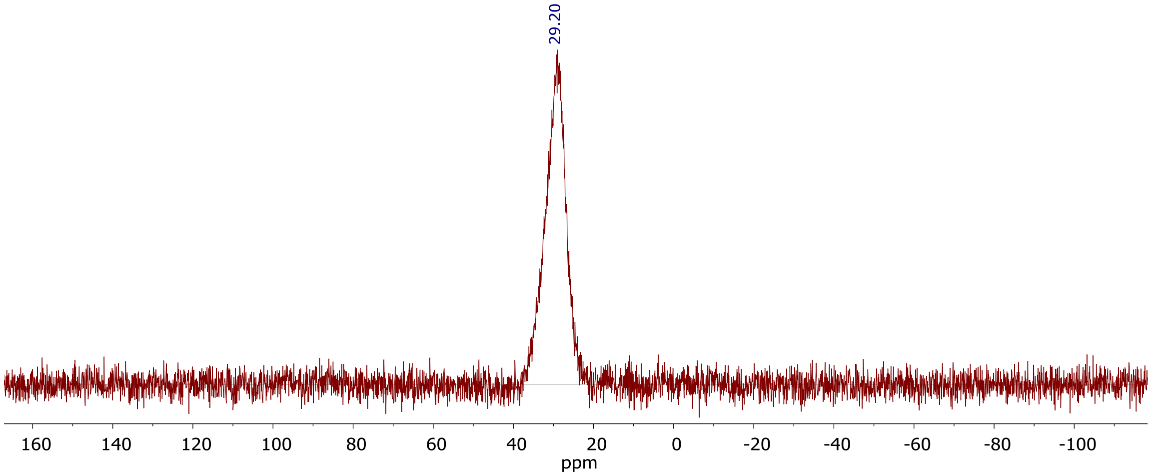

Figure 3-12. $^{11}$B NMR spectrum of **PtB2P2** recorded at 128 MHz in $C_6D_6$.

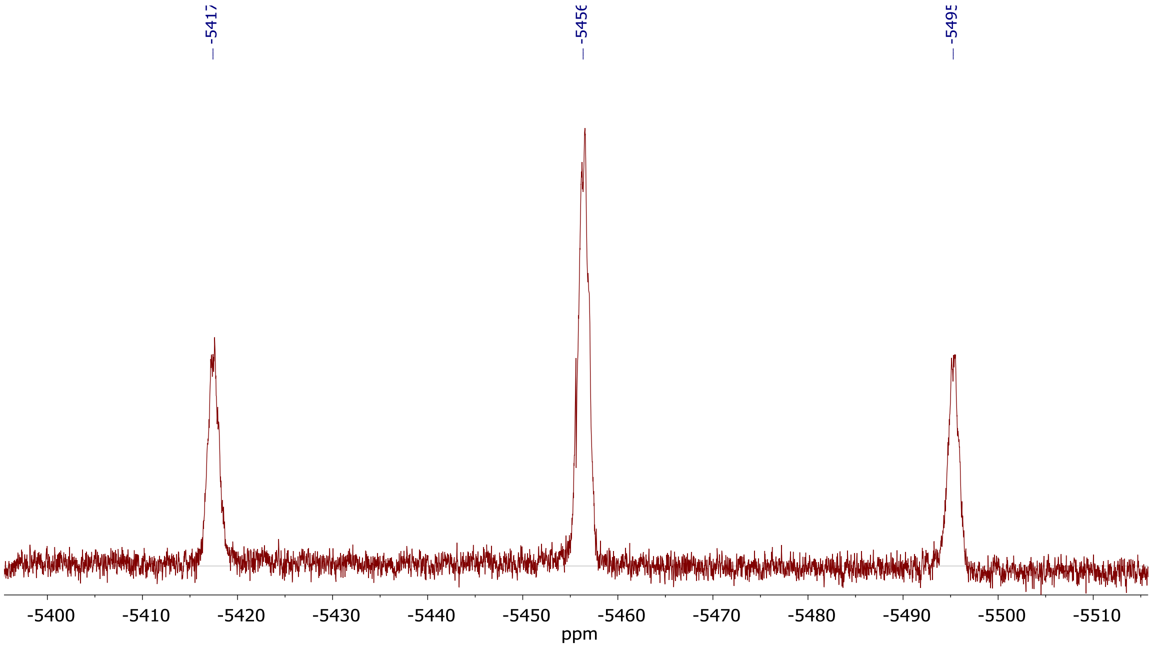

Figure 3-13. $^{195}$Pt NMR spectrum of **PtB$_2$P$_2$** recorded at 128 MHz in $C_6D_6$.

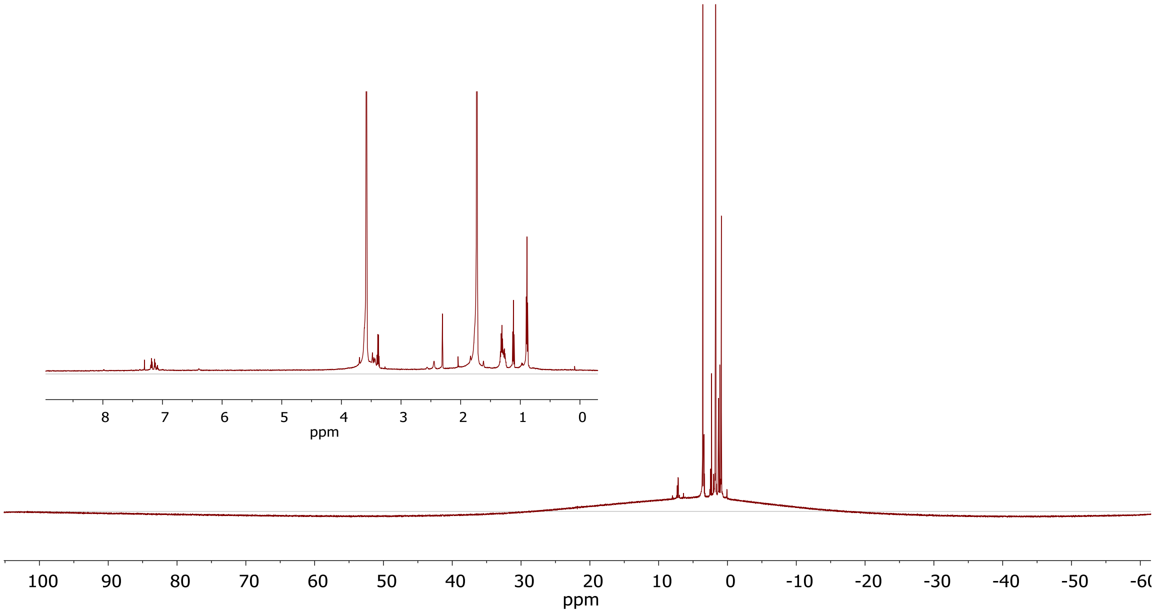

Figure 3-14. $^1$H NMR spectrum of **Kkrypt [PtB$_2$P$_2$]** recorded at 600 MHz in $d_8$-THF.

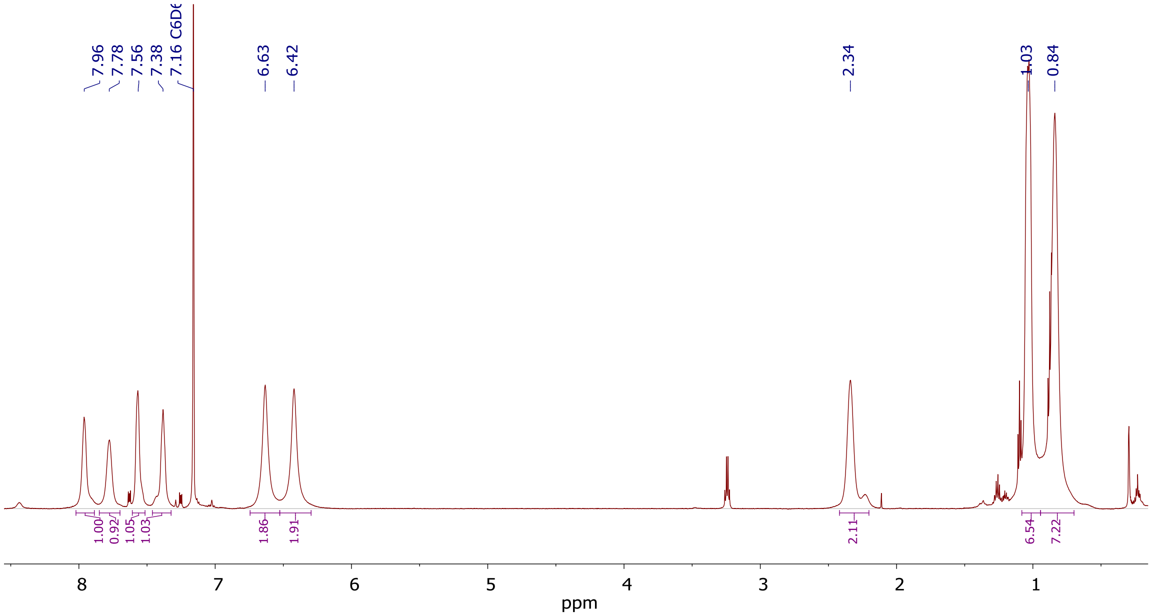

Figure 3-15. $^1$H NMR spectrum of **“brown solid”** recorded at 600 MHz in $C_6D_6$.

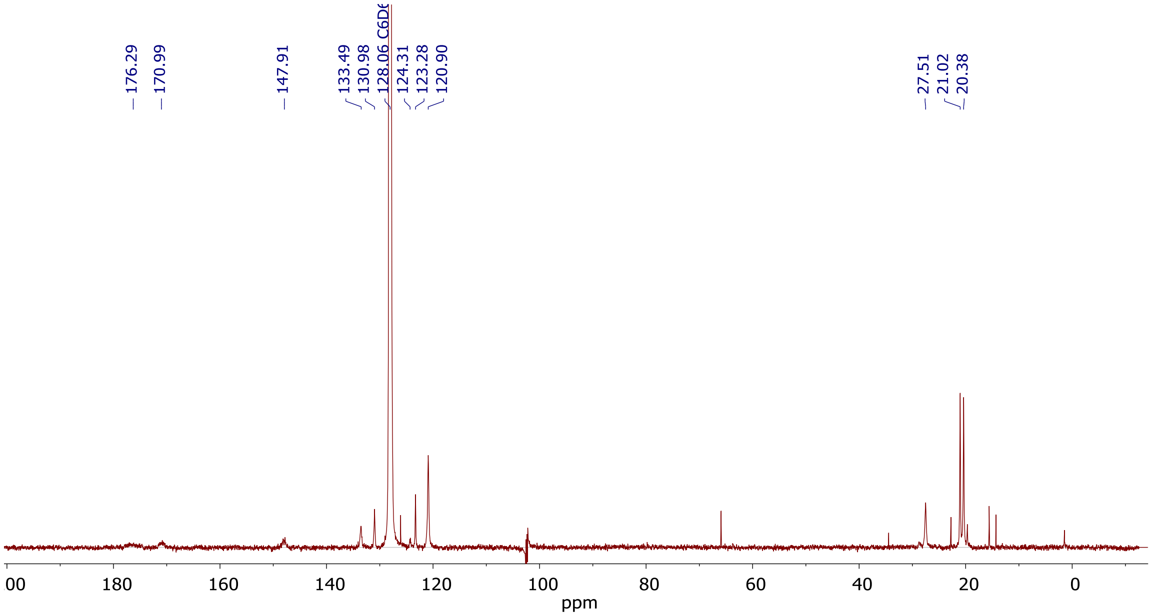

Figure 3-16. $^{13}$C NMR spectrum of **“brown solid”** recorded at 151 MHz in $C_6D_6$.

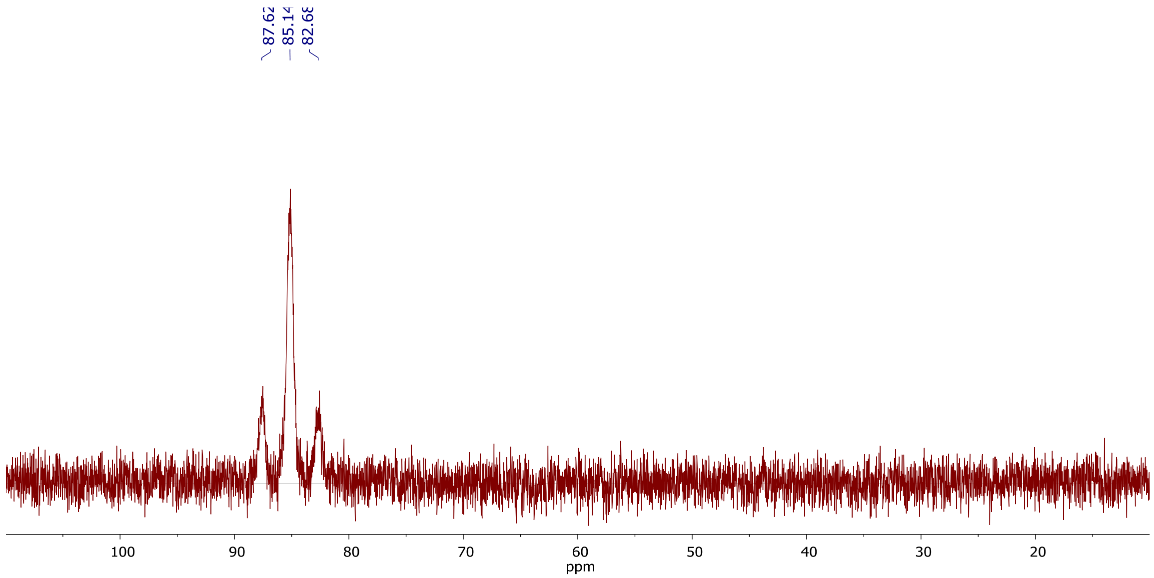

Figure 3-17. $^{31}P$ NMR spectrum of **“brown solid”** recorded at 243 MHz in $C_6D_6$.

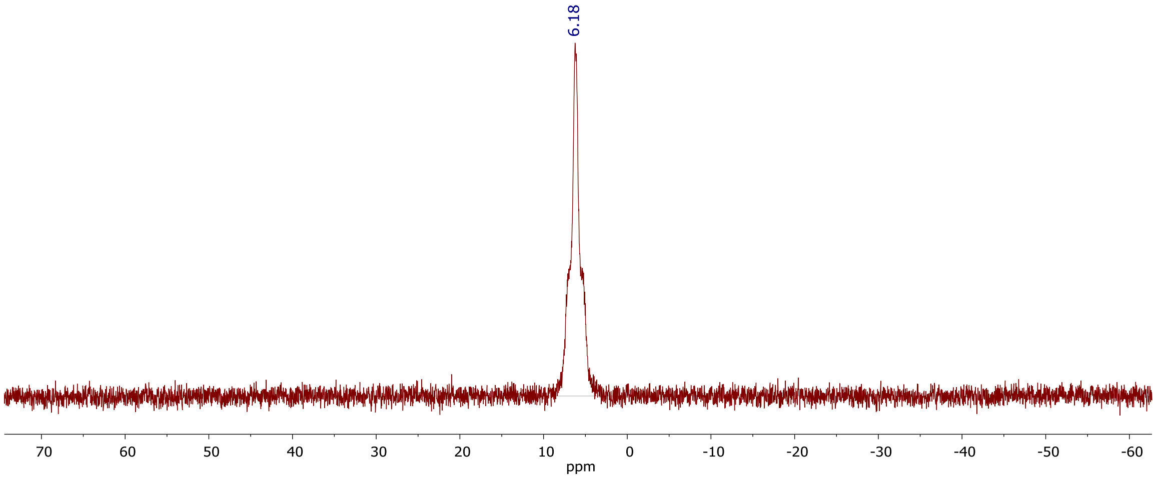

Figure 3-18. $^{11}B$ NMR spectrum of **“brown solid”** recorded at 192 MHz in $C_6D_6$.

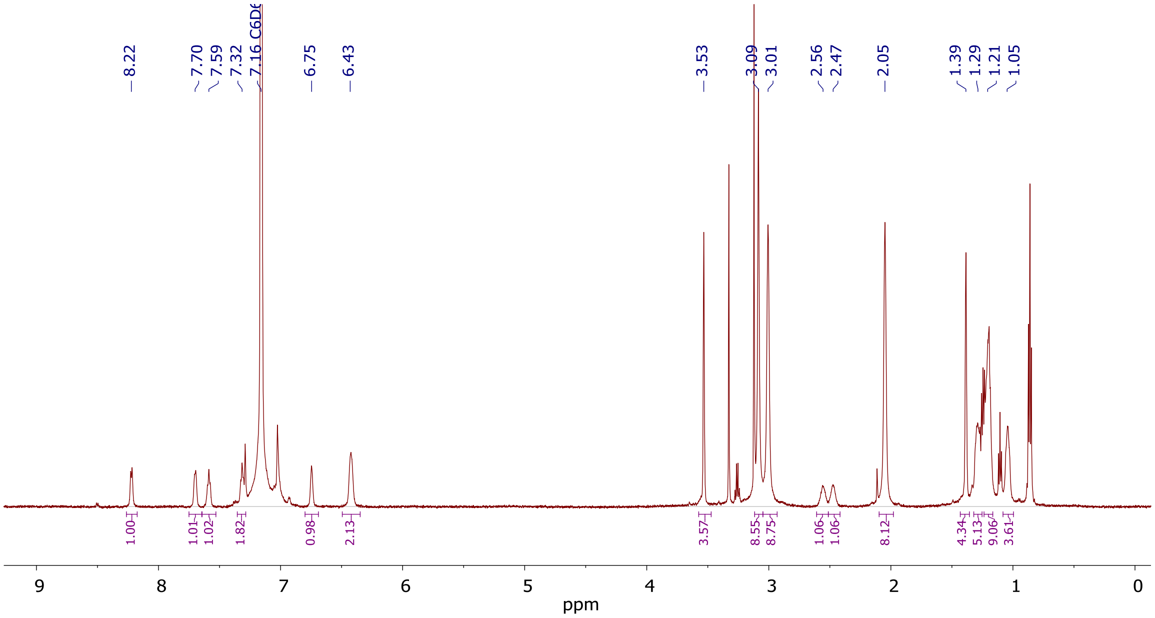

Figure 3-19. $^{1}$H NMR spectrum of **Kkrypt Kdme** [**PtB$_2$P$_2$]** recorded at 600 MHz in $C_6D_6$.

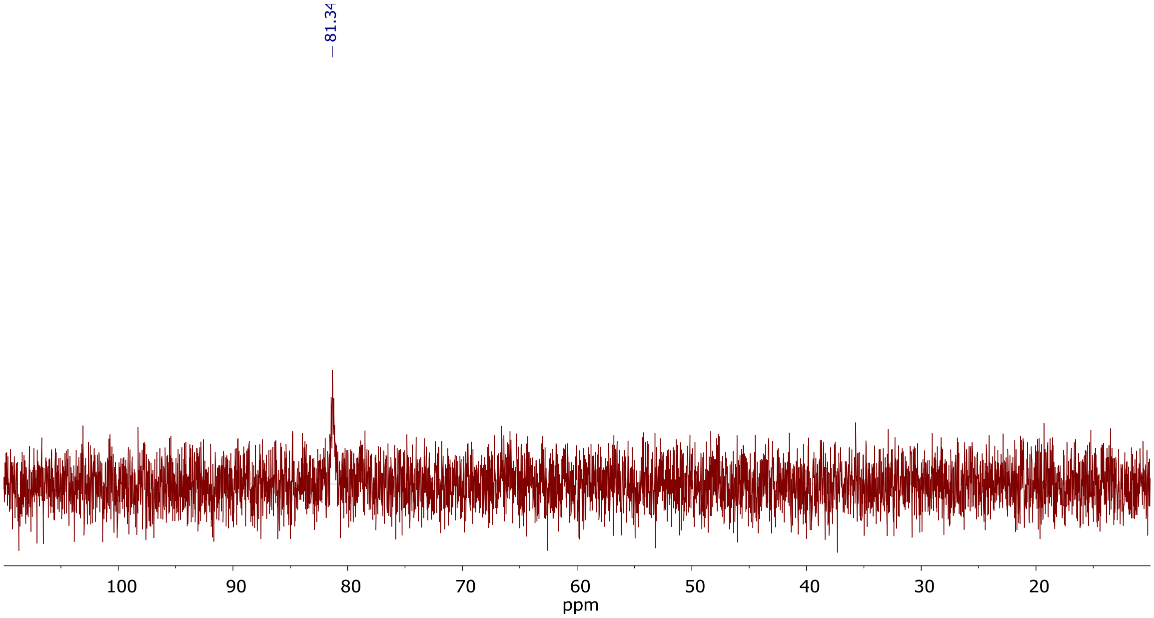

Figure 3-20. $^{31}$P NMR spectrum of **Kkrypt Kdme [PtB$_2$P$_2$]** recorded at 243 MHz in $C_6D_6$.

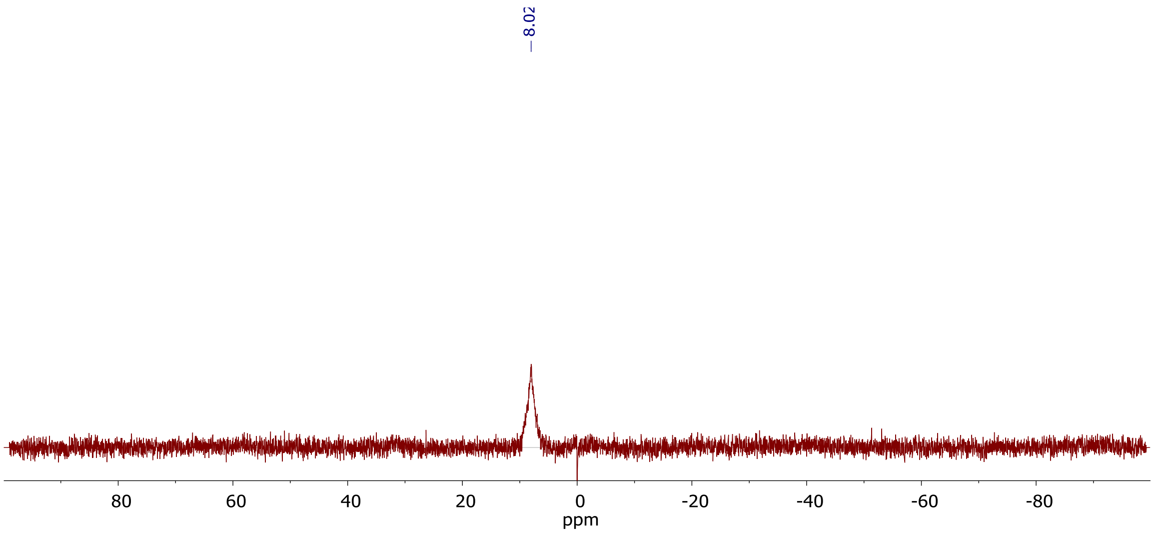

Figure 3-21. $^{11}$B NMR spectrum of **Kkrypt Kdme [PtB$_2$P$_2$]** recorded at 192 MHz in $C_6D_6$.

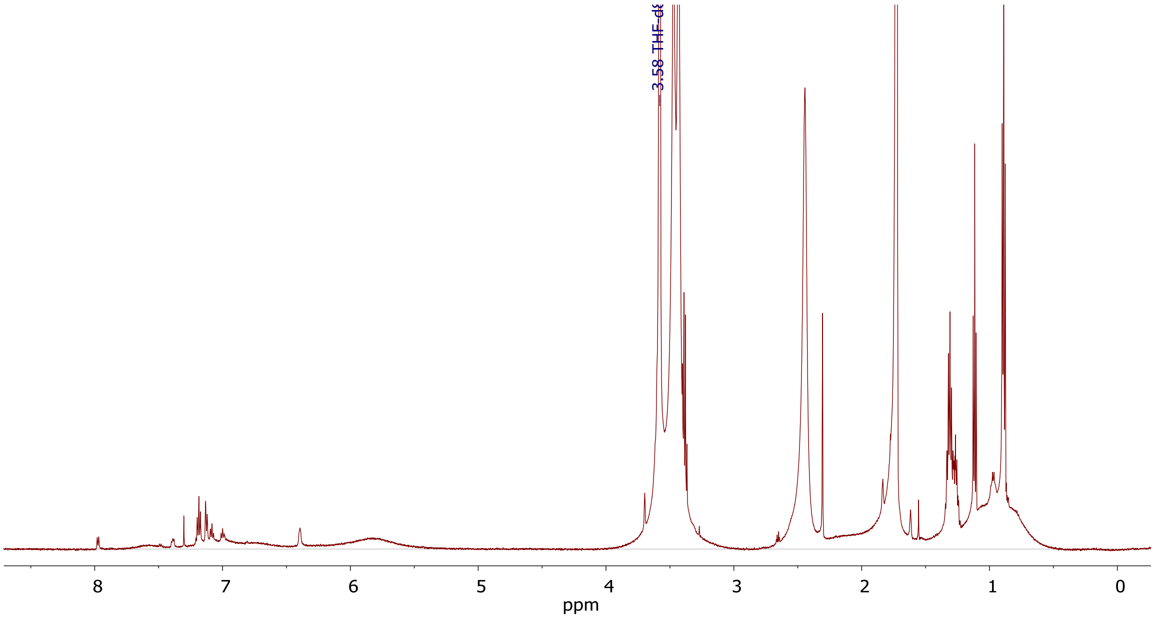

Figure 3-22. $^{1}$H NMR spectrum of **K$_2$ krypt$_2$ [PtB$_2$P$_2$]** recorded at 600 MHz in $d_8$-THF.

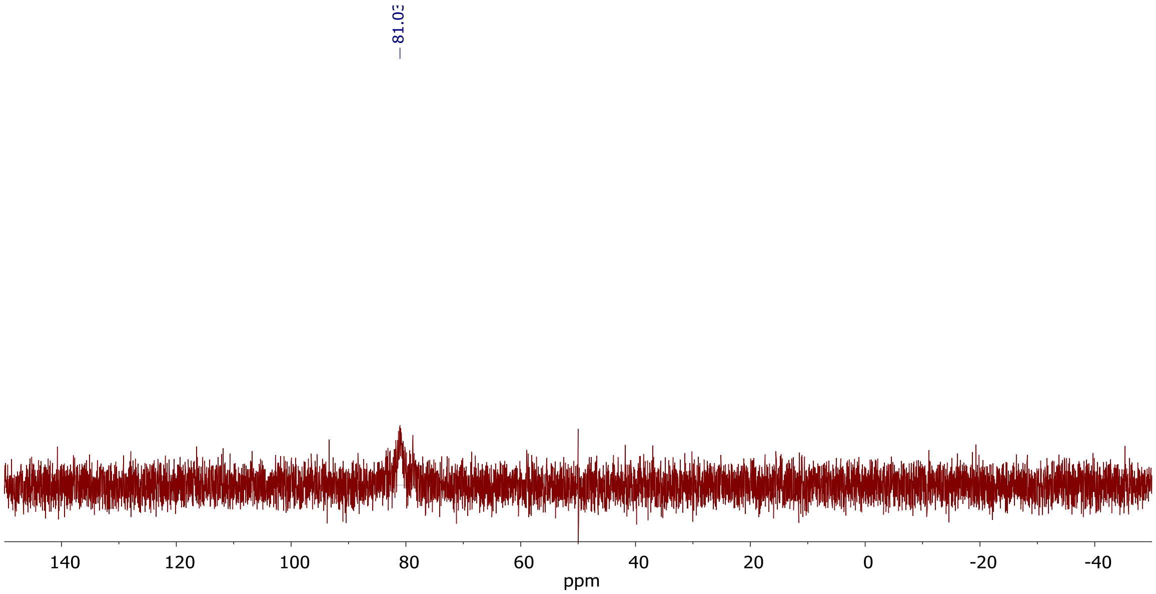

Figure 3-23. $^{31}$P NMR spectrum of **K$_2$ krypt$_2$ [PtB$_2$P$_2$]** recorded at 243 MHz in *d$_8$*-THF.

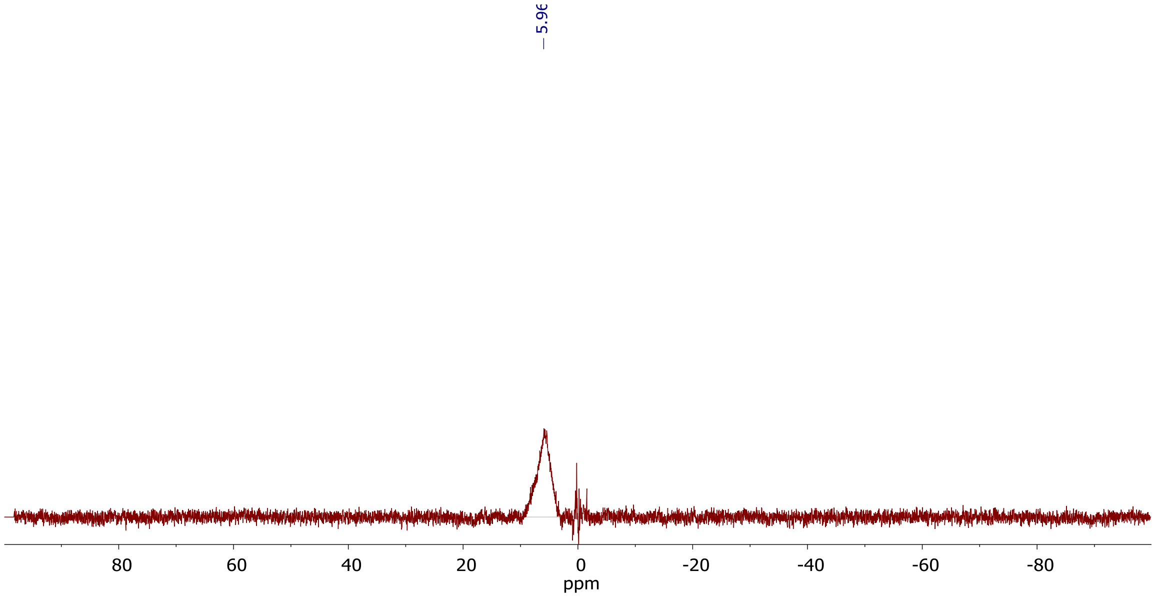

Figure 3-24. $^{11}$B NMR spectrum of **K$_2$ krypt$_2$ [PtB$_2$P$_2$]** recorded at 192 MHz in *d$_8$*-THF.

### *UV-Vis*

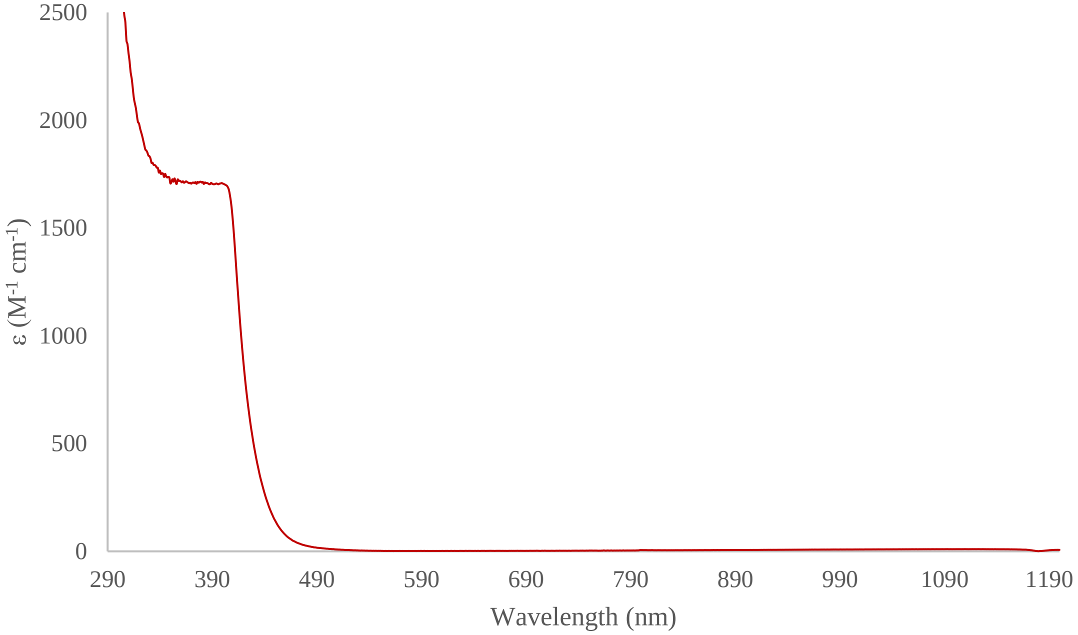

Figure 3-25. UV-Vis-NIR spectra of **Pt(B2P2)** in THF.

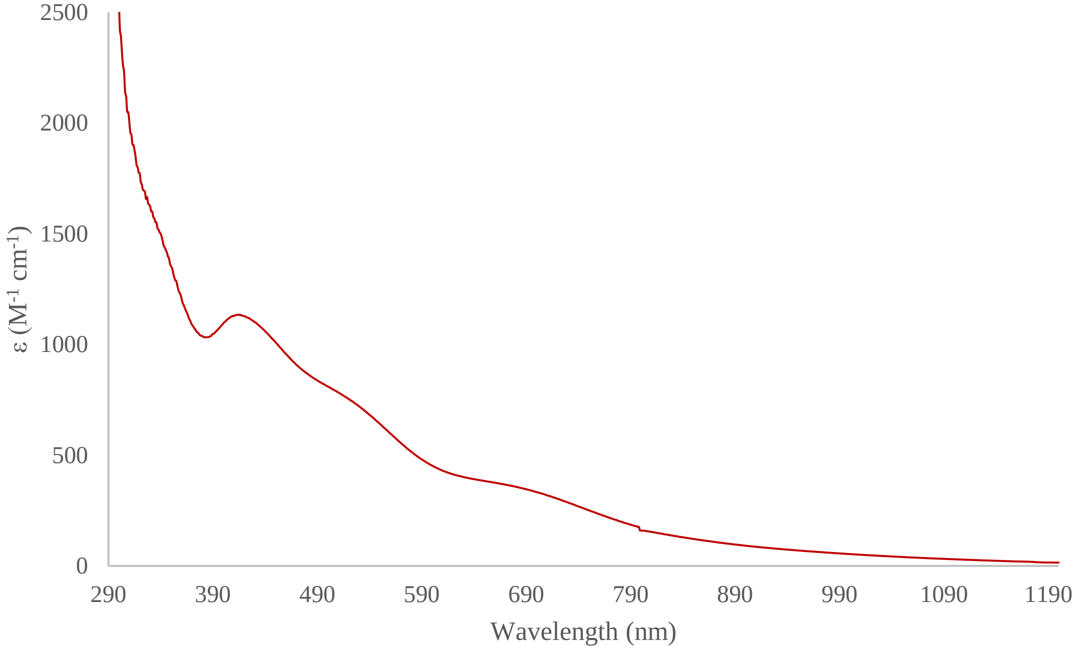

Figure 3-26. UV-Vis-NIR spectra of [**Pt(B2P2)**]$^{1-}$ in THF.

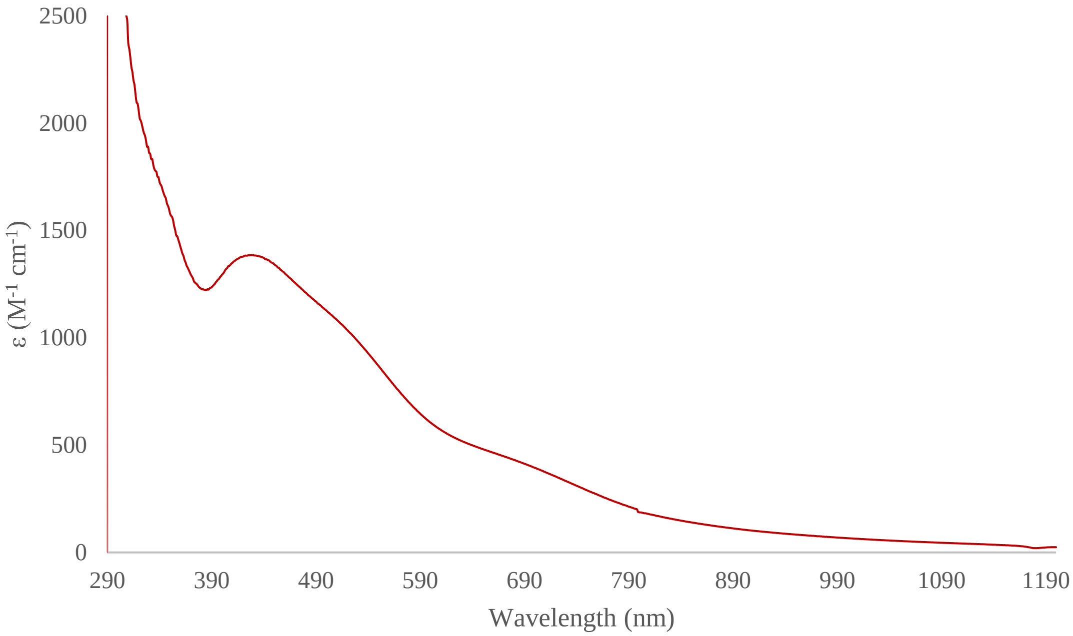

Figure 3-27. UV-Vis-NIR spectra of **K2krypt2[Pt(B2P2)]** in THF.

*EPR*

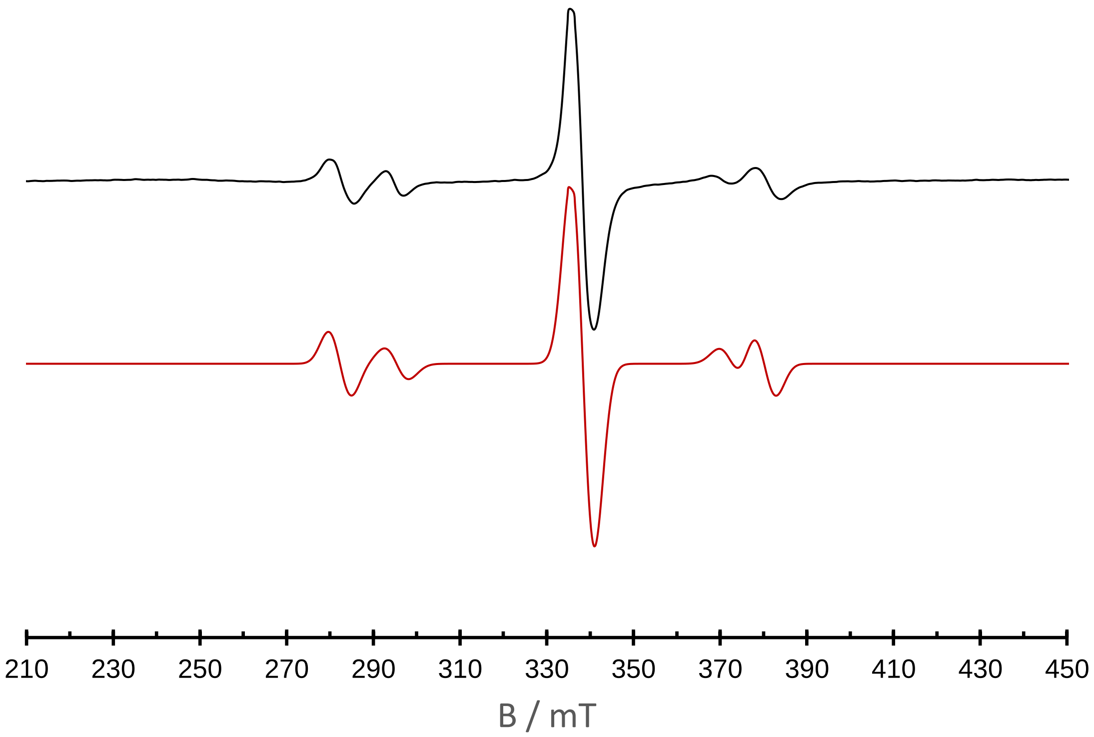

Figure 3-28. X-band EPR spectrum (9.318 GHz) of **Kkrypt[PtB2P2]** in toluene at 298 K (black) and its simulated spectrum (red). The simulated spectra was produced by a combination of two spin-systems (S = ½) in a 0.64:0.36 ratio. Simulation parameters: spin-system 1: g = 1.968, A[Pt] = 2647 MHz, A[P] = 65 MHz, weight = 0.64, lw = 4.7; spin-system 2: g = 1.968, A[Pt] = 2099 MHz, A[P] = 48 MHz, weight = 0.36, lw = 5.8.

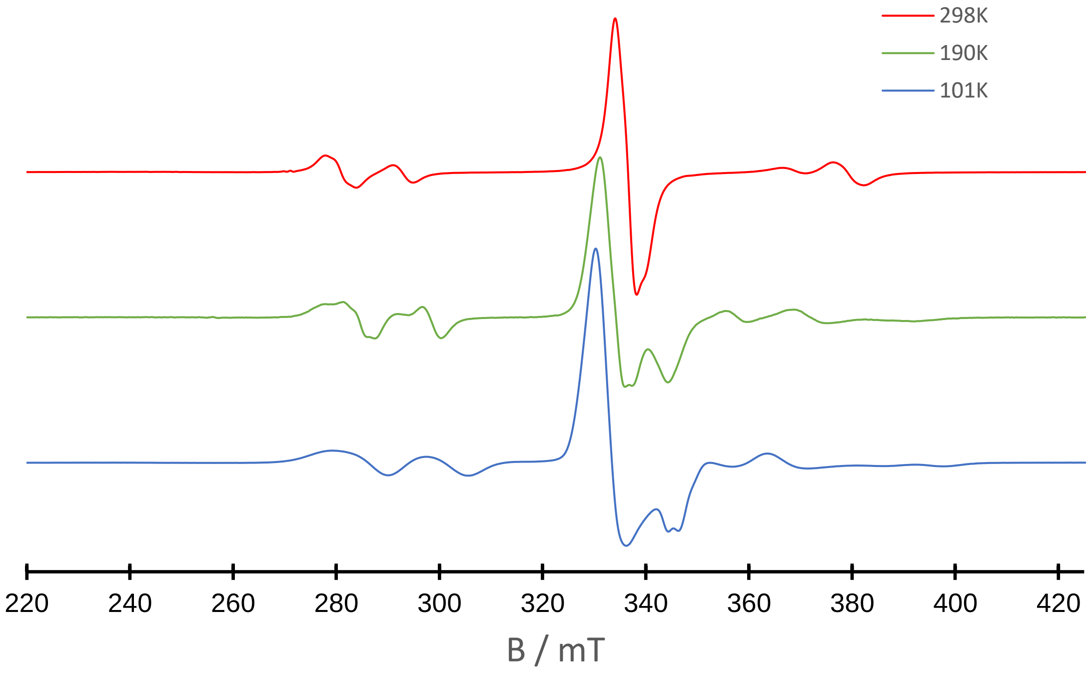

Figure 3-29. X-band EPR spectrum (9.335 GHz) of **Kkrypt[PtB2P2]** in toluene at 298 K (red), 192 K (green), and 101 K (blue).

### *Cyclic Voltammetry*

Cyclic voltammetry experiments were performed using a Pine AFP1 potentiostat. The cell consisted of a glassy carbon working electrode, a Pt wire auxiliary electrode and a Pt wire pseudo-reference electrode. All potentials are referenced vs. the Fc/Fc+ couple measured as an internal standard.

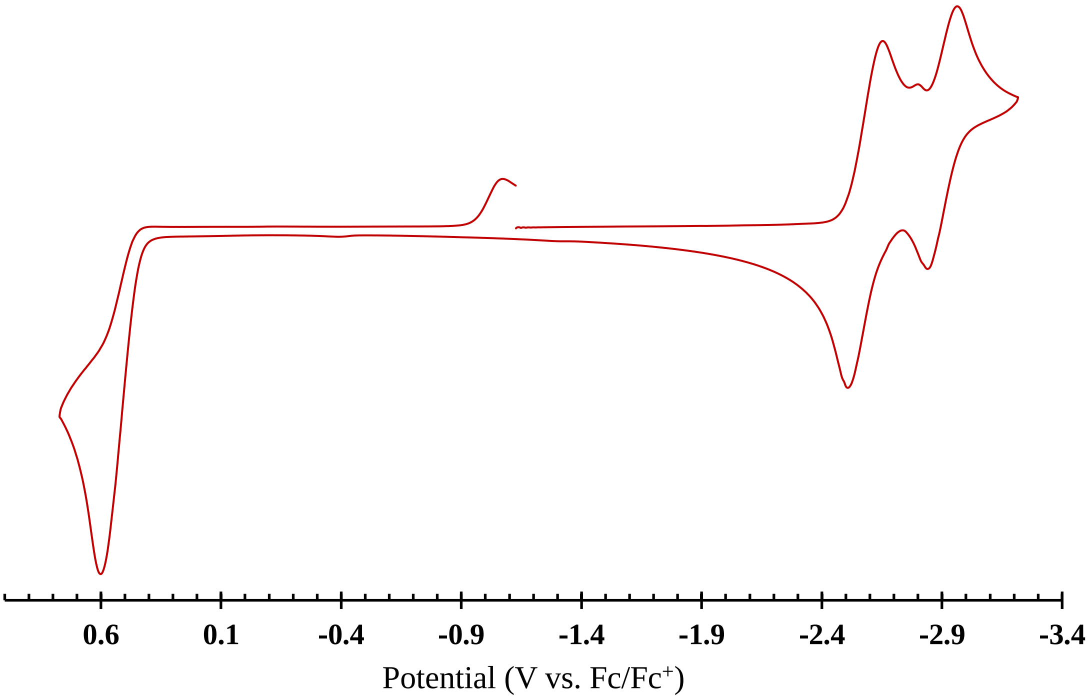

Figure 3-30. Cyclic voltammogram of **PtB2P2** in THF (0.1 M $[nBu_4N]PF_6$ as electrolyte; 100 mV/s scan rate).

### *X-Ray Crystallography*

**General Considerations**. Single crystals were coated with paratone oil and mounted on cryo-loop glass fibers. X-ray intensity data were collected at 100(2) K on a Bruker APEX2[16] platform-CCD X-ray diffractometer system using fine-focus Mo $K_\alpha$ radiation ($\lambda$ = 0.71073 Å, 50kV/30mA power). The CCD detector was placed at 5.0600 cm from the crystal. Frames were integrated using the Bruker SAINT software package[17] and using a narrow-frame integration algorithm. Absorption corrections were applied to the raw intensity data using the SADABS program.[18] The Bruker SHELXTL software package[19] was used for phase determination and structure refinement. Atomic coordinates, isotropic and anisotropic displacement parameters of all the non-hydrogen atoms were refined by means of a full matrix least-squares procedure on $F^2$. The H-atoms were included in the refinement in calculated positions riding on the atoms to which they were attached. Relevant details for individual data collections are reported in Tables 3-2 through 3-4.

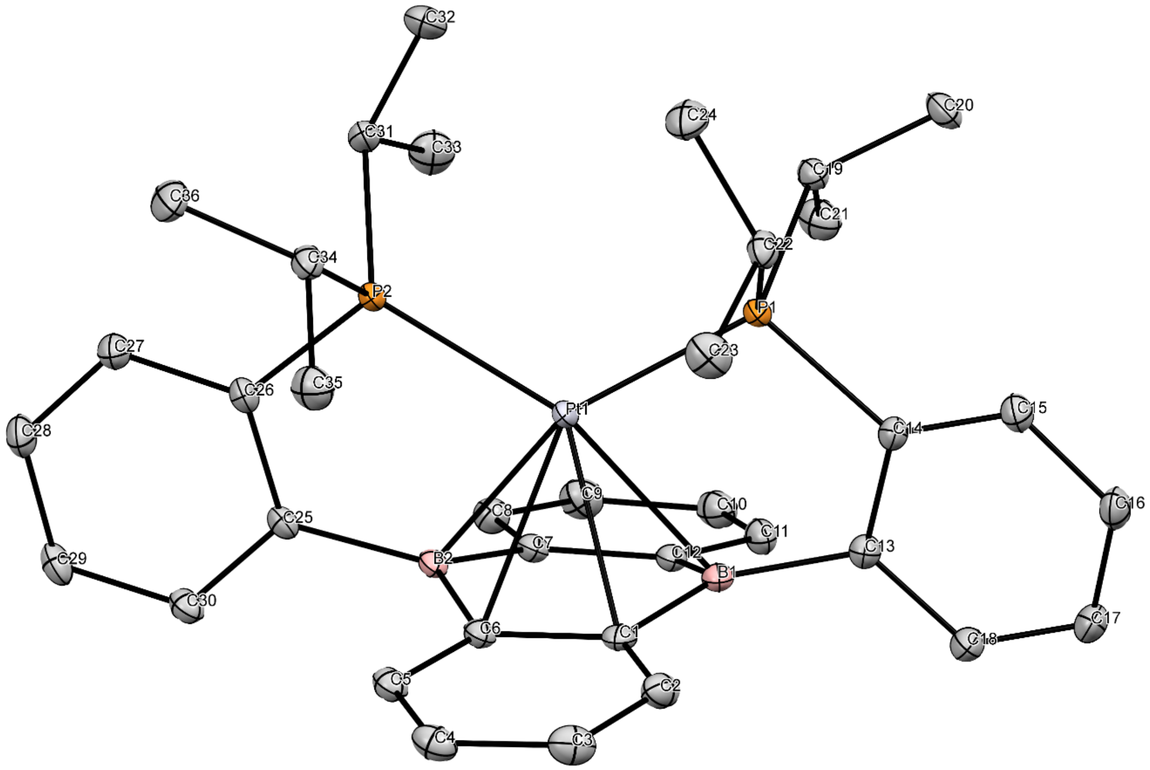

Figure 3-31. Labelled thermal ellipsoid plot (50%) for **$PtB_2P_2$ (1).**

Table 3-2. Crystal data and structure refinement for **$PtB_2P_2$ (1).**

| | | |
|---|---|---|
| Identification code | hh303jt | |
| Empirical formula | $C_{36}H_{44}B_2P_2Pt$ | |
| Formula weight | 755.36 | |
| Temperature | 100(2) K | |
| Wavelength | 0.71073 Å | |
| Crystal system | Monoclinic | |
| Space group | $P2_1/c$ | |
| Unit cell dimensions | a = 18.7106(6) Å | α = 90°. |
| | b = 11.1100(3) Å | β = 96.4297(13)°. |
| | c = 15.4649(5) Å | γ = 90°. |
| Volume | 3194.54(17) $Å^3$ | |
| Z | 4 | |
| Density (calculated) | 1.571 $mg/m^3$ | |
| Absorption coefficient | 4.517 $mm^{-1}$ | |
| F(000) | 1512 | |
| Crystal color | yellow | |
| Crystal size | 0.362 x 0.289 x 0.280 $mm^3$ | |
| θ range for data collection | 2.135 to 30.998° | |
| Index ranges | $-27 \leq h \leq 27$, $-16 \leq k \leq 16$, $-22 \leq l \leq 22$ | |
| Reflections collected | 83987 | |

| | |
|---|---|
| Independent reflections | 10183 [$R_{\mathrm{int}}$ = 0.0359] |
| Completeness to θ = 25.242° | 100.0 % |
| Absorption correction | Semi-empirical from equivalents |
| Max. and min. transmission | 0.7464 and 0.6344 |
| Refinement method | Full-matrix least-squares on $F^2$ |
| Data / restraints / parameters | 10183 / 0 / 378 |
| Goodness-of-fit on $F^2$ | 1.042 |
| Final *R* indices [$I > 2\sigma_I$ = 9212 data] | $R_1$ = 0.0200, $wR_2$ = 0.0438 |
| *R* indices (all data, 0.69 Å) | $R_1$ = 0.0240, $wR_2$ = 0.0451 |
| Largest diff. peak and hole | 3.462 and -2.451 e/Å$^3$ |

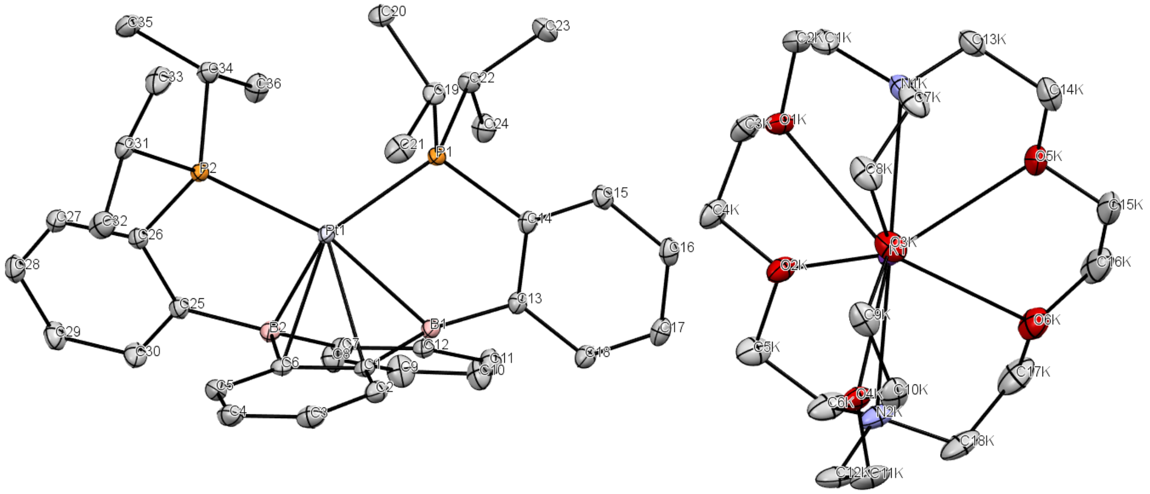

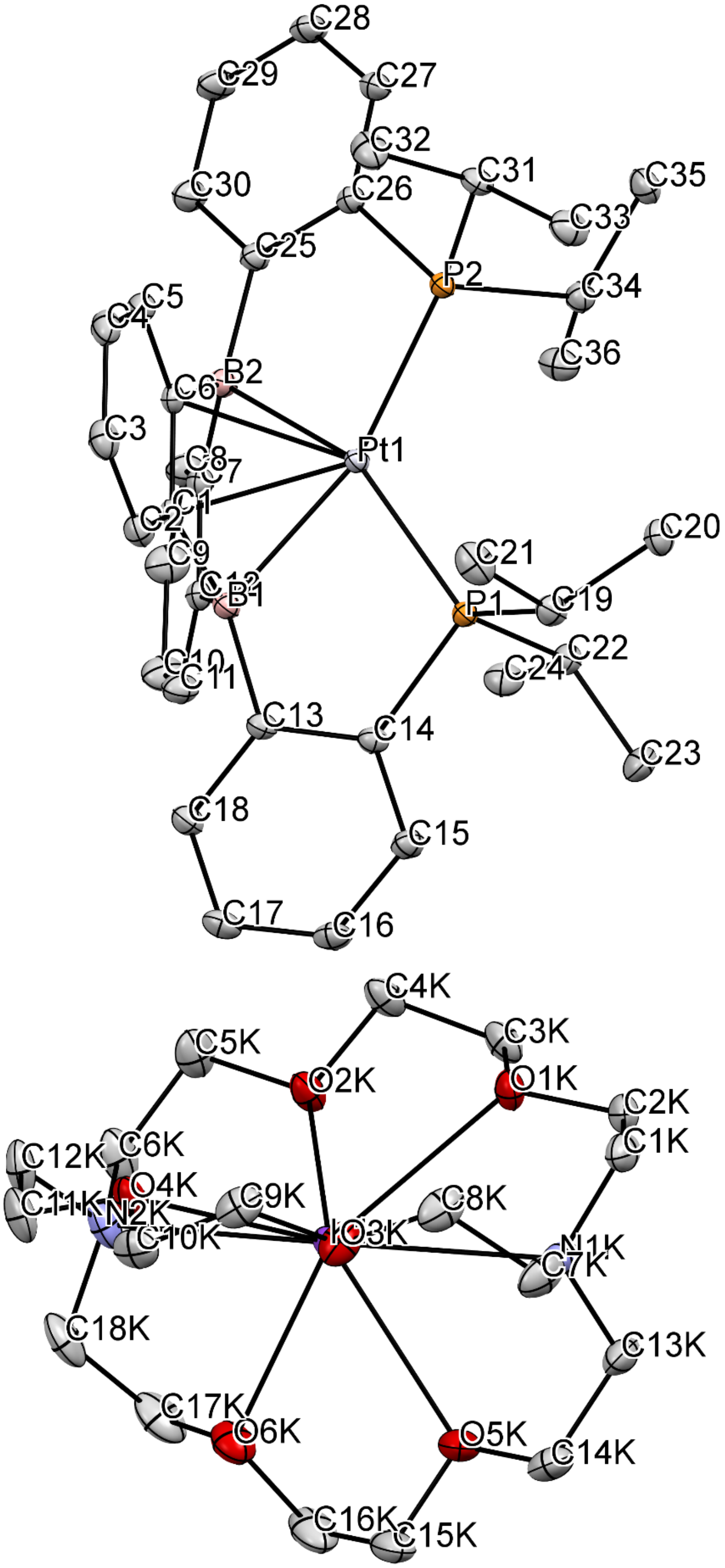
C28
C29
C27
C32
C31
C35
C30
C26
C33
C25
P2
C34
C5
C4
C36
C6
B2
C3
Pt1
C8
C7
C1
C2
C20
C9
C21
C12
B1
C19
P1
C22
C24
C10
C11
C13
C14
C23
C18
C15
C17
C16
C4K
C3K
C5K
O2K
O1K
C2K
C1K
C12K
C6K
O4K
C9K
C8K
C11K
N2K
K
O3K
C10K
N1K
C7K
C18K
C13K
C17K
O6K
O5K
C14K
C16K
C15K

Figure 3-32. Labelled thermal ellipsoid plot (50%) for **Kkrypt [PtB$_2$P$_2$] (2).**

Table 3-3. Crystal data and structure refinement for **Kkrypt [PtB$_2$P$_2$] (2).**

| | | |
|---|---|---|
| Identification code | hh339le | |
| Empirical formula | $C_{54}H_{80}B_2KN_2O_6P_2Pt$ | |
| Formula weight | 1170.95 | |
| Temperature | 100(2) K | |
| Wavelength | 0.71073 Å | |
| Crystal system | Triclinic | |
| Space group | P-1 | |
| Unit cell dimensions | a = 11.4301(4) Å | $\alpha$ = 78.9780(16)°. |
| | b = 15.6206(6) Å | $\beta$ = 88.5714(15)°. |
| | c = 15.8059(6) Å | $\gamma$ = 81.6565(16)°. |
| Volume | 2740.68(18) Å$^3$ | |
| Z | 2 | |
| Density (calculated) | 1.419 mg/m$^3$ | |
| Absorption coefficient | 2.743 mm$^{-1}$ | |
| F(000) | 1206 | |
| Crystal color | purple | |
| Crystal size | 0.163 x 0.099 x 0.088 mm$^3$ | |
| $\theta$ range for data collection | 2.086 to 31.506° | |
| Index ranges | $-16 \le h \le 16$, $-22 \le k \le 22$, $-23 \le l \le 23$ | |
| Reflections collected | 251205 | |
| Independent reflections | 18256 [$R_{\text{int}}$ = 0.0361] | |
| Completeness to $\theta$ = 25.242° | 99.9 % | |
| Absorption correction | Semi-empirical from equivalents | |
| Refinement method | Full-matrix least-squares on $F^2$ | |
| Data / restraints / parameters | 18256 / 0 / 621 | |
| Goodness-of-fit on $F^2$ | 1.052 | |
| Final $R$ indices [$I > 2\sigma_I$ = 17709 data] | $R_1$ = 0.0135, $wR_2$ = 0.0319 | |
| $R$ indices (all data, 0.68 Å) | $R_1$ = 0.0144, $wR_2$ = 0.0322 | |
| Largest diff. peak and hole | 1.739 and -1.272 e/Å$^3$ | |

Figure 3-33. Labelled thermal ellipsoid plot (50%) for **Kkrypt Kdme [PtB$_2$P$_2$] (3).**

Table 3-4. Crystal data and structure refinement for **Kkrypt Kdme [PtB$_2$P$_2$] (3).**

## References

(1) Andersen, T.; Haugen, H. K.; Hotop, H. Binding Energies in Atomic Negative Ions: III. *J. Phys. Chem. Ref. Data* **1999**, *28* (6), 1511–1533. https://doi.org/10.1063/1.556047.

(2) Ellis, J. E. Adventures with Substances Containing Metals in Negative Oxidation States. *Inorganic Chemistry*. American Chemical Society 2006, pp 3167–3186. https://doi.org/10.1021/ic052110i.

(3) Pyykko, P.; Desclaux, J. P. Relativity and the Periodic System of Elements. *Acc. Chem. Res.* **1979**, *12* (8), 276–281. https://doi.org/10.1021/ar50140a002.

(4) Dietzel, P. D. C.; Jansen, M. Synthesis and Crystal Structure Determination of Tetramethylammonium Auride. *Chem. Commun.* **2001**, No. 21, 2208–2209. https://doi.org/10.1039/b105648b.

(5) Taylor, J. W.; McSkimming, A.; Moret, M. E.; Harman, W. H. A Molecular Boroauride: A Donor–Acceptor Complex of Anionic Gold. *Angew. Chemie - Int. Ed.* **2017**, *56* (35), 10413–10417. https://doi.org/10.1002/anie.201703235.

(6) Karpov, A.; Nuss, J.; Wedig, U.; Jansen, M. Cs2Pt: A Platinide(-II) Exhibiting Complete Charge Separation. *Angew. Chemie - Int. Ed.* **2003**, *42* (39), 4818–4821. https://doi.org/10.1002/anie.200352314.

(7) Bontemps, S.; Bouhadir, G.; Gu, W.; Mercy, M.; Chen, C. H.; Foxman, B. M.; Maron, L.; Ozerov, O. V.; Bourissou, D. Metallaboratranes Derived from a Triphosphanyl-Borane: Intrinsic C 3 Symmetry Supported by a Z-Type Ligand. *Angew. Chemie - Int. Ed.* **2008**, *47* (8), 1481–1484. https://doi.org/10.1002/anie.200705024.

(8) Braunschweig, H.; Brenner, P.; Dewhurst, R. D.; Krummenacher, I.; Pfaffinger, B.; Vargas, A. Unsupported Boron-Carbon σ-Coordination to Platinum as an Isolable Snapshot of σ-Bond Activation. *Nat. Commun.* **2012**, *3* (1), 872. https://doi.org/10.1038/ncomms1884.

(9) Amgoune, A.; Ladeira, S.; Miqueu, K.; Bourissou, D. Coordination of Phosphinoboranes R 2PB(C 6F 5) 2 to Platinum: An Alkene-Type Behavior. *J. Am. Chem. Soc.* **2012**, *134* (15), 6560–6563. https://doi.org/10.1021/ja301929n.

(10) Barnett, B. R.; Moore, C. E.; Rheingold, A. L.; Figueroa, J. S. Cooperative Transition Metal/Lewis Acid Bond-Activation Reactions by a Bidentate (Boryl)Iminomethane Complex: A Significant Metal-Borane Interaction Promoted by a Small Bite-Angle Lz Chelate. *J. Am. Chem. Soc.* **2014**, *136* (29), 10262–10265. https://doi.org/10.1021/ja505843g.

(11) Cowie, B. E.; Emslie, D. J. H. Platinum Complexes of a Borane-Appended Analogue of 1,1'-Bis(Diphenylphosphino)Ferrocene: Flexible Borane Coordination Modes and in Situ Vinylborane Formation. *Chem. - A Eur. J.* **2014**, *20* (51), 16899–16912. https://doi.org/10.1002/chem.201404846.

(12) Holler, S.; Tüchler, M.; Steller, B. G.; Belaj, F.; Veiros, L. F.; Kirchner, K.; Mösch-Zanetti, N. C. Thiopyridazine-Based Palladium and Platinum Boratrane Complexes. *Inorg. Chem.* **2018**, *57* (12), 6921–6931. https://doi.org/10.1021/acs.inorgchem.8b00530.

(13) Essex, L. A.; Taylor, J. W.; Harman, W. H. Nickel Complexes of Phosphine-Appended Benzannulated Boron Heterocycles. *Tetrahedron* **2019**, *75* (15), 2255–2260. https://doi.org/10.1016/j.tet.2019.02.047.

(14) Deutsch, J. L.; Poling, S. M. The Determination of Paramagnetic Susceptibility by NMR: A Physical Chemistry Experiment. *J. Chem. Educ.* **1969**, *46* (3), 167. https://doi.org/10.1021/ed046p167.

(15) Schubert, E. M. Utilizing the Evans Method with a Superconducting NMR Spectrometer in the Undergraduate Laboratory. *J. Chem. Educ.* **1992**, *69* (1), 62. https://doi.org/10.1021/ed069p62.1.

(16) Bruker. APEX 2. Bruker AXS Inc.: Madison, Wisconsin, USA 2014.

(17) *SAINT, Version 8.34, Bruker (2012)*; Bruker AXS Inc.: Madison, Wisconsin, USA.

(18) *SADABS, Version 2012/1, Bruker (2012)*; Bruker AXS Inc.: Madison, Wisconsin, USA.

(19) Bruker. SHELXTL. Bruker AXS Inc.: Madison, Wisconsin, USA 2013.

# Chapter 4 : Nickel Complexes of Phosphine-Appended Benzannulated Boron Heterocycles

## Introduction

Boron for carbon substitution is a powerful method for modulating the properties of polycylic aromatic hydrocarbons (PAH), with applications in optoelectronic materials[1] and coordination chemistry.[2] The empty p orbital on boron can act as a Lewis acid[3] or can introduce electron deficiency into the molecule, engendering facile multi-electron redox chemistry in many cases.[4–7] This combination of redox activity and chemical reactivity have made boron heterocycles attractive platforms for small molecule activation.[8] Boron heterocycles also have applications as ligands to both transition and main-group metals. The boron-substituted analogues of classic ligands such as cyclopentadienyl and benzene have been used to prepare a range of metal complexes with interesting electronic properties and chemical reactivity. They are of special interest given their potential to function as acceptor or Z-type ligands.

The five-membered monoboron heterocycle borole ($C_4H_4BH$) is isoelectronic to the cyclopentadienyl cation and formally classified as an $L_2Z$ ligand. The antiaromatic character of borole engenders significant reactivity in the molecule, but borole and its doubly benzannulated analogue 9-borafluorene (BFlu) have found applications in small molecule activation.[9,10] For example, perfluoropentaphenylborole is capable of cleaving dihydrogen[11] or undergoing Diels-Alder or insertion reactions with alkynes.[12] Reduced 9-borafluorenes can be stabilized by *N*-heterocyclic carbenes, conferring boron-centered nucleophilicity with methyl iodide[13] or enabling single-electron transfer with trimethyltin chloride[14] Despite the wide-variety of reactivity observed for 9-borafluorenes,[9] relatively few metal complexes of BFlu are known.[15] Piers reported an adduct between a perfluoro-9-phenyl-9-borafluorene and Cp*Al,[16] and Bourissou used a phosphine-buttressed ligand (PBFlu, **1**) to prepare a BFlu complex exhibiting monohapto coordination through the boron, the first Au borane complex (Figure 4-1).[17]

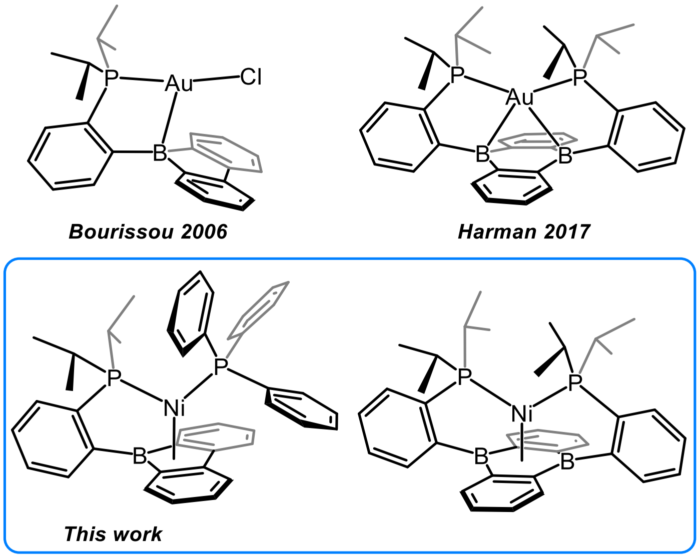

Figure 4-1. Previously reported Au complexes of PBFlu and $B_2P_2$ ligands (top). Ni complexes of PBFlu and $B_2P_2$ presented in this work (bottom).

The doubly benzannulated analogue of 9,10-dihydro-9,10-diborabenzene, 9,10-dihydro-9,10-diboraanthracene (DBA), is an electrochemically rich platform with broad synthetic flexibility and applications in organic electronic materials. Upon two electron reduction, Wagner has shown that DBA variants can cleave dihydrogen,[18] disproportionate $CO_2$,[19] break chalcogen-chalcogen bonds,[20] and activate sp C–H bonds.[21] We recently reported that NHC-stabilized 9,10-diboraanthracene undergoes formal [4+2] cycloaddition reactions at the boron centers with $O_2$, $CO_2$, and ethylene.[22] A number of electronically saturated metal complexes of DBA have been prepared, some of which contain multiple metal centers bound to a single DBA unit.[23] Due to the electron deficiency of DBA, oxidation of these complexes tends result in irreversible de-coordination of the ligand.[24]

We are interested in the emergent redox properties and chemical reactivity of metal complexes with heterocyclic boron-containing ligands. Recently, we reported the synthesis of a DBA-based ligand featuring two tethered phosphine donors straddling the central $C_4B_2$ ring (9,10-bis(2-(diisopropylphosphino)phenyl)-9,10-dihydroboranthrene, $B_2P_2$, **2**). Metal complexes of $B_2P_2$ can undergo DBA-centered redox events, as in the zwitterionic radical complexes ($B_2P_2$)Cu and ($B_2P_2$)Ag we recently described.[25] A series of Au complexes of $B_2P_2$ were also prepared in three states of charge, with the most reduced species, $[(B_2P_2)Au]^-$ being the first example of a molecular boroauride, featuring very short interactions between the Au atom and pyramidalized borons of the DBA core.[26] Given the intriguing chemistry uncovered for $d^{10}$ coinage metal complexes with both PBFlu and $B_2P_2$, we investigated the related Ni complexes. Herein we report the synthesis, structure, NMR, and electrochemical characterization of the neutral Ni complexes of both **1** and **2**. Unlike their coinage metal analogues, these Ni complexes form penta- and hexahapto complexes, respectively, with the central boron heterocycles (Figure 4-1). Although the BFlu and DBA heterocycles have one and two borane centers, respectively, DFT calculations indicate that these ligands, and thus their Ni complexes, are essentially isoelectronic and best described as $d^{10}$ $ML_4$ Ni(0) complexes with a backbonding component (Z') into a boron-centered empty orbital.

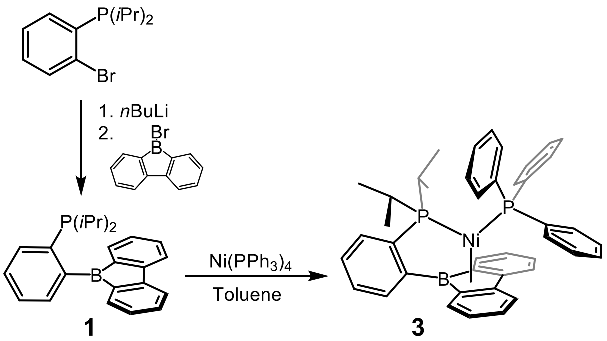

Scheme 4-1. Preparation of PBFlu and (PBFlu)Ni.

## *Results and Discussion*

The phosphine-appended BFlu ligand **1** was first prepared by Bourissou and metalated *in situ* with $(Me_2S)AuCl$ without isolation of the ligand.[17] In our hands, lithiation of 2-( diisopropylphosphino)bromobenzene in toluene proceeds cleanly at –40 °C and the lithiated species is very stable in this solvent, even at room temperature. Subsequent addition of 9-bromo-9-borafluorene at –60°C results in a yellow solution that, upon warming to –20°C, changes to an intense red color, indicating near complete decomposition of the desired ligand. However, by avoiding warming reaction mixtures past –20 °C, **1** can be isolated as a colorless crystalline solid in low yields (16%) (Scheme 4-1). Once isolated, **1** is stable at room temperature allowing its characterization by NMR spectroscopy. In solution, **1** exhibits a broad resonance centered at 0.9 ppm in the $^{11}B\{^1H\}$ NMR spectrum. For comparison, the $^{11}B$ resonance for 9-phenyl-9-borafluorene is 64.5 ppm, suggesting P–B interactions in **1**, although no $^{31}P$–$^{11}B$ coupling is observed (Figure 4-2).[27]

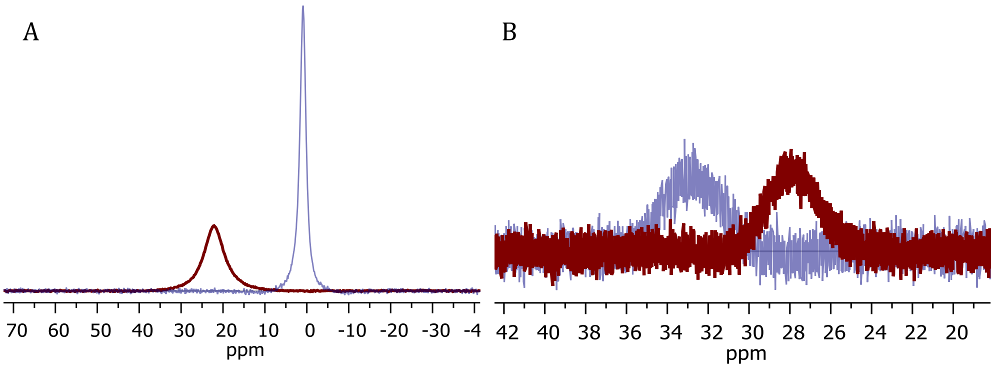

Figure 4-2. $^{11}B\{^{1}H\}$ NMR of (A) PBFlu **1** (blue) and **3** (red); (B) $B_2P_2$ (blue) and **4** (red).

Metalation of **1** with $Ni(PPh_3)_4$ affords the nickel complex (PBFlu)Ni (**3**), denoted by a downfield shift of the $^{11}B$ resonance to 22.5 ppm (Figure 4-2 – 11B). The analogous gold complex has a shift of 55.2 ppm, indicating a stronger boron-metal interaction in the former. Single-crystal X-ray diffraction (XRD) of **1** revealed an $\eta^5$-BFlu moiety coordinated to Ni with a Ni–B distance of 2.135(2) Å and Ni–C distances ranging from 2.217(2) to 2.230(2) Å (Figure 4-3). In contrast, the previously reported $\eta^1$-BFlu gold complex has a Au–B distance of 2.663(1) Å with no appreciable interaction between the Au center and other atoms of the BFlu unit (average $d_{\text{Au-C}\alpha} = 3.118(1)$ Å; $d_{\text{Au-C}\beta} = 3.750(1)$ Å) (Figure 4-3). While many $\eta^5$-borole complexes have been reported,[28–30] complex **3** is the first example of pentahapto coordination of BFlu.

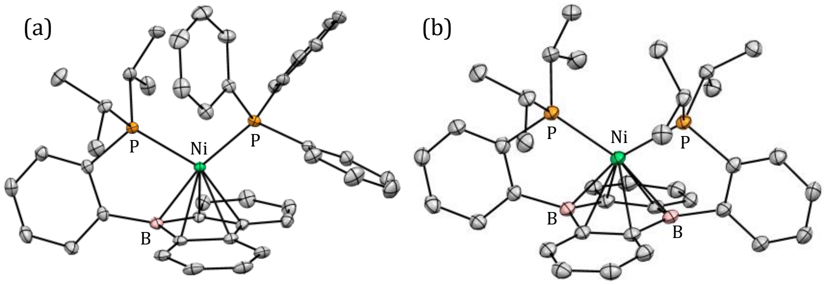

Figure 4-3. Labeled thermal ellipsoid plots (50%) of **1** (a) and **2** (b). Unlabeled ellpisoids correspond to carbon. Hydrogen atoms have been omitted for clarity.

The DBA-based ligand **2** allowed us to explore the effect of a second boron center in the coordination sphere of Ni. Metalation of **2** to give ($B_2P_2$)Ni (**4**) can be achieved using either $Ni(PPh_3)_4$ or treating by a mixture of **2** and $NiBr_2$ with metallic Na (Scheme 4-2). In solution, **4** features a $^{11}B\{^1H\}$ resonance at 27.8 ppm that is shifted slightly upfield to that of the free ligand (34.1 ppm). Single-crystal XRD reveals $\eta^6$ coordination of Ni to the DBA core with an average Ni-B distance of 2.196(2) Å (Figure 4-3). In contrast, $[(B_2P_2)Au]^+$ has Au–B distances of 2.610 and 2.678 Å and no Au–C contact shorter than 2.75 Å.[26] These differences can be rationalized both by the prevalence of 14-electron Au(I) complexes as well as the stronger backbonding ability of Ni(0).

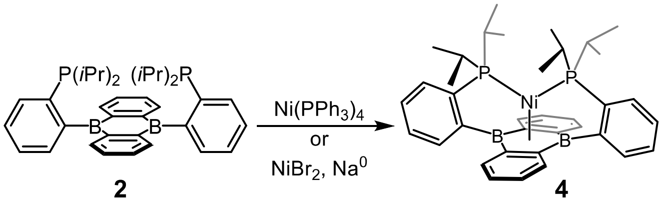

Scheme 4-2. Synthesis of ($B_2P_2$)Ni.

To further explore the acceptor properties of these two complexes, we investigated their electrochemistry by cyclic voltammetry. The CV of **3** features a single irreversible reduction at –3.00 V vs. $Fc/Fc^+$ with scans in the oxidative direction leading to significant decomposition (Figure 4-22). In contrast, **4** displays a reversible reduction event at −2.99 V vs. $Fc/Fc^+$ and an electrochemically sluggish but chemically reversible oxidation at +0.06 V (Figure 4-23). It is instructive to compare the electrochemistry of **3** and **4** to that of the corresponding free ligands **1** and **2**. The CV of **1** ligand displays two reduction events at –2.09 and –2.70 V, the first being reversible and the second irreversible (Figure 4-20). The irreversibility of the second reduction on the CV timescale may be attributable to the reductive cleavage of the endocyclic B–C bond, a phenomenon that has been observed in boroles and related molecules.[10,12,31] In contrast, **2** undergoes two reversible reductions at –2.18 and –2.71 V vs. Fc/Fc$^+$ (Figure 4-21). In both cases, the presence of the diphosphine Ni fragment renders these molecules significantly more difficult to reduce, consistent with strong donation from a filled Ni d-orbital into the empty boron centered orbitals on the BFlu and DBA fragments. These results are counter to what we have observed in the cases of the coinage metal complexes of **2** $[(B_2P_2)M]^+$ (M = Cu, Ag, Au), all of which are significantly easier to reduce than free **2** (Table 1). The positive charge on the coinage metal complexes is likely a significant contributor to this observation.

Table 4-1. Selected bonds, angles, $^{11}$B NMR data and CV data for PBFlu, $B_2P_2$ and their transition metal complexes.

| Compound | $^{11}$B NMR [ppm] | M-B$_{avg}$ [Å] | M-C$_{avg}$ [Å] | ΣB$_\alpha$ [°] | E$_{1/2}$ [V] |
|---|---|---|---|---|---|
| PBFlu | 0.90 | | | | –2.09[b], –2.70[c] |
| $B_2P_2$ | 34.1 | | | | –2.18, –2.71 |
| $(PPh_3)Ni(PBFlu)$ | 22.5 | 2.316 | 2.233, 2.216[a] | 360.0 | –3.00[c] |
| $Ni(B_2P_2)$ | 27.8 | 2.196 | 2.349 | 360.0 | 0.06, –2.99[b] |
| $[Cu(B_2P_2)][BAr^F_4]$ | 47.2 | 2.372 | 2.514 | 360.0 | –1.66[b] |
| $[Ag(B_2P_2)][BAr^F_4]$ | 29.2 | 2.567 | 2.730 | 360.0 | –1.56, –2.21[c] |
| $Ag(B_2P_2)$ | | 2.892 | 2.985 | 359.9 | |
| $[Au(B_2P_2)][BAr^F_4]$ | 32.0 | 2.644 | 2.832 | 360.0 | –1.60, –2.05 |
| $Au(B_2P_2)$ | | 3.049 | 3.189 | 360.0 | |
| $[Au(B_2P_2)][K(18\text{-}c\text{-}6)]$ | 11.1 | 2.239 | | 343.9 | |

DFT calculations were carried out on truncated models[32] of **3** and **4** as well as BFlu and DBA to shed light on the interaction between the Ni center and the boron heterocycles. The frontier orbitals for BFlu and DBA are shown in Figure 4 and reveal that in both cases, the LUMO is a boron-centered orbital. In the case of DBA, this orbital is composed of the out-of-phase combination of the two boron p orbitals. This orbital is analogous to the

HOMO of anthracene and has overall bonding character. The second unoccupied molecular orbital in DBA with significant boron character (LUMO+1) corresponds to the in-phase combination of the empty boron p-orbitals. As this orbital is analogous to the LUMO of anthracene, it is antibonding. Although there are in principle two relevant acceptor orbitals in DBA, the in-phase combination of the boron p orbitals is significantly higher in energy. The frontier molecular orbitals of **3** and **4** are shown in Figures 5 and 6, respectively. In both cases, the five highest energy filled orbitals have significant if not predominantly d-character, consistent with a $d^{10}$ Ni(0) description. In **3**, the Ni–B acceptor interaction serves to stabilize an orbital of d parentage that is antibonding with respect to the Ni–$PPh_3$ interaction (HOMO–2). In **4** the primary molecular orbital featuring Ni–B bonding is also the HOMO–2, which consists of the in-phase combination of a Ni d orbital and the LUMO of DBA described above. The HOMO–1 in **4** contains a small component of the in-phase combination of the boron p orbitals, corresponding to the LUMO+1 of DBA. This interaction is less pronounced, owing to the higher energy of the DBA LUMO+1 (in-phase boron p orbitals) relative to the LUMO (out-of-phase boron p orbitals). For these reasons, we favor a description of both BFlu and DBA in **3** and **4** as $L_2$ ligands with a significant backbonding component associated with the boron p orbitals. In both cases, the d-orbital splittings can be rationalized as perturbations on an approximately tetrahedral ligand field.

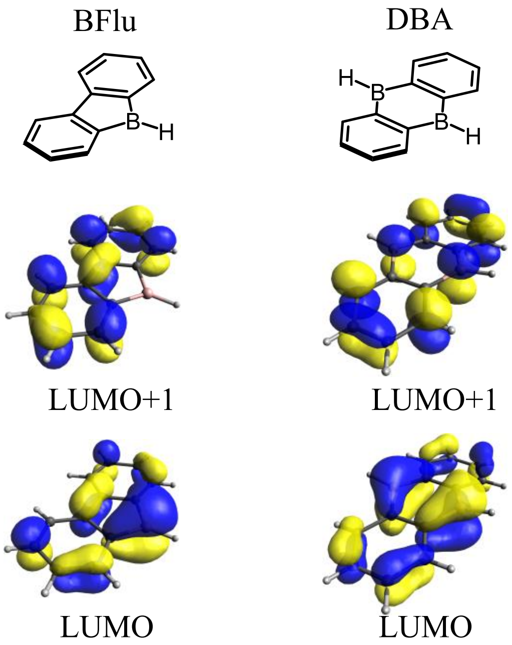

Figure 4-4. Kohn-Sham orbitals calculated for BFlu and DBA (see Experimental Section for computational details).

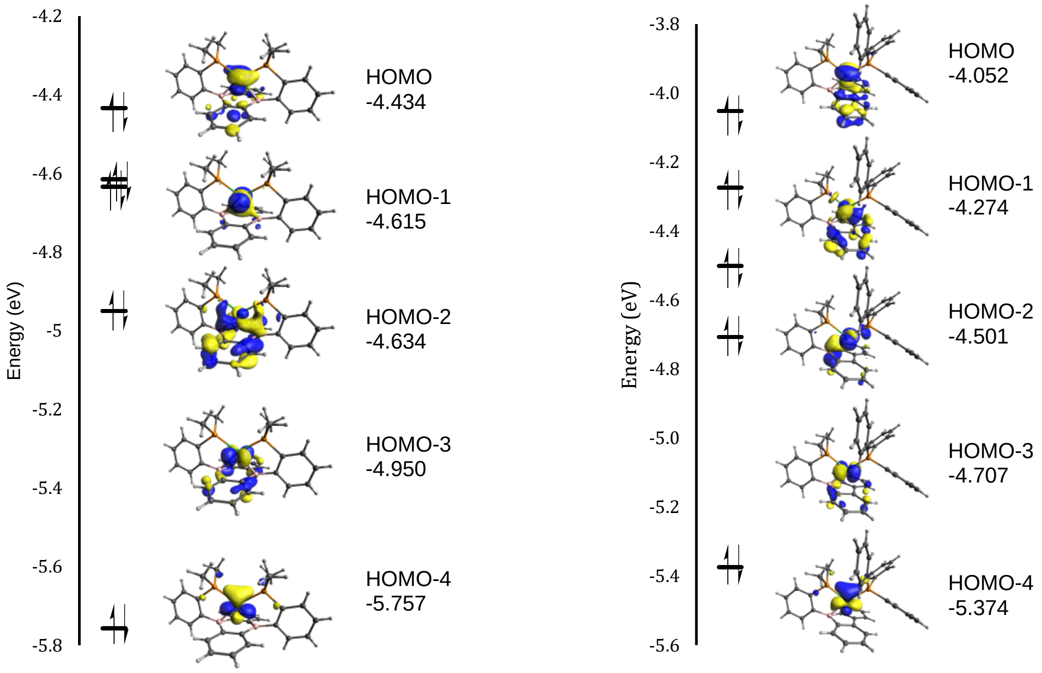

Figure 4-5. Kohn-Sham orbitals calculated via DFT for a truncated model of **4** (left) and **3** (right).

## *Conclusion*

In summary, we have synthesized two new nickel complexes **3** and **4** featuring strong interactions of the Ni center with boron heterocycles. The interaction between Ni and the boron heterocycles in these complexes is much more pronounced than in the analogous complexes of the coinage metal cations. Where the coinage metal complexes are easier to reduce than the corresponding free ligands, **3** and **4** are significantly more difficult, consistent with strong backbonding of the Ni center into the boron-based orbitals of the heterocycles. DFT calcluations on **3** and **4** are consistent with this description. The five highest energy orbitals in both **3** and **4** have significant d character, with the HOMO–2 in both cases possessing significant Ni–B bonding interactions. Given the presence of the Ni–B bonding orbital in the middle of the d manifold, we are inclined to describe these complexes are Ni(0) (as opposed to Ni(II)) in which the Ni–B interaction is best described as backbonding.

## *Experimental Section*

General considerations: Unless otherwise noted, all manipulations were carried out using standard Schlenk or glovebox techniques under a $N_2$ atmosphere. Hexanes, benzene, toluene, and acetonitrile were dried and deoxygenated by argon sparge followed by passage through activated alumina in a solvent purification system from JC Meyer Solvent Systems followed by storage over 4 Å molecular sieves. THF and $Et_2O$ were distilled from sodium-benzophenone ketyl under N2 followed by storage over 4Å molecular sieves for at least 24 hours prior to use. Non-halogenated and non-nitrile containing solvents were tested with a standard purple solution of sodium benzophenone ketyl in THF to confirm effective oxygen and moisture removal prior to use. Hexamethyldisiloxane (HMDSO) was distilled from sodium metal and stored over 4Å molecular sieves for 24 hours prior to use. All reagents were purchased from commercial suppliers and used without further purification unless otherwise noted. 9-bromo-9-borafluorene,[33] 2-(diisopropylphosphino)bromobenzene,[17] and 9,10-bis(2-(diisopropylphosphino)phenyl)-9,10-dihydroboranthrene ($B_2P_2$, **2**)[26] were synthesized according to literature procedures. Elemental analyses were performed by Midwest Microlab, LLC, Indianapolis, IN. Deuterated solvents were purchased from Cambridge Isotope Laboratories Inc., degassed, and dried over activated 3Å molecular sieves for at least 24 h prior to use. NMR spectra were recorded on Bruker Neo 400 MHz, and Bruker Avance 600 MHz spectrometers. $^{1}H$ and $^{13}C$ chemical shifts are reported in ppm relative to tetramethylsilane using residual solvent as an internal standard. $^{11}B$ chemical shifts are reported in ppm relative to $BF_3•Et_2O$. Original $^{11}B$ NMR spectra were processed using MestReNova 11.0.2 with a backwards-linear prediction applied to eliminate background signal from the borosilicate NMR tube. For $^{11}B$ NMR spectra with peaks overlapping the borosilicate signal, a manual baseline correction was applied. UV-Vis spectra were recorded using a Cary Bio 500 spectrometer using a 1 cm path length quartz cuvette with a solvent background subtraction applied. X-ray diffraction studies were performed using a Bruker-AXS diffractometer. Cyclic Voltammetry (CV) experiments were performed using a Pine AFP1 potentiostat. The cell consisted of a glassy carbon working electrode, a Pt wire auxiliary electrode and a Pt wire pseudo-reference electrode. All potentials are referenced vs. the $Fc/Fc^{+}$ couple measured as an internal standard. Calculations were run using Orca v4.0.1[34] and visualized with Avogadro v1.2.0.[35]

**9-(2-(diisopropylphosphino)phenyl)-9-borafluorene (1).** Using a modified procedure from Bourissou *et al*. n-BuLi (2.5 M in hexanes, 2.5 mL, 6.25 mmol) and 9-bromo-borafluorene (1.5 g, 6.2 mmol) were successively added at –40 °C and –60 °C to a solution of 1-bromo-2-diisopropylphosphinobenzene (1.5 g, 5.5 mmol) in toluene (80 mL).[17] The suspension was pumped down to a pale orange solid and brought into the glovebox. The solid was re-suspended in toluene (80 mL) that had been pre-chilled to –50°C and filtered through celite at the same temperature. The filtrate was concentrated *in vacuo* and layered with hexanes, providing colorless crystals. Yield: 0.311 g (16%). $^1$H NMR (400 MHz, $C_6D_6$) δ 7.87 (dd, *J* = 7.5, 0.9 Hz, 2H), 7.49 (dd, *J* = 7.2, 2.3 Hz, 2H), 7.36 (tdd, *J* = 7.5, 2.5, 1.3 Hz, 2H), 7.26 – 7.17 (m, 4H), 7.14 – 7.08 (m, 2H), 2.15 (dp, *J* = 9.3, 7.3 Hz, 2H), 0.80 (d, *J* = 7.1 Hz, 3H), 0.77 (d, *J* = 7.2 Hz, 3H), 0.73 (d, *J* = 7.4 Hz, 3H), 0.69 (d, *J* = 7.4 Hz, 3H).$^{13}$C{$^1$H} NMR (101 MHz, $C_6D_6$) δ 164.8 (br), 153.2 (br), 149.7 (d, *J* = 4.7 Hz), 136.1 (d, *J* = 48.1 Hz), 132.3 (d, *J* = 2.6 Hz), 131.4 (d, *J* = 39.0 Hz), 131.3 (d, *J* = 3.8 Hz), 127.2 (d, *J* = 3.5 Hz), 127.1, 125.8 (d, *J* = 3.7 Hz), 119.7 (d, *J* = 2.4 Hz), 23.5 (d, *J* = 8.5 Hz), 18.4, 18.0. $^{11}$B{$^1$H} NMR (128 MHz, $C_6D_6$) δ 0.9. $^{31}$P NMR (162 MHz, $C_6D_6$) δ 33.0. HRMS (ESI): *m/z* for $C_{24}H_{27}BP$ $[M+H]^+$ calcd.: 357.1938, found: 357.1978.

(**PBFlu)Ni(PPh$_3$) (3)**. A solution of **1** (69 mg, 0.19 mmol) in toluene (4 mL) was added to a stirring solution of tetrakis(triphenylphosphine)nickel(0) (213 mg, 0.19 mmol) in toluene

(10 mL). After 2 hours, the solution was concentrated *in vacuo* and layered with hexane (2 mL), providing burgundy-brown crystals of **2** that were washed with hexanes (2 x 3 mL) and dried *in vacuo*. Crystals suitable for XRD can be generated from layering hexane over toluene or ether over THF. Yield: 0.120 g (91%). $^1$H NMR (400 MHz, $C_6D_6$) δ 7.97 (d, *J* = 7.3 Hz, 1H), 7.66 (d, *J* = 7.6 Hz, 2H), 7.40 (tdd, *J* = 7.4, 2.5, 1.2 Hz, 1H), 7.21 (dddd, *J* = 9.5, 7.3, 4.9, 2.3 Hz, 7H), 7.14 – 7.07 (m, 3H), 7.07 – 6.96 (m, 11H), 6.51 (d, *J* = 8.0 Hz, 2H), 1.17 (h, *J* = 7.2 Hz, 2H), 0.85 (d, *J* = 7.0 Hz, 3H), 0.81 (d, *J* = 7.0 Hz, 3H), 0.53 (d, *J* = 7.1 Hz, 3H), 0.49 (d, *J* = 7.0 Hz, 3H). $^{13}$C{$^1$H} NMR (101 MHz, $C_6D_6$) δ 155.8, 144.8 (dd, *J* = 40.4, 15.1 Hz), 134.8, 134.6, 134.5 (d, *J* = 9.7 Hz), 131.9 (dd, *J* = 24.1, 2.7 Hz), 131.2, 129.9, 129.3, 129.2 (d, *J* = 2.5 Hz), 127.7, 127.7, 126.2 (d, *J* = 2.9 Hz), 125.7 (d, *J* = 5.6 Hz), 123.6, 121.1, 119.0 (d, *J* = 2.8 Hz), 114.9, 25.6 (d, *J* = 19.3 Hz), 19.3 (d, *J* = 5.6 Hz), 17.8. $^{11}$B{$^1$H} NMR (128 MHz, $C_6D_6$) δ 22.5. $^{31}$P NMR (162 MHz, $C_6D_6$) δ 55.66 (d, *J* = 24.2 Hz), 36.67 (d, *J* = 24.2 Hz). UV-vis (Benzene) $\lambda_{max}$ (nm) ($\varepsilon_{max}$ ($M^{-1}cm^{-1}$)) 560 (sh, 3.2 x $10^2$), 417 (sh, 3.5 x $10^3$). Anal. Calcd. for $C_{36}H_{44}B_2NiP_2$ (1 x $C_4H_{10}O$): C, 73.73 H, 6.59. Found: C, 73.47 H, 5.95.

**($B_2P_2$)Ni (4)**.

*Via $NiBr_2$*: A solution of $B_2P_2$ (0.200 g, 0.357 mmol) in THF (3 mL) was added to a slurry of $NiBr_2$ (0.080 g, 0.366 mmol) in THF (3 mL) and stirred 4 hours. The orange/red mixture had its volatiles removed, was added $Et_2O$ (5 mL) and again had its volatiles removed. The remaining orange/red foam was extracted with toluene (2 x 3 mL) and filtered through celite into a 20 mL vial containing sodium (0.021 g, 0.893 mmol). The solution was stirred

10 hours during which time a deep red solution formed. The mixture was filtered through celite and concentrated to ca. 2 mL before adding $Et_2O$ (5 mL). The mixture was filtered through a 1” pad of silica gel and rinsed with toluene:$Et_2O$ (2:5, 10 mL). Removal of the volatiles gave the product as a red solid. Overall yield: 0.157 g, 71%.

*Via Ni(PPh$_3$)$_4$*: A solution of $B_2P_2$ (0.200 g, 0.357 mmol) in THF (5 mL) was added to $Ni(PPh_3)_4$ (0.395 g, 0.357 mmol) in THF (3 mL) and the mixture stirred at 50 °C for 12 hours. The deep red solution had its volatiles removed *in vacuo* before dissolving the residue in THF:$Et_2O$ (1:9, 10 mL) and passing it through a 1” pad of silica. Removal of the volatiles *in vacuo* gave the product as a red/orange solid. Overall yield: 0.197 g, 89%. X-ray quality crystals were grown by layering a concentrated toluene solution with MeCN. $^1$H NMR (500 MHz, $C_6D_6$) δ 8.01 (d, *J* = 7.2 Hz, 2H), 7.62 (dd, *J* = 5.9, 3.4 Hz, 2H), 7.48 (t, *J* = 7.2 Hz, 1H), 7.36 – 7.30 (m, 2H), 7.27 (t, *J* = 7.5 Hz, 2H), 7.11 (dd, *J* = 6, 3.4 Hz, 2H), 2.04 (dp, *J* = 14.2, 7.3 Hz, 2H), 0.74 (d, *J* = 6.9 Hz, 3H), 0.72 (d, *J* = 6.9 Hz, 3H), 0.61 (d, *J* = 7.1 Hz, 3H), 0.58 (d, *J* = 7.1 Hz, 3H). $^{31}$P (202 MHz, $C_6D_6$) δ 45.6 (s). $^{11}$B{$^1$H} (160 MHz) δ 27.8 (bs). $^{13}$C{$^1$H} NMR (126 MHz, $C_6D_6$) δ 159.3, 143.1-142.9 (m), 135.0, 132.0 – 131.4 (m), 130.6, 130.1, 129.9, 126.9, 125.4, 27.7 (dt, *J* = 18.3, 8.5 Hz), 20.0, 18.9. UV-vis (THF): $\lambda_{max}$ (nm) ($\varepsilon_{max}$ ($M^{-1}cm^{-1}$)) 318 (sh, 2.5 x $10^4$), 372 (1.7 x $10^4$), 451 (7.9 x $10^3$), 577 (sh, 2.8 x $10^3$). Anal. Calcd. for $C_{36}H_{44}B_2NiP_2$ (1 x $C_4H_{10}O$): C, 69.31 H, 7.85. Found: C, 69.98 H, 8.62.

## *NMR Spectra*

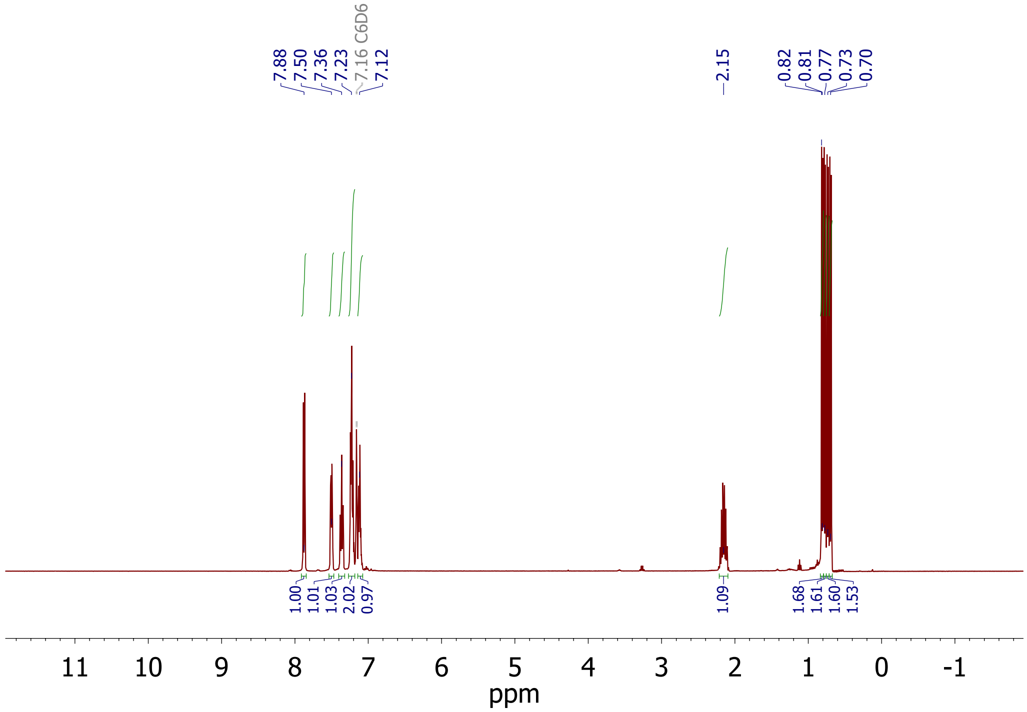

Figure 4-6. $^1$H NMR spectra of **$^{i}$Pr$_2$PPhBFlu** recorded at 400 MHz in $C_6D_6$.

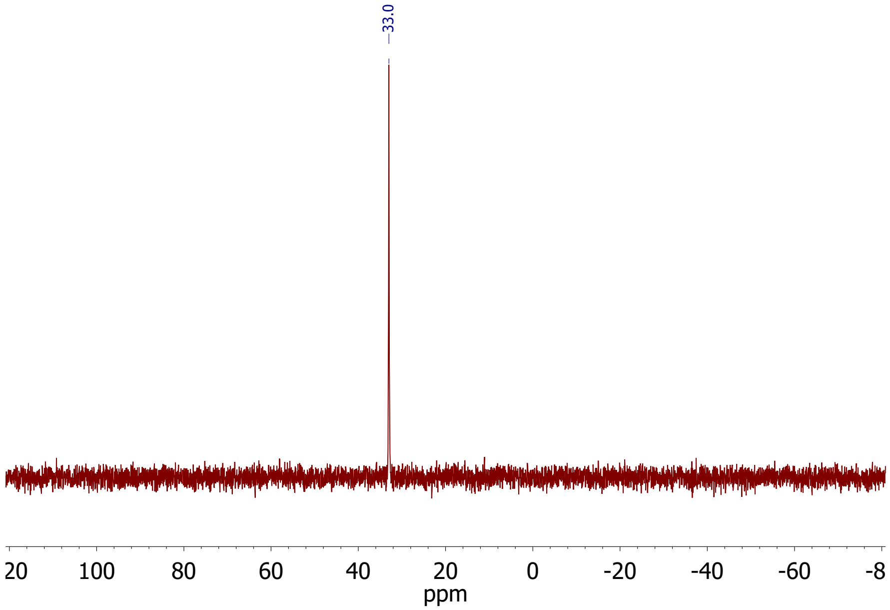

Figure 4-7. $^{31}$P NMR spectra of **$^{i}$Pr$_2$PPhBFlu** recorded at 162 MHz in $C_6D_6$.

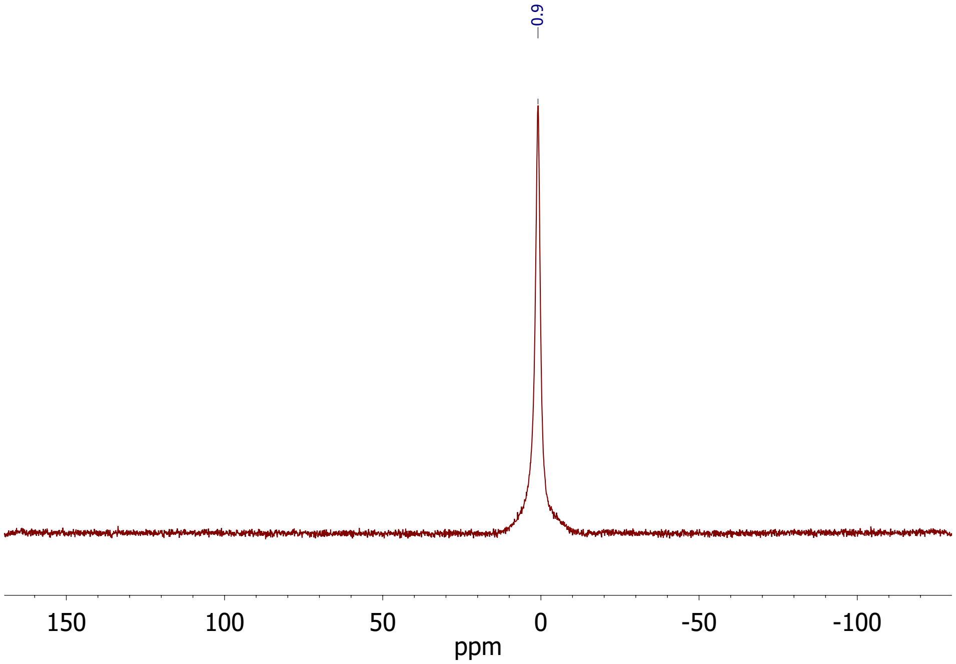

Figure 4-8. $^{11}$B NMR spectra of **$^{i}$Pr$_2$PPhBFlu** recorded at 128 MHz in $C_6D_6$.

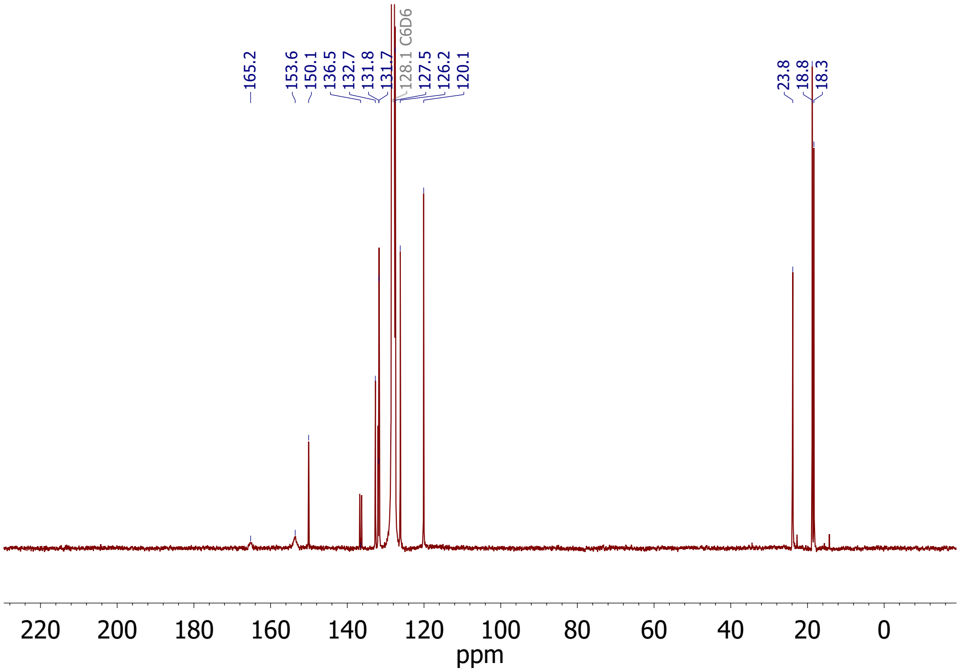

Figure 4-9. $^{13}$C NMR spectra of **$^{i}$Pr$_2$PPhBFlu** recorded at 101 MHz in $C_6D_6$.

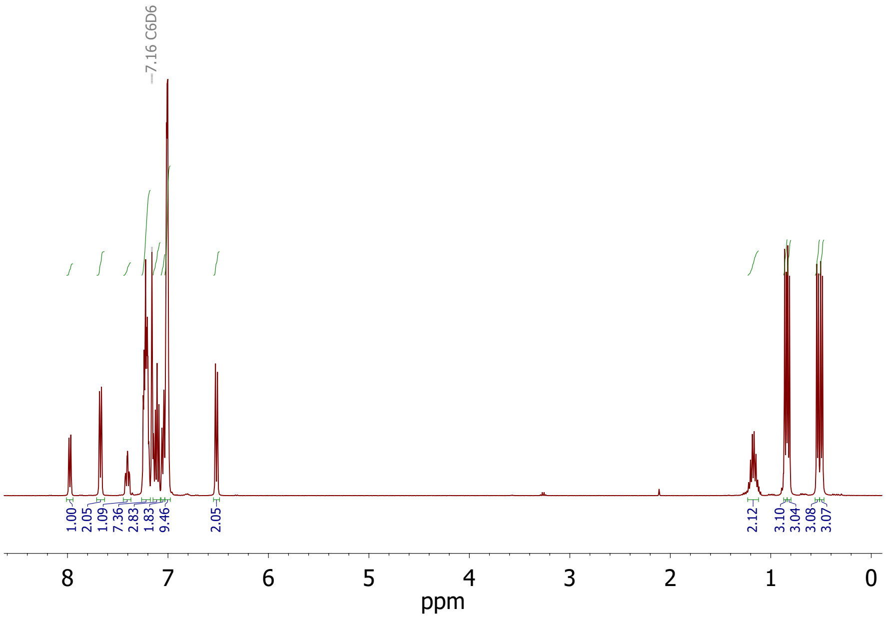

Figure 4-10. $^{1}$H NMR spectra of (**$^{i}$Pr$_2$PPhBFlu)Ni(PPh$_3$)** recorded at 400 MHz in $C_6D_6$.

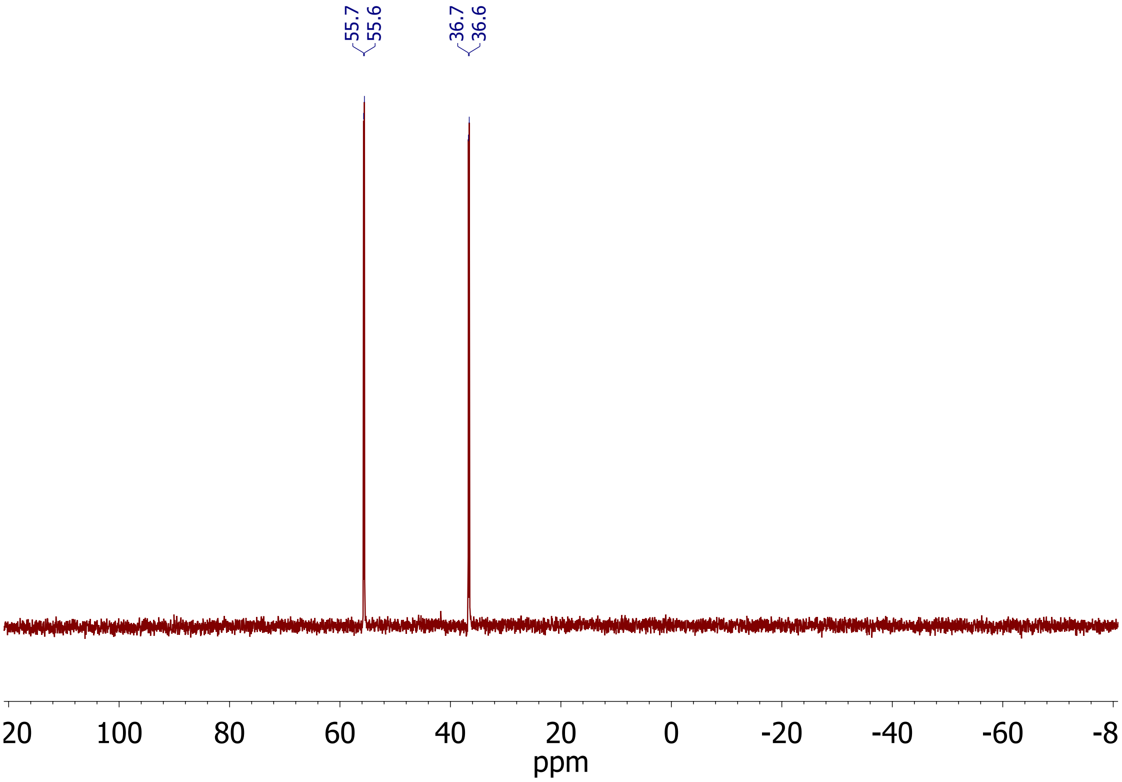

Figure 4-11. $^{31}$P NMR spectra of (**$^{i}$Pr$_2$PPhBFlu)Ni(PPh$_3$)** recorded at 162 MHz in $C_6D_6$.

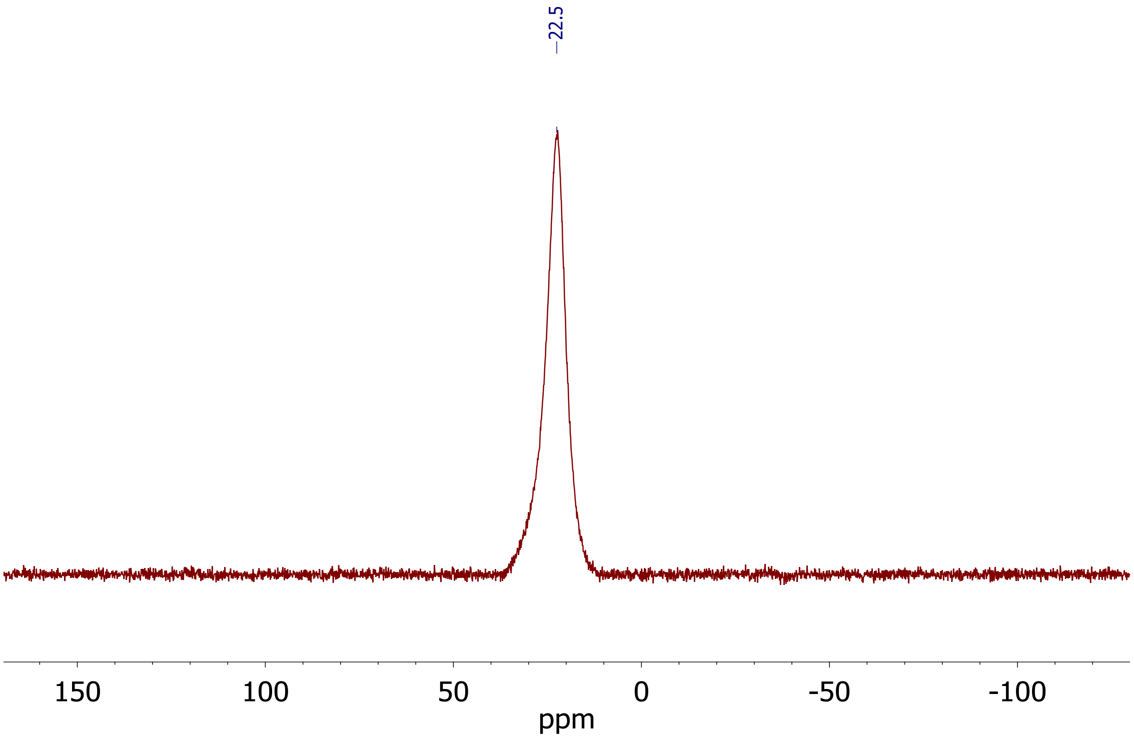

Figure 4-12. $^{11}$B NMR spectra of **($^{i}$Pr$_2$PPhBFlu)Ni(PPh$_3$)** recorded at 128 MHz in $C_6D_6$.

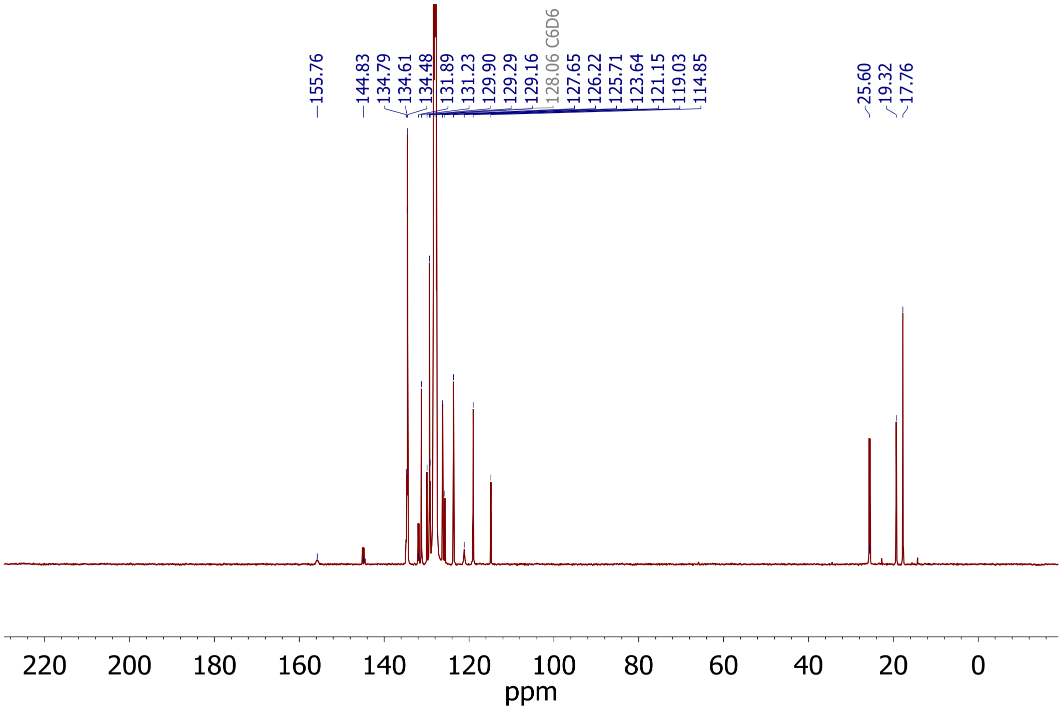

Figure 4-13. $^{13}$C NMR spectra of **($^{i}$Pr$_2$PPhBFlu)Ni(PPh$_3$)** recorded at 101 MHz in $C_6D_6$.

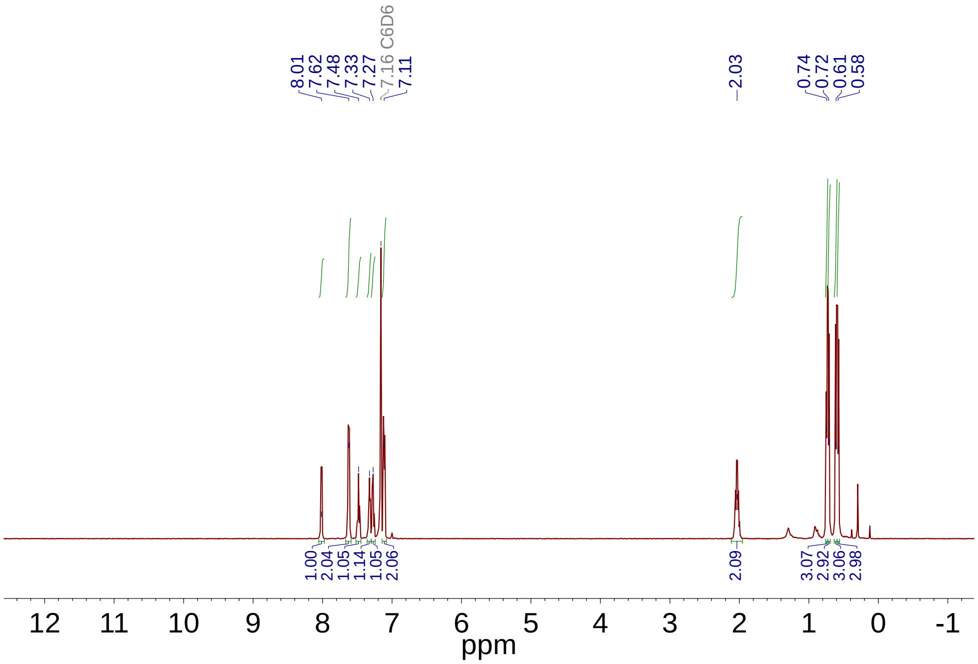

Figure 4-14. $^{1}$H NMR spectra of **Ni(B$_2$P$_2$)** recorded at 500 MHz in $C_6D_6$.

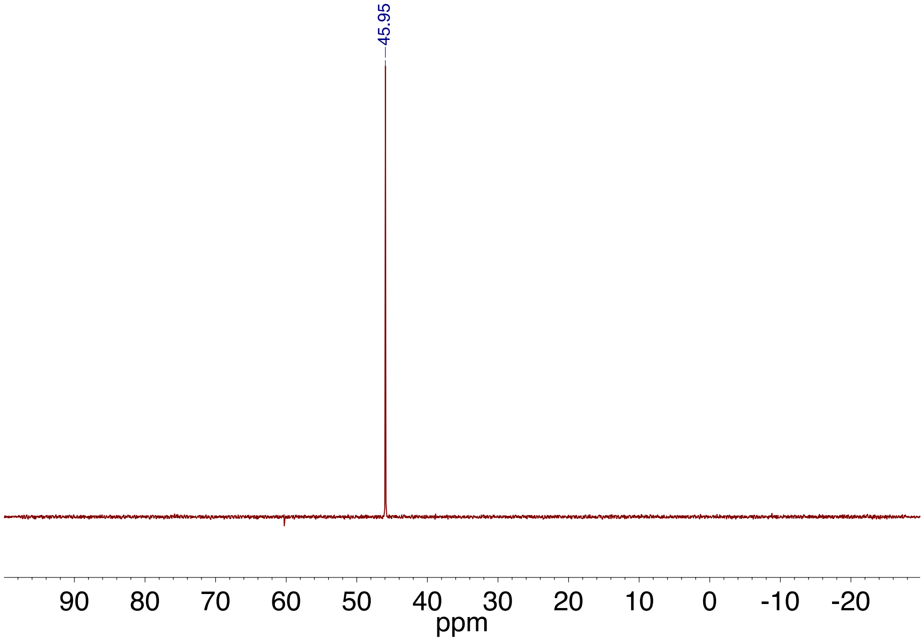

Figure 4-15. $^{31}$P NMR spectra of **Ni(B$_2$P$_2$)** recorded at 162 MHz in $C_6D_6$.

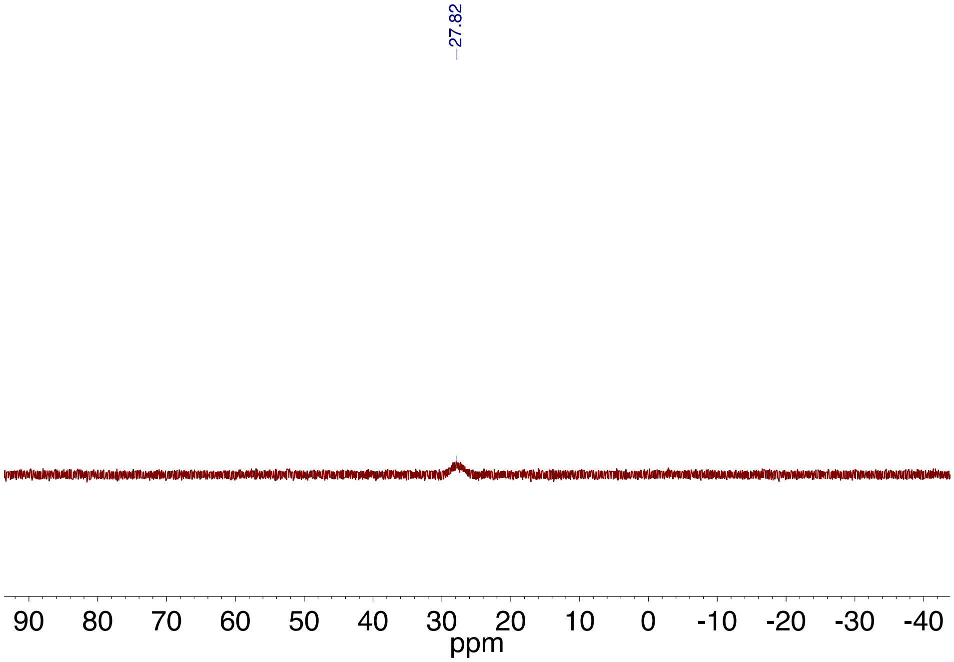

Figure 4-16. $^{11}$B NMR spectra of **Ni(B$_2$P$_2$)** recorded at 160 MHz in $C_6D_6$.

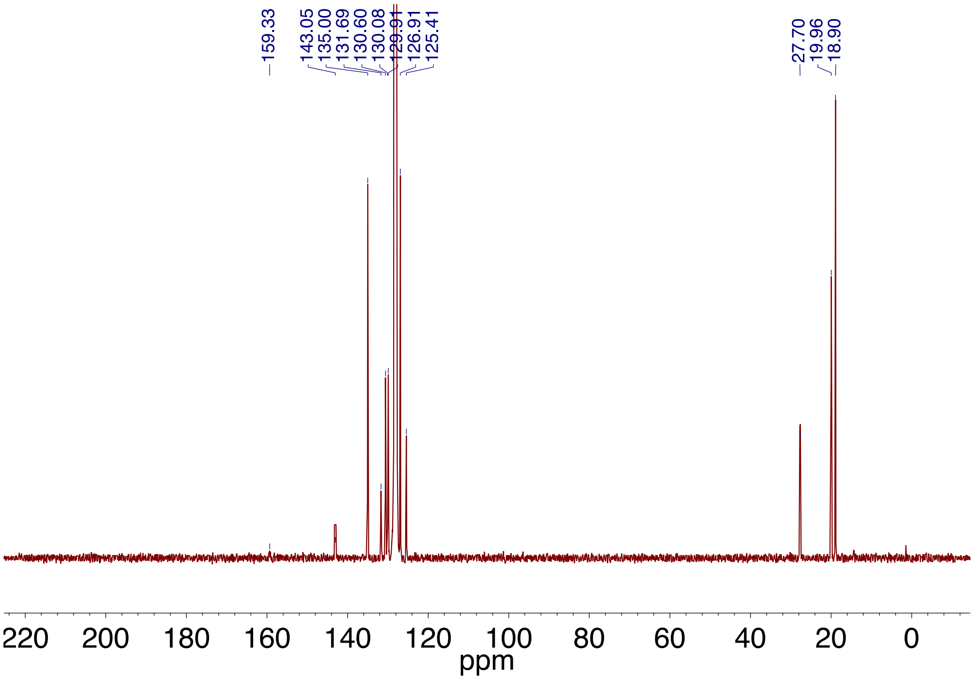

Figure 4-17. $^{13}$C NMR spectra of **Ni(B$_2$P$_2$)** recorded at 126 MHz in $C_6D_6$.

### *UV-Vis Spectra*

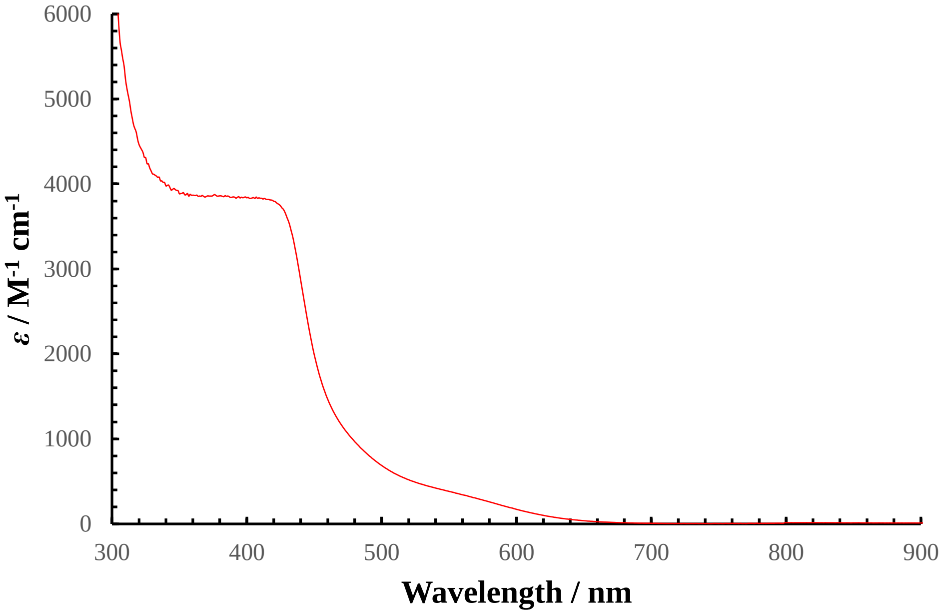

Figure 4-18. UV-Vis-NIR spectra of (**$^i$Pr$_2$PPhBFlu)Ni(PPh$_3$)** in THF.

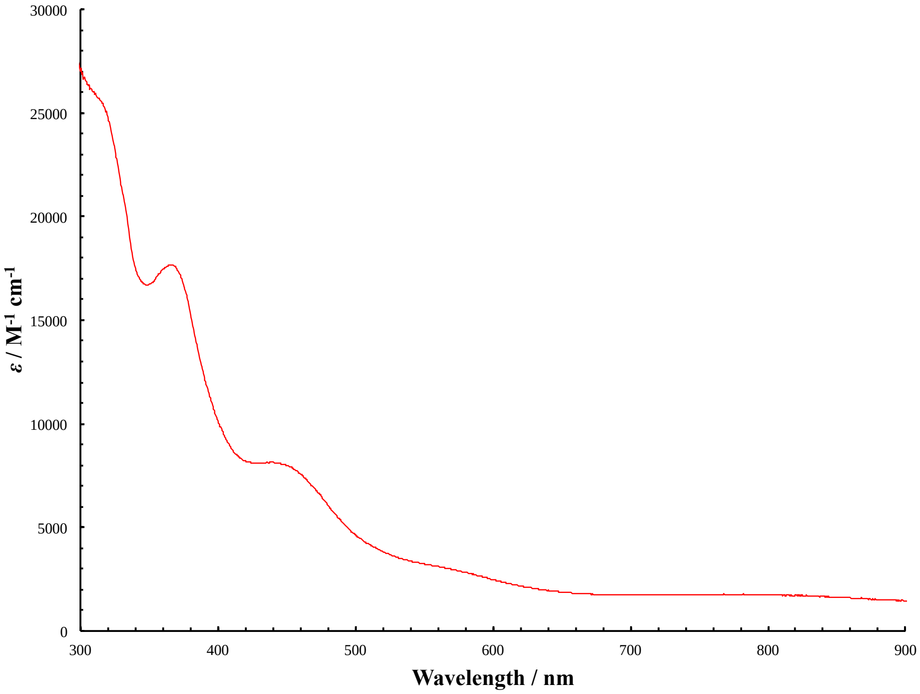

Figure 4-19. UV-Vis spectrum of **Ni(B$_2$P$_2$)** in THF.

*Cyclic Voltammetry*

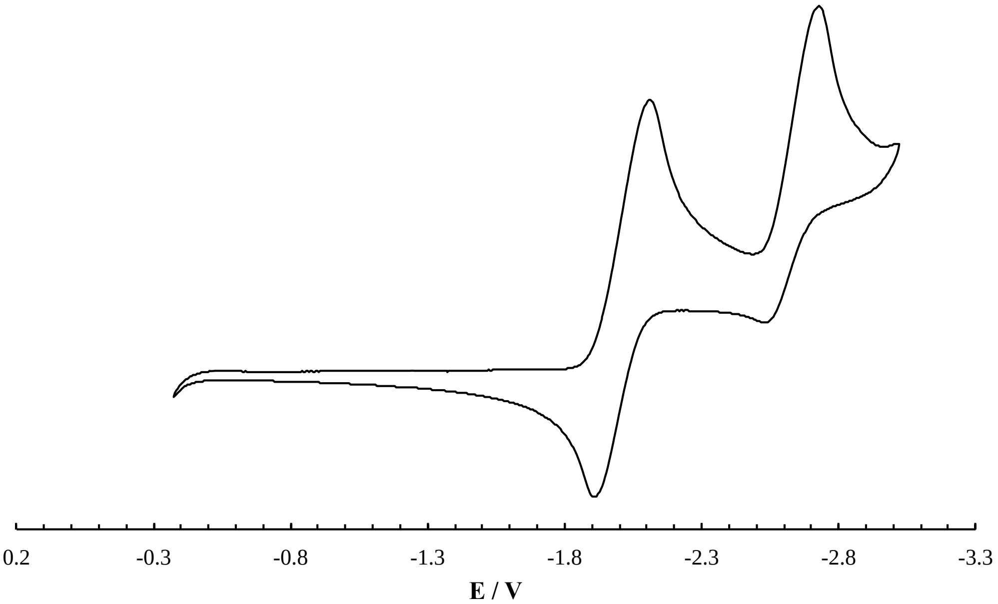

Figure 4-20. Cyclic voltammogram of $^{i}$**Pr$_2$PPhBFlu** in THF. (0.1 M *n*Bu$_4$NPF$_6$ as electrolyte, scan rate 100 mV/s).

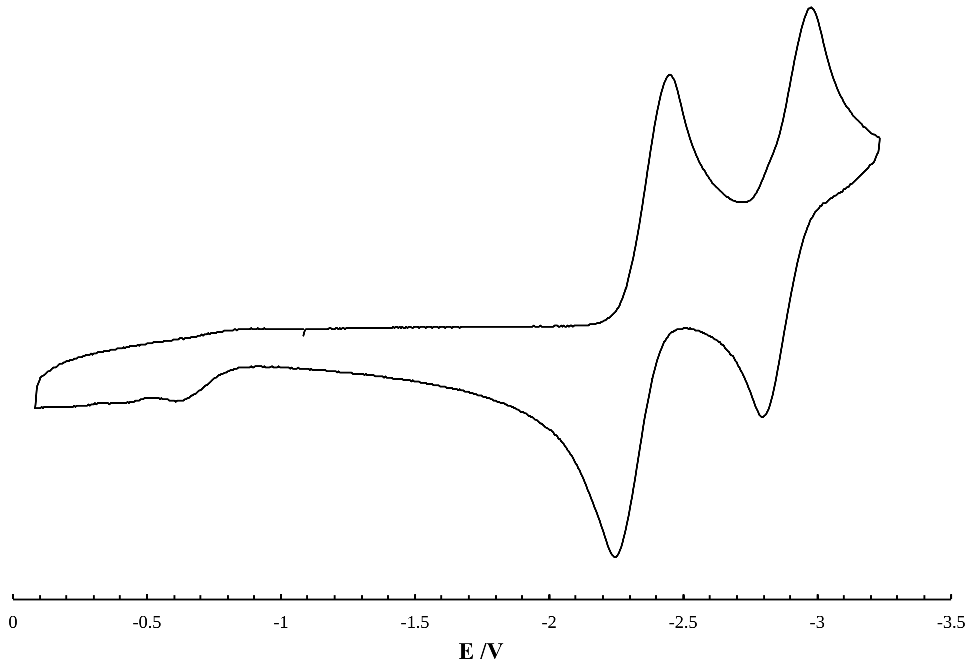

Figure 4-21. Cyclic voltammogram of **B$_2$P$_2$** in THF. (0.1 M *n*Bu$_4$NPF$_6$ as electrolyte, scan rate 100 mV/s).

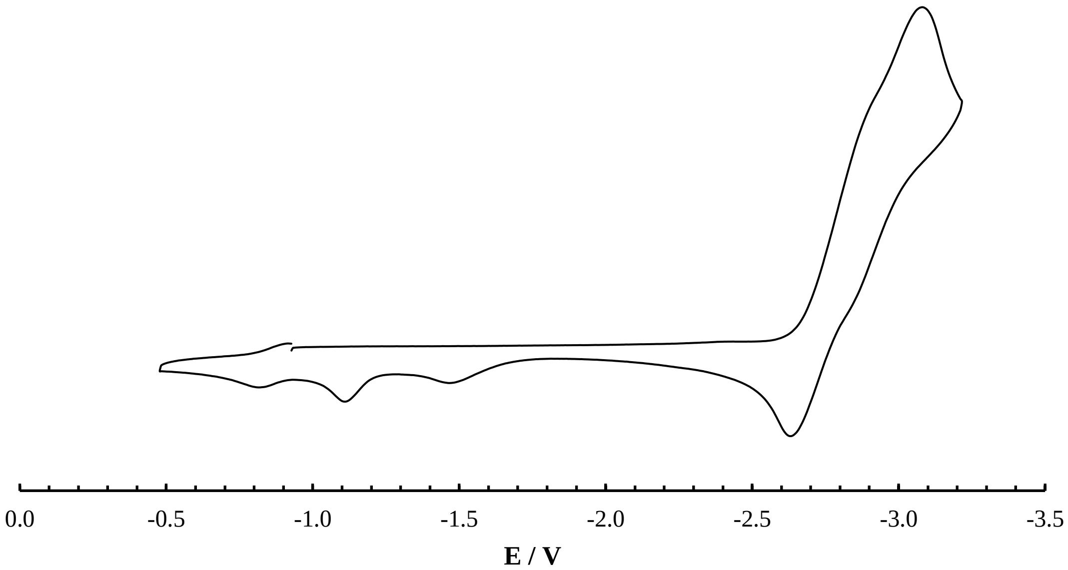

Figure 4-22. Cyclic voltammogram of (**$^{i}$Pr$_2$PPhBFlu)Ni(PPh$_3$)** in THF. (0.1 M *n*Bu$_4$NPF$_6$ as electrolyte, scan rate 100 mV/s).

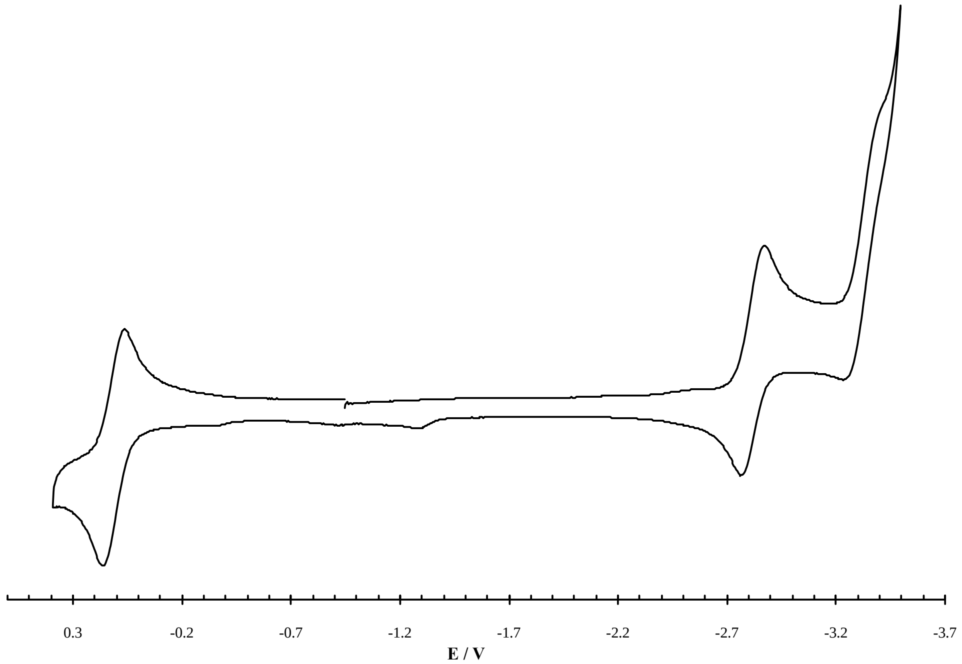

Figure 4-23. Cyclic voltammogram of **Ni(B$_2$P$_2$)** in THF. (0.1 M *n*Bu$_4$NPF$_6$ as electrolyte, scan rate 100 mV/s).

## *X-Ray Crystallography*

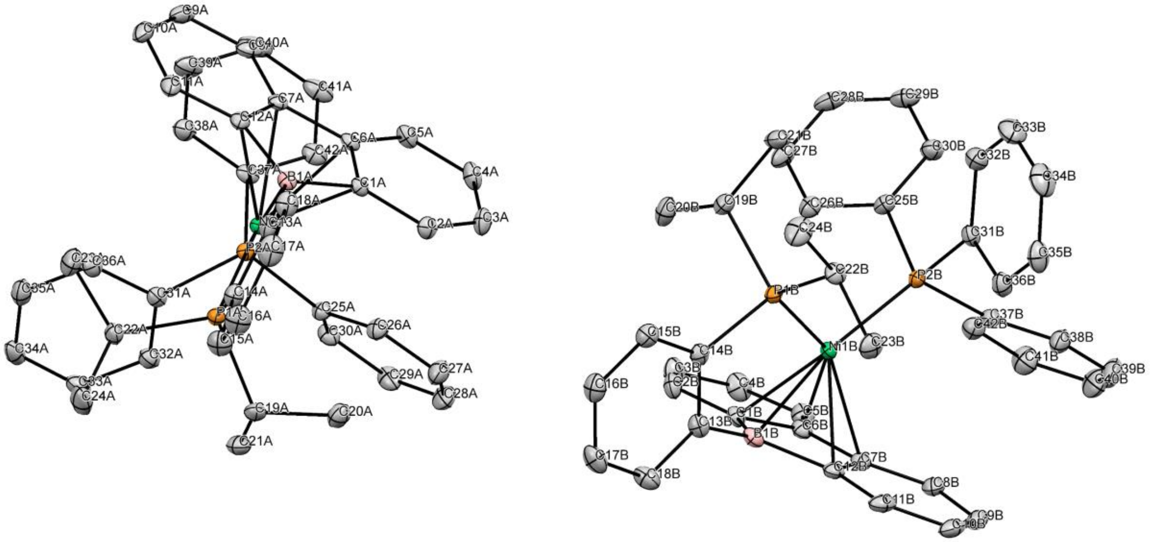

Figure 4-24. Labelled thermal ellipsoid plot (50%) for (**$^{i}$Pr$_2$PPhBFlu)Ni(PPh$_3$).**

Table 4-2. Crystal data and structure refinement for (**$^{i}$Pr$_2$PPhBFlu)Ni(PPh$_3$)**.

| | | |
|---|---|---|
| Identification code | hh126LE1_0m | |
| Empirical formula | $C_{42}H_{41}BNiP_2$ | |
| Formula weight | 677.21 g/mol | |
| Temperature | 100(2) K | |
| Wavelength | 0.71073 Å | |
| Crystal system | Orthorhombic | |
| Space group | $Pna2_1$ | |
| Unit cell dimensions | $a$ = 35.1597(17) Å | $\alpha$ = 90°. |
| | $b$ = 17.4014(8) Å | $\beta$ = 90°. |
| | $c$ = 11.3017(5) Å | $\gamma$ = 90°. |
| Volume | 6914.7(6) Å$^3$ | |
| Z | 8 | |
| Density (calculated) | 1.301 mg/m$^3$ | |
| Absorption coefficient | 0.683 mm$^{-1}$ | |
| F(000) | 2848 | |
| Crystal size | 0.558 x 0.156 x 0.044 mm$^3$ | |
| $\theta$ range for data collection | 1.647 to 30.507°. | |
| Index ranges | $-50 \leq h \leq 50$, $-24 \leq k \leq 24$, $-16 \leq l \leq 16$ | |
| Reflections collected | 196381 | |
| Independent reflections | 21113 [$R_{\mathrm{int}}$ = 0.0371] | |
| Completeness to $\theta$ = 25.242° | 100.0 % | |
| Absorption correction | Semi-empirical from equivalents | |
| Refinement method | Full-matrix least-squares on F$^2$ | |

| | |
|---|---|
| Data / restraints / parameters | 21113 / 1 / 837 |
| Goodness-of-fit on $F^2$ | 1.072 |
| Final $R$ indices [$I > 2\sigma_I$] | $R_1 = 0.0270$, $wR_2 = 0.0635$ |
| $R$ indices (all data) | $R_1 = 0.0303$, $wR_2 = 0.0649$ |
| Absolute structure parameter | 0.003(2) |
| Largest diff. peak and hole | 0.546 and –0.275 e/Å$^3$ |

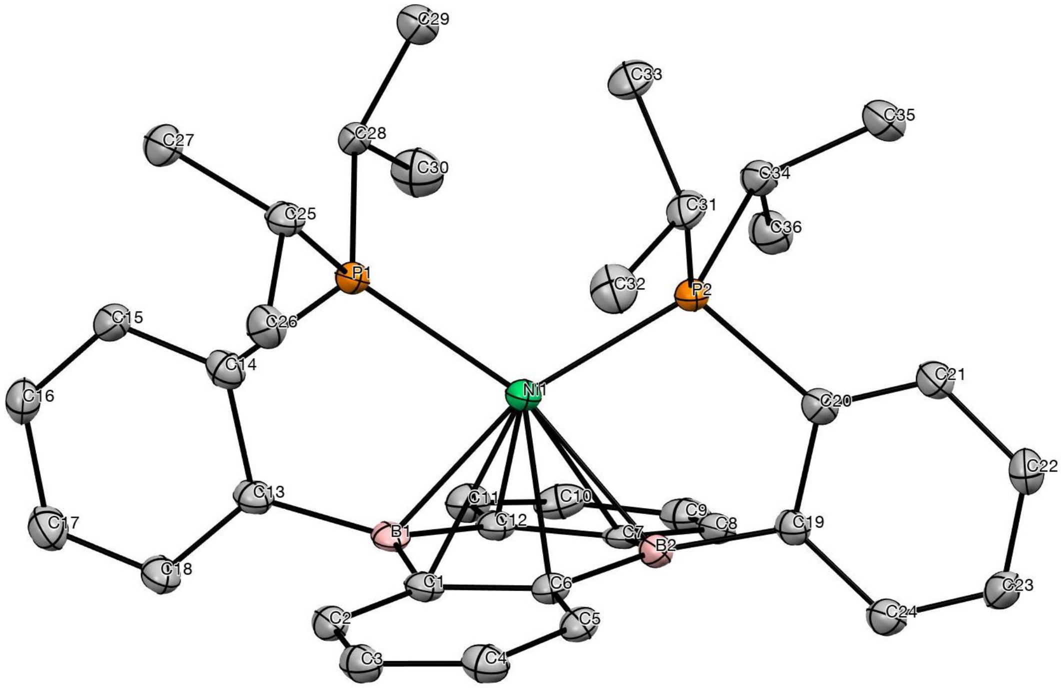

Figure 4-25. Labelled thermal ellipsoid plot (50%) for **Ni($B_2P_2$)**.

Table 4-3. Crystal data and structure refinement for **Ni($B_2P_2$)**.

| | | |
|---|---|---|
| Identification code | hh11JT6 | |
| Empirical formula | $C_{36}H_{44}B_2NiP_2$ | |
| Formula weight | 618.98 g/mol | |
| Temperature | 100(2) K | |
| Wavelength | 0.71073 Å | |
| Crystal system | Monoclinic | |
| Space group | $P2_1/c$ | |
| Unit cell dimensions | $a = 18.6867(17)$ Å | $\alpha = 90°$. |
| | $b = 10.9686(10)$ Å | $\beta = 97.5808(13)°$. |
| | $c = 15.4564(14)$ Å | $\gamma = 90°$. |
| Volume | 3140.4(5) Å$^3$ | |
| Z | 4 | |
| Density (calculated) | 1.309 mg/m$^3$ | |
| Absorption coefficient | 0.744 mm$^{-1}$ | |

| | |
|---|---|
| F(000) | 1312 |
| Crystal size | 0.298 x 0.179 x 0.096 mm$^3$ |
| $\theta$ range for data collection | 2.158 to 29.574° |
| Index ranges | $-25 \leq h \leq 25$, $-15 \leq k \leq 15$, $-21 \leq l \leq 21$ |
| Reflections collected | 82323 |
| Independent reflections | 8798 [$R_{\text{int}} = 0.0833$] |
| Completeness to $\theta = 25.242°$ | 100.0 % |
| Absorption correction | None |
| Refinement method | Full-matrix least-squares on F$^2$ |
| Data / restraints / parameters | 8798 / 0 / 378 |
| Goodness-of-fit on F$^2$ | 1.070 |
| Final $R$ indices [$I > 2\sigma_I$] | $R_1 = 0.0526$, $wR_2 = 0.1299$ |
| $R$ indices (all data) | $R_1 = 0.0805$, $wR_2 = 0.1466$ |
| Largest diff. peak and hole | 1.379 and –0.483 e/Å$^3$ |

## References

(1) Agnoli, S.; Favaro, M. Doping Graphene with Boron: A Review of Synthesis Methods, Physicochemical Characterization, and Emerging Applications. *J. Mater. Chem. A* **2016**, *4* (14), 5002–5025. https://doi.org/10.1039/C5TA10599D.

(2) Grimes, R. N. Boron-Containing Rings Ligated to Metals. In *Comprehensive Organometallic Chemistry III*; Elsevier, 2007; pp 1–48. https://doi.org/10.1016/B0-08-045047-4/00042-X.

(3) Amgoune, A.; Bourissou, D. σ-Acceptor, Z-Type Ligands for Transition Metals. *Chem. Commun.* **2011**, *47* (3), 859–871. https://doi.org/10.1039/C0CC04109B.

(4) Araki, T.; Fukazawa, A.; Yamaguchi, S. Electron-Donating Tetrathienyl-Substituted Borole. *Angew. Chemie Int. Ed.* **2012**, *51* (22), 5484–5487. https://doi.org/10.1002/anie.201201156.

(5) Braunschweig, H.; Dyakonov, V.; Jimenez-Halla, J. O. C.; Kraft, K.; Krummenacher, I.; Radacki, K.; Sperlich, A.; Wahler, J. An Isolable Radical Anion Based on the Borole Framework. *Angew. Chemie Int. Ed.* **2012**, *51* (12), 2977–2980. https://doi.org/10.1002/anie.201108632.

(6) Herberich, G. E.; Hostalek, M.; Laven, R.; Boese, R. Borole Dianions: Metalation of 1-(Dialkylamino)-2,5-Dihydro-LH-Boroles and the Structure of Li2(C4 H4 BNEt2)·TMEDA. *Angew. Chemie Int. Ed.* **1990**, *29* (3), 317–318. https://doi.org/10.1002/anie.199003171.

(7) Goettel, J. T.; Braunschweig, H. Recent Advances in Boron-Centered Ligands and Their Transition Metal Complexes. *Coord. Chem. Rev.* **2019**, *380*, 184–200. https://doi.org/10.1016/J.CCR.2018.09.013.

(8) Duan, J.; Chen, S.; Jaroniec, M.; Qiao, S. Z. Heteroatom-Doped Graphene-Based Materials for Energy-Relevant Electrocatalytic Processes. *ACS Catal.* **2015**, *5* (9), 5207–5234. https://doi.org/10.1021/acscatal.5b00991.

(9) Braunschweig, H.; Kupfer, T. Recent Developments in the Chemistry of Antiaromatic Boroles. *Chem. Commun.* **2011**, *47* (39), 10903. https://doi.org/10.1039/c1cc13071d.

(10) Bluer, K. R.; Laperriere, L. E.; Pujol, A.; Yruegas, S.; Adiraju, V. A. K.; Martin, C. D. Coordination and Ring Expansion of 1,2-Dipolar Molecules with 9-Phenyl-9-Borafluorene. *Organometallics* **2018**, *37* (17), 2917–2927. https://doi.org/10.1021/acs.organomet.8b00497.

(11) Fan, C.; Mercier, L. G.; Piers, W. E.; Tuononen, H. M.; Parvez, M. Dihydrogen

Activation by Antiaromatic Pentaarylboroles. *J. Am. Chem. Soc.* **2010**, *132* (28), 9604–9606. https://doi.org/10.1021/ja105075h.

(12) Fan, C.; Piers, W. E.; Parvez, M.; McDonald, R. Divergent Reactivity of Perfluoropentaphenylborole with Alkynes §. *Organometallics* **2010**, *29* (21), 5132–5139. https://doi.org/10.1021/om100334r.

(13) Braunschweig, H.; Chiu, C.-W.; Radacki, K.; Kupfer, T. Synthesis and Structure of a Carbene-Stabilized π-Boryl Anion. *Angew. Chemie Int. Ed.* **2010**, *49* (11), 2041–2044. https://doi.org/10.1002/anie.200906884.

(14) Bertermann, R.; Braunschweig, H.; Dewhurst, R. D.; Hörl, C.; Kramer, T.; Krummenacher, I. Evidence for Extensive Single-Electron-Transfer Chemistry in Boryl Anions: Isolation and Reactivity of a Neutral Borole Radical. *Angew. Chem. Int. Ed. Engl.* **2014**, *53* (21), 5453–5457. https://doi.org/10.1002/anie.201402556.

(15) Herberich, G. E.; Englert, U.; Hostalek, M.; Laven, R. Derivate Des Borols, XVI Bis(Borol)Nickel-Komplexe2). *Chem. Ber.* **1991**, *124* (1), 17–23. https://doi.org/10.1002/cber.19911240104.

(16) Romero, P. E.; Piers, W. E.; Decker, S. A.; Chau, D.; Woo, T. K.; Parvez, M. H1 versus H5 Bonding Modes in Cp*Al(I) Adducts of 9-Borafluorenes. *Organometallics* **2003**, *22* (6), 1266–1274. https://doi.org/10.1021/OM0209935.

(17) Bontemps, S.; Bouhadir, G.; Miqueu, K.; Bourissou, D. On the Versatile and Unusual Coordination Behavior of Ambiphilic Ligands O-R2P(Ph)BR'2. *J. Am. Chem. Soc.* **2006**, *128* (37), 12056–12057. https://doi.org/10.1021/ja0637494.

(18) von Grotthuss, E.; Diefenbach, M.; Bolte, M.; Lerner, H.-W.; Holthausen, M. C.; Wagner, M. Reversible Dihydrogen Activation by Reduced Aryl Boranes as Main-Group Ambiphiles. *Angew. Chemie Int. Ed.* **2016**, *55* (45), 14067–14071. https://doi.org/10.1002/anie.201608324.

(19) von Grotthuss, E.; Prey, S. E.; Bolte, M.; Lerner, H.-W.; Wagner, M. Selective CO $_2$ Splitting by Doubly Reduced Aryl Boranes to Give CO and [CO $_3$ ] $^{2-}$. *Angew. Chemie Int. Ed.* **2018**, *57* (50), 16491–16495. https://doi.org/10.1002/anie.201811135.

(20) von Grotthuss, E.; Nawa, F.; Bolte, M.; Lerner, H.-W.; Wagner, M. Chalcogen–Chalcogen-Bond Activation by an Ambiphilic, Doubly Reduced Organoborane. *Tetrahedron* **2019**, *75* (1), 26–30. https://doi.org/10.1016/J.TET.2018.11.012.

(21) Lorbach, A.; Bolte, M.; Lerner, H.-W.; Wagner, M. Dilithio 9,10-Diborataanthracene: Molecular Structure and 1,4-Addition Reactions. *Organometallics* **2010**, *29* (22), 5762–5765. https://doi.org/10.1021/om100825m.

(22) Taylor, J. W.; McSkimming, A.; Guzman, C. F.; Harman, W. H. N-Heterocyclic Carbene-Stabilized Boranthrene as a Metal-Free Platform for the Activation of Small Molecules. *J. Am. Chem. Soc.* **2017**, *139* (32), 11032–11035. https://doi.org/10.1021/jacs.7b06772.

(23) Müller, P.; Pritzkow, H.; Siebert, W. Ein-Und Mehrkernkomplexe Des 9,10-Dihydro-9,10-Dimethyl-9,10-Diboraanthracens. *J. Organomet. Chem.* **1996**, *524* (1–2), 41–47. https://doi.org/10.1557/opl.2011.1184.

(24) Müller, P.; Gangnus, B.; Pritzkow, H.; Schulz, H.; Stephan, M.; Siebert, W. Synthese, Struktur Und Eigenschaften Neuer Übergangsmetallkomplexe Des 9,10-Dihydro-9,10-Dimethyl-9,10-Diboraanthracens. *J. Organomet. Chem.* **1995**, *487* (1–2), 235–243. https://doi.org/10.1016/0022-328X(94)05101-G.

(25) Taylor, J. W.; McSkimming, A.; Moret, M.-E.; Harman, W. H. Copper and Silver Complexes of a Redox-Active Diphosphine-Diboraanthracene Ligand. *Inorg. Chem.* **2018**, acs.inorgchem.8b02710. https://doi.org/10.1021/acs.inorgchem.8b02710.

(26) Taylor, J. W.; McSkimming, A.; Moret, M.-E.; Harman, W. H. A Molecular Boroauride: A Donor-Acceptor Complex of Anionic Gold. *Angew. Chemie Int. Ed.* **2017**, *56* (35), 10413–10417. https://doi.org/10.1002/anie.201703235.

(27) Bontemps, S.; Bouhadir, G.; Dyer, P. W.; Miqueu, K.; Bourissou, D. Quasi-Thermoneutral P → B Interactions within Di- and Tri-Phosphine Boranes. *Inorg. Chem.* **2007**, *46* (13), 5149–5151. https://doi.org/10.1021/IC7006556.

(28) Herberich, G. E.; Hessner, B.; Ohst, H.; Raap, I. A. Borole Derivatives: XI. 1-(Diisopropylamino)Borole as Ligand in Transition Metal Complexes. Crystal and Molecular Structures of Cis-Cr(CO)2(C4H4BNP12)2 and Mn(CO)(C4H4BNPri2)2. *J. Organomet. Chem.* **1988**, *348* (3), 305–316. https://doi.org/10.1016/0022-328X(88)80412-1.

(29) Herberich, G. E.; Carstensen, T.; Koeffer, D. P. J.; Klaff, N.; Boese, R.; Hyla-Kryspin, I.; Gleiter, R.; Stephan, M.; Meth, H.; Zenneck, U. Borole Derivatives. 20. Three-Center Fe-H-B Bonding in (Borole)(Cyclopentadienyl)Hydridoiron Derivatives. *Organometallics* **1994**, *13* (2), 619–630. https://doi.org/10.1021/om00014a037.

(30) Herberich, G. E.; Eckenrath, H. J.; Englert, U. Borole Derivatives. 24.1 Synthesis of Cationic (Arene)(Phenylborole)Rhodium Complexes. Structures of the Trinuclear Complex (H5-C4H4BPh)Rh(M3-I)3-Rh(μ,H5:H6-C4H4BPh)Rh(H5-C4H4BMe)·CH2Cl2 and of the Polymeric Catena-(μ,H5:H6-1-Phenylborole)Rhodium Tetraflu. *Organometallics* **1998**, *17* (4), 519–523. https://doi.org/10.1021/OM970742+.

(31) Shoji, Y.; Tanaka, N.; Muranaka, S.; Shigeno, N.; Sugiyama, H.; Takenouchi, K.; Hajjaj, F.; Fukushima, T. Boron-Mediated Sequential Alkyne Insertion and C–C Coupling Reactions Affording Extended π-Conjugated Molecules. *Nat. Commun.* **2016**, *7* (1), 12704. https://doi.org/10.1038/ncomms12704.

(32) Isopropyl Groups Were Simplified to Methyl Groups. Isopropyl groups were simplified to methyls.

(33) Berger, C. J.; He, G.; Merten, C.; McDonald, R.; Ferguson, M. J.; Rivard, E. Synthesis and Luminescent Properties of Lewis Base-Appended Borafluorenes. *Inorg. Chem.* **2014**, *53* (3), 1475–1486. https://doi.org/10.1021/ic402408t.

(34) Neese, F. Orca 4.2.1. *Wiley Interdiscip. Rev. Comput. Mol. Sci.* **2012**, *2*, 73.

(35) Hanwell, M. D.; Curtis, D. E.; Lonie, D. C.; Vandermeersch, T.; Zurek, E.; Hutchison, G. R. Avogadro 1.2. *J. Cheminform.* **2012**, *4*, 17.

# Chapter 5 : Appendix of Loose Ends

## *Thioether-Decorated Ylides*

Inspired by the FeMoco cofactor in nitrogenase, we pursued ligand structures containing thiolates featuring a central ylide carbon to emulate the carbide of this co-factor in a simpler system. To build steric bulk around the metal, we synthesized two biaryl thiol arms: mesityl and 3,5-tert-butylphenyl (**1**). The latter is an unreported material. It is a colorless oil that has the consistency of thick honey. The synthesis is as follows:

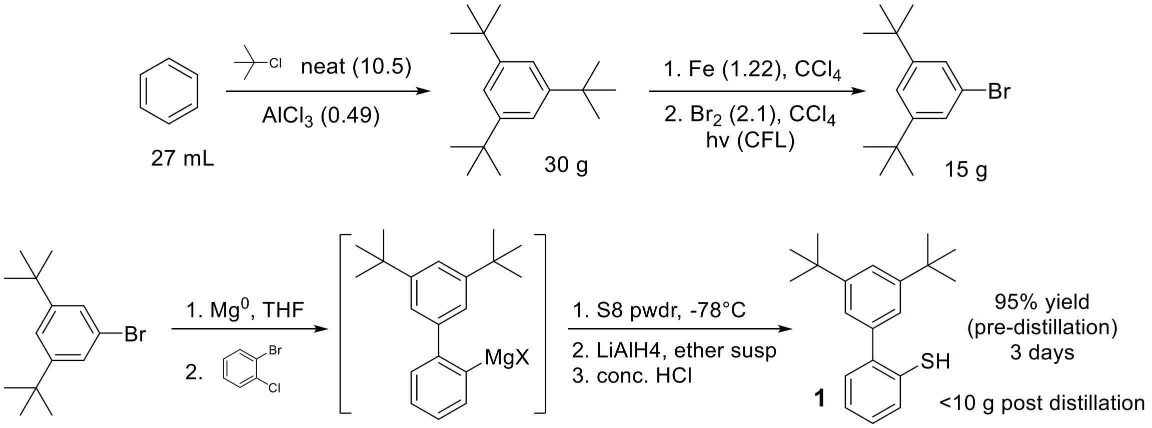

Scheme 5-1. Parallel synthesis of 3',5'-di-tert-butyl-[1,1'-biphenyl]-2-thiol (**1**).

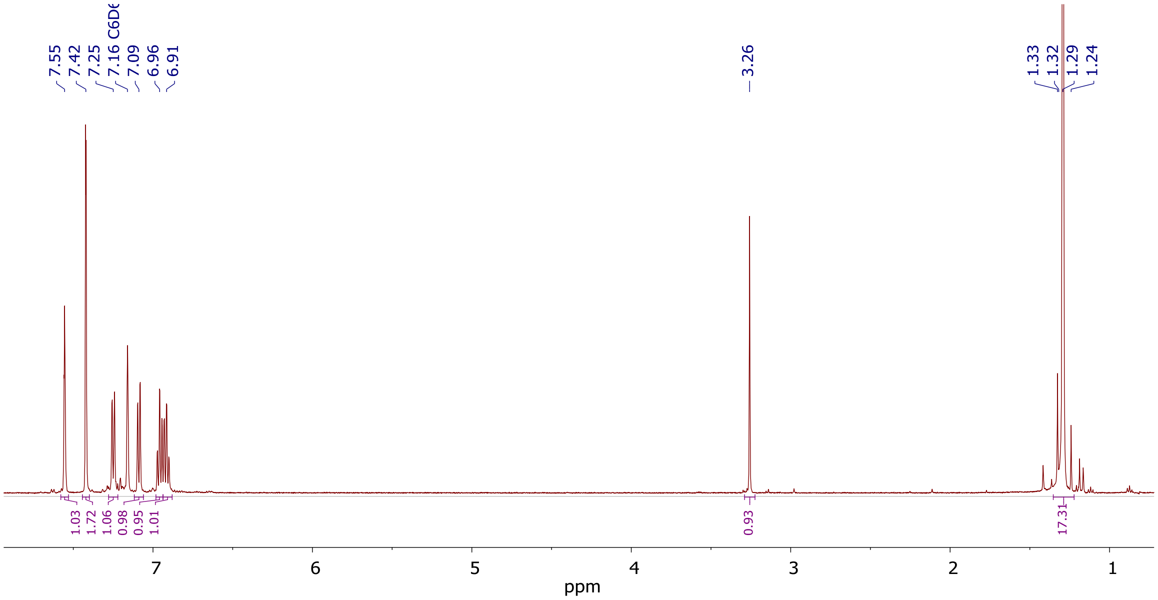

Figure 5-1. NMR spectrum of 3',5'-di-tert-butyl-[1,1'-biphenyl]-2-thiol (**1**) at 500 MHz in $C_6D_6$.

$^1$H NMR (500 MHz, $C_6D_6$) δ 7.56 (t, *J* = 1.7 Hz, 1H), 7.42 (d, *J* = 1.8 Hz, 2H), 7.25 (dd, *J* = 7.4, 1.3 Hz, 1H), 7.09 (dd, *J* = 7.7, 1.2 Hz, 1H), 6.96 (td, *J* = 7.4, 1.3 Hz, 1H), 6.91 (td, *J* = 7.5, 1.5 Hz, 1H), 3.26 (s, 1H), 1.29 (s, 18H).

The double lithiation strategy below was previously reported[1] using TMS and aliphatic groups. However this procedure when applied to our mesitylene or 3,5-tert-butylphenyl analogues produced intractable mixtures. Difficulties of ortho-lithiation of similar biaryl thiol substrates has been previously reported.[2]

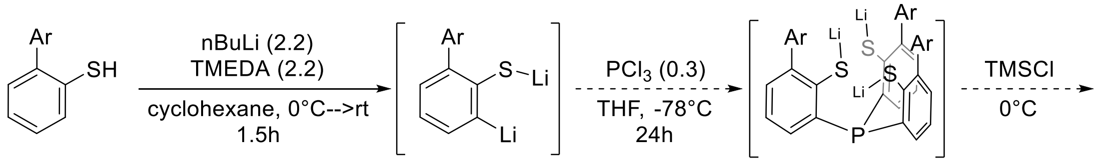

Scheme 5-2. Double lithiation strategy for accessing aryl thiolate appended phosphines.

Seeing that biaryls need to be avoided, we investigated thioethers as more readily isolable species which could be reductively deprotected.

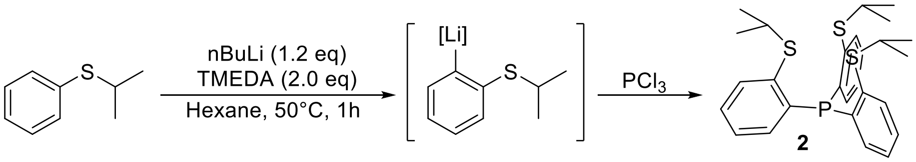

Scheme 5-3. Synthesis of tris(isopropyl-thioether) phosphine (**2**), previously reported.[3]

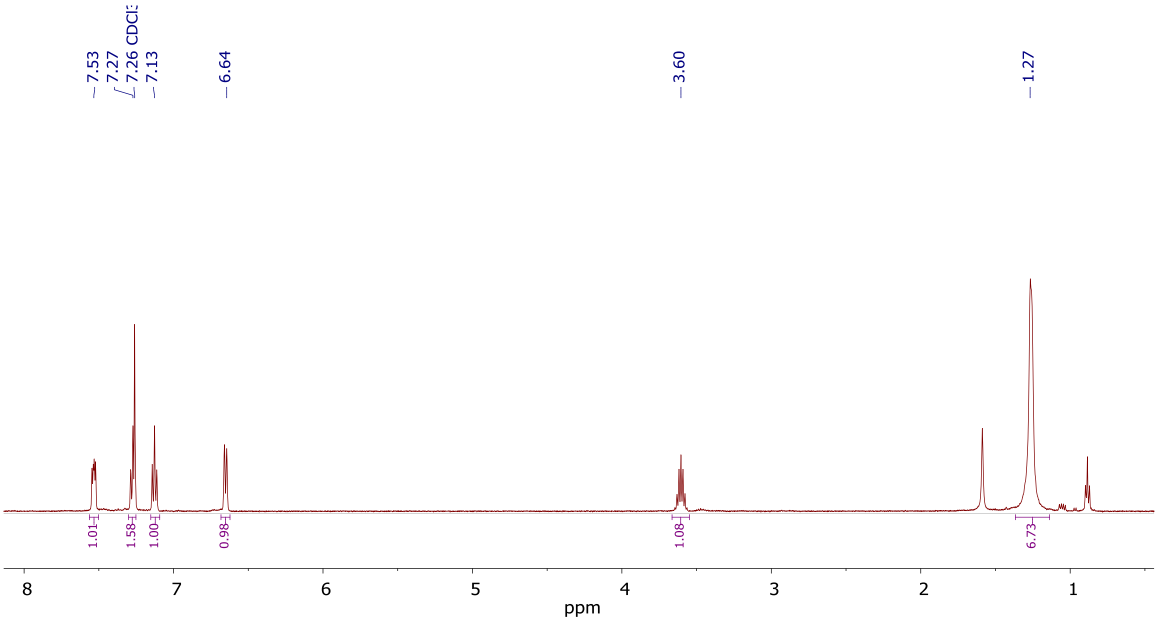

Figure 5-2. NMR spectrum of tris(isopropyl-thioether) phosphine (**2**) at 500 MHz in $CDCl_3$.

However, reductively removing ($Li^0$ + 4-(dimethylamino)pyridine) the isopropyl groups proved destructive towards the phosphine, so we turned to methyl-protected thioethers. We pursued both the tris-thioether and the bis-thioether **4**. We had more success with the latter. Methylation proved facile if the hassle of drying methyl iodide is ignored. $^{31}P$ decoupling of the $^1H$ peak at 3.12 ppm verified the assignment of the phosphonium methyl (Figure 5-3).

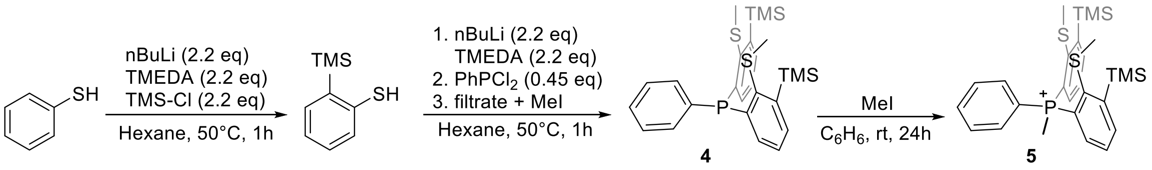

Scheme 5-4. Synthesis of thioether tethered phosphines.

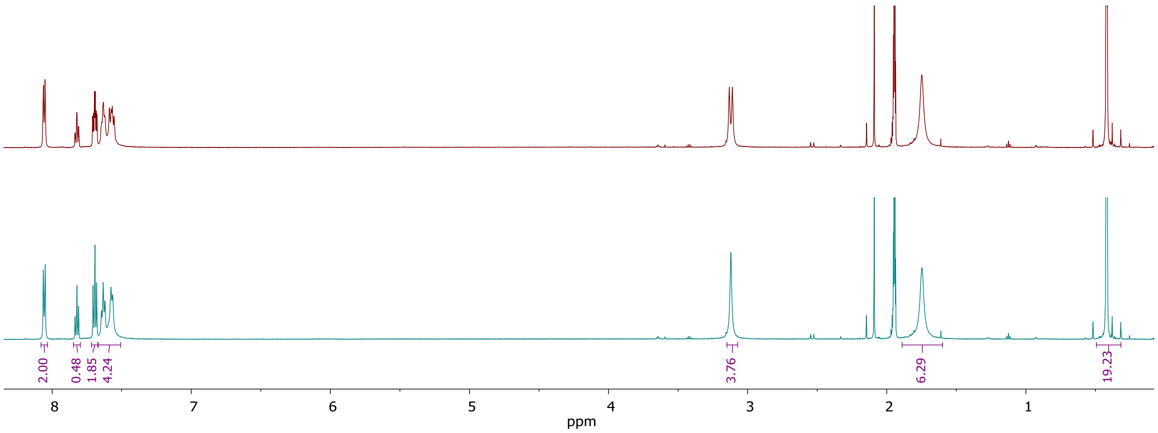

Figure 5-3. $^{1}$H-NMR (top) and $^{1}$H-{$^{31}$P} NMR of **4** at 600 MHz in CD$_3$CN. $^{2}J_{H,P}$ = 13.4 Hz.

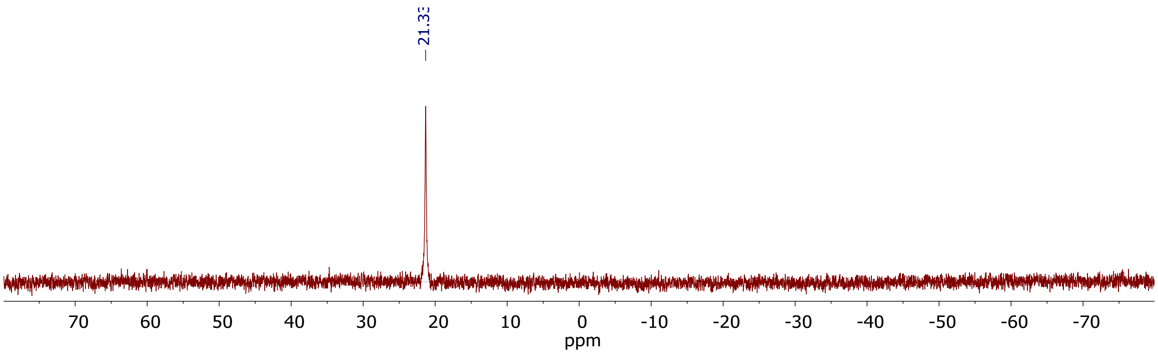

Figure 5-4. $^{31}$P-NMR of **4**.

Deprotonation occurred cleanly with sodium hydride generating the corresponding ylide **6**. This was signified by the phosphorus resonance shifting ~7.5 ppm downfield.

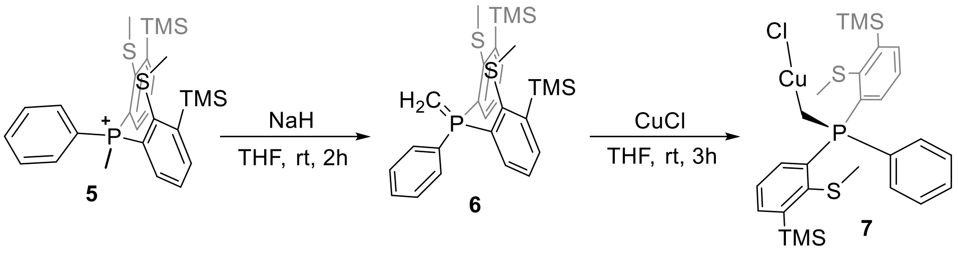

Scheme 5-5. Ylide generation and metallation with copper.

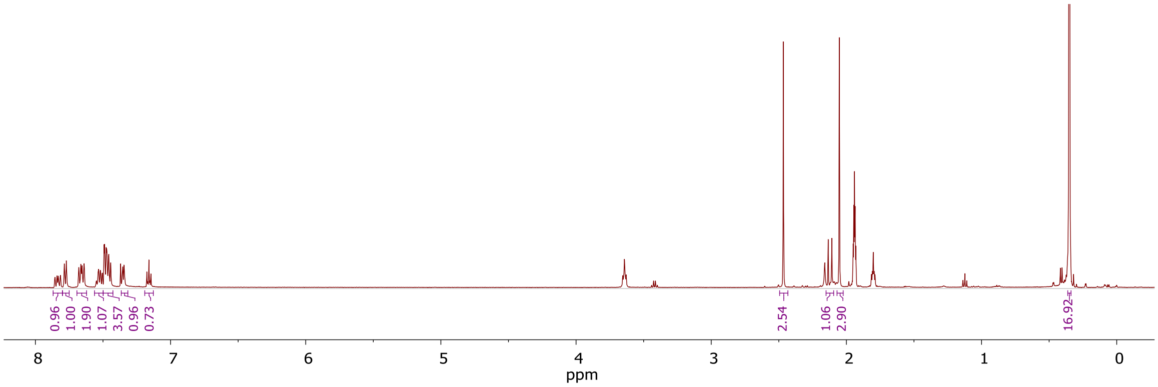

Figure 5-5. ${}^{1}$H-NMR of ylide **6** at 500 MHz in $CD_3CN$.

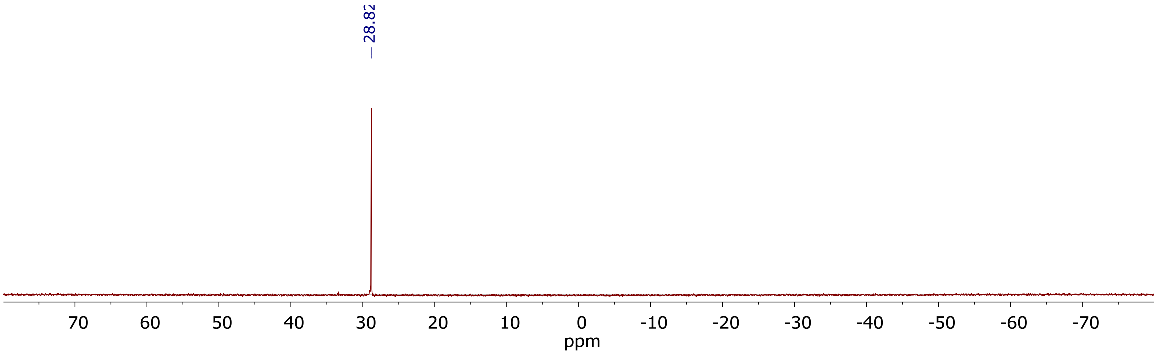

Figure 5-6. ${}^{31}$P-NMR of ylide **6** at 500 MHz in $CD_3CN$.

Metallation with copper chloride occurred cleanly generating **7** as a colorless white solid. The ${}^{31}$P signal drifted another ~4 ppm downfield in response (Figure 5-8). X-Ray diffraction revealed a copper-carbon bond of 1.925(6) Å and the two thioethers in the periphery oriented away from the metal center.

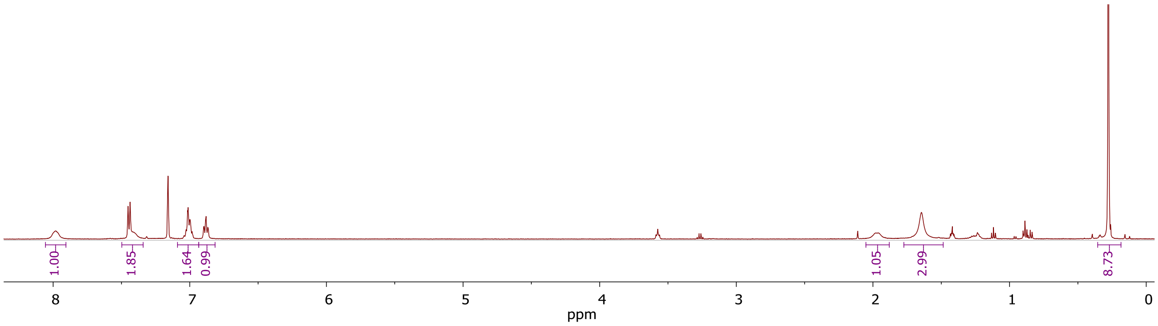

Figure 5-7. ${}^{1}$H-NMR of copper ylide **7** at 500 MHz in $C_6D_6$.

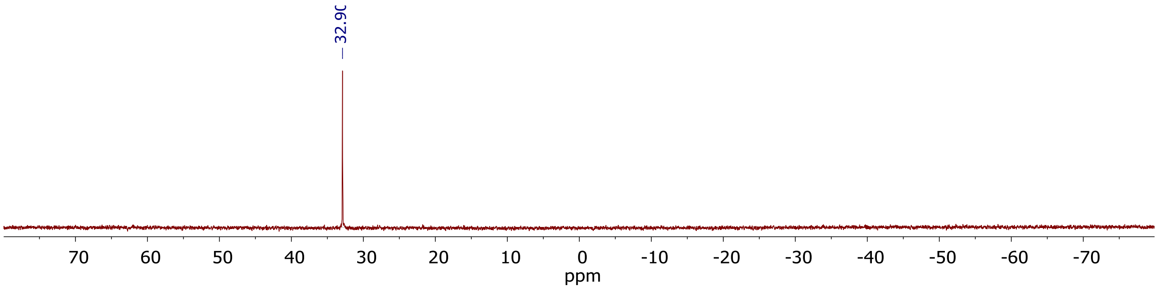

Figure 5-8. $^{31}$P-NMR of copper ylide **7** at 202 MHz in $C_6D_6$.

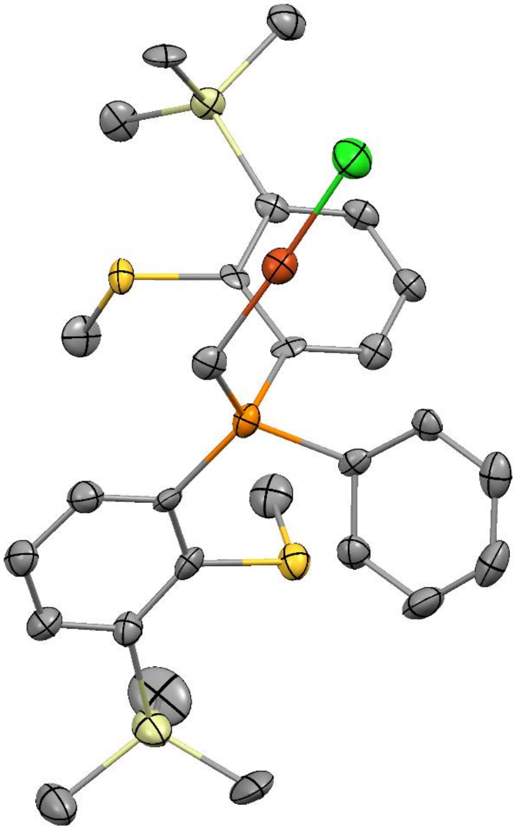

Figure 5-9. Labeled thermal ellipsoid plots (50%) of **7**. Orange, yellow, pale yellow, red, green, and gray ellipsoids represent P, S, Si, Cu, Cl, and C atoms, respectively. Hydrogen atoms and co-crystallized solvent molecules are omitted for clarity.

The synthetic difficulties associated with this ligand made it impractical relative to other ligands we were generating in our lab that yielded much more interesting results.

## *Dithiocarboxylate Terphenyls at Iron*

Continuing the obsession with FeMoco, we sought a simple ligand structure that would just get sulfurs nearby a reduced iron center—forget the carbide. Both the mesityl and tri-isopropyl phenyl terphenyl dithiocarboxylates have been previously synthesized.[4]

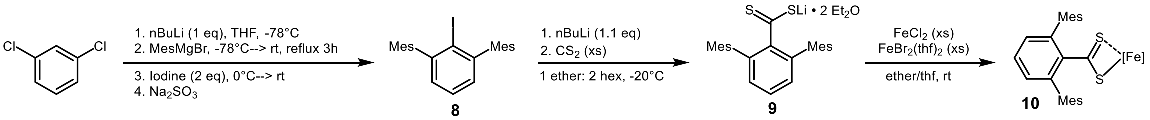

Scheme 5-6. Synthesis of Mes terphenyl thiocarboxylate and its metallation.

To verify the installation of the thiocarboxylate functionality, an aliquot was protonated with ammonium chloride (Figure 5-10). Upon protonation this species converts from a golden-orange color to a coral pink.

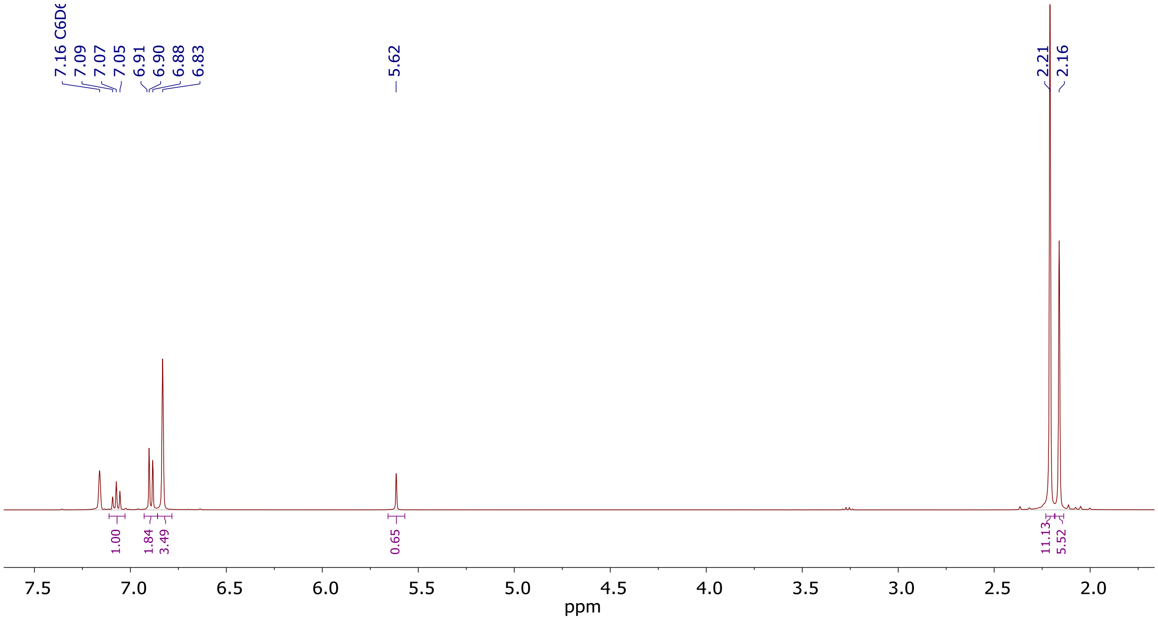

Figure 5-10. $^1$H-NMR the protonated of **9** at 500 MHz in $C_6D_6$.

Metallation of anionic ligands is always a pleasure. Bright orange crystals of **9** when mixed with $FeCl_2$ produced a deep green solution which readily crystallized. The NMR of the crystalline solid is what it is: a paramagnetic mess of peaks (Figure 5-11).

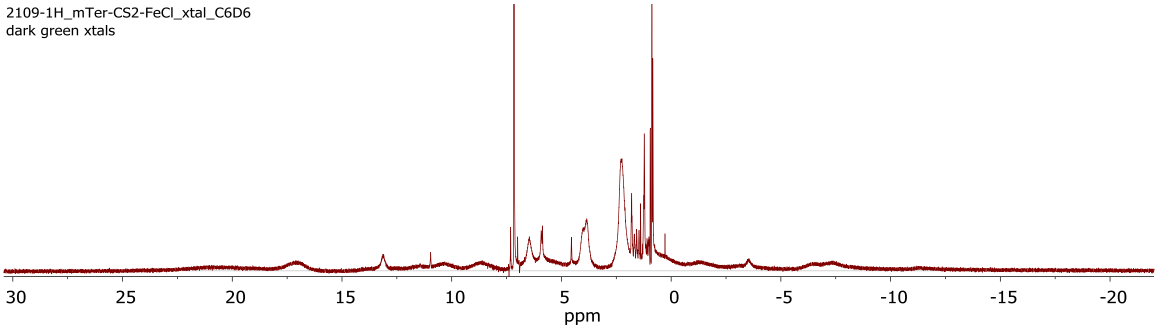

Figure 5-11. $^1$H-NMR of **10** at 500 MHz in $C_6D_6$.

X-Ray diffraction revealed an overlay of the 5-coordinate and 6-coordinate species with either a single ether or two THF’s bound to the iron (Figure 5-12).

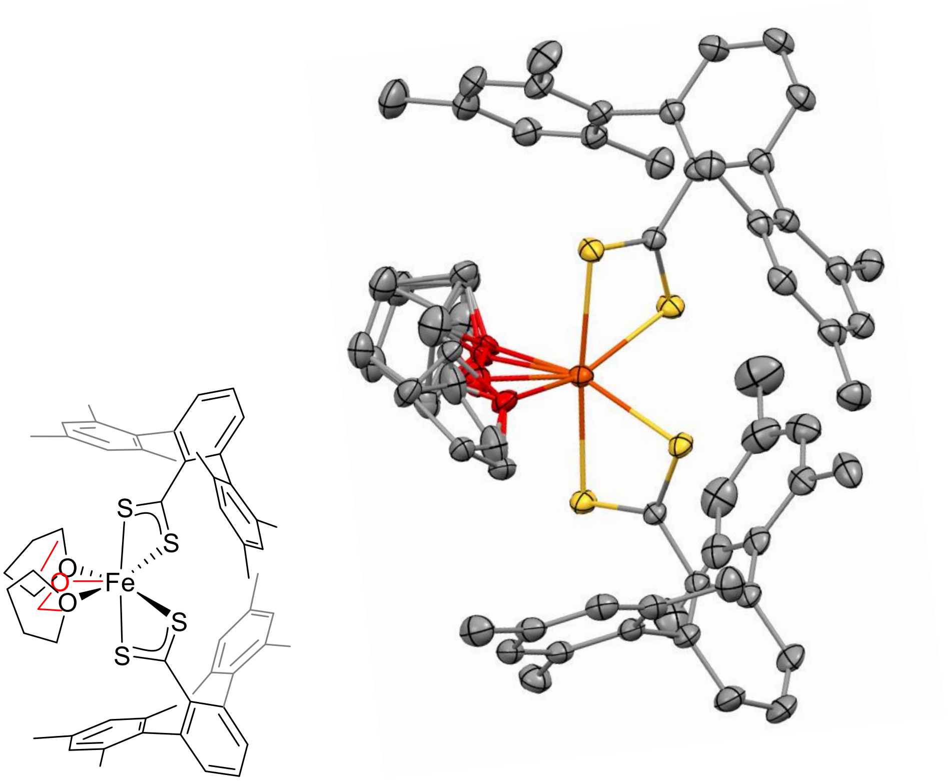

Figure 5-12. Labeled thermal ellipsoid plots (50%) of **10**. Red, orange, yellow, and gray ellipsoids represent O, Fe, S, and C atoms, respectively. Hydrogen atoms and co-crystallized solvent molecules are omitted for clarity.

We ran CV to assess the reductive capabilities of **10**. They looked very promising with at least two semi-reversible reduction events at −2.44 and −2.75 V vs. Fc/Fc$^+$ (Figure 5-13).

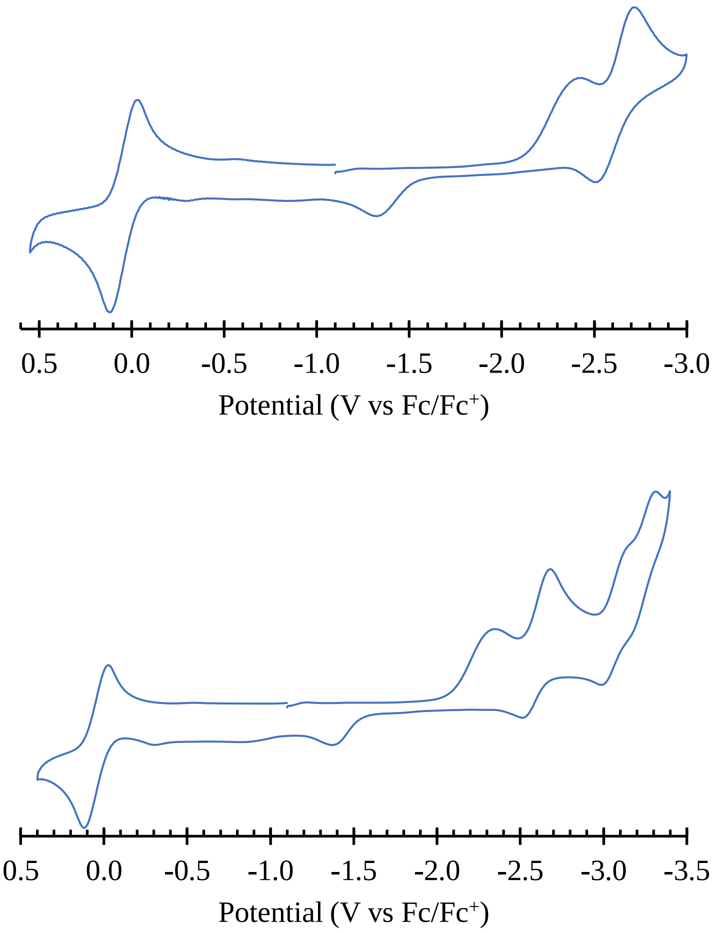

Figure 5-13. Cyclic voltammograms of mTerCS2Fe (**10**) in THF (0.1 M [*n*$Bu_4N$]$PF_6$ as electrolyte; 100 mV/s scan rate).

Metallation of the protonated version of **9** was also attempted using dimesityl iron. However, what was recovered were dark green crystals of the homoleptic iron (III) species (**11**). Unfortunately, chemical reduction of **10** proved much more problematic than the CV implied. Reduction recovered free ligand, the (mTerCS$_2$)Na(thf) dimer, or non-crystalline products (Figure 5-14).

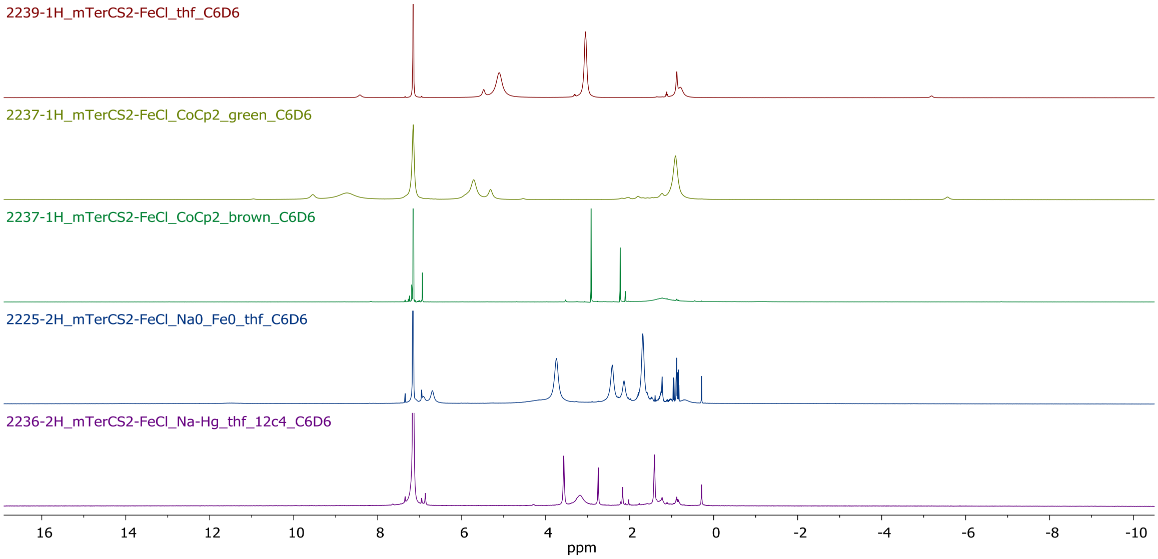

Figure 5-14. $^1$H-NMR of attempts at reducing **10**.

We explored other iron sources for metallation (Figure 5-15).

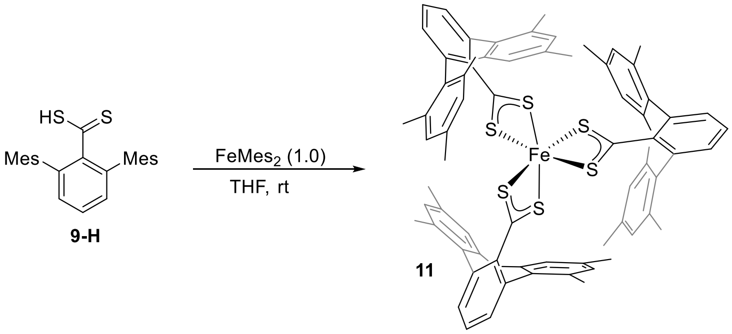

Figure 5-15. Metallation of **9**-H with FeMes$_2$ and oxidation to **11**.

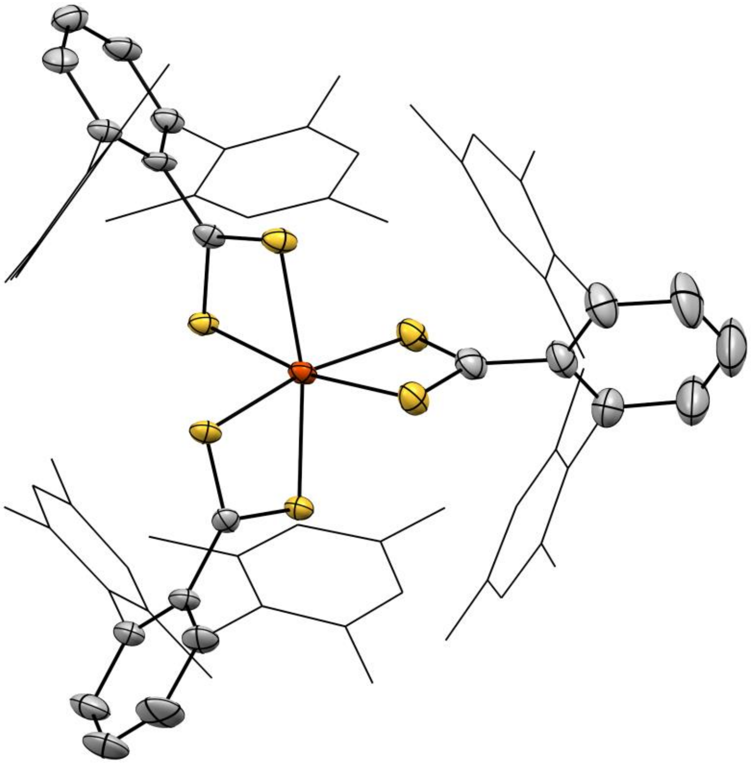

Figure 5-16. Labeled thermal ellipsoid plots (50%) of **11.** Orange, yellow, and gray ellipsoids represent Fe, S, and C atoms, respectively. Hydrogen atoms and co-crystallized solvent molecules are omitted for clarity.

Metallation using Bill Tolman's method[5] for metallation of carboxylate analogues using iron triflate produced dichroic red-green solution (Scheme 5-7). Black crystals formed the Fe(II) dimer **12** (Figure 5-17).

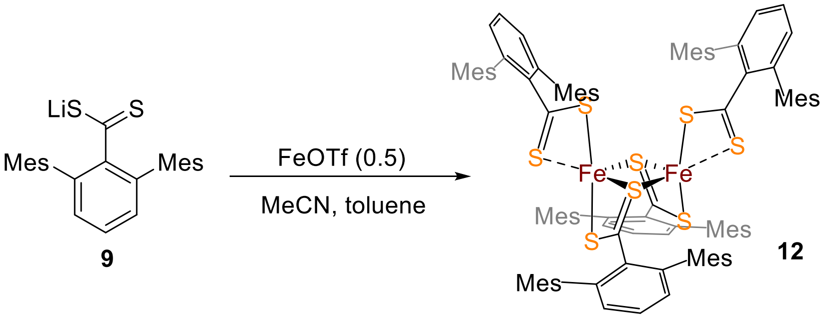

Scheme 5-7. Synthesis of μ-dimer **12**.

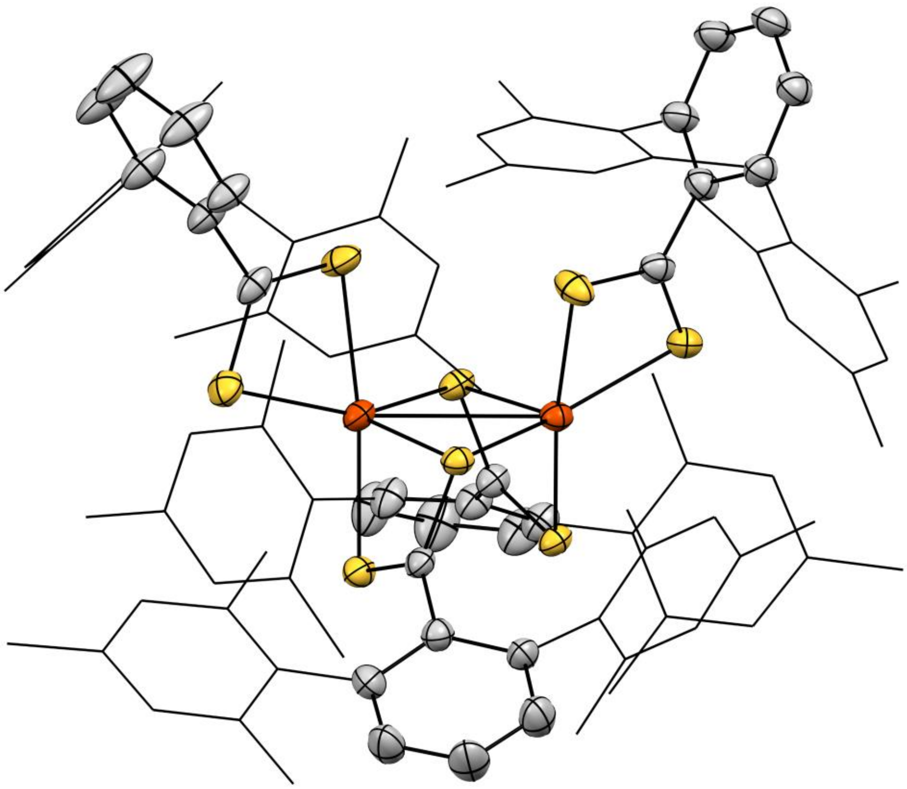

Figure 5-17. Labeled thermal ellipsoid plots (50%) of **12.** Orange, yellow, and gray ellipsoids represent Fe, S, and C atoms, respectively. Hydrogen atoms and co-crystallized solvent molecules are omitted for clarity.

We also explored the bulkier trip-terphenyl. We accessed the trip-terphenyl iodide via the route below, adding the thiocarboxylate functionality using the same procedure as the Mes analogue to produce **13** (Scheme 5-1).

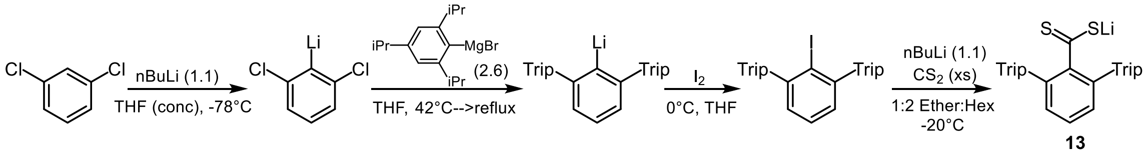

Scheme 5-8. Synthesis of trip terphenyl iodide.

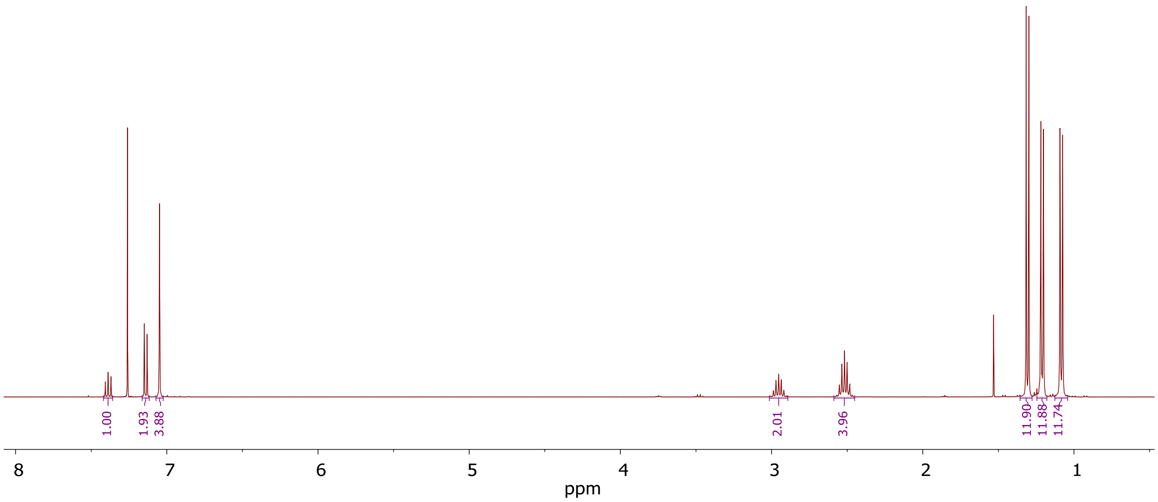

Figure 5-18. $^1$H-NMR of tTer-iodide at 500 MHz in $C_6D_6$.

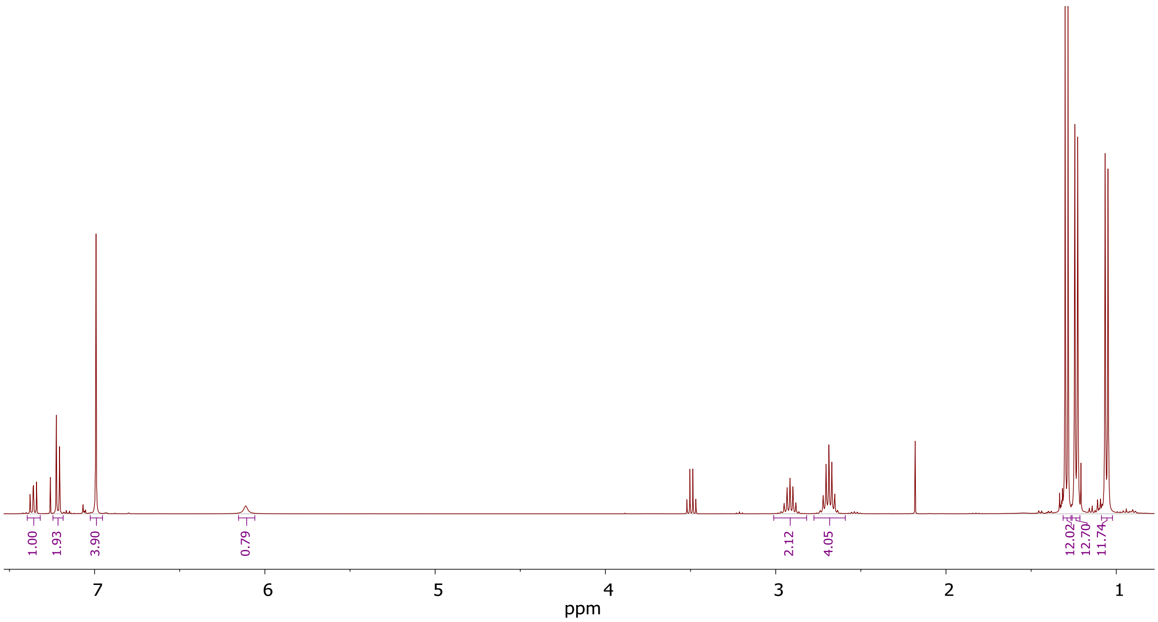

Figure 5-19. $^1$H-NMR of tTerCS$_2$H (**13-H**) at 500 MHz in $C_6D_6$.

Metallation of **13** with iron dichloride produced a dichroic red/green solution in toluene. This material changed color depending on which solvent it was dissolved in. When dissolved in benzene it was an army-green yellowish color, in ether it was an blue-ish green evergreen color, and in THF it was nearly colorless! By adding THF to an NMR sample, the peaks did indeed shift (Figure 5-20).

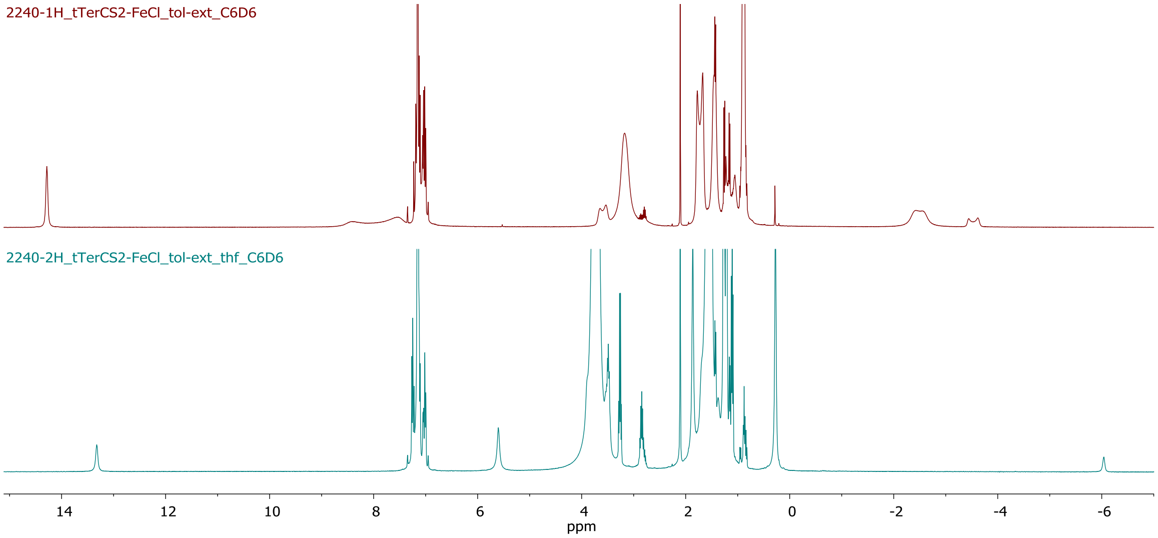

Figure 5-20. $^1$H-NMR of tTerCS$_2$Fe(THF)$_2$ (**14**) in $C_6D_6$ with out THF (top) and with THF (bottom).

The complex **14** also undergoes some dramatic color changes with temperature. At room temp it's green, but at −100°C it turns purple (Figure 5-21). Excited by the possibility of this color change initiated at −40°C indicated $N_2$ binding, we conducted a VT-NMR experiment to probe whether we could visualize potential $N_2$ binding, however no striking difference was observed (Figure 5-22). We thus concluded this was just an example of thermochromism.

Figure 5-21. Complex **14** dissolved in toluene at 25°C (left) and at −100°C (right).

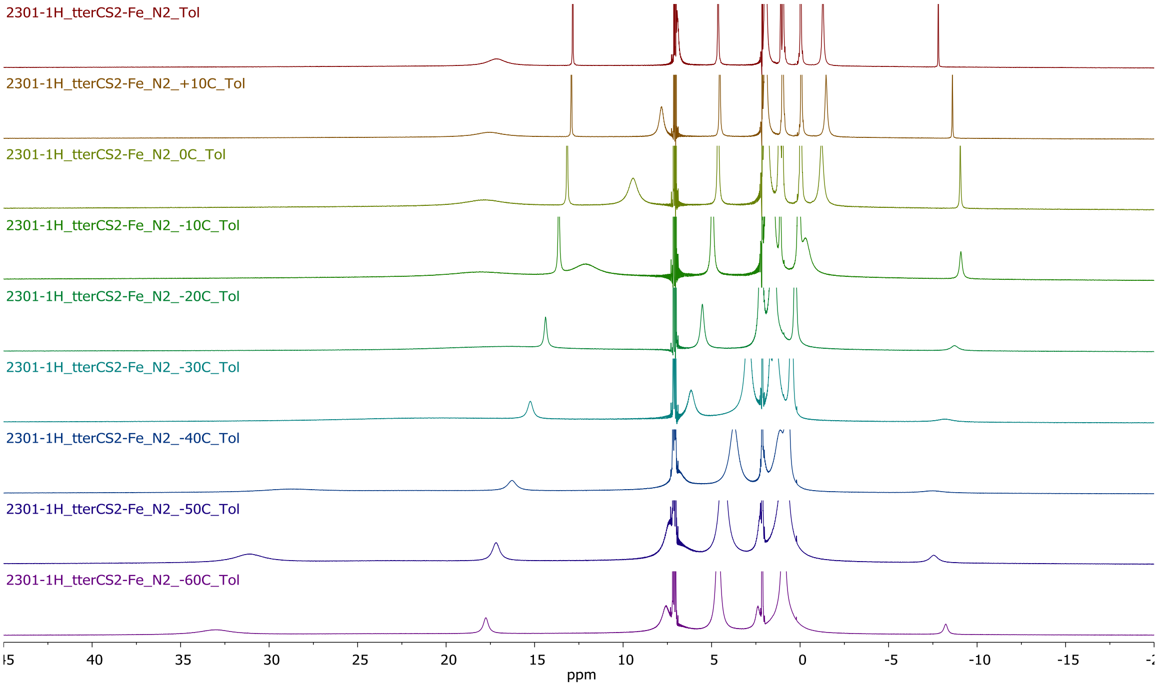

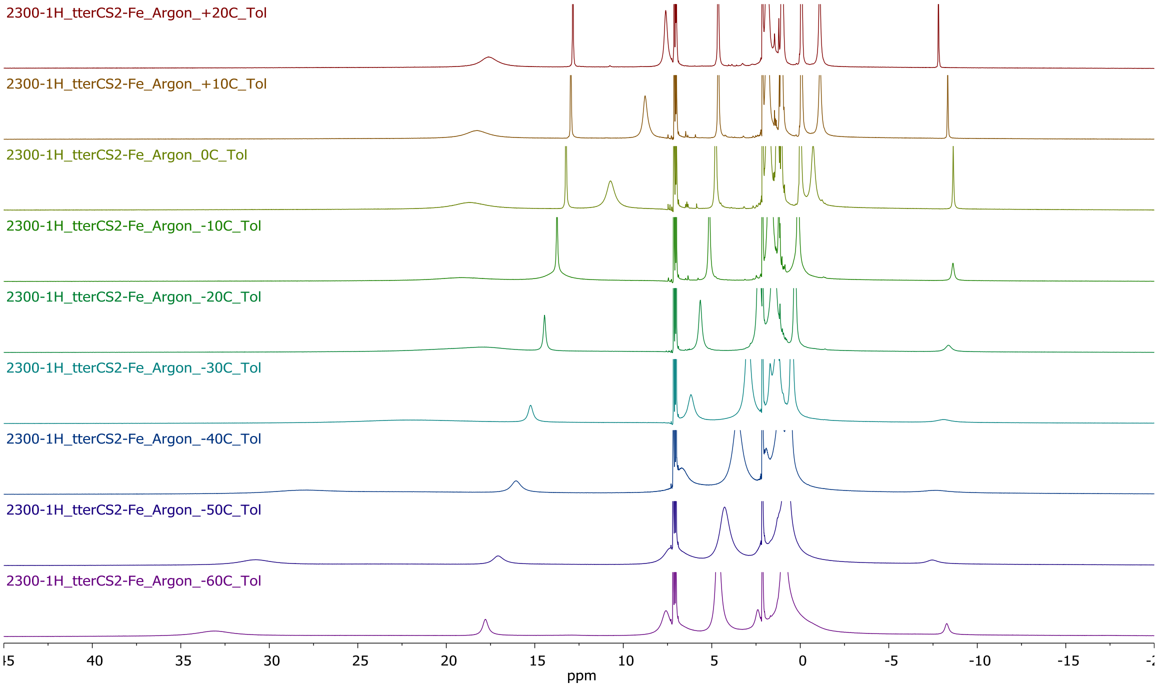

Figure 5-22. VT-NMR ($^1$H) of **14** from 20°C to −60°C under $N_2$ (top) and under argon (bottom).

The preliminary XRD structure for **14** revealed a trans orientation of the the two terphenyls in contrast to the cis arrangement observed in the Mes terphenyl analogue **10** (Figure 5-23).

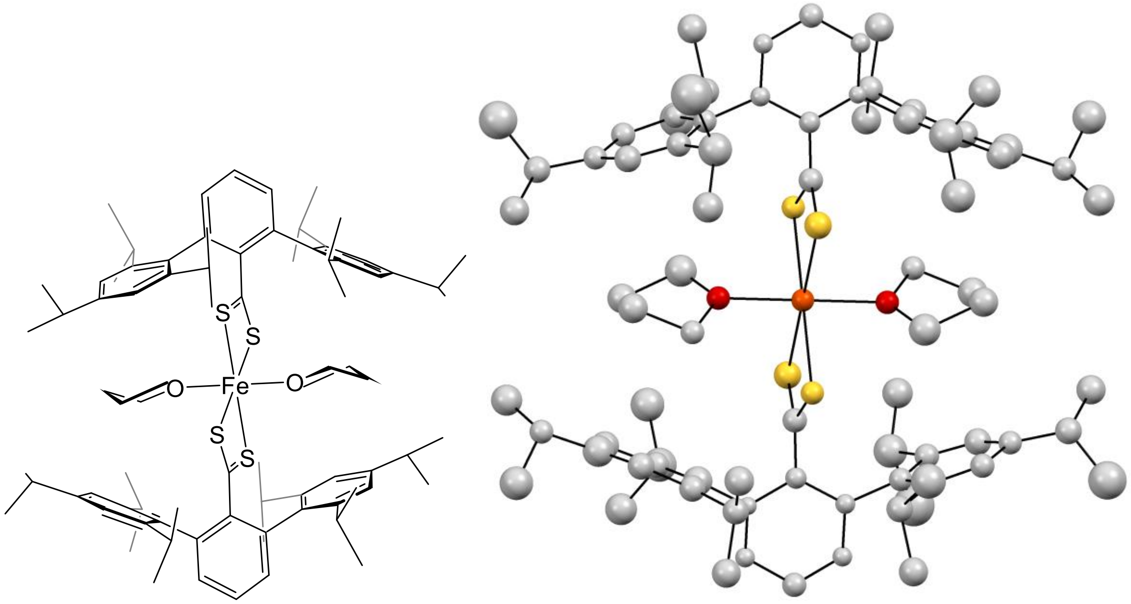

Figure 5-23. Preliminary solid-state structure of $tTerCS_2Fe(THF)_2$ (**14**). Light orange, yellow, red, and gray ellipsoids represent Fe, S, O, and C atoms, respectively. Hydrogen atoms and co-crystallized solvent molecules are omitted for clarity.

We performed cyclic voltammetry on **14**, revealing two semi-reversible reduction events at −2.10 and −2.57 V vs Fc/Fc+ (Figure 5-24). However, we were unable to chemically isolate either of these reduced species.

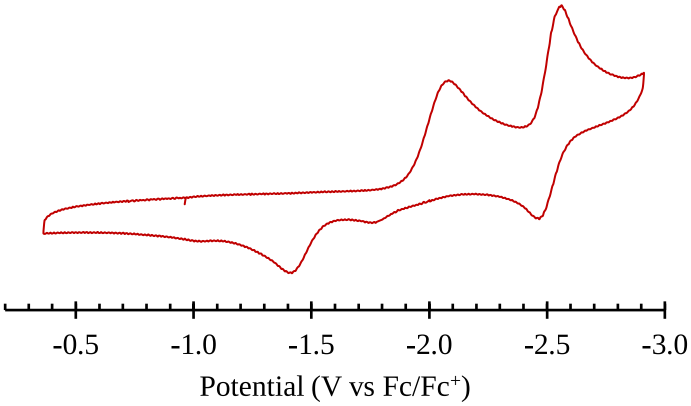

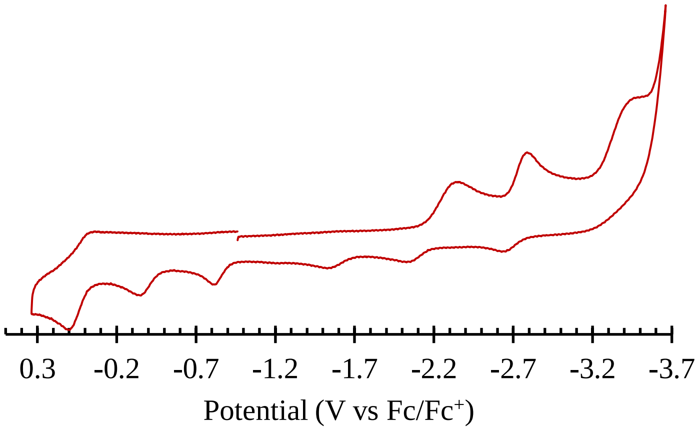

Figure 5-24. Cyclic voltammograms of mTerCS$_2$Fe (**14**) in THF (0.1 M [*n*Bu$_4$N]PF$_6$ as electrolyte; 100 mV/s scan rate).

Addition of CO to **14** produced the cis isomer with a C−O distance of 1.139(2) Å (Figure 5-25). IR yielded three CO stretches centered around 2100 cm$^{-1}$, which is typical for terminal carbonyls. Reduction of **14** with potassium naphthalenide produced free ligand and iron metal.

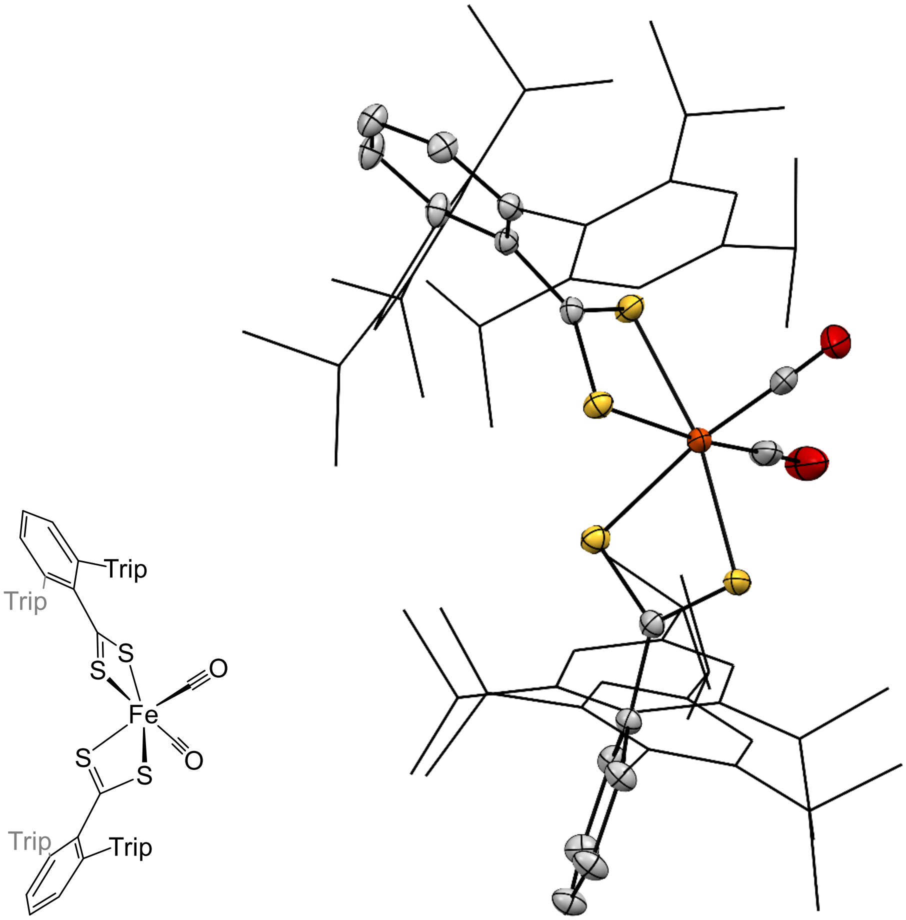

Figure 5-25. Thermal ellipsoid plots (50% probability) of the solid-state structure of tTerCS$_2$Fe(CO)$_2$ (**15**). Light orange, yellow, red, and gray ellipsoids represent Fe, S, O, and C atoms, respectively. Hydrogen atoms and co-crystallized solvent molecules are omitted for clarity.

Table 5-1. Crystal data and structure refinement for tTerCS$_2$Fe(CO)$_2$ (**15**).

| | | |
|---|---|---|
| Identification code | hh274LE39_0m | |
| Empirical formula | $C_{76}H_{98}FeO_2S_4$ | |
| Formula weight | 1227.63 | |
| Temperature | 100(2) K | |
| Wavelength | 0.71073 Å | |
| Crystal system | Monoclinic | |
| Space group | C 2/c | |
| Unit cell dimensions | a = 25.3610(18) Å | $\alpha$= 90°. |
| | b = 9.5529(7) Å | $\beta$= 104.4641(11)°. |
| | c = 29.891(2) Å | $\gamma$ = 90°. |
| Volume | 7012.2(9) Å$^3$ | |
| Z | 4 | |
| Density (calculated) | 1.163 mg/m$^3$ | |
| Absorption coefficient | 0.378 mm$^{-1}$ | |

| | |
|---|---|
| F(000) | 2640 |
| Crystal size | 0.483 x 0.348 x 0.308 mm$^3$ |
| θ range for data collection | 1.658 to 30.508°. |
| Index ranges | $-36 \le h \le 36$, $-13 \le k \le 13$, $-42 \le l \le 42$ |
| Reflections collected | 82106 |
| Independent reflections | 10732 [$R_{int}$ = 0.0374] |
| Completeness to θ = 25.242° | 100.0 % |
| Absorption correction | Semi-empirical from equivalents |
| Refinement method | Full-matrix least-squares on F$^2$ |
| Data / restraints / parameters | 10732 / 73 / 505 |
| Goodness-of-fit on F$^2$ | 1.039 |
| Final $R$ indices [$I > 2\sigma_I$] | $R_1$ = 0.0354, $wR_2$ = 0.0844 |
| $R$ indices (all data) | $R_1$ = 0.0464, $wR_2$ = 0.0910 |
| Extinction coefficient | n/a |
| Largest diff. peak and hole | 0.451 and -0.480 e/Å$^3$ |

### *Non-Iron Tp Chemistry*

Metallation of NaTpAd with cobalt(II) bromide produced complex **16** as royal blue crystalline solid. Reduction with potassium graphite in toluene produced the Co(I) dinitrogen adduct **17** (Figure 5-26).

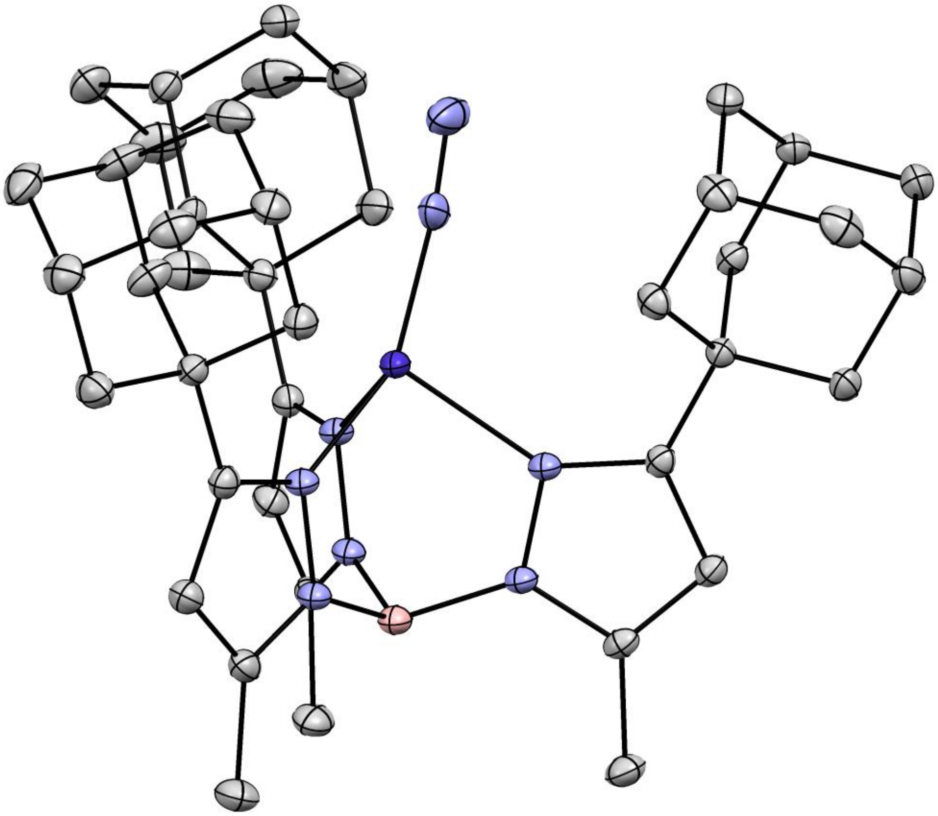

Figure 5-26. Thermal ellipsoid plots (50% probability) of the solid-state structure of $Tp^{Ad}CoN_2$ (**17**). Deep blue, light blue, pink, and gray ellipsoids represent Co, N, B, and C atoms, respectively. Hydrogen atoms and co-crystallized solvent molecules are omitted for clarity.

Table 5-2. Crystal data and structure refinement for $Tp^{Ad}CoN_2$ (**17**).

| | | |
|---|---|---|
| Identification code | hh282LE43_0m | |
| Empirical formula | $C_{45}H_{65}BCoN_8$ | |
| Formula weight | 787.79 | |
| Temperature | 100(2) K | |
| Wavelength | 0.71073 Å | |
| Crystal system | Monoclinic | |
| Space group | P 21/n | |
| Unit cell dimensions | a = 11.7875(8) Å | $\alpha$= 90°. |
| | b = 17.2905(12) Å | $\beta$= 105.1970(10)°. |

| | | |
|---|---|---|
| | c = 21.0024(15) Å | $\gamma$ = 90°. |
| Volume | 4130.8(5) Å$^3$ | |
| Z | 4 | |
| Density (calculated) | 1.267 mg/m$^3$ | |
| Absorption coefficient | 0.458 mm$^{-1}$ | |
| F(000) | 1692 | |
| Crystal size | 0.368 x 0.296 x 0.108 mm$^3$ | |
| $\theta$ range for data collection | 1.548 to 28.280°. | |
| Index ranges | $-15 \leq h \leq 15$, $-23 \leq k \leq 23$, $-28 \leq l \leq 28$ | |
| Reflections collected | 83154 | |
| Independent reflections | 10234 [$R_{\mathrm{int}}$ = 0.0364] | |
| Completeness to $\theta$ = 25.242° | 100.0 % | |
| Absorption correction | Semi-empirical from equivalents | |
| Refinement method | Full-matrix least-squares on F$^2$ | |
| Data / restraints / parameters | 10234 / 0 / 503 | |
| Goodness-of-fit on F$^2$ | 1.032 | |
| Final $R$ indices [$I > 2\sigma_I$] | $R_1$ = 0.0342, $wR_2$ = 0.0871 | |
| $R$ indices (all data) | $R_1$ = 0.0431, $wR_2$ = 0.0926 | |
| Extinction coefficient | n/a | |
| Largest diff. peak and hole | 0.699 and −0.272 e/Å$^3$ | |

This species is notably canted unlike it’s iron analogue (Figure 5-27). This phenomenon has been previously described.[6]

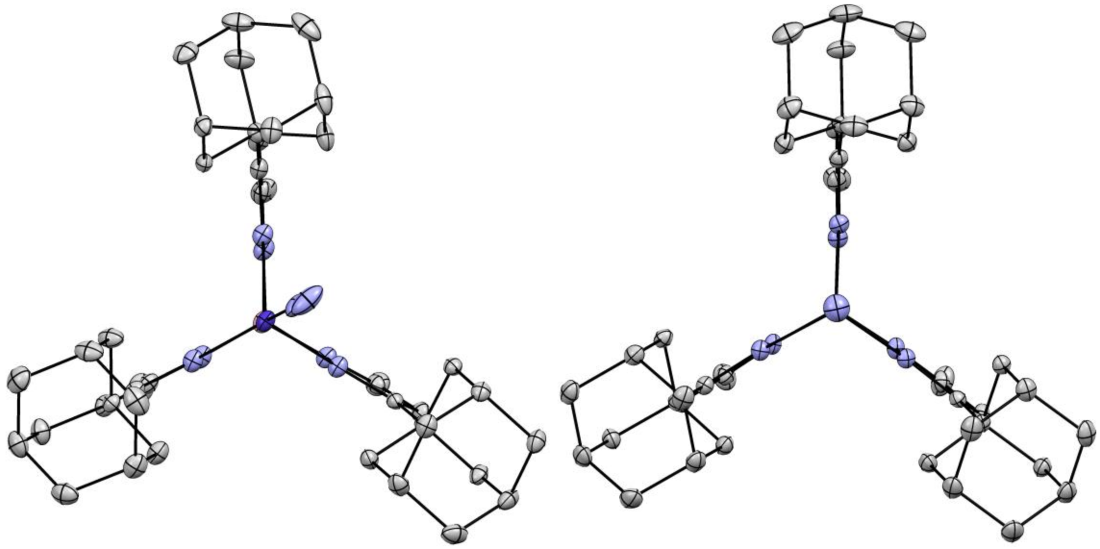

Figure 5-27. Top-down view of Tp$^{Ad}$CoN$_2$ (**17**) (left) and Tp$^{Ad}$FeN$_2$ (right).

Its reactivity was quite similar to the iron analogue. Bonding with arenes and alkenes was observed. Under argon, it was notably able to bind allylbenzene (Figure 5-28). However it was unable to do the C-H activation chemistry described in Ch 1.

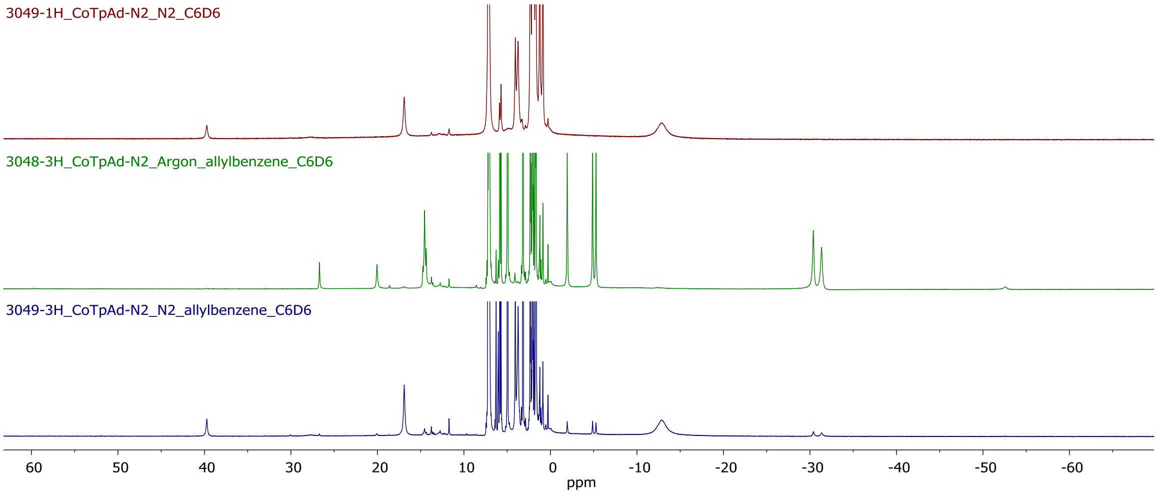

Figure 5-28. $^1$H-NMR of Tp$^{Ad}$CoN$_2$ (top), in the prescence of allyl benzene under argon (middle), and in the presence of allyl benzene after being exposed to N$_2$.

Metallation of NaTp$^{Me,Ad}$ with CuCl under ethylene produced the Cu$_4$Tp$_2$ species **18** as revealed by a preliminary XRD structure (Figure 5-29). We were hoping for the monomeric ethylene adduct.

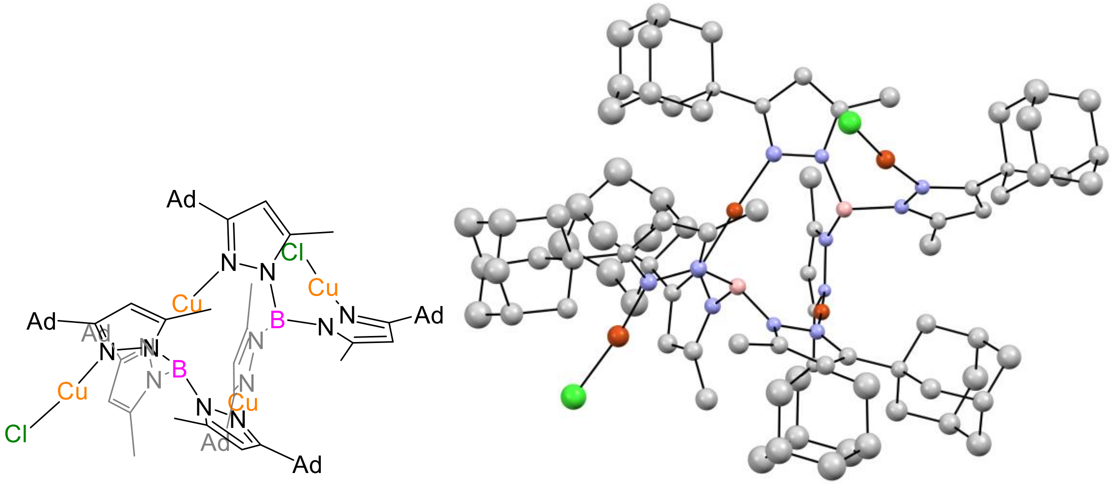

Figure 5-29. Preliminary solid-state structure of [Tp$^{Ad}$CuCl,Cu]$_2$ (**18**). Brick-red, green, blue, pink, and gray ellipsoids represent Cu, Cl, N, B, and C atoms, respectively. Hydrogen atoms and co-crystallized solvent molecules are omitted for clarity.

Metallation of NaTp$^{Ad}$ with manganese(II) bromide produced the expected Mn(II) species as colorless crystals with especially broad paramagnetic resonances (Figure 5-30, Figure 5-31). Addition of $KC_8$ to dissolved solutions produced no visible color change.

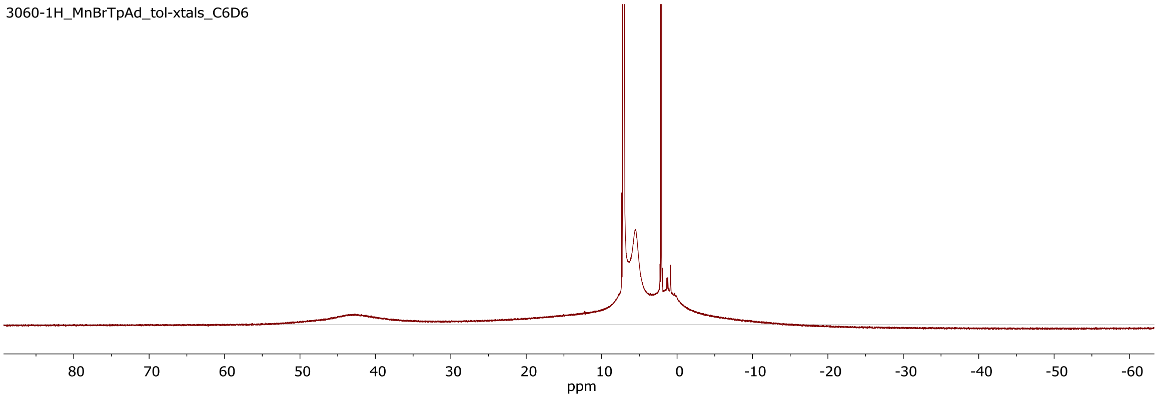

Figure 5-30. $^1$H-NMR of Tp$^{Ad}$MnBr (**19**) at 400 MHz in $C_6D_6$.

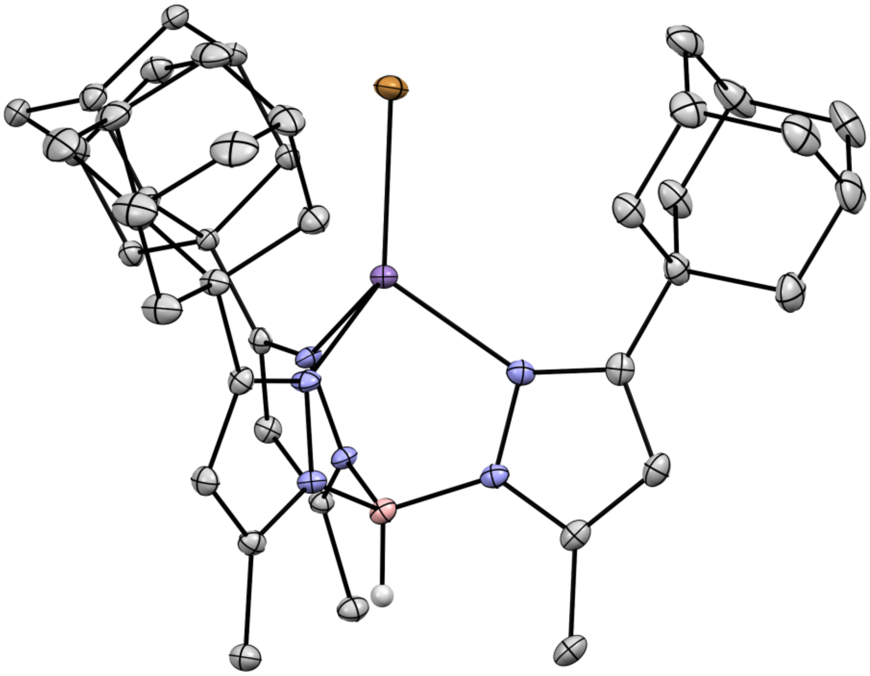

Figure 5-31. Thermal ellipsoid plots (50% probability) of the solid-state structure of Tp$^{Ad}$MnBr (**19**). Purple, brown, blue, pink, and gray ellipsoids represent Mn, Br, N, B, and C atoms, respectively. Most hydrogen atoms and co-crystallized solvent molecules are omitted for clarity.

Table 5-3. Crystal data and structure refinement for Tp$^{Ad}$MnBr (**19**).

| | | |
|---|---|---|
| Identification code | hh286le | |
| Empirical formula | $C_{42}H_{58}BBrMnN_6$ | |
| Formula weight | 792.60 | |
| Temperature | 100(2) K | |
| Wavelength | 0.71073 Å | |
| Crystal system | Monoclinic | |
| Space group | $P2_1/c$ | |
| Unit cell dimensions | a = 11.0970(3) Å | $\alpha = 90°$. |
| | b = 14.3623(3) Å | $\beta = 99.2545(11)°$. |
| | c = 24.6014(6) Å | $\gamma = 90°$. |
| Volume | 3869.90(16) Å$^3$ | |
| Z | 4 | |
| Density (calculated) | 1.360 mg/m$^3$ | |
| Absorption coefficient | 1.412 mm$^{-1}$ | |
| F(000) | 1668 | |
| Crystal color | colourless | |
| Crystal size | 0.329 x 0.257 x 0.170 mm$^3$ | |
| θ range for data collection | 1.647 to 30.998° | |
| Index ranges | $-16 \leq h \leq 16$, $-20 \leq k \leq 20$, $-35 \leq l \leq 35$ | |
| Reflections collected | 88522 | |
| Independent reflections | 12328 [$R_{\text{int}} = 0.0628$] | |
| Completeness to θ = 25.242° | 100.0 % | |
| Absorption correction | Semi-empirical from equivalents | |
| Refinement method | Full-matrix least-squares on F$^2$ | |
| Data / restraints / parameters | 12328 / 1 / 466 | |
| Goodness-of-fit on F$^2$ | 1.028 | |
| Final *R* indices [$I > 2\sigma_I$ = 8929 data] | $R_1 = 0.0352$, $wR_2 = 0.0736$ | |
| *R* indices (all data, ? Å) | $R_1 = 0.0631$, $wR_2 = 0.0829$ | |
| Extinction coefficient | n/a | |
| Largest diff. peak and hole | 0.493 and -0.582 e/Å$^3$ | |

## *More Iron Tp Chemistry*

Some of these compounds weren't included in the previous chapters in order to simplify the storytelling. In Chapter 1, the C−H activation of aliphatic substrates via Fe(I)-radical pairs is discussed. We also prepared (2,2,6,6-tetramethylpiperidin-1-yl)oxyl (TEMPO) analogue, Tp$^{Me,Ad}$Fe(TEMPO) **20** (Figure 5-32). Interestingly, it is able to perform the C−H activation of phenylacetylene and MeCN, but not 2-butyne or ethylene.

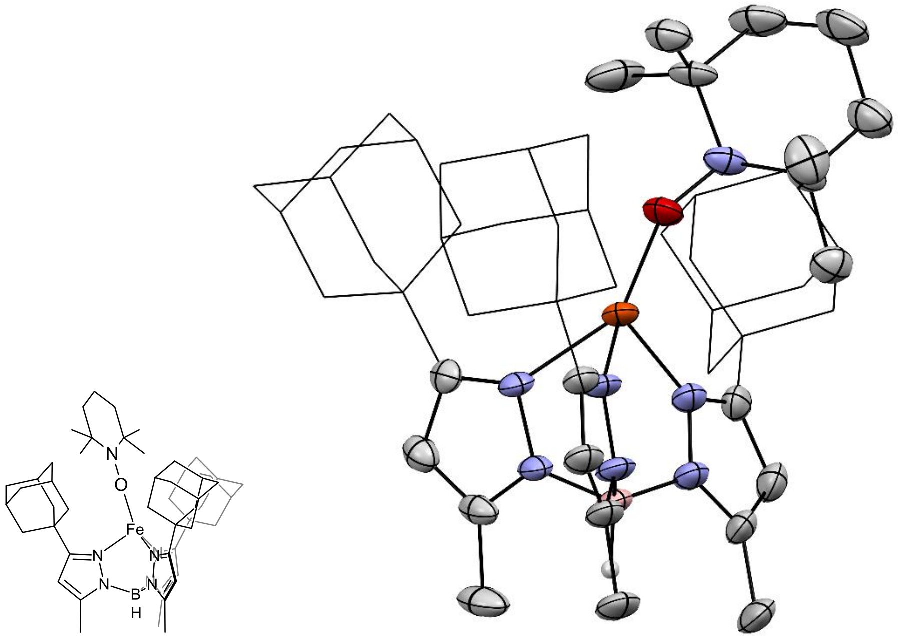

Figure 5-32. Thermal ellipsoid plots (50% probability) of the solid-state structure of Tp$^{Me,Ad}$Fe(TEMPO) (**20**). Orange, red, blue, pink, and gray ellipsoids represent Fe, O, N, B, and C atoms, respectively. Most hydrogen atoms and co-crystallized solvent molecules are omitted for clarity.

### *Preparation of Tp$^{Me,Ad}$Fe(TEMPO)* **20**.

A solution of TEMPO (6 mg, 0.038 mmol) in toluene (~1 mL) was added to a solution of [Tp$^{Me,Ad}$Fe($N_2$)] (27 mg, 0.037 mmol) in toluene (3 mL). After stirring for 10 minutes at room temperature, the volatiles were removed *in vacuo* to afford a yellow glaze. Pentane (1 mL) was added to dissolve the glaze and subsequently removed *in vacuo,* twice. Another 1 mL portion of pentane was added producing a pale yellow solution. This was filtered, then concentrated to half the volume. Upon cooling to −19°C, this solution produced pale yellow crystals. Overall yield: 21 mg (66%). $^1$H NMR ($C_6D_6$): δ 36.04. Evans Method ($C_6D_6$): $\mu_B$ 6.0±0.1. UV-Vis (THF): $\lambda_{max}$ nm ($\varepsilon_{max}$ $M^{-1}$ $cm^{-1}$) 931 (p, $7.3 \times 10^1$), 348 (p, $1.1 \times 10^3$). Calc. for $C_{50}H_{74}BFeN_7O$: C: 70.54; H: 8.72; N: 11.46. Found: C: 70.54; H: 9.03; N: 11.29.

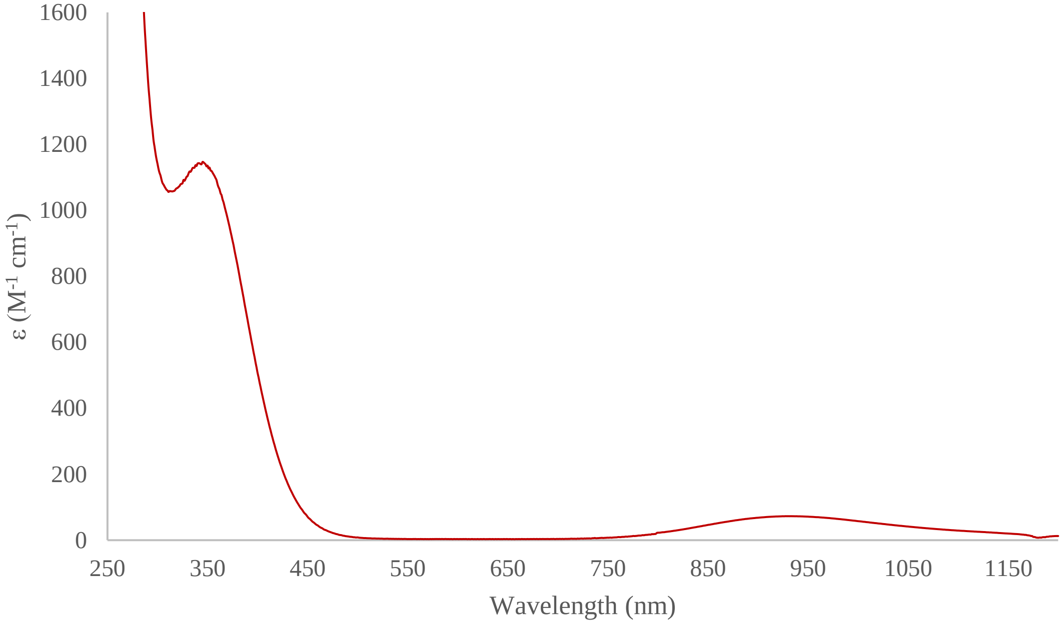

Figure 5-33 UV-Vis-NIR spectra of Tp$^{Me,Ad}$Fe(TEMPO) (**20**) in THF.

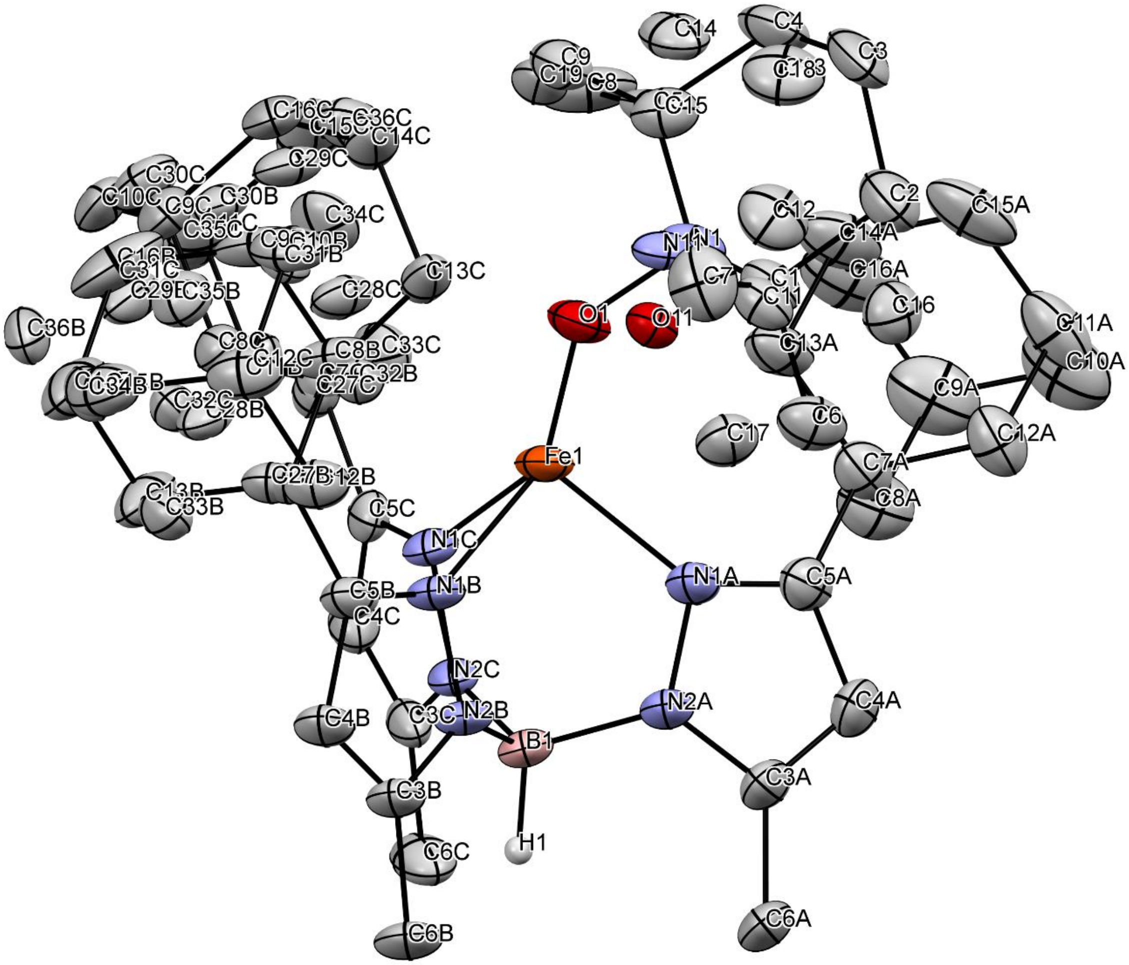

Figure 5-34. Labelled thermal ellipsoid plot (50%) for $Tp^{Me,Ad}Fe(TEMPO)$ (**20**).

Table 5-4. Crystal data and structure refinement for $Tp^{Me,Ad}Fe(TEMPO)$ (**20**).

| | | |
|---|---|---|
| Goodness-of Identification code | hh329le_sq | |
| Empirical formula | $C_{51}H_{76}BFeN_7O$ | |
| Formula weight | 869.84 | |
| Temperature | 100(2) K | |
| Wavelength | 0.71073 Å | |
| Crystal system | Triclinic | |
| Space group | P-1 | |
| Unit cell dimensions | a = 12.3511(3) Å | α = 64.7778(11)°. |
| | b = 15.3038(4) Å | β = 77.1959(12)°. |
| | c = 15.3905(4) Å | γ = 85.9452(12)°. |
| Volume | 2565.38(12) $Å^3$ | |
| Z | 2 | |
| Density (calculated) | 1.126 $mg/m^3$ | |
| Absorption coefficient | 0.335 $mm^{-1}$ | |
| F(000) | 940 | |

| | |
|---|---|
| Crystal color | yellow |
| Crystal size | 0.230 x 0.163 x 0.136 mm$^3$ |
| θ range for data collection | 1.471 to 26.022° |
| Index ranges | $-15 \leq h \leq 15$, $-18 \leq k \leq 18$, $-18 \leq l \leq 18$ |
| Reflections collected | 53503 |
| Independent reflections | 10094 [$R_{\mathrm{int}}$ = 0.0446] |
| Completeness to θ = 25.242° | 100.0 % |
| Absorption correction | Semi-empirical from equivalents |
| Refinement method | Full-matrix least-squares on F$^2$ |
| Data / restraints / parameters | 10094 / 1695 / 820 |
| Goodness-of-fit on F$^2$ | 1.011 |
| Final $R$ indices [I > 2σ$_I$ = 7760 data] | $R_1$ = 0.0409, $wR_2$ = 0.0963 |
| $R$ indices (all data, 0.81 Å) | $R_1$ = 0.0608, $wR_2$ = 0.1091 |
| Largest diff. peak and hole | 0.444 and -0.385 e/Å$^3$ |

We also prepared the 2,4,6-tri-tert-butylphenoxyl (OMes*) analogue, Tp$^{\mathrm{Me,Ad}}$Fe(OMes*) **21** (Figure 5-35). Its reactivity is identical to the Tp$^{\mathrm{Me,Ad}}$Fe(OPhAd) described in Chapter 1.

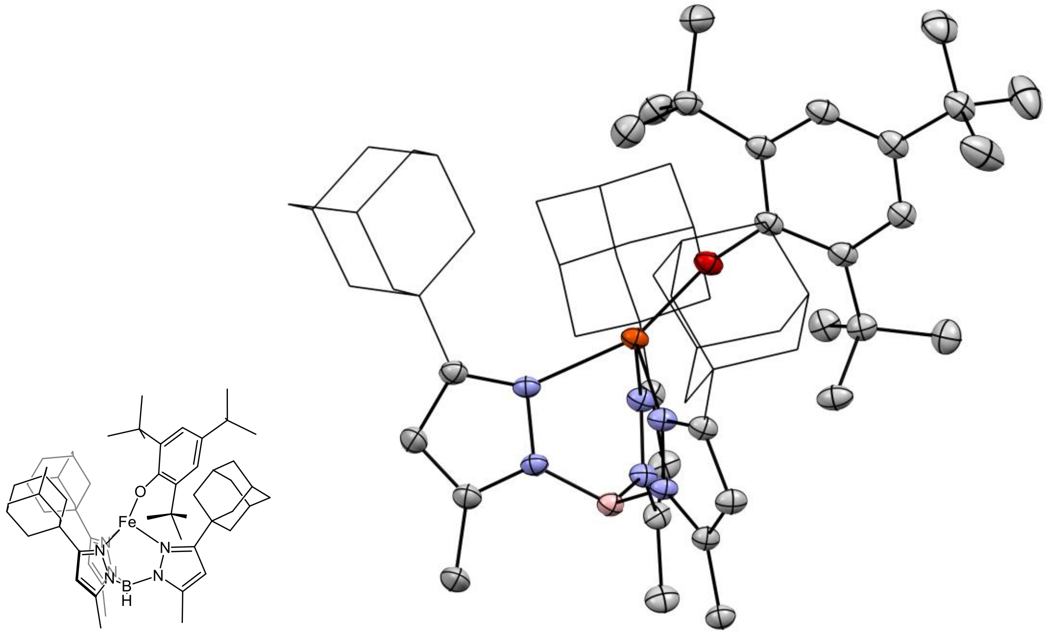

Figure 5-35. Thermal ellipsoid plots (50% probability) of the solid-state structure of Tp$^{\mathrm{Me,Ad}}$Fe(OMes*) (**21**). Orange, red, blue, pink, and gray ellipsoids represent Fe, O, N, B, and C atoms, respectively. Most hydrogen atoms and co-crystallized solvent molecules are omitted for clarity.

*Preparation of* $Tp^{Me,Ad}Fe(OMes^*)$ **21**.

A solution of OMes* (10 mg, 0.039 mmol) in toluene (~1 mL) was added to a solution of $[Tp^{Me,Ad}Fe(N_2)]$ (27 mg, 0.037 mmol) in toluene (X mL). After stirring for 10 minutes at room temperature, the volatiles were removed *in vacuo* to afford an yellow glaze. Pentane (1 mL) was added to dissolve the glaze and subsequently removed *in vacuo,* twice. Another 1 mL portion of pentane was added producing an orange-yellow solution. This was filtered, then concentrated to half the volume. Upon cooling to −19°C, this solution produced yellow crystals. Overall yield: 11 mg (31%). $^1H$ NMR ($C_6D_6$): δ 36.04. Evans Method ($C_6D_6$): $\mu_B$ 4.0±0.3. UV-Vis (THF): $\lambda_{max}$ nm ($\varepsilon_{max}$ $M^{-1}$ $cm^{-1}$) 929 (p, $1.1 \times 10^2$), 390 (p, $1.5 \times 10^3$). Calc. for $C_{42}H_{58}BFeN_8$: C: 68.02; H: 7.88; N: 15.11. Found: C: 68.17; H: 7.77; N: 14.97.

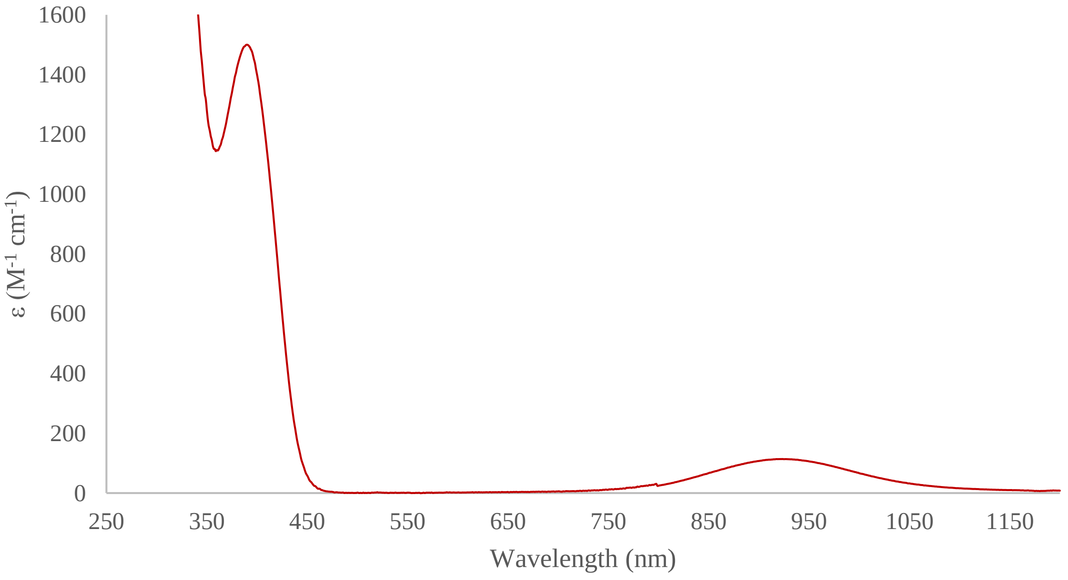

Figure 5-36. UV-Vis-NIR spectra of $Tp^{Me,Ad}Fe(OMes^*)$ (**21**) in THF.

To conduct a competition experiment between the activation of sp C−H bonds versus a $sp^3$ C−H bonds, we generated the propyne compound, $Tp^{Me,Ad}Fe(propyne)$ **22** (Figure 5-37).

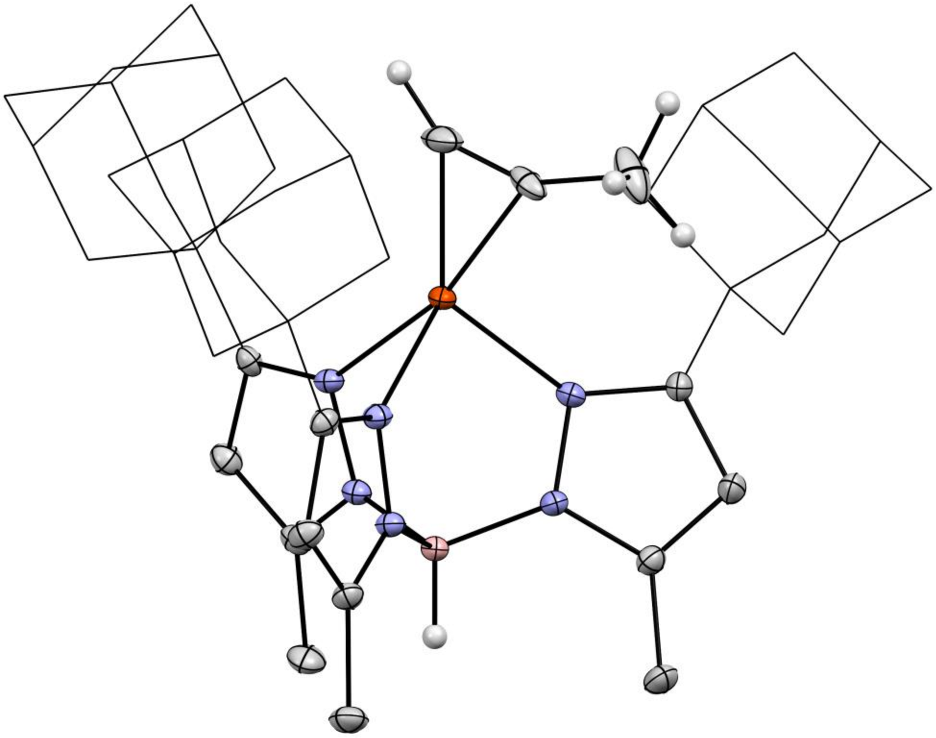

Figure 5-37. Thermal ellipsoid plots (50% probability) of the solid-state structure of $Tp^{Me,Ad}Fe(propyne)$ (**22**). Orange, blue, pink, and gray ellipsoids represent Fe, N, B, and C atoms, respectively. Most hydrogen atoms and co-crystallized solvent molecules are omitted for clarity.

*Preparation of $Tp^{Me,Ad}Fe(propyne)$* (**22**).

A solution of $[Tp^{Me,Ad}Fe(N_2)]$ (67 mg, 0.092 mmol) in toluene (20 mL) was degassed *via* 3 freeze-pump-thaw-cycles and placed under an atmosphere of propyne. An immediate color change from magenta to deep green occurred. After stirring 10 minutes at room temperature, the solution was concentrated *in vacuo,* (~1 mL). This was layered with pentane (~2 mL). Cooling this solution to −19 °C overnight yielded hunter green crystals suitable for XRD. Overall yield: 66 mg (97%). $^1H$ NMR ($C_6D_6$): δ 69.56, 28.56, 25.77, 0.93, 0.70, −1.88, −24.69, −29.14.

Evans Method ($C_6D_6$): $\mu_B$ 3.9±0.1. UV-Vis (THF): $\lambda_{max}$ nm ($\varepsilon_{max}$ $M^{-1}$ $cm^{-1}$) 642 (p, 2.5 × $10^2$), 444 (p, 3.0 × $10^2$).

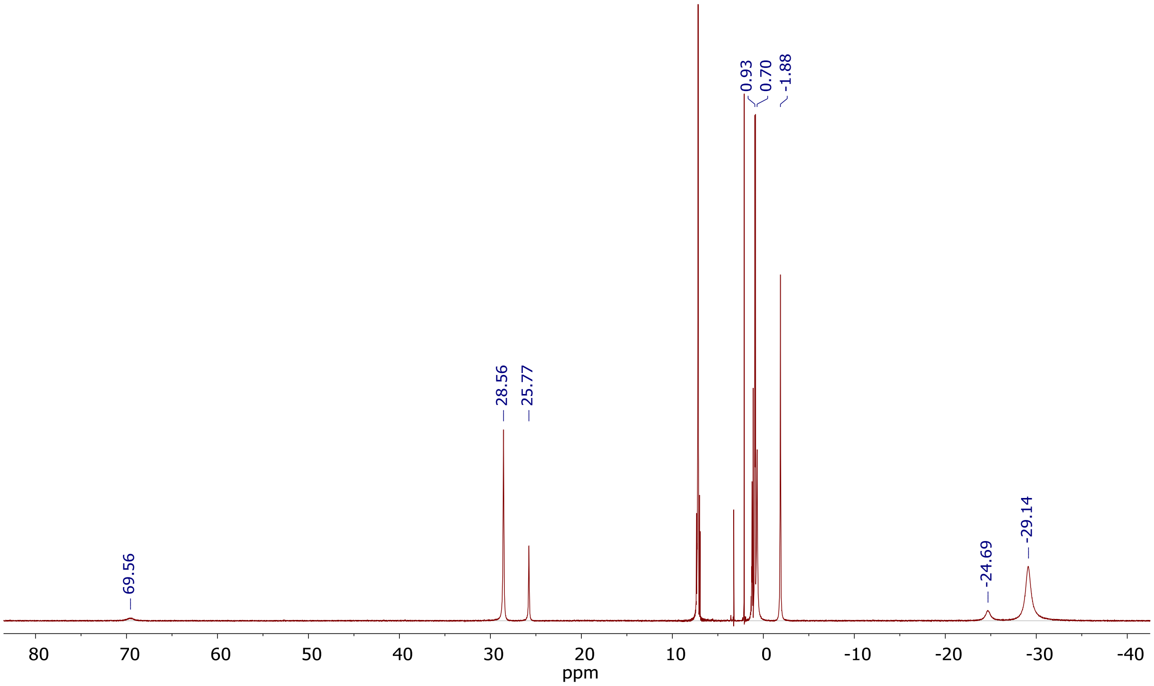

Figure 5-38. $^1H$ NMR spectrum of $Tp^{Me,Ad}Fe(propyne)$ (**22**) recorded at 400 MHz in $C_6D_6$.

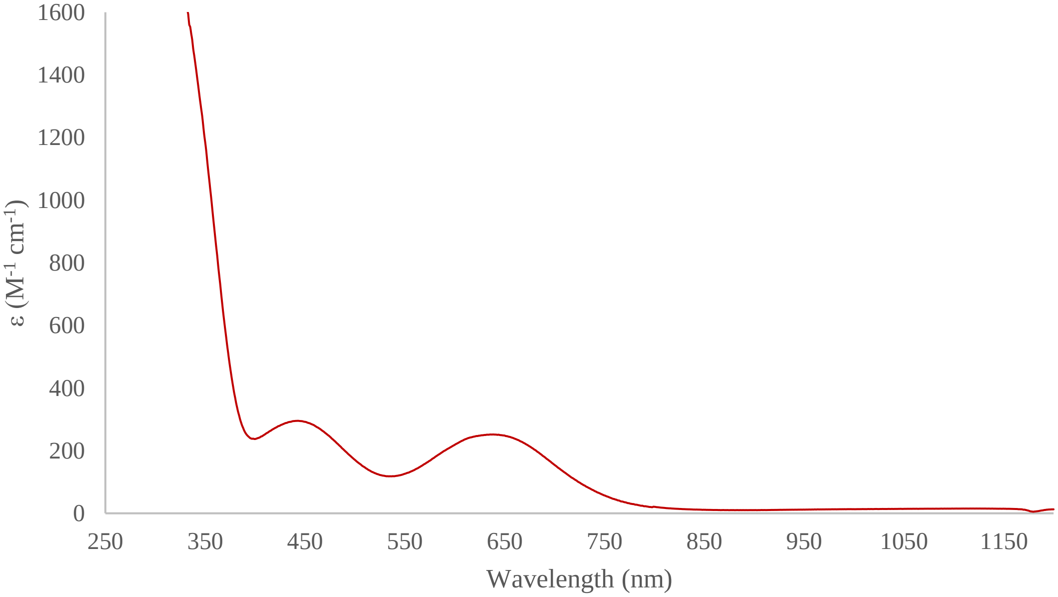

Figure 5-39. UV-Vis-NIR spectrum of $Tp^{Me,Ad}Fe(propyne)$ (**22**) in THF.

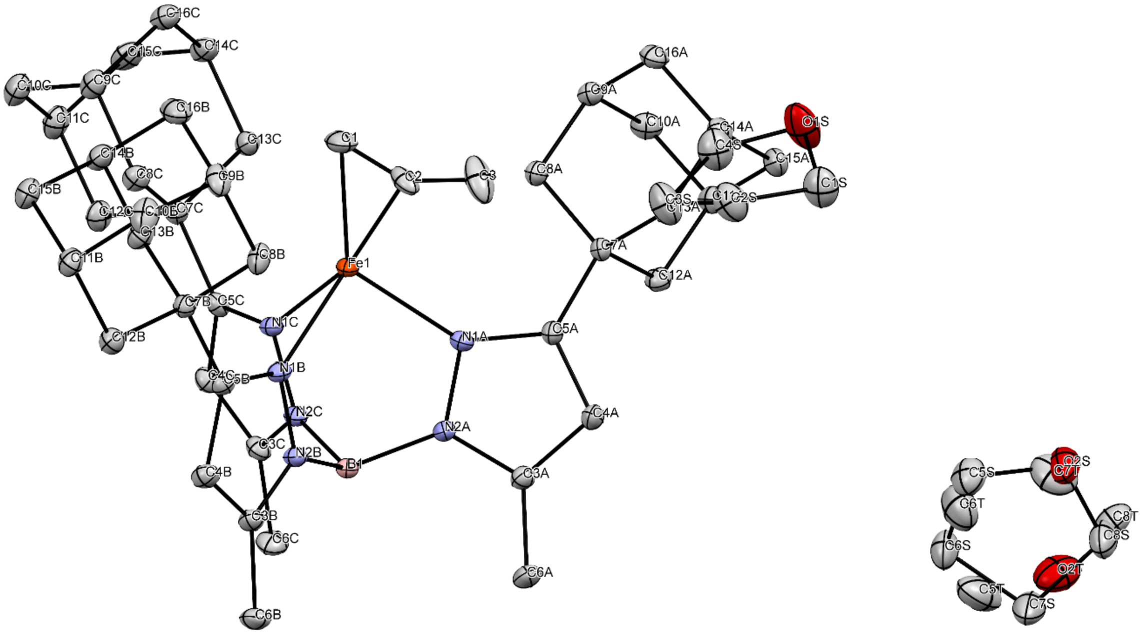

Figure 5-40. Labelled thermal ellipsoid plot (50%) for $\mathrm{Tp^{Me,Ad}}$Fe(propyne) (**22**).

Table 5-5. Crystal data and structure refinement for $\mathrm{Tp^{Me,Ad}}$Fe(propyne) (**22**).

| | | |
|---|---|---|
| Identification code | hh336le_t5 | |
| Empirical formula | $C_{53}H_{78}BFeN_6O_2$ | |
| Formula weight | 897.87 | |
| Temperature | 100(2) K | |
| Wavelength | 0.71073 Å | |
| Crystal system | Triclinic | |
| Space group | P-1 | |
| Unit cell dimensions | a = 12.4505(5) Å | α = 68.6023(16)°. |
| | b = 13.4431(5) Å | β = 68.9730(17)°. |
| | c = 16.1370(6) Å | γ = 79.2869(18)°. |
| Volume | 2342.58(16) $Å^3$ | |
| Z | 2 | |
| Density (calculated) | 1.273 $mg/m^3$ | |
| Absorption coefficient | 0.370 $mm^{-1}$ | |
| F(000) | 970 | |
| Crystal color | green | |
| Crystal size | 0.363 x 0.223 x 0.078 $mm^3$ | |
| θ range for data collection | 1.630 to 31.709° | |
| Index ranges | $-16 \leq h \leq 18$, $-18 \leq k \leq 19$, $0 \leq l \leq 23$ | |
| Reflections collected | 15263 | |
| Independent reflections | 15263 [$R_{\mathrm{int}} = 0.0412$] | |
| Completeness to θ = 25.242° | 99.7 % | |
| Absorption correction | Semi-empirical from equivalents | |

| | |
|---|---|
| Refinement method | Full-matrix least-squares on $F^2$ |
| Data / restraints / parameters | 15263 / 238 / 625 |
| Goodness-of-fit on $F^2$ | 1.031 |
| Final R indices [$I > 2\sigma_I$ = 13763 data] | $R_1 = 0.0360$, $wR_2 = 0.0842$ |
| $R$ indices (all data, 0.68 Å) | $R_1 = 0.0456$, $wR_2 = 0.0890$ |
| Largest diff. peak and hole | 0.461 and −0.313 e/Å$^3$ |

When **22** was combined with radical ($OPhAd_2$) at room temperature, the major product isolated was the sp C−H activation product $Tp^{Me,Ad}Fe(CCCH_3)$ **22** (Scheme 5-9, Figure 5-41). At low temperature, a mixture of ~90% **23** and ~10% another product was produced, however this minor product evaded characterization by XRD.

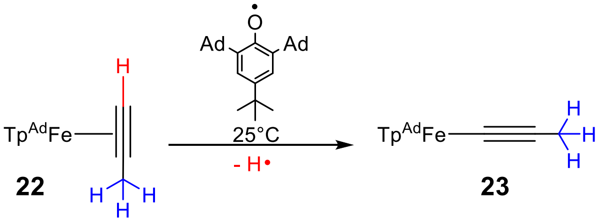

Scheme 5-9. Competition experiment with $Tp^{Me,Ad}Fe(CCCH_3)$.

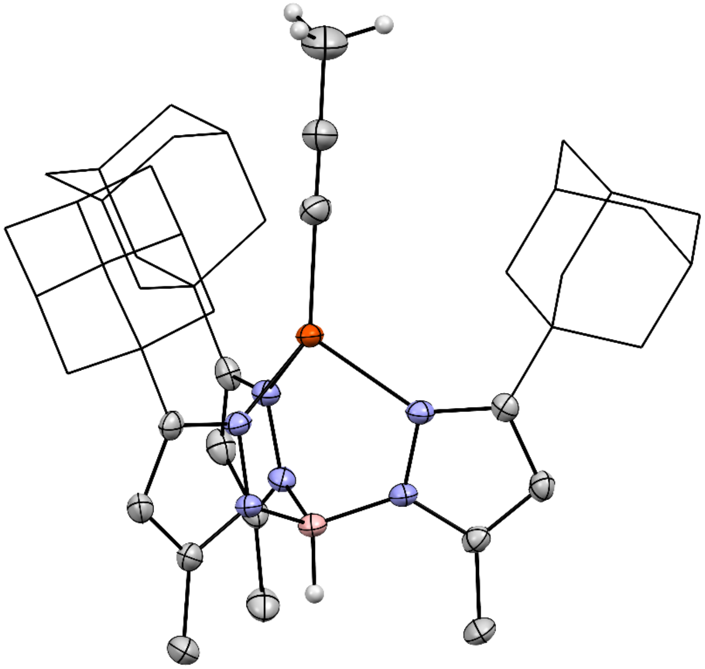

Figure 5-41. Thermal ellipsoid plots (50% probability) of the solid-state structure of Tp$^{Me,Ad}$Fe(CCCH$_3$) (**23**). Orange, blue, pink, and gray ellipsoids represent Fe, N, B, and C atoms, respectively. Most hydrogen atoms and co-crystallized solvent molecules are omitted for clarity.

### *Preparation of Tp$^{Me,Ad}$Fe(CCCH$_3$)* **22.**

A solution of Ad$_2$PhO (14 mg, 0.033 mmol) in ether (1 mL) was added to a suspension of [Tp$^{Me,Ad}$Fe(propyne)] (24 mg, 0.032 mmol) in ether (2 mL) at 25°C. The reaction was allowed to stir for 30 minutes. The volatiles were removed *in vacuo* to affording a colorless precipitate. This was extracted with toluene, filtered, and concentrated to (~200 μL). Layering this with hexane and cooling to −19°C produced colorless crystals overnight. Overall yield: 16 mg (66%). $^1$H NMR (C$_6$D$_6$): δ 126.43. Evans Method (C$_6$D$_6$): μ$_B$ 4.0±0.3.

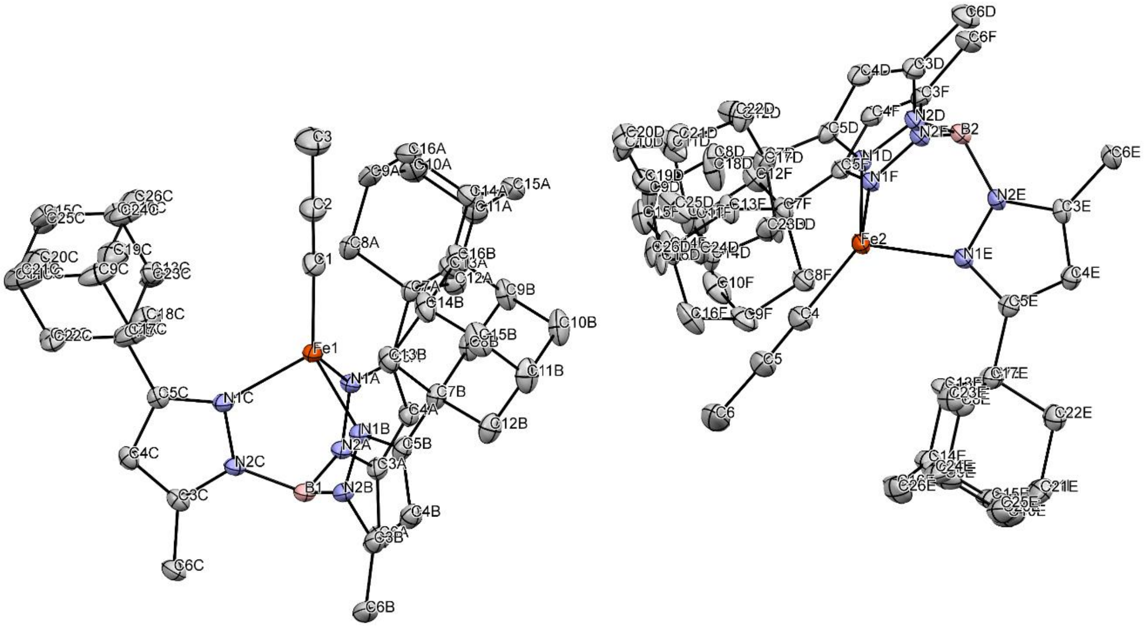

Figure 5-42. Labelled thermal ellipsoid plot (50%) for Tp$^{Me,Ad}$Fe(CCCH$_3$) (**23**).

Table 5-6. Crystal data and structure refinement for Tp$^{Me,Ad}$Fe(CCCH$_3$) (**23**).

| | |
|---|---|
| Identification code | hh337le |
| Empirical formula | $C_{45}H_{61}BFeN_6$ |

| | | |
|---|---|---|
| Formula weight | 752.65 | |
| Temperature | 100(2) K | |
| Wavelength | 0.71073 Å | |
| Crystal system | Monoclinic | |
| Space group | $P2_1/c$ | |
| Unit cell dimensions | a = 22.1172(5) Å | α = 90°. |
| | b = 17.2201(4) Å | β = 117.1048(9)°. |
| | c = 23.6316(5) Å | γ = 90°. |
| Volume | 8011.9(3) $Å^3$ | |
| Z | 8 | |
| Density (calculated) | 1.248 $mg/m^3$ | |
| Absorption coefficient | 0.416 $mm^{-1}$ | |
| F(000) | 3232 | |
| Crystal color | colourless | |
| Crystal size | 0.159 x 0.109 x 0.080 $mm^3$ | |
| θ range for data collection | 1.936 to 26.372° | |
| Index ranges | $-27 \leq h \leq 27$, $-21 \leq k \leq 21$, $-29 \leq l \leq 29$ | |
| Reflections collected | 230609 | |
| Independent reflections | 16373 [$R_{\text{int}} = 0.0908$] | |
| Completeness to θ = 25.242° | 100.0 % | |
| Absorption correction | Semi-empirical from equivalents | |
| Refinement method | Full-matrix least-squares on $F^2$ | |
| Data / restraints / parameters | 16373 / 1667 / 1212 | |
| Goodness-of-fit on $F^2$ | 1.005 | |
| Final R indices [$I > 2\sigma_I$ = 12384 data] | $R_1 = 0.0392$, $wR_2 = 0.0840$ | |
| *R* indices (all data, 0.80 Å) | $R_1 = 0.0622$, $wR_2 = 0.0947$ | |
| Largest diff. peak and hole | 0.693 and -0.570 e/$Å^3$ | |

In Chapter 2, we described only a single heterocycle adduct: $Tp^{Me,Dr}$Fe(furan). However the $Tp^{Me,Dr}$Fe(I) fragment also engages other heterocycles. Addition of pyridine to the μ-$N_2$ dimer produces the C−C coupled product, $(Tp^{Me,Dr}Fepy)_2$ **24**. This same chemistry has already been explored using Fe(NacNac).[7]

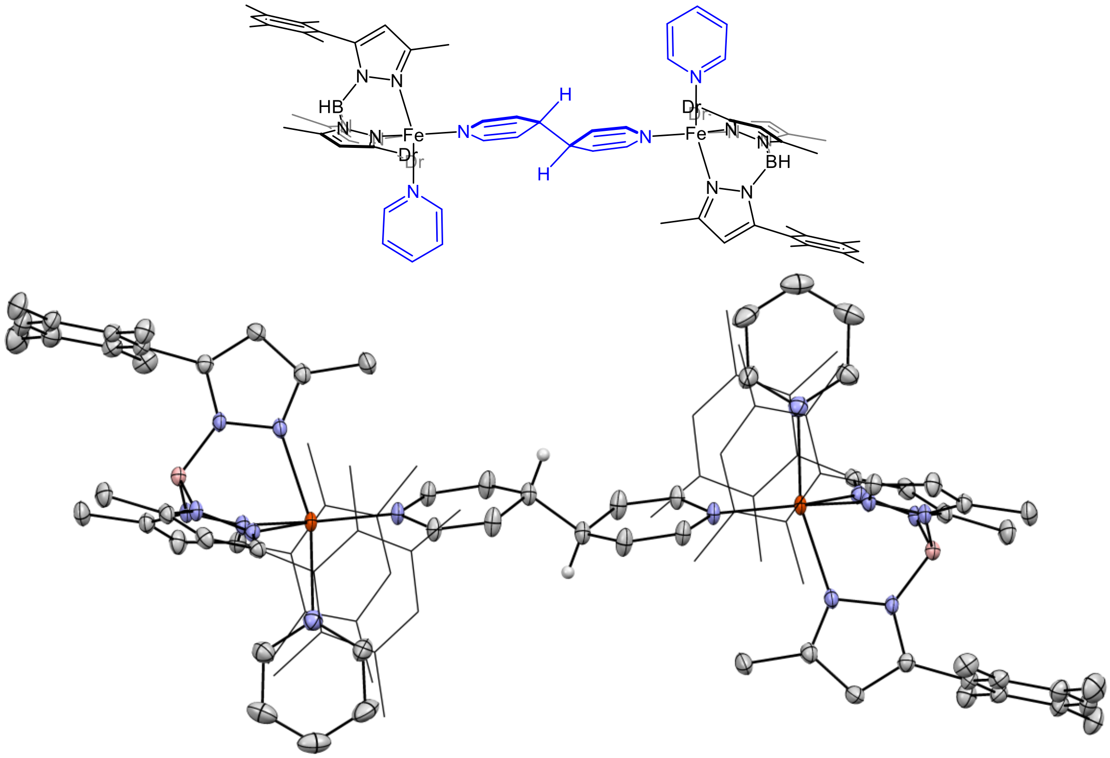

Figure 5-43. Thermal ellipsoid plots (50% probability) of the solid-state structure of (Tp$^{Me,Dr}$Fepy)$_2$ (**24**). Orange, blue, pink, and gray ellipsoids represent Fe, N, B, and C atoms, respectively. Most hydrogen atoms and co-crystallized solvent molecules are omitted for clarity.

Addition of 2-methylpyridine (picoline) to the μ-$N_2$ dimer produces (Tp$^{Me,Dr}$Fe)$_2$(picoline) **25**, where the picoline unit is pinced between two iron centers (Figure 5-44). This has also been previously reported with Fe(NacNac).[8]

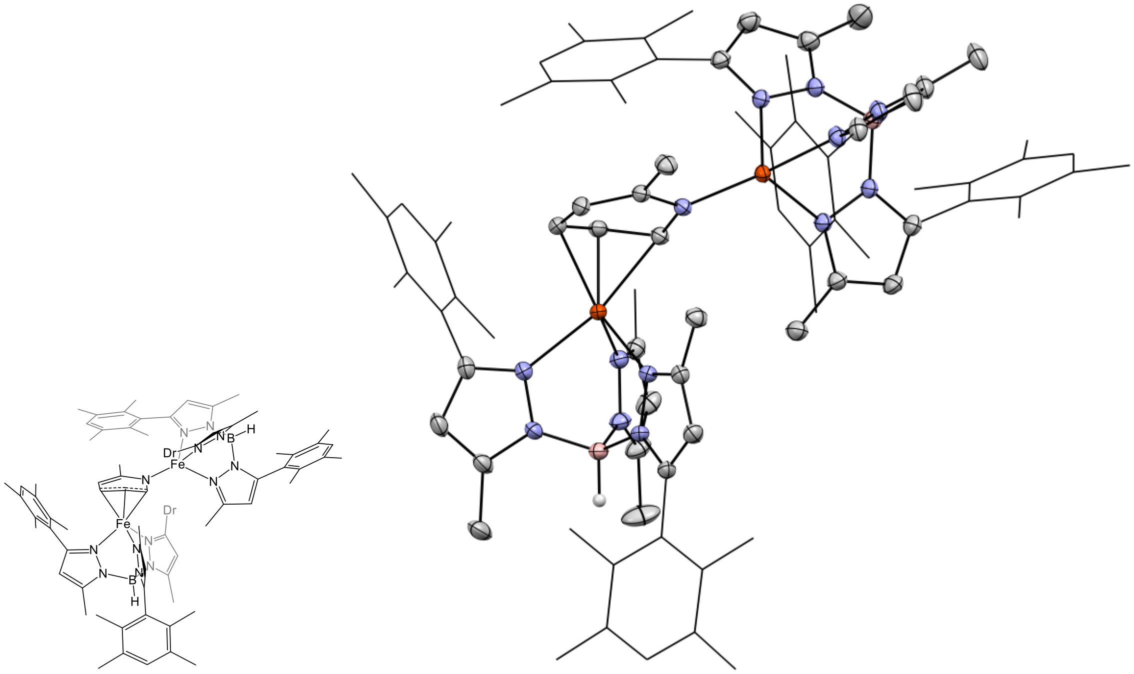

Figure 5-44. Thermal ellipsoid plots (50% probability) of the solid-state structure of $(\mathrm{Tp}^{\mathrm{Me,Dr}}\mathrm{Fe})_2$(picoline) (**25**). Orange, blue, pink, and gray ellipsoids represent Fe, N, B, and C atoms, respectively. Most hydrogen atoms and co-crystallized solvent molecules are omitted for clarity.

Addition of benzaldehyde produces the C−C coupled benzil (**26**). This same product is produced whether benzaldehyde or benzil is added to μ-$N_2$ dimer (Scheme 5-10, Figure 5-45).

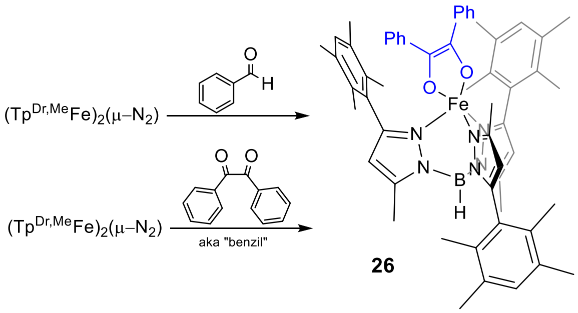

Scheme 5-10. Preparation of $\mathrm{Tp}^{\mathrm{Me,Dr}}$Fe(benzil) **26**.

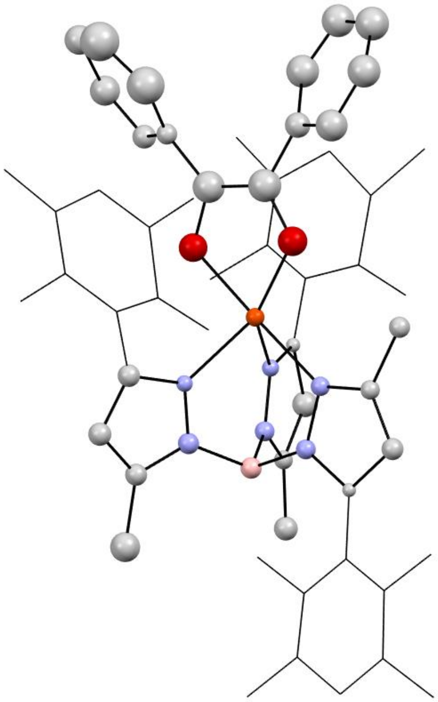

Figure 5-45. Preliminary solid-state structure of $\mathrm{Tp^{Me,Dr}Fe(benzil)}$ **26**. Orange, red, blue, pink, and gray ellipsoids represent Fe, O, N, B, and C atoms, respectively. Hydrogen atoms and co-crystallized solvent molecules are omitted for clarity.

In the presence of $\mathrm{CO_2}$ at low temperature, $\mathrm{(Tp^{Me,Dr}Fe)_2(\mu\text{-}N_2)}$ goes through a dicarbonyl intermediate $\mathrm{(Tp^{Me,Dr}Fe)(CO)_2}$ **27**, before rapidly converting to the carboxylate dimer, $\mathrm{(Tp^{Me,Dr}Fe)_2(\mu\text{-}CO_3)}$ **28**. This was verified by a freeze-trapping EPR experiment and its comparison to synthetically prepared **27** (Figure 5-46). This reactivity has been previously described.[9]

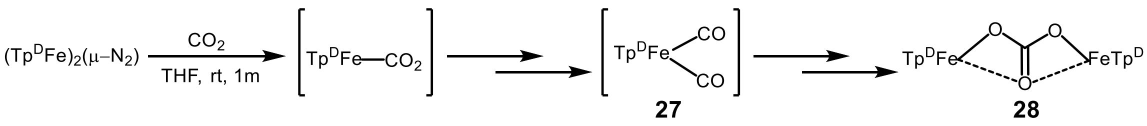

Scheme 5-11. Reactivity of $\mathrm{(Tp^{Me,Dr}Fe)2(\mu\text{-}N_2)}$ and carbon dioxide.

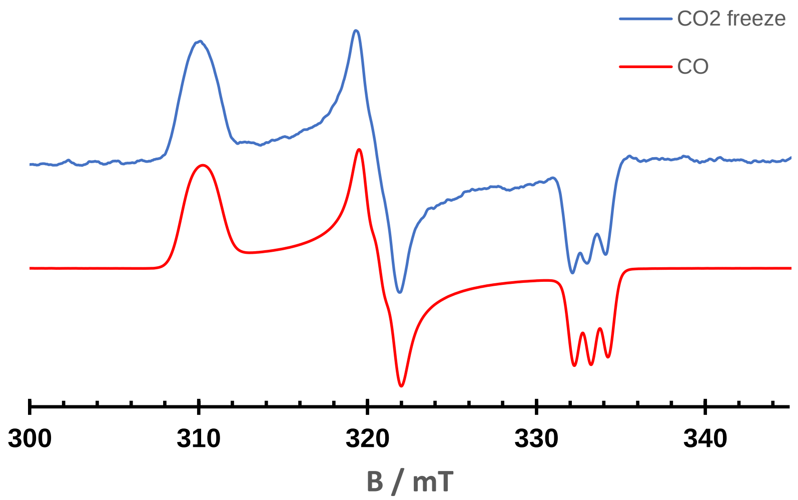

Figure 5-46. X-Band EPR of freeze-trapped intermediate of $(Tp^{Me,Dr}Fe)_2(\mu\text{-}N_2)$ + $CO_2$ and synthetically prepared **27**.

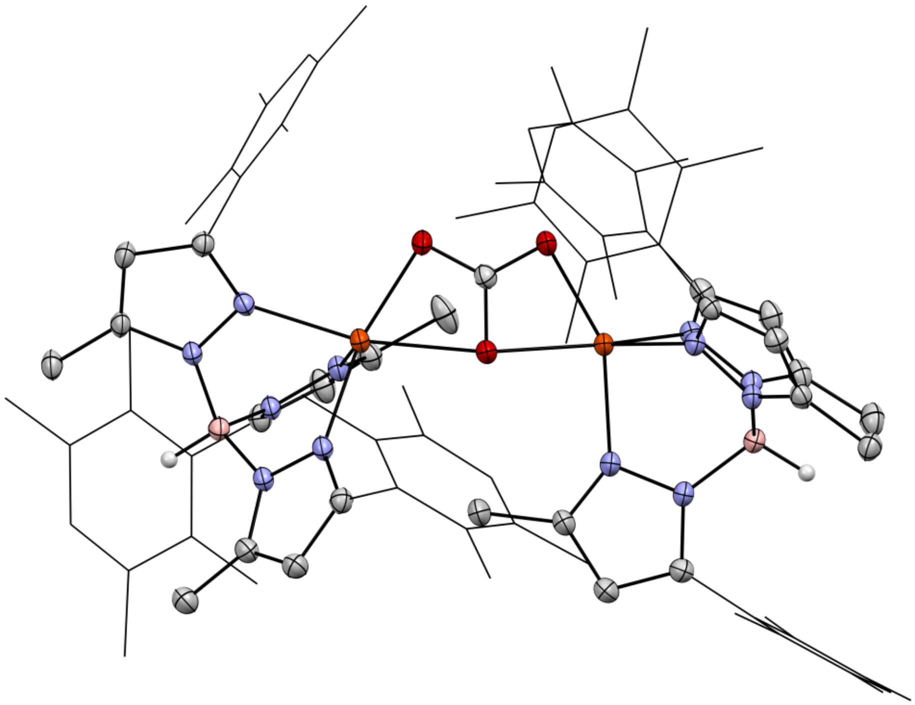

Figure 5-47. Solid-state structure of $(Tp^{Me,Dr}Fe)_2(\mu\text{-}CO_3)$ **28**. Orange, red, blue, pink, and gray ellipsoids represent Fe, O, N, B, and C atoms, respectively. Most hydrogen atoms and co-crystallized solvent molecules are omitted for clarity.

### *Imine and Pyridine-Appended 9,10-Diboraanthracene*

Phosphine-appended donors were highly compatible with the diboroanthracene (DBA) core, however we had much synthetic difficulty in trying to append other donors (N, O, S) to this framework. Here are two examples of those. We attempted to prepare **29** (Scheme 5-12. Preparation of **29**.Scheme 5-12), however in the crystals we prepared one of the arms had been hydrolyzed off (Figure 5-50). Regardless, samples of purported **29** (colorless crystals) did not react with Ni(COD)$_2$ or Ru(COD)(COT), or when heated with VCl$_3$(thf)$_3$. Only the B-OH peak is visible in the $^{11}$B NMR spectrum for the hydrolyzed 29 (Figure 5-49).

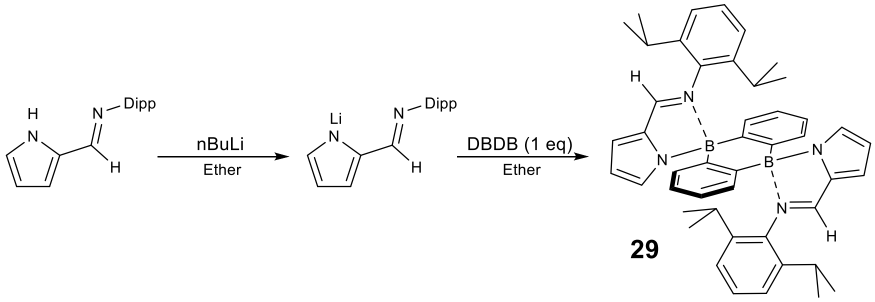

Scheme 5-12. Preparation of **29**.

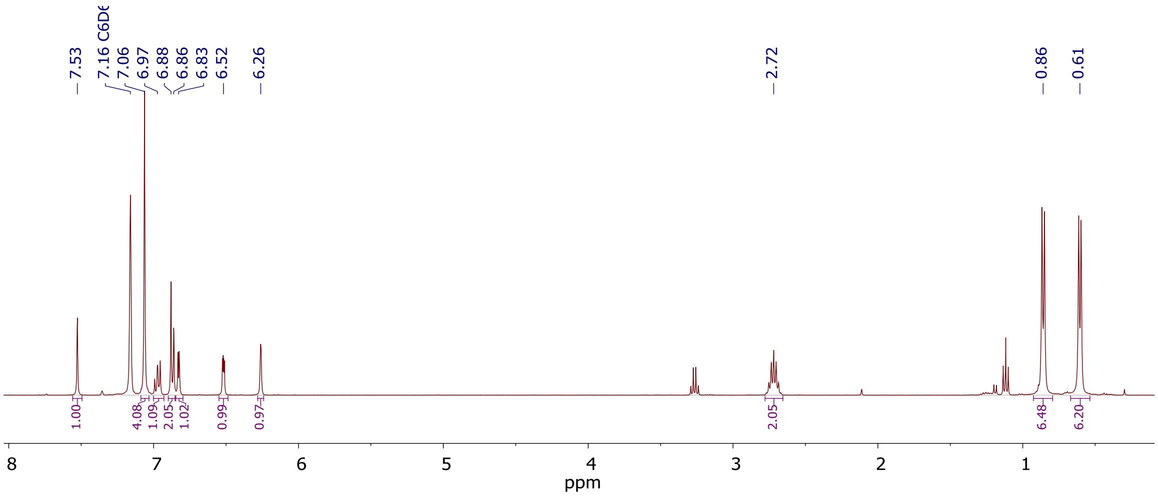

Figure 5-48. $^{1}$H NMR spectrum of hydrolyzed **29** at 400 MHz in $C_6D_6$.

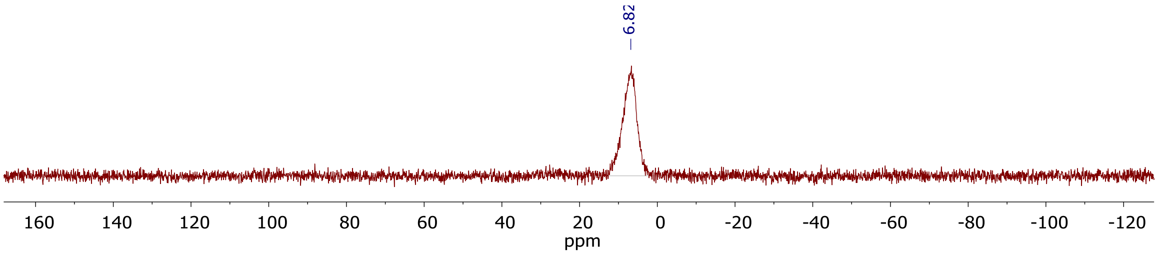

Figure 5-49. $^{11}$B NMR spectrum of hydrolyzed **29** at 128 MHz in $C_6D_6$.

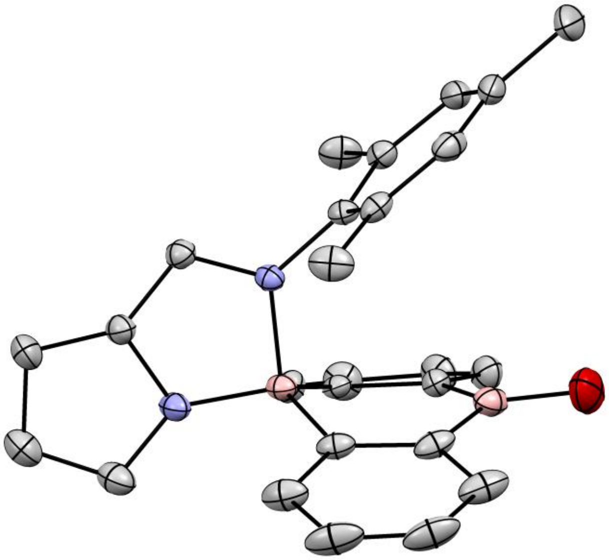

Figure 5-50. Solid-state structure of hydrolyzed **29**. Red, blue, pink, and gray ellipsoids represent O, N, B, and C atoms, respectively. Hydrogen atoms and co-crystallized solvent molecules are omitted for clarity.

Compound **30** was prepared by the route below as ruby-red crystals (Scheme 5-13, Figure 5-52). THF was added to the NMR sample in order to solubilize it in this solvent. In solution the two arms on either side of the DBA are inequivalent (Figure 5-51). No $^{11}$B peak was resolved.

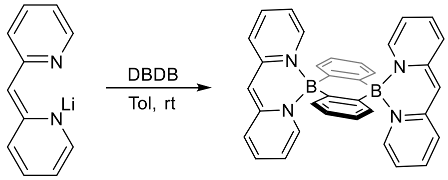

Scheme 5-13. Preparation of $(py_2CH_2)_2$DBA **30**.

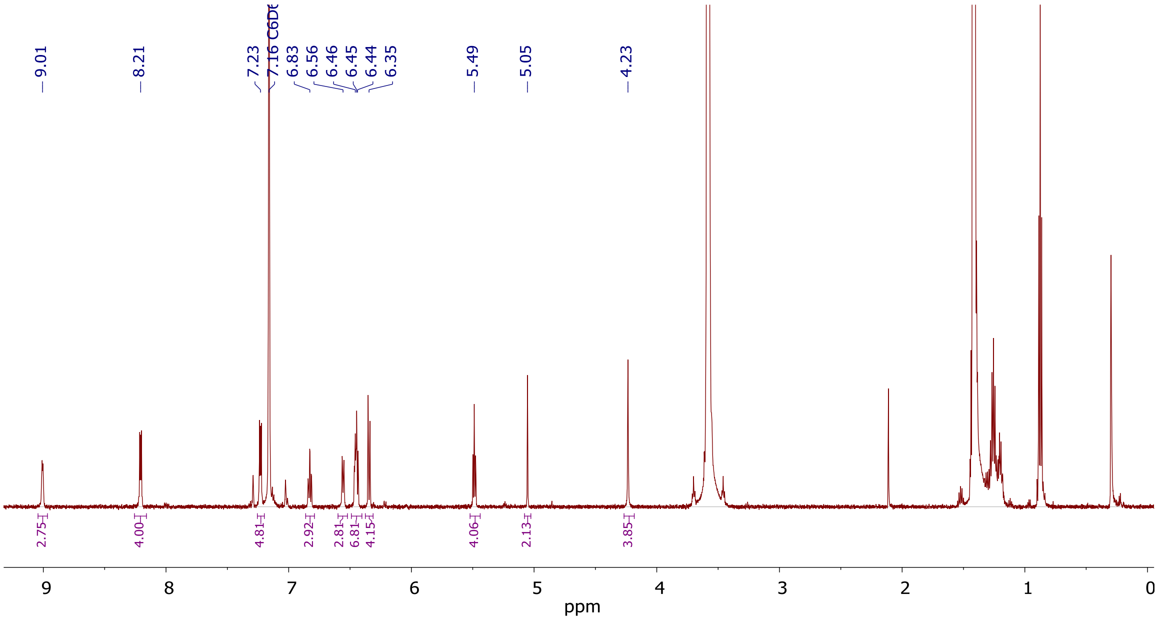

Figure 5-51. $^1$H NMR spectrum of **30** at 600 MHz in 10% THF:$C_6D_6$.

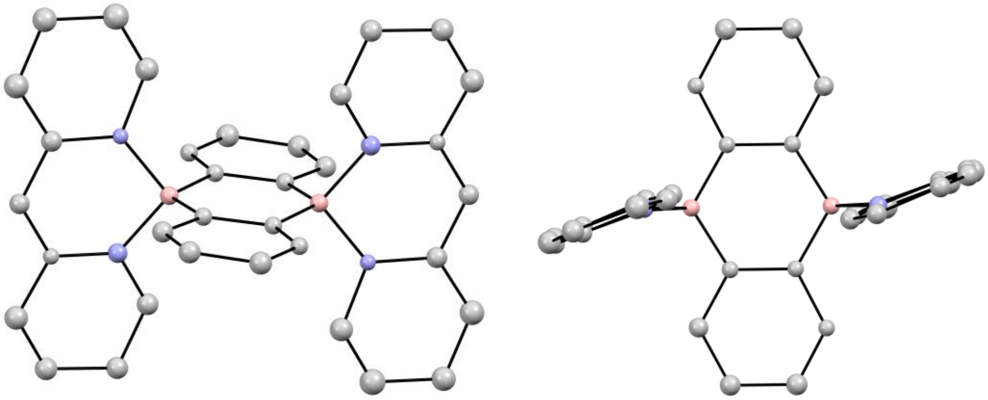

Figure 5-52. Preliminary solid-state structure of $(py_2CH_2)_2$DBA **30**. Blue, pink, and gray ellipsoids represent N, B, and C atoms, respectively. Hydrogen atoms and co-crystallized solvent molecules are omitted for clarity.

## *References*

(1) Chang, Y. H.; Chan, P. M.; Tsai, Y. F.; Lee, G. H.; Hsu, H. F. Catalytic Reduction of Hydrazine to Ammonia by a Mononuclear Iron(II) Complex on a Tris(Thiolato)Phosphine Platform. *Inorg. Chem.* **2014**, *53* (2), 664–666. https://doi.org/10.1021/ic402108w.

(2) Mondragón, A.; Monsalvo, I.; Regla, I.; Flores-Alamo, M.; Castillo, I. Directed Ortho-Metalation versus Reductive Amination in the Preparation of Polytopic, Highly Substituted, and Sterically Congested Amine-S-Arylthiocarbamates as Thiophenol Precursors. *Tetrahedron* **2013**, *69* (45), 9499–9506. https://doi.org/10.1016/j.tet.2013.08.044.

(3) Takeda, N.; Tanaka, Y.; Sakakibara, F.; Unno, M. Synthesis and Structure of Group 10 Metal Complexes with New Tripodal Tetradentate Ligand Bearing One Phosphine and Three Thioether Moieties. *Bull. Chem. Soc. Jpn.* **2010**, *83* (2), 157–164. https://doi.org/10.1246/bcsj.20090187.

(4) Ives, C.; Fillis, E. L.; Hagadorn, J. R. Lithium, Titanium and Vanadium Dithiocarboxylates. *J. Chem. Soc. Dalt. Trans.* **2003**, No. 4, 527–531. https://doi.org/10.1039/b210691d.

(5) Hagadorn, J. R.; Que L., J.; Tolman, W. B. A Bulky Benzoate Ligand for Modeling the Carboxylate-Rich Active Sites of Non-Heme Diiron Enzymes [10]. *Journal of the American Chemical Society*. American Chemical Society December 11, 1998, pp 13531–13532. https://doi.org/10.1021/ja983333t.

(6) Cummins, D. C.; Yap, G. P. A.; Theopold, K. H. Scorpionates of the “Tetrahedral Enforcer” Variety as Ancillary Ligands for Dinitrogen Complexes of First Row Transition Metals (Cr–Co). *Eur. J. Inorg. Chem.* **2016**, *2016* (15–16), 2349–2356. https://doi.org/10.1002/ejic.201501326.

(7) Dugan, T. R.; Bill, E.; MacLeod, K. C.; Christian, G. J.; Cowley, R. E.; Brennessel, W. W.; Ye, S.; Neese, F.; Holland, P. L. Reversible C-C Bond Formation between Redox-Active Pyridine Ligands in Iron Complexes. *J. Am. Chem. Soc.* **2012**, *134* (50), 20352–20364. https://doi.org/10.1021/ja305679m.

(8) Lewis, R. A.; MacLeod, K. C.; Mercado, B. Q.; Holland, P. L. Geometric and Redox Flexibility of Pyridine as a Redox-Active Ligand That Can Reversibly Accept One or Two Electrons. *Chem. Commun.* **2001**, *50* (76), 11114–11117. https://doi.org/10.1039/c4cc05495d.

(9) Kitajima, N.; Hikichi, S.; Tanaka, M.; Moro-oka, Y. Fixation of Atmospheric CO2 by a Series of Hydroxo Complexes of Divalent Metal Ions and the Implication for the Catalytic Role of Metal Ion in Carbonic Anhydrase. Synthesis, Characterization,

and Molecular Structure of [LM(OH)]n (n = 1 or 2) and LM(μ-CO3). *J. Am. Chem. Soc.* **1993**, *115* (13), 5496–5508. https://doi.org/10.1021/ja00066a018.